Design of functional materials from molecular building blocks

Anastasia Voevodin

Submitted in partial fulfillment of the requirements for the degree of
Doctor of Philosophy
in the Graduate School of Arts and Sciences

Columbia University
2019

ABSTRACT

Design of functional materials from molecular building blocks

Anastasia Voevodin

This dissertation is a summary of my research developing the synthesis and assembly of functional materials from nanoscale building blocks and studying their emergent properties.

Chapter 1 introduces superatoms as exciting atomically precise supramolecular building blocks for materials design. Bottom-up assembly of these superatoms into materials with increased dimensionality (0D, 1D, 2D, and 3D) offers exciting opportunities to create novel solid-state compounds with tailored functions for widespread technological applications. I review recent advances to assemble superatomic materials and focus on assemblies from metal chalcogenide clusters and fullerenes. In subsequent chapters, I employ several of these nanoscale superatoms as the precursors to functional materials.

Chapter 2 describes the synthesis and structural characterization of a hybrid solid-state compound assembled from two building blocks: a nickel telluride superatom and an endohedral fullerene. Although a varied library of binary superatomic solids has been assembled from fullerenes, this is the first demonstration of a superatomic assembly using an endohedral fullerene as a building block. $Lu_3N@C_{80}$ fullerenes are dimerized in this new solid-state compound with an unpreceded orientation of the encapsulated metal nitride cluster. I explore the structural characterization of this material supported with computational evidence to explain the dimerization and orientation of the endohedral fullerenes.

In Chapter 3 I begin to detail my exploration into assembling superatoms at micro and meso-scales –which will be the focus of Chapters 3-5. Polymers offer attractive mechanical and self-assembly properties that when combined with the attractive redox, optical, and magnetic properties of molecular clusters, these materials chart new paths to developing advanced materials and technologies. Chapter 3 describes charge transfer interactions between perylene diimide and cobalt telluride superatoms that drive the assembly of a solid-state compound from these two building blocks and inspired the design of a diblock copolymer template.

Chapters 4 and 5 detail the synthesis and characterization of a polymer with functionalized cobalt selenide side units. I describe a cationic homopolymer in Chapter 4 and diblock copolymer in Chapter 5 synthesized from ring opening polymerization of norbornene-derived monomers. Chapter 4 describes potential applications of the homopolymer system such as thin film fabrication. Chapter 5 discusses the self-assembly of the redox-active diblock copolymer into cross-linkable vesicle structures that can encapsulate molecular cargo.

Finally, in Chapter 6 I introduce a new molecular building block to form gold metal surface bonds. Bisaminocyclopropenylidenes (BACs) are a class of carbenes that, much like N-heterocyclic carbenes, have been widely employed for catalysis but have yet to be explored for materials design. This chapter describes the structure and binding orientation of a BAC on an Au(111) surface.

Each of these chapters illustrates how the synthetic flexibility of molecular building blocks enables the design of functional materials with tunable properties.

TABLE OF CONTENTS

LIST OF FIGURES AND TABLES

ACKNOWLEDGEMENTS

I’d like to begin by acknowledging the privilege it is to be trained as a scientist. My entire education has focused on developing my scientific knowledge, critical thinking, curiosity, work ethic and the many other admirable traits that scientists possess. No matter where my future takes me, I will forever be thankful to be trained, to this highest level that academia provides, as a scientist.

I thank my advisor, Xavier Roy, at Columbia University for his support of my graduate research. Xavier has an unmatched enthusiasm and curiosity for science that is energizing to be around. His door was always open to discuss not only science but also to navigate the many political and emotional challenges that arise during grad school. The Roy group members are some of the most inspiring young scientists that I have met and many of them became my closest friends. I want to thank Andrew, Bonnie, and Evan for their mentorship and more importantly for their friendship. I don’t know how the lab, especially our beloved Lucilles, would have run without Evan Doud. I am so lucky to have had Evan next to me in the office, lab, and on call whenever needed (even when a mouse invaded my apartment).

I want to thank Luis Campos for allowing me to be a part of his group. The Campos group members (especially Helen, Spencer, Sam, Jessica, Jonathan, and Andrew) welcomed me as a first-year graduate student and cultivated an energizing and motivating team to be a part of.

I sincerely thank my committee members, Colin Nuckolls, Michael Steigerwald, Laura Kaufman, and Andrew Crowther. I am grateful to have you as my role models with whom I have been able to discuss both scientific and non-scientific topics that greatly impacted my development. Thank you to all of my collaborators that made this research possible.

Melissa, Bonnie, Helen, Makeda, Anouck, Natalia, and Ilana are just some of the remarkable female graduate students who have continuously inspired me and provided a sense of belonging in this department. I am so proud that together we started the Women in Chemistry group. I can't wait to see the impact this group will have on the chemistry community in the future.

Many of my peers (and by many I really mean that there are too many to list you all here) became my closest friends and together we formed our Columbia family. I would not have gotten through graduate school without our Sunday night dinners, Friendsgivings, dance parties, sunrises in Brooklyn, wine nights, and all the adventures in between. It is really an honor to be graduating amongst so many talented chemists who are also some of the best people I have met. Thank you all for making Columbia feel like home.

I would not have been able to complete my PhD without all of my non-Columbia people who put up with hearing about Columbia non-stop. Thank you to my Theta tribe (Susan, Mary, Alice, Andrea) for embarking on our NYC adventure together after college and reminding me to make the most of my time here. Alyssa you have been calming me down, cracking me up, and fueling my Beyoncé obsession since we were roommates in college and I'm so lucky that you haven't stopped. Thank you to my running partners, Kaitlin and Dennis, for letting me rant about experiments, fires, and papers during our warmups and ignoring my protests that we were going "too fast". It's been amazing to have made such great friends while also running some incredible PRs. The Titova sisters, who also make me feel like an honorary sister, thank you for the weekends in NYC and Amsterdam that hit pause on grad school and for your persistent reminders and encouragement to think about what comes next.

I wouldn't have made it to Columbia without the amazing advisors who mentored me before. Dr. Tim Bunning gave me my first research experience at Wright Patterson AFB before I even got to college. Being able to get started doing research at such a young age was an incredible jumping board to success. Prof. Aaron Beeler immediately set the bar on the work ethic and dedication required to be a successful scientist. I have him to thank for encouraging me to finish my degree and continue to grad school even during what was the most difficult period of my life.

I am deeply indebted to the role the US government has had in my education. Being paid by NSF to pursue my PhD is an exceptionally privileged position to be in. Columbia's MRSEC created an amazing network of resources. The Materials and Manufacturing Directorate of AFRL, especially Dr. Michael Donley and Dr. Jeffrey Zabinski, opened their labs and their hearts when they welcomed my parents from Russia. I am forever appreciative of AFRL's support of my family as I grew up at WPAFB. I hope that our government continues to fund, welcome, and invite the scientists and engineers that progress our society forward.

My thesis defense coincides with the 25-year anniversary of my family's immigration to the United States. It is impossible to fully express my gratitude for everything my parents have provided. I was lucky enough to be raised by two scientists who instilled a sense of curiosity about how things work at a young age. My dad was my first lab partner and scientific advisor, a fact that undoubtedly helped at my science fairs. I cannot imagine the challenges my mother surmounted as she earned her PhD in a foreign country, while working, and being a mother to two children. Thank you for having the courage and determination to change everything in order to pursue greater opportunities for Artem and me. One of the last conversations I had with Artem was about my application to Columbia. Throughout graduate school, I have tried to capture my brother's enthusiasm and curiosity and to remind myself, as he often did, to stop taking everything so seriously and let myself enjoy the process.

This PhD is the result of the support of all these individuals and many more. Thank you.

For my parents,

Professor Andrey Voevodin and Dr. Natasha Voevodin

Chapter 1

Introduction to superatomic solids in materials science

1.0 Preface

This chapter has been modified from a manuscript in preparation by Anastasia Voevodin, Evan Doud, Taylor Hochuli, Anouck Champsaur, Xavier Roy, and Colin Nuckolls to be published as an invited review in *Nature Reviews Materials*.

1.0.1 Overview

Crystalline solids are the foundation of countless technologies, from solar cells to lithium ion batteries to quantum computers. Harnessing the unique functions of such materials requires an ability to precisely control or tune their properties. As an example, most modern electronic devices (e.g. computers, cellphones) are based upon our ability to tune the electrical behavior of silicon by introducing small amounts of impurities in the crystalline lattice without changing its overall structure. The Periodic Table of the elements contains 82 stable, non-radioactive, fundamental atomic building blocks that can be used to assemble crystalline materials. Each atom has a set of intrinsic characteristics that governs whether it can bond with other atoms and what structures they will form. This is the foundation of solid-state chemistry. While the fundamental characteristics are intrinsic to each element, the atom itself cannot be altered. This presents an immense challenge for the design of materials with tunable properties because substituting one type of atom for another often leads to wholly new structures with different properties.

The ability to tailor the properties of crystalline solids, by controlling their structures and compositions at the *atomic level* presents unique opportunities for the development of new functional materials by design and the discovery of novel phenomena. Crystalline solids are typically synthesized from elemental and polyatomic precursors though high temperature reactions that intrinsically produce thermodynamically stable compounds. This process inhibits the creation of metastable structures and leaves little room for rational tuning of the materials and their properties. Within this context, assembling hierarchical materials from preformed nanoscale building blocks with well-controlled and tunable properties offers significant benefits over traditional solid-state reactions. One of the key challenges in this approach is to design building blocks that combine both atomic precision and synthetic flexibility. Nanocrystals, for instance, have remarkably tunable compositions and thus have useful electronic and optoelectronic properties, but they are polydisperse and have ill-defined surface chemistry, creating challenges in understanding and controlling the structure-properties relationships of the resulting solids.

Clusters are collections of atoms intermediate in size between a molecule and a bulk solid. Certain clusters adopt structural motifs that confer unique stability and enable the constituent atoms to behave as single units exhibiting collective behaviors. By combining atomic precision, synthetic flexibility and tunable properties, such clusters have emerged as exciting building blocks (or “superatoms”) for materials design. These include noble metal “magic number” clusters, metal chalcogenide molecular clusters, fullerenes, Zintl ions, and boron/silicon/aluminum clusters. Many of these building blocks are stabilized with capping ligands that can act as barriers to limit interactions between cluster cores. These ligands are important in that they direct self-assembly and control coupling between clusters. Theoretical studies of select atomic clusters (e.g., Al_{13}^{-}) have shown that their electronic structures resemble that of traditional atoms, with delocalized cluster-based *s*-, *p*-, and *d*-like orbitals. These clusters were originally named "superatoms", but the term has since then been applied more widely to clusters whose behaviors mimic those of traditional atoms. For this dissertation, I will apply the more inclusive definition of superatoms to refer to the group of atomically precise and synthetically tunable metal chalcogenide clusters.

Figure 1.1 illustrates the general vision of accessing desired materials properties from superatomic solids by employing a bottom-up synthetic approach to judiciously synthesize tunable superatoms and control their assembly into higher dimensional structures. Recent excellent

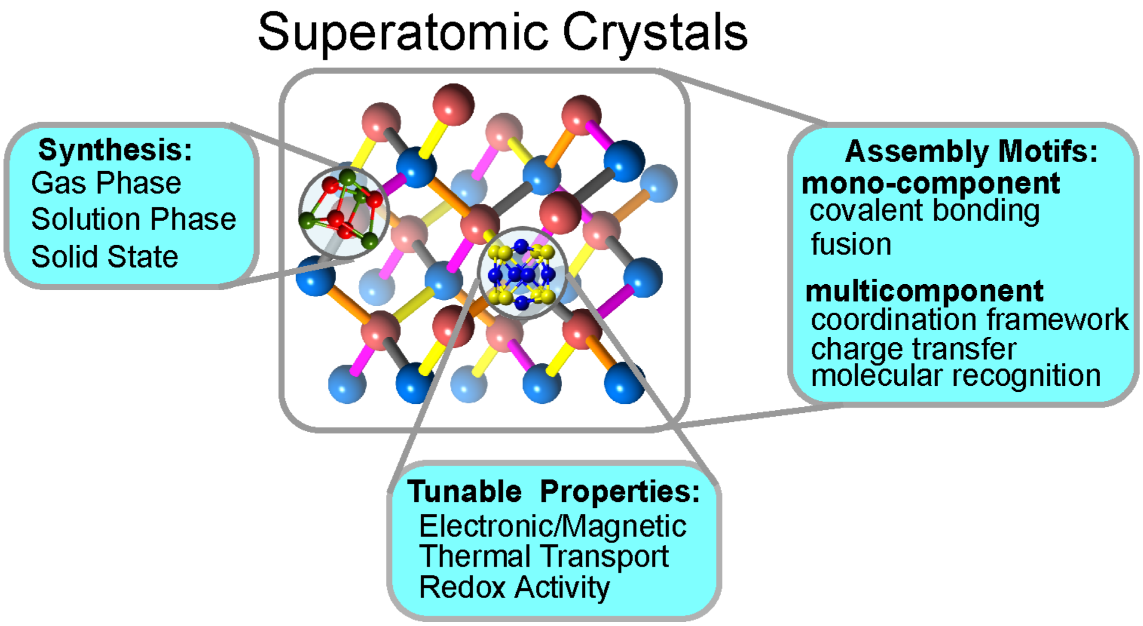

Figure 1.1 Achieving assemblies of superatomic materials is enabled by the tunable synthesis of the individual superatoms which enable control of the composition, shape, and size of the building blocks and thus effect their material's properties. Several synthetic strategies have been developed for the assembly of mono-component and multi-component superatomic materials using covalent bonding, fusion, coordination frameworks, charge transfer and molecular recognition motifs by functionalization of the superatoms' ligands. These assemblies have enhanced electronic coupling resulting in the emergence of tunable materials properties with enhanced redox activity, new magnetic, electronic, and thermal transport behaviors.

reviews by Khanna[1] and Jena[2] explore the detailed theoretical work on superatoms[3] that highlight the unique potential of their emergent properties.

1.1 Strategies for the synthesis of superatoms

The creation of superatomic crystals begins with the design and synthesis of superatomic building blocks capable of assembling together while maintaining their individual structure. The synthesis of metallic clusters and transition metal chalcogenide molecular clusters has been extensively reviewed.[4-6] In this section, I will highlight three general synthetic strategies (gas phase synthesis, solution phase synthesis, and excision from solid state compounds) to form molecular clusters used in creating cluster-assembled materials and discuss their isolated properties. These general synthetic approaches are highlighted in Figure 1.2.

***Gas Phase Synthesis*.**

Superatoms were originally discovered in gas phase experiments. References to the formation of atomic aggregates date back to the 1930s but the systematic study of clusters in mass spectrometer began in earnest in the 1970s and 1980s. The concept of superatoms was originally theoretically proposed by Khanna and Jena[7] and first reported experimentally by Casselman and co-workers for Al clusters produced in the gas phase[8]. Beyond Al clusters, many other types of magic size clusters can be produced by laser induced vaporization of metal substrates or other vaporization methods, and detected by mass spectroscopy.[9-11] This approach presents two major limitations: the clusters are typically unstable and highly reactive when removed from the vacuum environment, and the amount of cluster produced is generally too small to be used as building block for creating solid state materials.

Long[12] and co-workers developed a modified gas phase method to prepare transition metal chalcogenide clusters that could be handled outside the vacuum chamber by evaporating bulk binary compounds within a partial vacuum containing vapors of a capping ligands. One key limitation of this method is that it produces many different clusters, which need to be separated and characterized individually, resulting in very low yields for any superatom.

Solution phase synthesis.

Solution phase synthesis is the most widely used and efficient approach to prepare noble metal and metal chalcogenide molecular clusters with varied structures.[4-5, 13] For noble metals, the synthesis of their clusters has been reviewed extensively.[14-16] For metal chalcogenide clusters, Dance and Fisher[5] classify the most common strategies to synthesize them in two categories: i) association of ions, and ii) reaction of a metal atom precursor with a chalcogen atom precursor.

In the first approach, a M^{n+} ion is reacted with an E^{2-} source under conditions that result in the formation of a cluster.[5] The synthesis of the magnetic cluster $[Fe_6S_8(PEt_3)_6][BPh_4]_2$[17] is an archetypical example: $Fe(BF_4)_2.6H_2O$ is reacted with bubbling H_2S through the solution that contains excess of PEt_3. Upon addition of $NaBPh_4$, black crystals of $[Fe_6S_8(PEt_3)_6][BPh_4]_2$ form. A modified strategy, primarily developed by Fenske, reacts trialkyl silyl chalcogenide reagents with metal halide to eliminate trialkyl silyl halides and form metal-chalcogen bonds. The use of trialkyl silyl chalcogenide reagents is a preferred approach due to their ease of handling over gaseous reagents as well as the facile removal of the trialkyl silyl halides.

The second approach to synthesize metal chalcogenide superatoms combines a reactive source of metal [functionally, a metal(0)] with a reactive source of chalcogen (typically a phosphine chalcogenide).[5] The quintessential example of this approach was pioneered by Steigerwald and co-workers[18] in the synthesis of $Ni_9Te_6(PEt_3)_8$, which is obtained by combining $Ni(COD)_2$, $TePEt_3$, and PEt_3 in a 1:1:1 molar ratio in toluene.

Excision from solid state compounds.

Several bulk solids have identifiable superatoms as their fundamental structural units, which can be excised from the lattice. These materials are typically second and third row early transition metal chalcogenides or halide such as $Re_6E_8X_2$,[19-21] Mo_6E_8,[22-23] and $Li_2Nb_6X_{16}$ [E = S, Se, Te, and X = Cl, Br, I].[24-25] Excision typically involves heating the solid with excess capping ligand (e.g., cyanide, hydroxide, halide) that then coordinates the excised clusters to stabilize the core. These capping ligands can then be substituted with a variety of organic molecules.

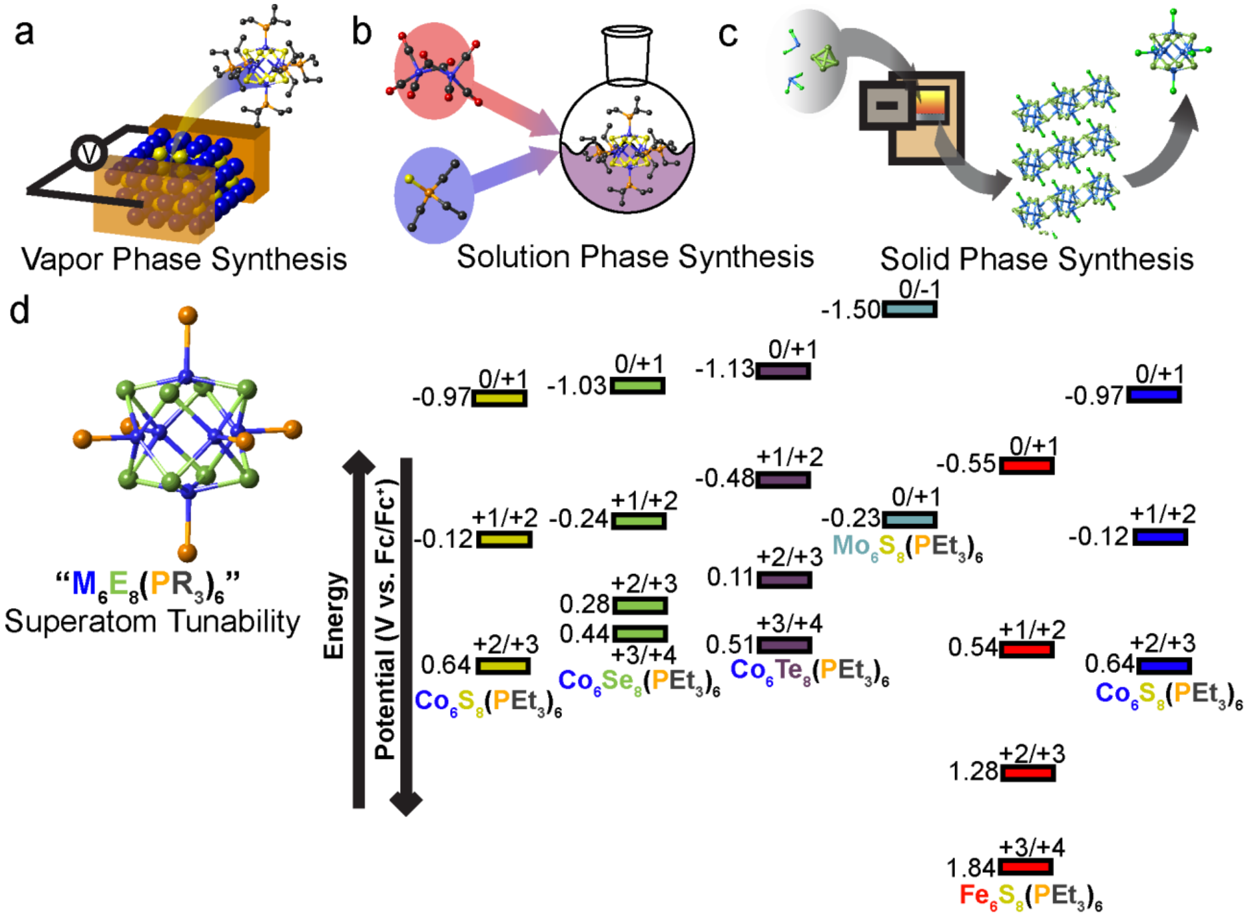

Figure 1.2. (a, b, c) Schematics of three methods of superatom synthesis described in the sections above (d) Changes in the cyclic voltammetry measured redox events of a family of “$M_6E_8(PR_3)_6$” superatoms illustrating the tunability by varying superatom core composition. Energy levels are adapted from previously published data.[26-29]

1.2 Isolated properties of superatoms overview

The properties of atomic solids are determined by their constituent atoms and similarly, superatomic materials have collective properties that result from the constituent superatoms and their interactions in the solid state. The choice of superatoms is thus critical in the design of these materials. Unlike isolated atoms which have fixed properties, the properties of superatoms can be tuned in several ways (constituent atoms, ligand shell, etc.) which allows for the tuning of the properties of superatomic crystals. In the following sections, I will describe several properties relevant to materials design (electrochemical, magnetic, optical) and how those properties can be precisely controlled in superatoms.

Electronic properties of isolated superatoms.

Bonding within the cluster core produces a highly delocalized electronic structure,[30] providing the reversible electron transfer ability. The composition and structure of the core dictates the electrochemical properties. Metal chalcogenide clusters are typically electron rich with oxidation potentials that can rival alkali metals. Other artificial atoms such as $Fe_8O_4(pz)_{12}Cl_4$ (pz = pyrazolate anion, $C_3H_3N_2^-$) and Al_{13}^- are excellent electron acceptors.

The electrochemical properties of clusters can also be fine-tuned through rational design of the ligand shell. Varying the capping ligand on the core can modulate the potentials at which the reversible redox processes occur. When capped with strong σ-donor ligands such as trialkyl phosphines, metal chalcogenide building blocks are electron-rich. By replacing some of these phosphines with weaker σ-donor or π-acceptor ones, one can effectively and precisely shift the oxidation potential. Khanna recently published calculations on $Ni_9Te_6(PEt_3)_8$ showing that the ionization energy increases by ~2.5 V when PEt_3 ligands are removed from the core, and by an additional ~0.4 V when CO ligands are subsequently attached.[31]Furthermore, the tunable effects of the ligand shell on the electrochemical properties of the hexanuclear cobalt sulfide superatoms was demonstrated both theoretically and experimentally.[32] A series of $Co_6S_8(PEt_3)_{6-x}(CO)_x$ ($x = 1 – 3$) superatoms were synthesized and anion photoelectron spectroscopy was used to probe their electron affinity and electronic structures. It was found that increasing the degree of carbonylation of the superatom produced superatoms with higher electron affinities, agreeing with the previous calculations presented above.[32]

The examples above highlight the electrochemical flexibility of superatoms. An additional dimension of tunability emerges by adding multiple types of metal atoms to the cores. For example, the Long group modified the redox behavior of the Re_6Se_8 core by replacing one of the metal atoms with Os.[33]

Magnetic properties of isolated superatoms.

The traditional metallic superatoms first described by Khanna and Jena[7] have closed shell electronic structures and are thus of limited used for their magnetic properties. Many theoretical studies suggest that magnetic metallic clusters could be produced by incorporating transition metal or rare earth metal atoms into the core of a diamagnetic cluster or by assembling the cluster entirely from magnetic elements.[34-37] This attractive concept lacks experimental demonstrations because such magnetic superatoms are too unstable to be used as building blocks.[38-40]

In addition to metallic properties, a wide range of magnetic states are experimentally accessible in binary superatoms.[41] Metal oxide clusters often exhibit large spin states resulting from the coupling of the metal spins through superexchange.[42] Heavier chalcogens can also promote strong magnetic coupling, leading to ferromagnetic or antiferromagnetic ground states.[43] A few theoretical studies have begun to explore how the complex relationship between superatom composition, structure and charge state, and the resulting magnetic behavior. For example, one such study recently demonstrated the theoretical magnetic tunability of the superatom $Ni_9Te_6(PR_3)_8$.[31]

In a strategy related to that for magnetic metallic superatoms, new magnetic metal chalcogenide superatoms can be created by varying the core electron count via metal atom substitution. For instance, replacing one Re atom in the diamagnetic core of Re_6Se_8 with Os produces a S = ½ core.[33]

Optical properties in isolated superatoms.

The optical properties of superatoms have received widespread attention ever since the octahedral Re_6Q_8 and Mo_6X_8 families were first shown to exhibit intense and long-lived photoemission. These superatoms are particularly attractive building blocks because their emission energy can be tuned by modifying the composition or charge of the core, or substituting their capping ligands.[44-46] In a recent development, non-centrosymmetric Sn_4S_6 superatoms were used to create a spectrally broadband and highly directional warm-white-light emitter that is driven by an inexpensive, low-power continuous-wave infrared laser diode.[47]

1.3 Introduction to monocomponent superatomic assemblies.

Until recently, superatoms have been used infrequently as building blocks to create solid state materials.[3, 48] In the past few years, however, superatomic crystals have received much attention, resulting in materials with broader compositions, structures and properties. For this introduction, we will classify the superatomic crystals based on the number of heterogeneous components that make up the assembly. Monocomponent compounds have one type of superatom while multicomponent compounds contain more than one type of superatom. Both types of superatomic crystals can exhibit collective properties due to inter-superatom coupling in the solid state. The following sections review synthetic methods to assemble superatomic crystals and discuss the relationship between the structure and properties of the materials.

Monocomponent superatomic crystals display properties that that depend not only on the identity of the superatom but also how these superatoms are arranged in a lattice and how they couple to each other.

Ligand Interactions.

Capping ligands on the superatoms can direct the assembly of the superatomic crystals and can influence the resulting collective properties. In a recent report, Li and co-workers[49] installed two 1,1-bis(diphenylphosphino)methane (PCP) ligand on Au_{21} which act as “hooks” to link neighboring superatoms together through π–π and π–anion interactions. This ligand modification allows for the formation of 1D nanofibrils that further assemble into a 3D superatomic crystal. This process results in a material with tunable electrical conductivity: by changing the counterions used in the assembly, the electrical conductivity can be modulated by over two orders of magnitude.

Ligands with functional groups can engage into specific inter-superatom interactions. In one illustrative study, p-mercaptobenzoic acid (p-MBA) ligands were used to assemble the silver superatoms ($Na_4Ag_{44}(p\text{-}MBA)_{30}$) into a crystalline structure held together by H-bonds.[50] These interactions lead to a cooperative, chiral mechanical response in which the clusters rotate in concert in the same direction when an external pressure is applied to the crystal, akin to meshing gears rotating.

Covalent union of superatoms.

While engineering superatoms with ligands that direct the formation of superatomic crystals can be a powerful tool, it is of limited use. It can be difficult to predict and finely control, and it leads to structures with weak inter-superatom coupling. Developing the chemistry to make discreet oligomers from superatoms is a necessary first step to creating extended assemblies of covalently linked superatoms. Providing stability and solution processability, the capping ligands on the surface atoms of superatoms are also the entry point forming inner-sphere bonds.

A promising strategy to control the coordination spheres of superatoms was recently developed to yield site-differentiated superatoms in octahedral metal chalcogenide, $M_6E_{8,}$ clusters. By using ligands that can be selectively dissociated or exchanged, this approach can be used to form discrete oligomers or dimensionally controlled polymers of superatoms. Figure 1.3 illustrates two strategies for the formation of discrete oligomers: the core of the site-differentiated superatoms can be connected either by bridging linkers formed with reactive capping ligands (e.g. -NH2, -COOH, -RNC, olefins) or by direct fusion of the cores upon removal of the reactive ligand. Both methods require a site-differentiated superatom with at least one unique chemically reactive ligand for modification. The next few sections will detail the formation and properties of the bridged and fused dimers and oligomers of metal chalcogenide superatoms. I will then introduce my work on templating of superatoms into polymer materials using the reaction chemistry developed to form oligomers of superatoms.

Site-differentiated superatoms.

A powerful approach to create oligomers of superatoms is to design the building blocks with differentiated sites, which can be selectively modified, dissociated or substituted post-synthesis. Figure 1.3 presents examples how such building blocks can be used to form dimers of superatoms. Site-differentiated superatoms can be prepared by installing inert ligands at certain positions on a preformed core or by synthesizing the cores with both inert and labile ligands.

The first approach is exemplified by the synthesis of $[Re_6E_8(PR_3)_{n(}X_{(6-n)}]^{(n-4)+}$ superatoms, which are prepared from $[Re_6E_8X_6]^{3–/4–}$ [51] by substituting some of the halide ligands with various phosphines PR_3. Labile acetonitrile ligands can then be installed on the core to form site-differentiated clusters such as $[Re_6Se_8(PR_3)_4(MeCN)_2]^{2+}$.[52] These clusters have been used as building blocks for the creation of a variety of oligomers and supramolecular arrays via ligand substitution with bridging 4,4'-bipyridine (Figure 1.3a)[53-54].

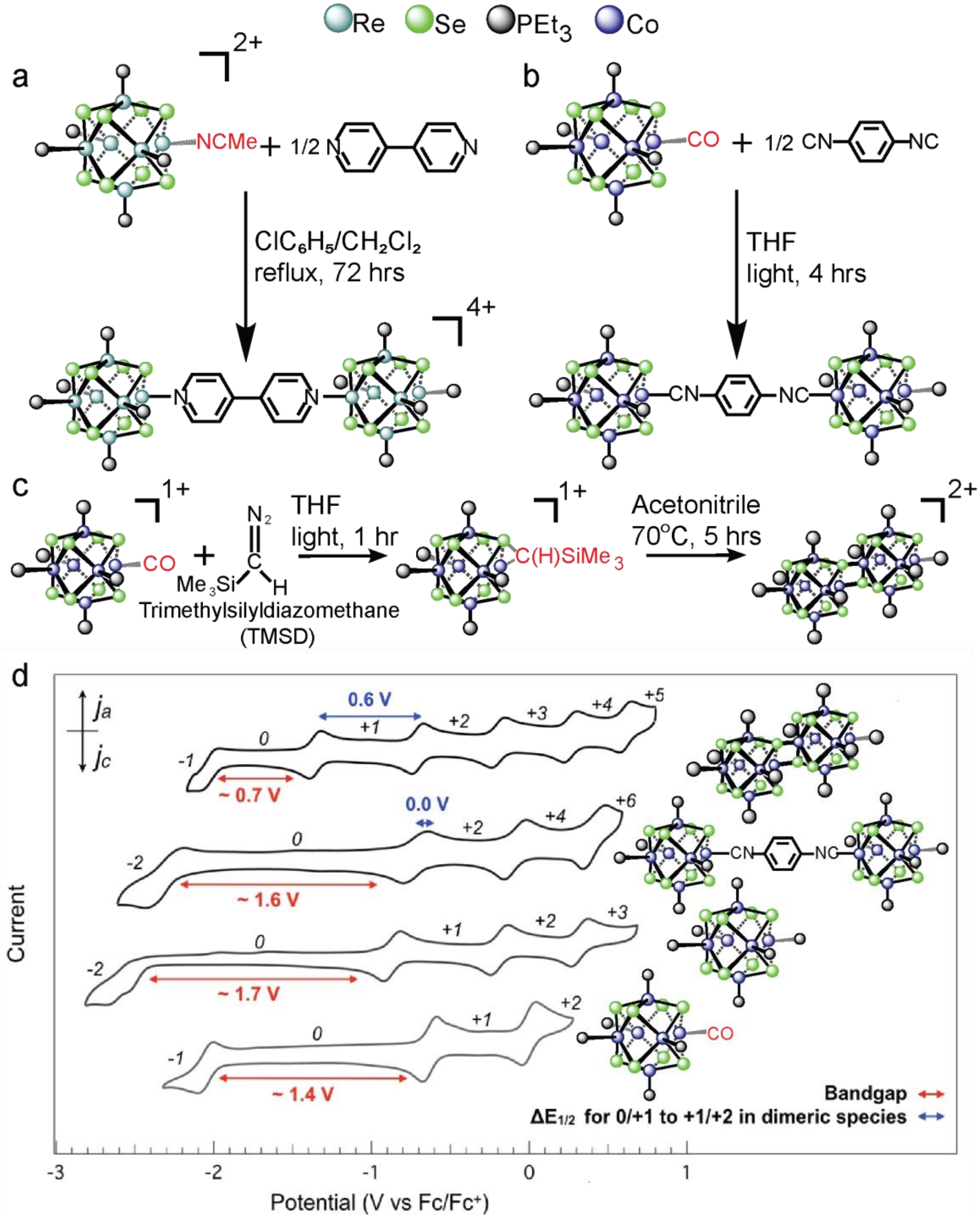

Figure 1.3. (a) Synthetic strategy for the formation of a bridged dimer a with a $[Re_6Se_8(PEt_3)_4(MeCN)_2]^{2+}$ building block cluster and 4,4'-dipyridyl bridging ligand, and with (b) a $Co_6Se_8(PEt_3)_5(CO)$ building block cluster and a 1,4-phenylene diisocyanide bridging ligand. (c) Synthesis of fused dimer with a $Co_6Se_8(PEt_3)_5(CO)$ building block cluster and trimethylsilyldiazomethane.[54-56] (d) Cyclic voltammograms comparing the electrochemical properties of cobalt-selenide superatom building blocks, including the monomeric clusters of $Co_6Se_8(PEt_3)_5(CO)$ and $Co_6Se_8(PEt_3)_6$ unit, and two oligomeric species: the isonitrile-bridged dimer and the fused dimer. The red arrow shows the effective bandgap as estimated from CV and the blue arrow shows the ΔE1/2 for both dimer species.

The second approach is exemplified by the carbonylated superatoms $Co_6Se_8(CO)_x(PEt_3)_{6-x}$.[55] The important finding that enabled isolation of these site-differentiated clusters was that an excess of elemental Se in combination with $Co_2(CO)_8$ and a phosphine yields a distribution of carbonylated products that can be easily separated by traditional silica gel chromatography or fractional crystallization. The CO group is a synthetically useful handle that can be easily manipulated. The Co_6Se_8 cores can be dimerized by replacing the CO with a rigid ditopic linker, 1,4-phenylene diisocyanide (CNC_6H_4NC), shown in Figure 1.3b. This bridging strategy gives rise to a diversity of superatom dimer structures simply by varying the linking group and allows weakly coupled dimers to be studied. This approach has been championed as a breakthrough in nanoscience.[57]

Fused dimers.

While the ligand-bridging strategy allows superatom dimers to be studied in the weakly coupled limit, fusing them together leads to much stronger inter-superatom coupling. Until recently, there were only a few examples of discrete superatom fusion and these existing strategies are not generalizable.[58-61] Dr. Anouck Champsaur (former graduate student of Professor Colin Nuckolls group) developed a novel chemical transformation to covalently expand the Co_6Se_8 core to a $Co_{12}Se_{16}$ core through direct fusion.[56] The key intermediate is obtained in one step, in high yield, from a carbonylated cluster and contains a carbene ligand that acts as a bifunctional protecting group for the Se and Co atoms involved in the subsequent fusion shown in Figure 1.3c.

Electrochemical properties of Co_6Se_8 dimers.

The electrochemical properties of Co_6Se_8 dimers depends on the type of inter-superatom linkage, as illustrated in Figure 1.3d. Both the $Co_6Se_8(PEt_3)_6$ and $Co_6Se_8(CO)(PEt_3)_5$ superatoms exhibit three reversible one-electron redox transformations. The carbonyl ligand on the site-differentiated core, however, shifts the energy levels so that the charge states 0 to 3+ and 1– to 2+ are accessible for $Co_6Se_8(PEt_3)_6$ and $Co_6Se_8(CO)(PEt_3)_5$, respectively. Three redox couples are also observed for the diisonitrile-bridged dimer (BD) $Co_{12}Se_{16}(PEt_3)_{10}(CNC_6H_4NC)$ synthesized from $Co_6Se_8(CO)(PEt_3)_5$ precursors. The three redox couples come from the additive shuttling of two electrons with each redox event resulting in double number of electrons being shuttled. The fused dimer (FD) of $Co_{12}Se_{12}(PEt_3)_{10}$, however, displays a drastically different redox behavior: the cyclic voltammogram shows five distinct and reversible one-electron events giving access to the 1– to 5+ charge states. Accessing more redox states and thus enhancing the electrochemical activity of this 1D structure is a result of the direct coupling of superatomic cores.

Higher order oligomers and dendrimers.

One-dimensional (1D) structures can be prepared via stepwise ligand substitution of zero-dimensional (0D) superatomic units. For instance, trimers of Co_6Se_8 are prepared by reacting *trans*-$Co_6Se_8(CNC_6H_4NC)_2(PEt_3)_4$ (formed from *trans*-$Co_6Se_8(CO)_2(PEt_3)_4$) with two site-differentiated $Co_6Se_8(CO)(PEt_3)_5$ units to link them together via photodissociation of the CO ligand.[55] This is a general strategy that is currently being explored to make 1D wires with a diversity of core structures.

In Figure 1.4, we present an oligomer as another type of 1D nanostructure created from superatoms: a metallodendrimer array. Zheng and co-workers synthesized the oligomer[62-63] by reacting six equivalents of the site-differentiated unit $[Re_6Se_8(PEt_3)_5(L)]^{2+}$ (L is a ditopic bipyridyl ligand) with one equivalent of $[Re_6Se_8(MeCN)_6]^{2+}$. The labile acetonitrile ligand is substituted with the pyridine group, leading to coupling of the superatomic units.

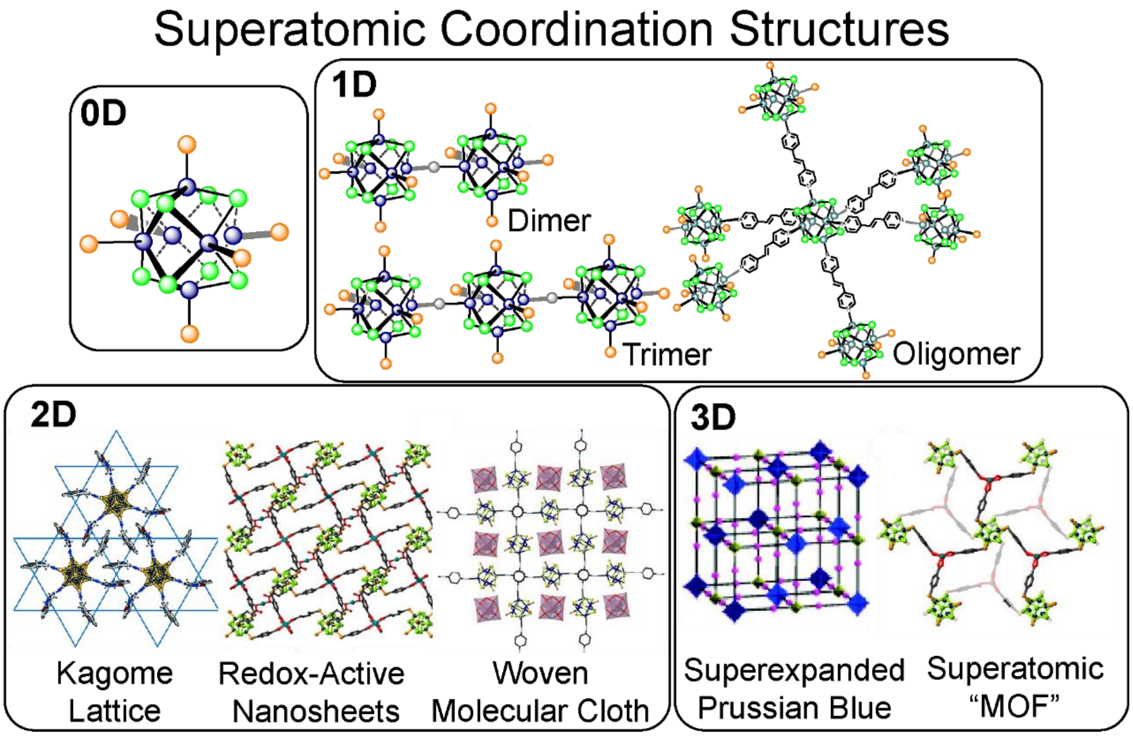

Figure 1.4. Coordinating frameworks are formed through ligand interactions of superatoms which are 0D structures using hydrogen and covalent bonding and metal coordination to form 1D dimers[55], trimers[55], and oligomers[54]. The 1D structures can be further extended to form 2D assemblies such as the Kagome lattice[64], redox-active nanosheets[65], and woven molecular cloth[66]. 3D assemblies can also be formed using coordination frameworks and examples of this type include a superatomic "MOF"[65] and superexpanded Prussian Blue structures[25].

Diblock copolymer containing superatoms.

My initial aim was to develop a strategy to expand the assembly of superatoms beyond crystals and into mesoscale structures using a polymer template. In Chapter 2, I will discuss my initial attempts of using charge transfer interactions between cobalt telluride superatoms and block copolymers with pendant perylene diimide molecules to access mesoscale assemblies of superatoms. The synthetic strategy developed by Anouck Champsaur and Alexandra Velian (former Nuckolls' group members) to prepare and functionalize the site-differentiated $Co_6Se_8CO(PEt_3)_5$ cluster[55] enabled the covalent functionalization of the cobalt selenide superatom onto a polymer backbone. Using this site-differentiated cluster, I was sought to synthesize and self-assemble a diblock copolymer containing pendant cobalt selenide superatoms.[67] Chapter 4 will detail my research on the synthesis, assembly, and properties of a diblock copolymer with pendant cobalt selenide clusters that self-assembles into vesicles.

1.4. Multicomponent superatomic crystals

Achieving enhanced coupling between superatomic building blocks is not limited to synthesis of extended materials through covalent bonding in 1D nanostructures. Two dimensional (2D) and three dimensional (3D) multicomponent solids were inspired by earlier examples of inorganic-organic multicomponent solids having hierarchical order. The cyanide-functionalized cluster $[Re_6Se_8(CN)_6]^{4-}$ was used by Batail and co-workers as a building block to create the inorganic-organic hybrid material (EDT-TTF-CONH$_2$)$_6$[Re$_6$Se$_8$(CN)$_6$] (EDT-TTF-CONH$_2$ = amide-functionalized ethylenedithiotetrathiafulvalene) with a Kagome lattice shown in the 2D panel of Figure 1.4 that exhibits metallic electrical transport.[64, 66] A series of other atomically precise clusters with M_6E_8 motifs have been reported to have charge transfer interactions with organic molecules such as TTF, TCNQ or other inorganic clusters yielding interesting conductivity behavior in assembled solids.[61, 68-73] In Chapter 2, I will introduce a new binary superatomic ionic solid [Co$_6$Te$_8$(PEt$_3$)$_6$][C$_5$-CN$_2$-PDI] whose assembly was driven by the transfer of electrons from electron-rich cobalt telluride superatom to the perylene diimide acceptor molecule.

Building on this foundation of inorganic-organic superatomic materials, metal chalcogenide molecular building blocks have been assembled with fullerenes into binary superatomic crystals[74] held together by charge transfer interactions. This initial discovery was led by my advisor, Professor Xavier Roy while under the guidance of Professor Colin Nuckolls and

Dr. Michael Steigerwald. Since then, an entire library of multicomponent superatomic solids (several highlighted in Figures 1.5-7) has since been synthesized by members of both Nuckolls and Roy groups. In addition to exploiting inter-superatom charge transfer to drive the assembly of the materials, superatoms have been functionalized with capping ligands capable of molecular recognition.

In the past few years, there has also been exciting new direction of synthesizing 2D and 3D superatomic coordination structures by harnessing the utility of the ligands of metal chalcogenide superatoms. For example, octahedral superatoms functionalized with cyanide ligands, $[M_6E_8(CN)_6]^{n-}$ (M = Re, Mo, W; E = S, Se, Te) and $[M_6Cl_{12}(CN)_6]^{n-}$ (M = Nb, Ta), have been used to replace the traditional atomic building block $[Fe(CN)_6]^{4-}$ to form cluster-expanded PB analogs[66, 75-76] and more exotic superatom-based PB frameworks can also be produced.[76] Metal organic framework (MOF) synthetic strategies have been applied to create 2D and 3D frameworks from preformed carboxylic acid-functionalized Co_6Se_8 superatoms[66] that react with Zn^{2+} ions to form a crystalline superatomic molecular framework with carboxylate-zinc-carboxylate nodes. Another example, is the use of electrocrystallization to oxidize *trans*-$Co_6Se_8(CNC_6H_4NC)_2(PEt_3)_4$ in the presence of shape complementary anionic template ($Mo_6O_{19}^{2-}$) to yield covalent 2D interwoven superatom polymer strands (see 2D panel in Figure 1.4)[66] .

Fullerene-based superatomic crystals from charge transfer assembly.

Superatoms can be electron rich or electron poor, depending on their core composition and capping ligands. By combining superatoms with complementary redox characteristics in solution, one can assemble superatomic crystals via charge transfer as illustrated in Figure 1.5a. The synthetic strategy employs an electron rich superatom (e.g., $Co_6Te_8(PEt_3)_6$, $Ni_9Te_6(PEt_3)_8$) that transfers charge to an electron accepting unit (e.g., C_{60}) to produce binary ionic compounds whose structures are characterized by single crystal x-ray diffraction (SCXRD).

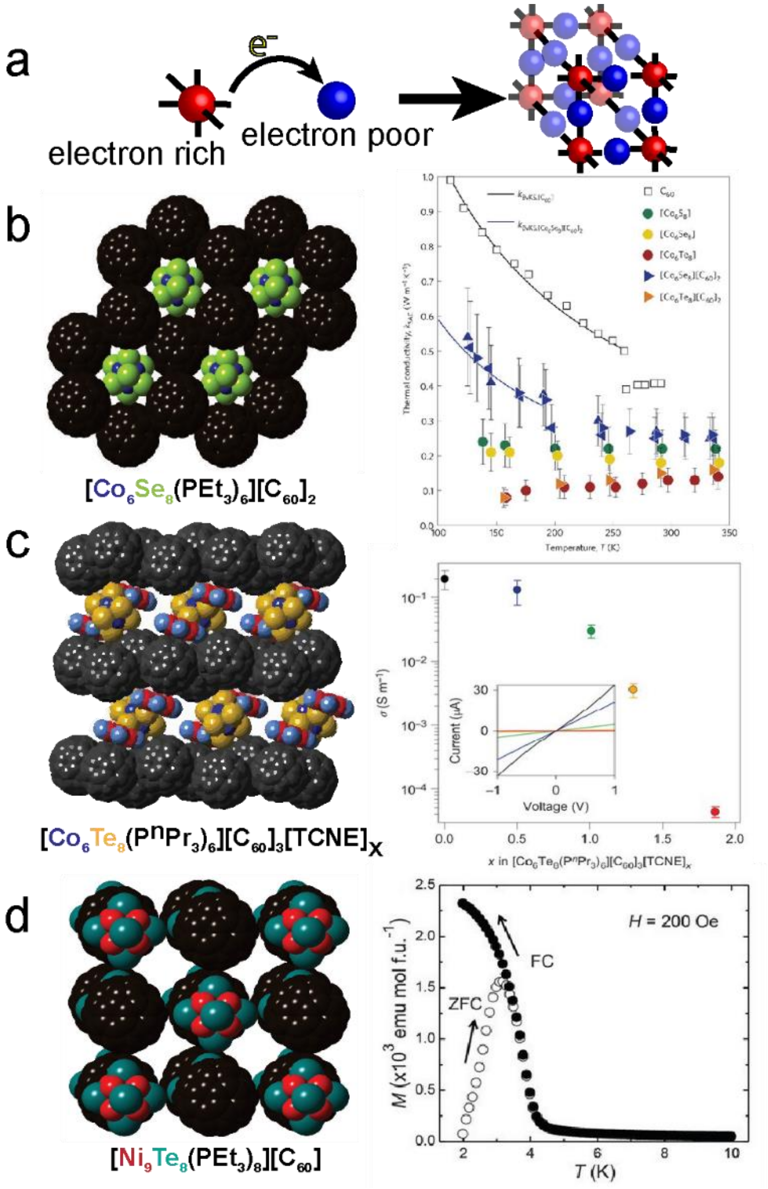

Figure 1.5. (a) General synthetic strategy in which an electron transfer occurs between an electron rich superatom to and electron poor one for assembly into binary three dimensional solids. (b,c,d) Multicomponent superatomic assemblies with C_{60} are shown in (b)[74], (c)[81], and (d)[82]. Ligands have been omitted for clarity. (b) Thermal conductivity of C_{60}, $Co_6E_8(PEt_3)_6$, and $[Co_6E_8(PEt_3)_6][C_{60}]_2$ solids where E = S, Se, or Te. (c) Effect on the electrical conductivity upon intercalation of increasing amounts of x = TCNE in $[Co_6Te_8(P^nPre)_6][C_{60}]_2[TCNE]x$. (d) Zero field cooled (ZFC) and field cooled (FC) traces of $[Ni_9Te_6(PEt_3)_8][C_{60}]$ indicating long-range ferromagnetic ordering[74].

Superatomic crystals assembled from C_{60}.

Being good electron acceptors with complementary size and shape, C_{60} fullerenes are attractive superatomic building blocks to create superatomic crystals from electron rich metal chalcogenide clusters. The reaction of $Co_6Se_8(PEt_3)_6$, $Cr_6Te_8(PEt_3)_6$ and $Ni_9Te_6(PEt_3)_8$ in toluene with C_{60} forms the solids $[Co_6Se_8(PEt_3)][C_{60}]_2$, $[Cr_6Te_8(PEt_3)_6][C_{60}]_2$ and $[Ni_9Te_6(PEt_3)_8][C_{60}]$.[74, 81] The structure of the binary superatomic solids mimicks the packing of traditional binary ionic compounds: $[Co_6Se_8(PEt_3)][C_{60}]_2$ and $[Cr_6Te_8(PEt_3)_6][C_{60}]_2$ adopt the CdI_2 structure while the $[Ni_9Te_6(PEt_3)_8][C_{60}]$ crystallizes as the NaCl rock-salt lattice (Figure 1.5b).

More complex structures can be assembled by modifying the superatoms. One example is the superatom $Co_6Te_8(P^nPr_3)_6$, which crystallizes with three C_{60} fullerenes to form the layered compound $[Co_6Te_8(P^nPr_3)_6][C_{60}]_3$[83] (Figure 1.5b). Another example is the trinuclear nickel superatoms $[Ni_3X_2(dppm)_3]$ (X = I, Te; dppm= 1,1-Bis(diphenylphosphino)methane), which form the binary solids $[Ni_3X_2(dppm)_3][C_{60}]$[84].

In all of these examples of superatomic crystals, the internal structures of the constituent clusters remain unchanged, resulting in atomically precise solids. Electron transfer produces superatoms whose charge states can be determined using a combination of spectroscopy and crystallography. The superatom $Co_6Te_8(P^nPr_3)_6$, for instance, donates one electron, which is shared among the three fullerenes, resulting in the charge states: $[Co_6Te_8(P^nPr_3)_6^{+}][C_{60}^{1/3-}]_3$[83].

Collective propeties in C_{60}-based superatomic crystals.

Fullerenes are unique building blocks due to their exposed spherical π-surface capable of electronic coupling in all directions. Such interactions have enabled the emergence of numerous collective properties in superatomic crystals as a result of the unique complementarity in the size, structure and redox of fullerenes and superatoms. This section will highlight some of the exciting emergent materials' properties that have been characterized in superatom-fullerene assemblies.

Electrical and optical conductivity properties.

Superatomic crystal assembled from C_{60} typically exhibit good electrical conductivity. The close packing of superatoms and C_{60} produces electrically activated transport behavior with the majority carriers being electrons transferred from the inorganic superatom to the fullerenes sublattice. Depending on the building blocks and the structure of the material, the room temperature conductivity and activation energy can range from 8 x 10^{-5} to 0.1 S/m, and 100 to 400 meV,[3, 74, 84] respectively.

Intercalation.

Evan O'Brien (former graduate student of Roy group) recently led the discovery[83] that the intercalation of redox active guests into the lattice of a superatomic crystal, $[Co_6Te_8(P^nPr_3)_6][C_{60}]_3$, can modulate the electrical and optical properties of the material while maintaining its superstructure. The host is a layered structure composed of alternating 2D sheets of spaced-out $Co_6Te_8(P^nPr_3)_6$ and close-packed C_{60} with an overall charge state $[Co_6Te_8(P^nPr_3)_6^{+}][C_{60}^{1/3-}]_3$. The pristine material can be intercalated with tetracyanoethylene (TCNE) in a single-crystal-to-single crystal transformation driven by transfer of electrons from the superatoms to the redox-active organic guest molecule. Remarkably, the fully intercalated material, $[Co_6Te_8(P^nPr_3)_6][C_{60}]_3[TCNE]_2$, has a significantly widened optical gap and its electrical conductivity can be modulated over 4 orders of magnitude by controlling the composition the relative number of TCNE inserted in the lattice.

Magnetism.

The superatomic cluster assemblies $[Co_6Se_8(PEt_3)][C_{60}]_2$, $[Cr_6Te_8(PEt_3)_6][C_{60}]_2$, $[Ni_9Te_6(PMe_3)_8][C_{60}]$, and $[Ni_9Te_6(PEt_3)_8][C_{60}]$ have all been magnetically characterized[74, 82]. As expected, the identity of the superatom used in the assembly influences the magnetic properties of the material. For $[Co_6Se_8(PEt_3)][C_{60}]_2$, there is a temperature-independent effective magnetic moment, $\mu_{eff} = 2.7\ \mu_B$ and is expected due to the transfer of one electron to each of the two C_{60}s as determined by Raman spectroscopy. Magnetic measurements of the $[Cr_6Te_8(PEt_3)_6][C_{60}]_2$ indicate that the presence of the Cr^{III} atoms within the superatom result in a more complex magnetic behavior[74].

Magnetic measurements of both $[Ni_9Te_6(PEt_3)_8][C_{60}]$ and $[Ni_9Te_6(PMe_3)_8][C_{60}]$ reveals that at low temperatures, a spontaneous ferromagnetic ordering occurs. $[Ni_9Te_6(PMe_3)_8][C_{60}]$ shows stronger electronic coupling than the triethyl phosphine analogue because of the decreased ligand shell size thus highlighting the tunability of the magnetic properties of superatomic assemblies.

Thermal transport.

Limited by the size of single crystals for experimental measurements and the introduction of inter-superatom cooperative behaviors, the analysis and prediction of emergent collective thermal transport behavior in superatomic materials is still in its infancy. A first study was recently published in a collaboration between research teams at Columbia University and Carnegie Mellon that evaluates the collective thermal conductivity and transport in mono-component and multi-component superatomic assemblies[81]. Figure 1.5b shows the improved thermal conductivity of multicomponent superatomic solids assembled from $Co_6E_8(PEt_3)_6$ and C_{60} building blocks due to the additional inter-superatom interactions between building blocks in comparison to the measurements of the unary compounds.

Multi-component superatomic crystals can undergo phase transitions that modify the orientational ordering and thus inter-superatom coupling. The change in inter-superatom interactions alters the thermal transport behavior of the solid. $[Co_6Se_8][C_{60}]_2$ undergoes a phase transition around 190 K that contracts the centroid-centroid C_{60} distances and the multi-component binary solid becomes orientationally ordered[81]. Above 190 K, the superatomic crystal is orientationally disordered and scatters phonons in an amorphous-type behavior. The thermal conductivity in the solid is temperature-dependent below 180 K and behaves as a typical crystalline solid with increasing mean free path lengths with decreasing temperature as shown in Figure 1.6b. In comparison, the isostructural $[Co_6Te_8][C_{60}]_2$ solid continuously decreases its conductivity with decreasing temperature. The larger chalcogenide cluster prevents the fullerene units from being close enough to have the short-range anisotropic interactions that cause orientational ordering and the solid never undergoes a temperature-dependent phase transition. Thermal transport in superatomic crystals is thus dependent on the structural properties of the solids including its inter-superatom spacing and interactions. This study suggests that by controlling the atomically precise ordering and coupling between building blocks, scientists can target the design of next-generation thermoelectric materials.

1.5 Superatomic crystals assembled from fullerenes other than C_{60}

Replacing the C_{60} building block with C_{70} provides further opportunity to uncover novel structures and properties in superatomic crystals. For example, the larger and oblong C_{70} assembles with the trinuclear nickel superatoms to form $[Ni_3X_2(dppm)_3][C_{70}]_2$ (X = I, Te)[84]. Remarkably, C_{70}

dimerizes upon reduction, forming C_{140}^{2-} dumbbells within the lattice (Figure 1.6c). When C_{70} is combined with $Co_6Te_8(PEt_3)_6$, a structure that is analogous to $[Co_6Te_8(PEt_3)_6][C_{60}]_2$ is obtained but half of the C_{70} units are dimerized, forming the superatomic crystal $[Co_6Te(PEt_3)_6][(C_{140})_{1/2}(C_{70})]$.[88] The interfullerene bond within the C_{140}^{2-} dimers is remarkably long (1.6 Å) and can be cleaved by heating the superatomic crystals, leading to coupled electronic/structural phase transition that produce an abrupt change in the material properties.

Optical properties.

The observed structural phase transition upon heating $[Co_6Te_8(PEt_3)_6][(C_{70})_2]$ material and cleaving the C_{70} dimers produces a remarkable new feature in its electronic absorption spectra[88]. The optical band gap energy of 0.4 eV is held constant across the material's phase transitions in which the C_{70} units transform from being orientationally ordered, to dynamically disordered, to electronically delocalized. However, upon heating to 330 K and releasing the electrons in the inter-fullerene bond, a new spectral feature appears at 0.1 eV attributed to a new band in the fullerene sublattice.

Electrical properties.

The appearance of a new spectral band in the electronic absorption spectra of the Co_6Te_8 assembly is indicative of increased conductivity in the crystal caused by the electron delocalization on the fullerenes. The liberation of the inter-fullerene electrons increases the electrical conductivity from 0.1 S/m at 320 K to 10 S/m at 340 and correspondingly decreases its activation energy from 500 to 300 meV[88]. As in assemblies with C_{60}, the material is thermally activated, and conductivity increases exponentially with temperature. Comparatively, both of the $[Ni_3X_2(dppm)_3][C_{70}]_2$ (X = I, Te) crystals exhibit significantly lower conductivities than its C_{60} analogues with values of 1.0

x10^{-5} S/m and 2.0 x10^{-4} and 8 x10^{-5} S/m for the $[Ni_3X_2(dppm)_3][C_{70}]_2$ and $[Ni_3I_2(dppm)_3][C_{60}]_2$ $[Ni_3Te_2(dppm)_3][C_{60}]_2$ respectively[84].

Magnetism.

The electronic reconfiguration that occurs upon the cleaving of the C_{70} dimers in the Co_6Te_8 assembly increases the lattice spin density of the material[88]. At low temperatures, the sample behaves as expected given the diamagnetic character of both C_{70} and C_{140}^{2-} units and the $S = ½$ magnetic ground state of $Co_6Te_8(PEt_3)_6^+$ and a measured X_MT~0.43 cm^3 $mol^{-1}K$ at 2K. X_MT reaches 0.70 cm^3 mol^{-1} K in a linear fashion upon heating from 10 to 310 K which is attributed to low lying magnetic states in the system. Upon generation of the C_{70}- radical anions, the lattice spin density abruptly increases to 0.28 cm3 mol-1 K and the unpaired electrons in the fullerene sublattice experience antiferromagnetic interactions.

Thermal behavior.

Thermal conductivity (*k*) of the Co_6Te_8 assembly with C_{70} is significantly altered by the initial phase transition from a phonon crystal at low temperature when the fullerenes are orientationally ordered to exhibiting amorphous thermal transport behavior when the fullerenes freely rotate[88]. Above 240 K, the $[Co_6Te_8(PEt_3)_6][C_{70}]_2$ single crystals *k* consistently ranges from 0.11 ± 0.02 to 0.20 ± 0.04 W/mK independent of temperature and upon cooling, *k* increases with decreasing temperature as the solid becomes increasingly crystalline. The increased phonon mean-free-path reaches a maximum *k* value of 0.49 ± 0.19 W/mK at 125 K.

Superatomic crystals assembled from endohedral fullerenes.

Endohedral fullerenes offer the opportunity of introducing an additional level of compositional variety into superatomic crystal by encapsulating different clusters within the conjugated carbon π-surface. Assembling multicomponent superatomic assemblies with endohedral fullerene building blocks offers exciting opportunities to observe novel electronic and magnetic coupling and phenomena. However, in comparison to C_{60} or C_{70}, which have been widely used charge transfer for self-assembly, endohedral fullerenes have lower electron affinities which limits the selection of its redox-complimentary building block [89-91]. In Chapter 3 I will discuss my assembly of the first superatomic crystal comprising an endohedral fullerene: $[Ni_{12}Te_{12}(PEt_3)_8][(Lu_3N@C_{80})_2]$[92]. As with C_{70}, the reduced endohedral fullerenes form dimers in the solid state, as illustrated in Figure 1.6.

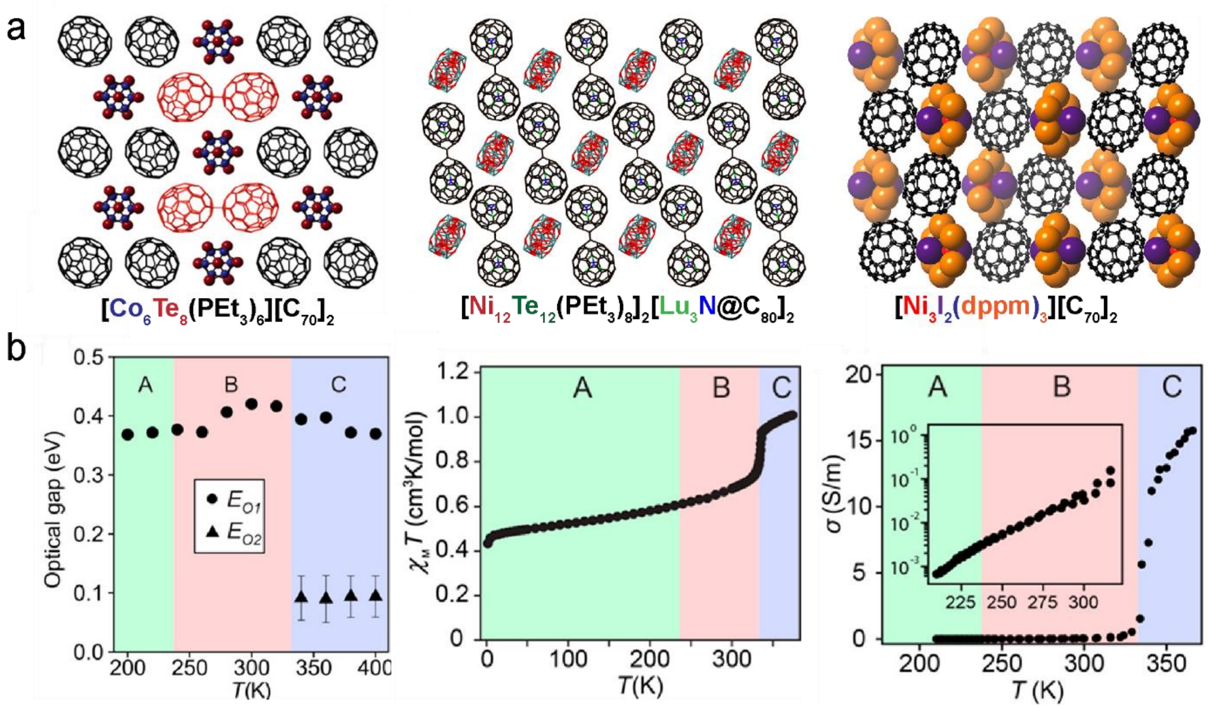

Figure 1.6. Superatomic assemblies with C_{70} of $[Co_6Te_8(PEt_3)_6][C_{70}]_2$ (left), $[Ni_{12}Te_{12}(PEt_3)_8]_2[Lu_3N@C_{80}]_2$ (middle), and $[Ni_3I_2(dppm)_3][C_{70}]_2$ (right). Ligands have been omitted for clarity. (b) Optical band gap (left), magnetic ordering (middle) and electrical conductivity (right) of $[Co_6Te_8(PEt_3)_6][C_{70}]_2$ shown in (a) (left)[84, 88, 92].

Superatomic crystals from inorganic building blocks.

Beyond fullerenes, multicomponent superatomic assemblies can be assembled from electronically complementary inorganic building blocks, including metal chalcogenide, metal oxide and metal halide clusters. For instance, combining the electron-donating $Co_6Se_8(PEt_3)_6$ and electron-accepting $Fe_8O_4pz_{12}Cl_4$ in toluene forms black single crystals of $[Co_6Se_8(PEt_3)_6][Fe_8O_4pz_{12}Cl_4]$[29] whose primitive cubic lattice can be approximated as the superatomic analog of the CsCl lattice. Substitution of the phosphines, halides and/or chalcogens can produce subtle changes to the atomic structure of the binary solids or entirely new packing structures. The compounds $[Co_6Se_8(PEt_3)_6][Fe_8O_4pz_{12}Cl_4]$, $[Co_6Te_8(PEt_3)_6][Fe_8O_4pz_{12}Cl_4]$ and $[Co_6Te_8(PEt2Ph)_6][Fe_8O_4pz_{12}Cl_4]$ and $[Co_6Te_8(PEt_3)_6][Fe_8O_4pz_{12}Br_4]$ all form the same CsCl packing structure, with slight differences in the orientation of the superatoms. The material $[Co_6Te_8(P^nPr_3)6][Fe_8O_4pz_{12}Cl_4]$, by contrast, adopts an entirely different and highly unusual superstructure in which the two superatoms form alternating hexagonal close-packed layers with an *hccc* packing stacking sequence. These examples demonstrate how modification of the superatoms allows subtle tuning of the superstructure.

Superatomic crystals assembled from molecular recognition.

In addition to electrostatic interactions resulting from inter-superatom charge transfer, multicomponent crystals can be assembled using molecular recognition motifs. Figure 1.7 presents an example in which a superatom decorated with phenanthrene groups is used as a nanoscale director to form a layered van der Waals solid, which can be exfoliated, akin to conventional atomic van der Waals materials[93]. Figure 1.7a shows a side view of how the phenanthrene ligands on $Co_6Se_8(PEt_2phen)_6$ extend, rotate, and organize to form two antipodal buckybowls interacting with C_{60} to create a dumbbell unit that templates the extended layered structure. The resulting bulk solid, $[Co_6Se_8(PEt_2phen)_6][C_{60}]_5$, contains two distinct layers: a heterogeneous cluster-fullerene in which each cluster is surrounded by two C_{60}, and a homogeneous layer of close-packed neutral fullerenes (Figure 1.7). Unlike charge transfer assemblies, the layers in $[Co_6Se_8(PEt_2phen)_6][C_{60}]_5$ are held together by relatively weak van der Waals forces.

By analogy to graphene and transition metal dichalcogenides, single crystal of $[Co_6Se_8(PEt_2phen)_6][C_{60}]_5$ can be exfoliated to produce nanosheet materials[94]. To enable exfoliation, the structure needs to be mechanically strengthened. This is accomplished by photopolymerizing the close-packed 2D C_{60} layers within the structure. Once crosslinked the crystals can be dissolved in toluene to release nanosheets of the material, which can be collected on a substrate. Figure 1.7 shows an atomic force microscopy (AFM) image of the isolated nanosheet after exfoliation in toluene and deposited onto a silicon oxide substrate. The image of 5 nm step heights of the nanosheet correspond to sandwich layers of FL/CFL/FL of the material. Remarkably, the exfoliated 2D photopolymerized material can be reverted to its pristine molecular state by thermal depolymerization at 450 K.

Collective properties of 2D superatomic crystal.

Assembling superatoms into synthetic 2D materials offers exciting opportunities for tuning the material properties through chemical design and for discovering new behaviors. As a bulk crystal, $[Co_6Se_8(PEt_2phen)_6][C_{60}]_5$ exhibits in-plane activated electrical transport behavior with an activation energy E_a of ∼400 meV. The optical gap of the material, estimated from electronic absorption spectroscopy, is ~390 meV. Upon photopolymerization and exfoliation, the nanosheets behave as a direct bandgap semiconductor with an optical gap of ~250 meV. This unusual reduction of the optical gap in the 2D limit suggests that the C_{60} layers in the parent structure are electronically decoupled from each other. The effect is instead attributed to shorter intermolecular distances, resulting from the polymerization of the C_{60} layer. The decrease in C_{60}–C_{60} distance enhances the coupling between C_{60} units and thus reduces the gap.

1.6. Reduction of 3D materials to lower dimensions

The focus of this introduction has been on a bottom-up approach to fabricate 1D, 2D, and 3D superatomic coordination structures from 0D building blocks. An alternative approach is the atomically precise top-down reduction of 3D materials to lower 1D and 2D constituents. Interest in such methods has grown with the advent of 2D semiconductors that many groups currently target via top-down approaches. Recently, work done in a collaboration with members of Professor Roy, Zhu, and Batail groups accessed a 2D semiconductor material through a top-down exfoliation of Re_6Se_8 bulk material.[95-96] The superatomic material is a 2D semiconductor with electronic bandgaps of ~1.6 eV. The Chevrel-type $Re_6Se_8Cl_2$ is the first member of a 2D hierarchical

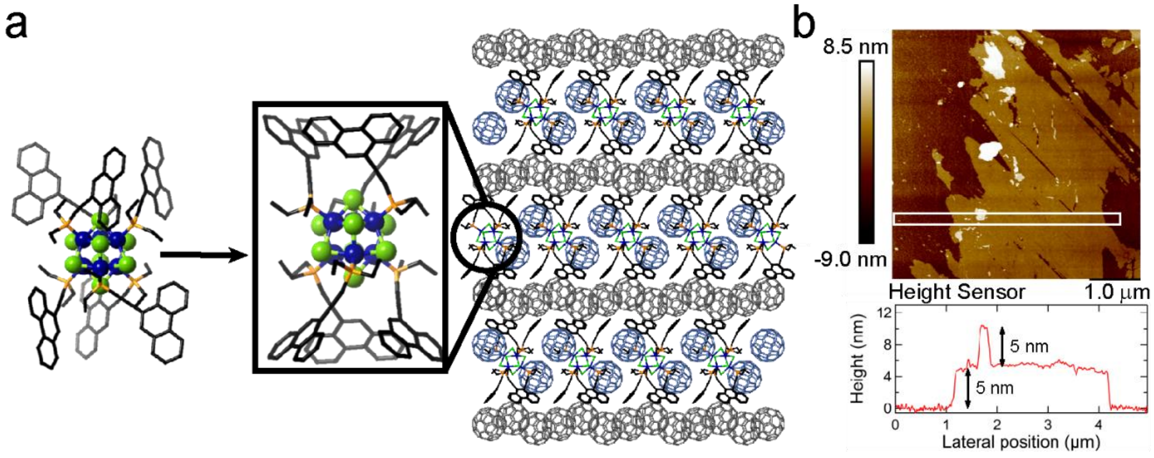

Figure 1.7. The self-assembly of $Co_6Se_8(PEt_2Phen)_6$ results in the extension and rotation of the phenanthrene ligands forming a buckeybowl that experiences van der Waal interactions with the fullerene layers. The cluster is held within the dumbbell-templated cluster-fullerene layer surrounded by two additional C_{60} molecules[93-94]. (b) AFM image of the exfoliated nanosheet. Step heights of 5 nm are shown below the AFM image and correspond to a single sandwich layer (FL/CFL/FL) of the structure[94].

semiconductor family. Calculations indicate that the bandgap increases from ~1.5 eV in the bulk to ~1.7 eV in the monolayer while remaining an indirect bandgap material. Remarkably, the 2D monolayers retain the crystalline [Re$_6$Se$_8$] structure after exfoliation and surface functionalization. I had the opportunity to contribute to the work in confirming the retention of the crystallinity of the [Re$_6$Se$_8$] structure after exfoliation and chemical functionalization of the surface. Figure 1.8 shows a few of the transmission electron microscopy (TEM) images I took showing isolated monolayers whose selected area electron diffraction (SAED) patterns match well with the expected crystal structure. Further surface functionalization[96] and exfoliation techniques could expose a new vein of research to design superatomic materials with novel electronic behaviors for functional applications.

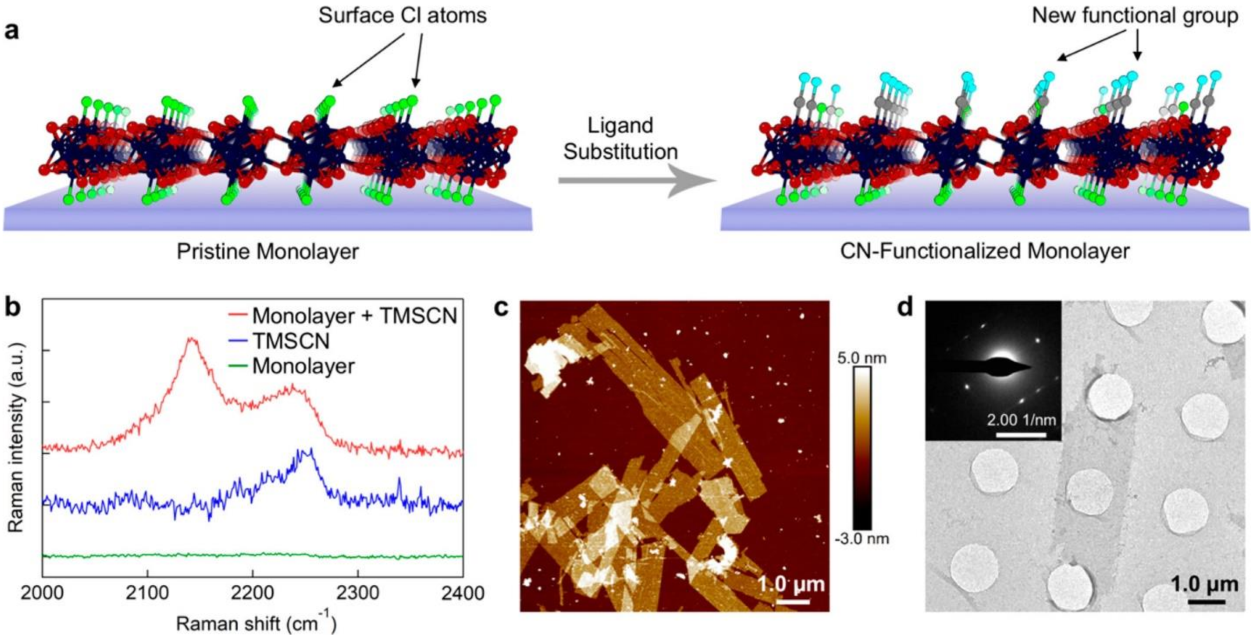

Figure 1.8. (a) Schematic of the surface functionalization reaction of monolayers supported on a substrate. Color as in Figure 1; C, gray; N, aqua. (b) Raman spectra (2000−2400 cm−1 region) of monolayers on sapphire substrate (green), monolayers after reaction with TMSCN (red), and pristine sapphire substrate exposed to TMSCN in air (blue). The signal from the sapphire background has been subtracted in all the spectra. (c) AFM image and (d) TEM micrograph (inset: corresponding SAED pattern) of monolayers after surface functionalization.

1.7 Future Directions

The studies described here reveal the great potential for the fabrication of functional materials from superatomic building blocks. To date synthetic strategies to access superatoms with varied chemical core and ligand composition have been well explored. More recently, there has been a shift in focus onto the discovery of new strategies to assemble monocomponent and multicomponent extended materials from superatomic precursors. As new superatomic coordination structures are synthesized, the characterization of their emergent collective materials' properties (*i.e. magnetism, thermal conductivity, electron transport*) is required in order to apply these materials in the design of new technologies. Already, there are several examples of synthesized superatomic assemblies whose material properties have yet to be explored. Some of the next steps the field will take will be the robust synthesis and characterization of these materials to demonstrate the tunability of emergent behaviors and potential in future applications.

The main direction of assembling superatoms into larger materials are to enhance the favorable properties listed above in two ways: varying the constituent building blocks of known assemblies and developing new ways to assemble atomically precise clusters. There are many more opportunities in building superatomic functional materials through the development of new synthetic strategies for superatom functionalization and assembly as well as novel techniques to probe their resulting individual and collective properties. The ultimate vision is to develop a deep fundamental understanding of the individual and collective properties of atomically precise assemblies of superatoms. This fundamental knowledge will allow chemists to judiciously select the superatomic composition and assembly strategy for fabrication of the desired functional material.

1.8 References

1. Claridge, S. A.; Castleman, A. W.; Khanna, S. N. *et al*. Cluster-Assembled Materials. *ACS Nano* **2009,** *3*, 244-255.

2. Jena, P.; Sun, Q., Super Atomic Clusters: Design Rules and Potential for Building Blocks of Materials. *Chem. Rev.* **2018,** *118*, 5755-5870.

3. Pinkard, A.; Champsaur, A. M.; Roy, X., Molecular Clusters: Nanoscale Building Blocks for Solid-State Materials. *Acc. Chem. Res.* **2018,** *51*, 919-929.

4. Steigerwald, M. L., Clusters as Small Solids. *Polyhedron* **1994,** *13*, 1245-1252.

5. Dance, I.; Fisher, K., Metal Chalcogenide Cluster Chemistry. *Prog. Inorg. Chem.* **1994,** *41*, 637-803.

6. MacDonald, D. G.; Corrigan, J. F., Metal chalcogenide nanoclusters with 'tailored' surfaces via 'designer' silylated chalcogen reagents. *Philos. Trans. Royal Soc. A* **2010,** *368*, 1455-1472.

7. Khanna, S. N.; Jena, P., Atomic clusters: Building blocks for a class of solids. *Phys Rev B Condens Matter* **1995,** *51*, 13705-13716.

8. Bergeron, D. E.; Castleman, A. W.; Morisato, T.; Khanna, S. N., Formation of Al13I-: Evidence for the superhalogen character of Al-13. *Science* **2004,** *304*, 84-87.

9. Dietz, T. G.; Duncan, M. A.; Powers, D. E.; Smalley, R. E., Laser Production of Supersonic Metal Cluster Beams. *J. Chem. Phys.* **1981,** *74*, 6511-6512.

10. Bondybey, V. E.; English, J. H., Laser-Induced Fluorescence of Metal-Clusters Produced by Laser Vaporization - Gas-Phase Spectrum of Pb-2. *J. Chem. Phys.* **1981,** *74*, 6978-6979.

11. Knight, W. D.; Clemenger, K.; Deheer, W. A. *et al.* Electronic Shell Structure and Abundances of Sodium Clusters. *Phys. Rev. Lett.* **1984,** *52*, 2141-2143.

12. Crawford, N. R. M.; Hee, A. G.; Long, J. R., Cluster synthesis via ligand-arrested solid growth: Triethylphosphine-capped fragments of binary metal chalcogenides. *J. Am. Chem. Soc.* **2002,** *124*, 14842-14843.

13. Fenske, D.; Ohmer, J.; Hachgenei, J.; Merzweiler, K., New Transition-Metal Clusters with Ligands from Main Group-5 and Group-6. *Angew. Chem.-Int. Ed.* **1988,** *27*, 1277-1296.

14. Chakraborty, I.; Pradeep, T., Atomically Precise Clusters of Noble Metals: Emerging Link between Atoms and Nanoparticles. *Chem. Rev.* **2017,** *117*, 8208-8271.

15. Sokolov, M. N.; Abramov, P. A., Chalcogenide clusters of Groups 8-10 noble metals. *Coord.Chem. Rev.* **2012,** *256*, 1972-1991.

16. Hidai, M.; Kuwata, S.; Mizobe, Y., Synthesis and reactivities at cubane-type sulfido clusters containing noble metals. *Acc. Chem. Res.* **2000,** *33*, 46-52.

17. Cecconi, F.; Ghilardi, C. A.; Midollini, S., A Novel Paramagnetic Octahedral Iron Cluster - Synthesis and X-Ray Structural Characterization of [Fe6(Mu-3-S)8(Pet3)6][Bph4]2. *Chem. Comm.* **1981**, 640-641.

18. Brennan, J. G.; Siegrist, T.; Stuczynski, S. M.; Steigerwald, M. L., The Transition from Molecules to Solids - Molecular Syntheses of Ni9te6(Pet3)8, Ni20te18(Pet3)12, and Nite. *J. Am. Chem. Soc.* **1989,** *111*, 9240-9241.

19. Speziali, N. L.; Berger, H.; Leicht, G.; Sanjines, R.; Chapuis, G.; Levy, F., Single-Crystal Growth, Structure and Characterization of the Octahedral Cluster Compound Re6Se8Br2. *Mater. Res. Bull.* **1988,** *23*, 1597-1604.

20. Fischer, C.; Fiechter, S.; Tributsch, H.; Reck, G.; Schultz, B., Crystal-Structure and Thermodynamic Analysis of the New Semiconducting Chevrel Phase Re6s8cl2. *Phys. Chem. Chem. Phys.* **1992,** *96*, 1652-1658.

21. Leduc, L.; Perrin, A.; Sergent, M., The Structure of Hexarhenium Dichloride and Octaselenide, Re6Se8Cl2 - a Bidimensional Compound of Re6 Octahedral Clusters. *Acta Crystallogr. Sec. C-Cryst. Strct. Comm.* **1983,** *39*, 1503-1506.

22. Mironov, Y. V.; Virovets, A. V.; Naumov, N. G.; Ikorskii, V. N.; Fedorov, V. E., Excision of the {Mo6Se8} cluster core from a chevrel phase: Synthesis and properties of the first molybdenum octahedral cluster selenocyanide anions [Mo6Se8(CN)(6)](7-) and [Mo6Se8(CN)(6)](6-). *Chem. Euro.* **2000,** *6*, 1361-1365.

23. Magliocchi, C.; Xie, X. B.; Hughbanks, T., A cyanide-bridged chain of Mo6Se8 clusters: A product of cyanide-melt cluster synthesis. *Inorg. Chem.* **2000,** *39*, 5000-5001.

24. Bajan, B.; Meyer, H. J., Two-dimensional networks in the structure of Li-2[Nb6Cl16]. *Z. Anorg. Und Allg. Chem.* **1997,** *623*, 791-795.

25. Zhang, J. J.; Lachgar, A., Superexpanded prussian-blue analogue with [Fe(CN)(6)](4-), [Nb6Cl12(CN)(6)](4-), and [Mn(salen)](+) as building units. *J. Am. Chem. Soc.* **2007,** *129*, 250-251.

26. Cecconi, F.; Ghilardi, C. A.; Midollini, S.; Orlandini, A.; Zanello, P., Synthesis, properties and structures of the two “electron rich” cobalt-sulphur clusters [Co6(μ3-S)8(PEt3)6]1+,0. *Polyhedron* **1986,** *5*, 2021-2031.

27. Saito, T.; Yamamoto, N.; Nagase, T. *et al.* Molecular-Models of the Superconducting Chevrel Phases - Syntheses and Structures of [Mo6x8(Pet3)6] and [Ppn][Mo6x8(Pet3)6] (X = S, Se, Ppn = (Ph3p)2n). *Inorg. Chem.* **1990,** *29*, 764-770.

28. Cecconi, F.; Ghilardi, C. A.; Midollini, S.; Orlandini, A.; Zanello, P., Redox behaviour of the iron–sulphur cluster [Fe6(μ3-S)8(PEt3)6]2+. Synthesis and crystal structure of the new paramagnetic monopositive species [Fe6(μ3-S)8(PEt3)6]+ as its [PF6]– salt. *Dalt Trans.* **1987**, 831-835.

29. Turkiewicz, A.; Paley, D. W.; Besara, T. *et al.* Assembling Hierarchical Cluster Solids with Atomic Precision. *J. Am. Chem. Soc.* **2014,** *136*, 15873-15876.

30. Reber, A. C.; Khanna, S. N.; Castleman, A. W., Superatom compounds, clusters, and assemblies: Ultra alkali motifs and architectures. *J. Am. Chem. Soc.* **2007,** *129*, 10189-10194.

31. Reber, A. C.; Chauhan, V.; Khanna, S. N., Symmetry and magnetism in Ni9Te6 clusters ligated by CO or phosphine ligands. *J. Chem. Phys.***2017,** *146*.

32. Liu, G. X.; Pinkard, A.; Ciborowski, S. M. *et al.* Tuning the electronic properties of hexanuclear cobalt sulfide superatoms via ligand substitution. *Chem. Sci.* **2019,** *10*, 1760-1766.

33. Tulsky, E. G.; Long, J. R., Heterometal substitution in the dimensional reduction of cluster frameworks: Synthesis of soluble [Re6-nOSnSe8Cl6]((4-n)-) (n=1-3) cluster-containing solids. *Inorg. Chem.* **2001,** *40,* 6990-7002.

34. Khanna, S. N.; Linderoth, S., Magnetic-Behavior of Clusters of Ferromagnetic Transition-Metals. *Physical Review Letters* **1991,** *67,* 742-745.

35. Kortus, J.; Baruah, T.; Pederson, M. R.; Ashman, C.; Khanna, S. N., Magnetic moment and anisotropy in FenCom clusters. *Appl. Phys. Lett.* **2002,** *80*, 4193-4195.

36. Zhang, X. X.; Wang, Y.; Wang, H. P. *et al.* On the Existence of Designer Magnetic Superatoms. *J. Am. Chem. Soc.* **2013,** *135*, 4856-4861.

37. Chauhan, V.; Medel, V. M.; Reveles, J. U. *et al.* Shell magnetism in transition metal doped calcium superatom. *Chem. Phys. Lett.* **2012,** *528*, 39-43.

38. Xu, X. S.; Yin, S. Y.; Moro, R.; de Heer, W. A., Magnetic moments and adiabatic magnetization of free cobalt clusters. *Phys. Rev. Lett.* **2005,** *95*.

39. Billas, I. M. L.; Chatelain, A.; Deheer, W. A., Magnetism from the Atom to the Bulk in Iron, Cobalt, and Nickel Clusters. *Science* **1994,** *265*, 1682-1684.

40. Cox, A. J.; Louderback, J. G.; Bloomfield, L. A., Experimental-Observation of Magnetism in Rhodium Clusters. *Phys. Rev. Lett.* **1993,** *71*, 923-926.

41. Datta, S.; Saha-Dasgupta, T., Structural, electronic and magnetic properties of transition metal binary alloy clusters with isoelectronic components: case study with MnmTcn, TimZrn and MnmRen. *J. Phys. Condens. Matter* **2013,** *25*.

42. Gatteschi, D.; Sessoli, R., Quantum tunneling of magnetization and related phenomena in molecular materials. *Angew. Chem. Int. Ed. Engl* **2003,** *42*, 268-297.

43. Bencini, A.; Midollini, S., Some Synthetic and Theoretical Aspects of the Chemistry of Polynuclear Transition-Metal Complexes. *Coord. Chem. Rev.* **1992,** *120,* 87-136.

44. Cordier, S.; Grasset, F.; Molard, Y. *et al*. Inorganic Molybdenum Octahedral Nanosized Cluster Units, Versatile Functional Building Block for Nanoarchitectonics. *J. Inorg. Organomet. Polym. Mater.* **2015,** *25,* 189-204.

45. Shestopalov, M. A.; Mironov, Y. V.; Brylev, K. A. *et al.* Cluster core controlled reactions of substitution of terminal bromide ligands by triphenylphosphine in octahedral rhenium chalcobromide complexes. *J. Am. Chem. Soc.* **2007,** *129*, 3714-3721.

46. Kitamura, N.; Ueda, Y.; Ishizaka, S. *et al.* Temperature dependent emission of hexarhenium(III) clusters [Re-6(mu(3)-S)(8)X-6](4-) (X = Cl-, Br-, and I-): Analysis by four excited triplet-state sublevels. *Inorg. Chem.* **2005,** *44,* 6308-6313.

47. Rosemann, N. W.; Eussner, J. P.; Beyer, A. *et al.* A highly efficient directional molecular white-light emitter driven by a continuous-wave laser diode. *Science* **2016,** *352,* 1301-1304.

48. Castleman, A. W.; Khanna, S. N., Clusters, Superatoms, and Building Blocks of New Materials. *J. Phys. Chem. C* **2009,** *113,* 2664-2675.

49. Li, Q.; Russell, J. C.; Luo, T. Y.; Roy, X.; Rosi, N. L.; Zhu, Y.; Jin, R. C., Modulating the hierarchical fibrous assembly of Au nanoparticles with atomic precision. *Nat. Comm.* **2018,** *9*.

50. Yoon, B.; Luedtke, W. D.; Barnett, R. N. *et al.* Hydrogen-bonded structure and mechanical chiral response of a silver nanoparticle superlattice. *Nat. Mater.* **2014,** *13*, 807-811.

51. Long, J. R.; McCarty, L. S.; Holm, R. H., A solid-state route to molecular clusters: Access to the solution chemistry of [Re(6)Q(8)](2+) (Q=S, Se) core-containing clusters via dimensional reduction. *J. Am. Chem. Soc.* **1996,** *118*, 4603-4616.

52. Zheng, Z. P.; Long, J. R.; Holm, R. H., A basis set of Re6Se8 cluster building blocks and demonstration of their linking capability: Directed synthesis of an Re12Se16 dicluster. *J. Am. Chem. Soc.* **1997,** *119*, 2163-2171.

53. Roland, B. K.; Selby, H. D.; Carducci, M. D.; Zheng, Z. P., Built to order: Molecular tinkertoys from the [Re-6(mu(3)-Se)(8)](2+) clusters. *J. Am. Chem. Soc.* **2002,** *124*, 3222-3223.

54. Selby, H. D.; Roland, B. K.; Zheng, Z. P., Ligand-bridged oligomeric and supramolecular arrays of the hexanuclear rhenium selenide clusters-exploratory synthesis, structural characterization, and property investigationt. *Acc. Chem. Res.* **2003,** *36*, 933-944.

55. Champsaur, A. M.; Velian, A.; Paley, D. W.; Choi, B.; Roy, X.; Steigerwald, M. L.; Nuckolls, C., Building Diatomic and Triatomic Superatom Molecules. *Nano Letters* **2016,** *16*, 5273-5277.

56. Champsaur, A. M.; Hochuli, T. J.; Paley, D. W.; Nuckolls, C.; Steigerwald, M. L., Superatom Fusion and the Nature of Quantum Confinement. *Nano Letters* **2018,** *18*, 4564-4569.

57. Super-Molecules from Superatoms. *Scientific American* **2016,** *315*, 41-41.

58. Zheng, Z. P.; Holm, R. H., Cluster condensation by thermolysis: Synthesis of a rhomb-linked Re12Se16 dicluster and factors relevant to the formation of the Re24Se32 tetracluster. *Inorg. Chem.* **1997,** *36*, 5173-5178.

59. Amari, S.; Imoto, H.; Saito, T., Synthesis of a molybdenum cluster complex [Mo-12(mu(3)-S)(14)(mu(4)-S)(2)(PEt3)(10)] with Chevrel phase type intercluster bondings. *Chem. Lett.* **1997**, 967-968.

60. Saito, T., Group 6 Metal Chalcogenide Cluster Complexes and their Relationships to Solid-State Cluster Compounds. *Adv. Inorg. Chem.* **1996**; Vol. 44, pp 45-91.

61. Cecconi, F.; Ghilardi, C. A.; Midollini, S.; Orlandini, A., Dimerization of the Stellated Octahedral Unit Co6s8p6 - Synthesis and X-Ray Crystal-Structure of [Co12(Mu-3-S)14(Mu-4-S)2(Pet3)10][Tcnq]2, Where Tcnq = Tetracyanoquinodimethane. *Inorg.Chim. Acta* **1993,** *214*, 13-15.

62. Roland, B. K.; Carter, C.; Zheng, Z., Routes to Metallodendrimers of the [Re6(μ3-Se)8]2+ Core-Containing Clusters. *J. Am. Chem. Soc.* **2002,** *124*, 6234-6235.

63. Roland, B. K.; Flora, W. H.; Selby, H. D.; Armstrong, N. R.; Zheng, Z. P., Dendritic arrays of [Re-6(mu(3)-Se)(8)](2+) core-containing clusters: Exploratory synthesis and electrochemical studies. *J. Am. Chem. Soc.* **2006,** *128*, 6620-6625.

64. Baudron, S. A.; Batail, P.; Coulon, C.; Clerac, R.; Canadell, E.; Laukhin, V.; Melzi, R.; Wzietek, P.; Jerome, D.; Auban-Senzier, P.; Ravy, S., (EDT-TTF-CONH2)(6)[Re6Se8(CN)(6)],

a metallic Kagome-type organic-inorganic hybrid compound: Electronic instability, molecular motion, and charge localization. *J. Am. Chem. Soc.* **2005,** *127*, 11785-11797.

65. Champsaur, A. M.; Yu, J.; Roy, X.; Paley, D. W.; Steigerwald, M. L.; Nuckolls, C.; Bejger, C. M., Two-Dimensional Nanosheets from Redox-Active Superatoms. *Acs Cent. Sci.* **2017,** *3*, 1050-1055.

66. Champsaur, A. M.; Meziere, C.; Allain, M.; Paley, D. W.; Steigerwald, M. L.; Nuckolls, C.; Batail, P., Weaving Nanoscale Cloth through Electrostatic Templating. *J. Am. Chem. Soc.* **2017,** *139*, 11718-11721.

67. Voevodin, A.; Campos, L. M.; Roy, X., Multifunctional Vesicles from a Self-assembled Cluster-Containing Diblock Copolymer. *J. Am. Chem. Soc.* **2018,** *140*, 5607-5611.

68. Renault, A.; Pouget, J. P.; Parkin, S. S. P.; Torrance, J. B.; Ouahab, L.; Batail, P., Evidence for a Spin-Peierls-Like Transition in the 1-D Organic Cation Radical Salt - Beta-(Tmtsf)2re6se5cl9. *Mol. Cryst. Liq. Cryst.* **1988,** *161*, 329-334.

69. Penicaud, A.; Batail, P.; Coulon, C.; Canadell, E.; Perrin, C., Novel Redox Properties of the Paramagnetic Hexanuclear Niobium Cluster Halide Nb6cl18(3-) and the Preparation, Structures, and Conducting and Magnetic-Properties of Its One-Dimensional Mixed-Valence Tetramethyltetra(Selena and Thia)Fulvalenium Salts - [Tmtsf and Tmttf]5[Nb6cl18].(Ch2cl2)0.5. *Chem. Mat.* **1990,** *2*, 123-132.

70. Baird, P.; Bandy, J. A.; Green, M. L. H. *et al.* Charge-Transfer Salts Formed from Redox-Active Cubane Cluster Cations (M4(Eta-C5H4R)4(Mu-3-E)4)N+ (M = Cr, Fe or Mo E = S or Se) and Various Anions. *Dalt. Trans.* **1991**, 2377-2393.

71. Allen, D. P.; Bottomley, F.; Day, R. W.; Decken, A.; Sanchez, V.; Summers, D. A.; Thompson, R. C., Organometallic oxides: Oxidation of the cubane [(eta-C5R5)Cr(mu(3)-O)](4) and the structures and magnetic properties of the salts {[(eta-C5R5)Cr(mu(3)-O)](4)}{tcnq} and {[(eta-C5R5)Cr(mu(3)-O)](4)}{BF4}. *Organometallics* **2001,** *20*, 1840-1848.

72. Feliz, M.; Llusar, R.; Uriel, S.; Vicent, C.; Coronado, E.; Gomez-Garcia, C. I., Cubane-type Mo3CoS4 molecular clusters with three different metal electron populations: Structure, reactivity and their use in the synthesis of hybrid charge-transfer salts. *Chem. Euro. J.* **2004,** *10*, 4308-4314.

73. Karadas, F.; Avendano, C.; Hilfiger, M. G.; Prosvirin, A. V.; Dunbar, K. R., Use of a rhenium cyanide nanomagnet as a building block for new clusters and extended networks. *Dalt. Trans.* **2010,** *39*, 4968-4977.

74. Roy, X.; Lee, C. H.; Crowther, A. C.; Schenck, C. L.; Besara, T.; Lalancette, R. A.; Siegrist, T.; Stephens, P. W.; Brus, L. E.; Kim, P.; Steigerwald, M. L.; Nuckolls, C., Nanoscale Atoms in Solid-State Chemistry. *Science* **2013,** *341*, 157-160.

75. Shores, M. P.; Beauvais, L. G.; Long, J. R., Cluster-expanded Prussian blue analogues. *J. Am. Chem. Soc.* **1999,** *121*, 775-779.

76. Beauvais, L. G.; Shores, M. P.; Long, J. R., Cyano-bridged Re(6)Q(8) (Q = S, Se) cluster-metal framework solids: A new class of porous materials. *Chem. Mat.* **1998,** *10*, 3783-+.

77. Tulsky, E. G.; Crawford, N. R. M.; Baudron, S. A.; Batail, P.; Long, J. R., Cluster-to-metal magnetic coupling: Synthesis and characterization of 25-electron [Re6-nOSnSe8(CN)(6)]((5-n)-)

(n=1, 2) clusters and {Re6-nOSnSe8[CNCu(Me(6)tren)](6)}(9+) (n=0, 1, 2) assemblies. *J. Am. Chem. Soc.* **2003,** *125*, 15543-15553.

78. Nguyen, H. L.; Gandara, F.; Furukawa, H.; Doan, T. L. H.; Cordova, K. E.; Yaghi, O. M., A Titanium-Organic Framework as an Exemplar of Combining the Chemistry of Metal- and Covalent-Organic Frameworks. *J. Am. Chem. Soc.* **2016,** *138*, 4330-4333.

79. Feng, D. W.; Wang, K. C.; Wei, Z. W. *et al*. Kinetically tuned dimensional augmentation as a versatile synthetic route towards robust metal-organic frameworks. *Nat. Comm.* **2014,** *5*.

80. Wang, K. C.; Feng, D. W.; Liu, T. F. *et al.* A Series of Highly Stable Mesoporous Metalloporphyrin Fe-MOFs. *J. Am. Chem. Soc.* **2014,** *136*, 13983-13986.

81. Ong, W. L.; O'Brien, E. S.; Dougherty, P. S. M.; Paley, D. W.; Higgs, C. F.; McGaughey, A. J. H.; Malen, J. A.; Roy, X., Orientational order controls crystalline and amorphous thermal transport in superatomic crystals. *Nat. Mater.* **2017,** *16*, 83-88.

82. Lee, C. H.; Liu, L.; Bejger, C.; Turkiewicz, A. *et al*. Ferromagnetic Ordering in Superatomic Solids. *J. Am. Chem. Soc.* **2014,** *136*, 16926-16931.

83. O'Brien, E. S.; Trinh, M. T.; Kann, R. L.; Chen, J. *et al.* Single-crystal-to-single-crystal intercalation of a low-bandgap superatomic crystal. *Nat. Chem.* **2017,** *9*, 1170-1174.

84. Shott, J. L.; Freeman, M. B.; Saleh, N. A.; Jones, D. S.; Paley, D. W.; Bejger, C., Ball and Socket Assembly of Binary Superatomic Solids Containing Trinuclear Nickel Cluster Cations and Fulleride Anions. *Inorg. Chem.* **2017,** *56*, 10984-10990.

85. Cahill, D. G.; Ford, W. K.; Goodson, K. E.; Mahan, G. D.; Majumdar, A.; Maris, H. J.; Merlin, R.; Sr, P., Nanoscale thermal transport. *J. App. Phys.* **2003,** *93*, 793-818.

86. Cahill, D. G.; Braun, P. V.; Chen, G. *et al*. Nanoscale thermal transport. II. 2003-2012. *App. Phys. Rev.* **2014,** *1*.

87. Kaiser, J.; Feng, T.; Maassen, J.; Wang, X.; Ruan, X.; Lundstrom, M., Thermal transport at the nanoscale: A Fourier's law vs. phonon Boltzmann equation study. *J. App.Phys.* **2017,** *121*.

88. O'Brien, E. S.; Russell, J. C.; Bartnof, M. *et al.* Spontaneous Electronic Band Formation and Switchable Behaviors in a Phase-Rich Superatomic Crystal. *J. Am. Chem. Soc.* **2018,** *140*, 15601-15605.

89. Chaur, M. N.; Melin, F.; Ortiz, A. L.; Echegoyen, L., Chemical, Electrochemical, and Structural Properties of Endohedral Metallofullerenes. *Angew. Chem. Int. Ed. Engl* **2009,** *48*, 7514-7538.

90. Ueno, H.; Aoyagi, S.; Yamazaki, Y.; Ohkubo, K. *et al.* Electrochemical reduction of cationic Li+ @C-60 to neutral Li+@C-60(center dot-): isolation and characterisation of endohedral [60] fulleride. *Chem. Sci.* **2016,** *7*, 5770-5774.

91. Popov, A. A.; Dunsch, L., Electrochemistry In Cavea: Endohedral Redox Reactions of Encaged Species in Fullerenes. *J. Phys. Chem. Lett.* **2011,** *2*, 786-794.

92. Voevodin, A.; Abella, L.; Castro, E.; Paley, D. W.; Campos, L. M.; Rodriguez-Fortea, A.; Poblet, J. M.; Echegoyen, L.; Roy, X., Dimerization of Endohedral Fullerene in a Superatomic Crystal. *Chem. Eur. J.* **2017,** *23*, 13305-13308.

93. Choi, B.; Yu, J.; Paley, D. W.; Trinh, M. T. *et al*. van der Waals Solids from Self-Assembled Nanoscale Building Blocks. *Nano Letters* **2016,** *16*, 1445-1449.

94. Lee, K. H.; Choi, B.; Plante, I. J. L.; Paley, M. V. *et al.* Two-Dimensional Fullerene Assembly from an Exfoliated van der Waals Template. *Angew. Chem. Int. Ed. Engl.* **2018,** *57*, 6125-6129.

95. Zhong, X.; Lee, K.; Choi, B.; Meggiolaro, D. *et al.* Superatomic Two-Dimensional Semiconductor. *Nano Letters* **2018,** *18*, 1483-1488.

96. Choi, B.; Lee, K.; Voevodin, A.; Wang, J. *et al.* Two-Dimensional Hierarchical Semiconductor with Addressable Surfaces. *J. Am. Chem. Soc.* **2018**.

Chapter 2

Dimerization of endohedral fullerene in a superatomic crystal

2.0 Preface

Significant portions of this chapter are adapted from publication on this research entitled *Dimerization of Endohedral Fullerene in a Superatomic Crystal* by Anastasia Voevodin, Laura Abella, Edison Castro, Daniel W. Paley, Luis M. Campos, Antonio Rodriguez-Fortea, Josep M. Poblet, Luis Echegoyen, and Xavier Roy published in *Chemistry: A European Journal*, **2017**, *23*, 13305-13308.[1] This research was an international collaboration with Prof. Luis Echegoyen's group of University of Texas, El Paso and Prof. Josep Poblet of Universitat Rovira I Virgili in Tarragona, Spain. I carried out the synthesis of the nickel telluride cluster and superatomic crystal. Edison Castro of Prof. Luis Echegoyen's group synthesized the endohedral fullerenes. Antonio Rodriguez-Fortea, and Laura Abella of Prof. Josep Poblet's group carried out the theoretical calculations. Dan Paley performed single crystal refinement.

2.1 Introduction

The assembly of solid-state materials from molecular building blocks offers significant benefits over traditional solid-state reactions; the synthetic flexibility of the building blocks enables the development of functional materials with tunable properties. Building blocks can be chosen based on their redox or shape-complimentary features.

Fullerenes are attractive building blocks as electron acceptors, and their spherical pi-surface enables electronic coupling in all directions. Such electronic interactions in fullerene-based materials have enabled the emergence of remarkable collective properties such as ferromagnetism and superconductivity.[2,3] Building on this foundation, our team has been developing a new class of solid state materials[4] assembled from electronically and structurally complementary molecular clusters. These materials, which we term superatomic crystals,[4–8] provide a bridge between traditional semiconductors, molecular solids, and nanocrystal arrays by combining tunability and atomic precision. Fullerenes have been particularly useful to produce collective properties in superatomic crystals, including ferromagnetic ordering,[9] coherent thermal transport[10] and semiconducting behavior.[4] Many of these properties are described in further detail in Chapter 1 of this thesis.

The synthetic flexibility of molecular clusters offers the possibility to create whole families of multifunctional materials by varying the constitution of the superatomic building blocks. By contrast, the use of fullerenes has been, by and large, restricted to C_{60} and C_{70}. Endohedral fullerenes present the added benefit of varying the composition of the encapsulated guest while maintaining the advantageous properties of the carbon pi-surface.[11–13] These compounds have been explored as MRI contrast reagents, electron acceptors for photovoltaic cells, and single molecule magnets.[14–16] Within the large family of endohedral fullerenes, metal nitride cluster fullerenes $M_3N@C_{80}$ stand out due to their compositional diversity and relatively high synthetic yields.[16–18]

In this chapter we will discuss a new multicomponent superatomic crystal assembled from $Lu_3N@C_{80}$ and a $Ni_9Te_{12}(PEt_3)_{12}$ building blocks.

Here we report on a new material, $[Ni_{12}Te_{12}(PEt_3)_8]_2[(Lu_3N@C_{80})_2]$, which we discovered during our initial exploration of the reaction involving $Ni_9Te_6(PEt_3)_8$ and $Lu_3N@C_{80}$. Using single crystal x-ray diffraction (SCXRD), we find that the anionic $Lu_3N@C_{80}$ fullerenes form dimers in this crystal. The triangular planar Lu_3N clusters inside the dimerized C_{80} cages are coplanar and collinear with the bridging C–C single bond and point at each other. This observation contrasts with theoretical calculations[19] and a recent experimental report of $[(Sc_3N@C_{80})_2]^{2-}$ dimers in which the clusters point away from each other.[20] To understand this unusual orientation, we complement our experimental results with density functional theory (DFT) calculations. Our results chart a clear path to assembling novel superatomic crystals from endohedral fullerenes.

When compared to C_{60} or C_{70}, $M_3N@C_{80}$ have lower electron affinity.[12,21,22] This presents an additional challenge for their assembly into superatomic crystals via charge transfer. To overcome this challenge, our initial plan was to react $Lu_3N@C_{80}$ with $Ni_9Te_6(PEt_3)_8$, a building block with a high ionization energy.[23]

Black crystals are obtained at the interface of two solutions containing $Ni_9Te_6(PEt_3)_8$ and $Lu_3N@C_{80}$ dissolved in mixtures of quinoline and toluene kept at –35 °C for seven days. SCXRD reveals that the solid is a 1:1 stoichiometric combination of a new cluster, $Ni_{12}Te_{12}(PEt_3)_8$, and $Lu_3N@C_{80}$. Refinement of the crystallographic data indicates that $Lu_3N@C_{80}$ forms dimers and the stoichiometry of the compound is $[Ni_{12}Te_{12}(PEt_3)_8]_2[(Lu_3N@C_{80})_2]$. Based on previous work on superatomic crystals,[23] fullerene dimers[18,24] and endohedral fullerene dimers,[11,24] we can assign the following charges to the building blocks: $[Ni_{12}Te_{12}(PEt_3)_8]$ and the dimer $[(Lu_3N@C_{80})_2]$ bear 1+ and 2– charges, respectively. DFT calculations presented below agree with this assignment.

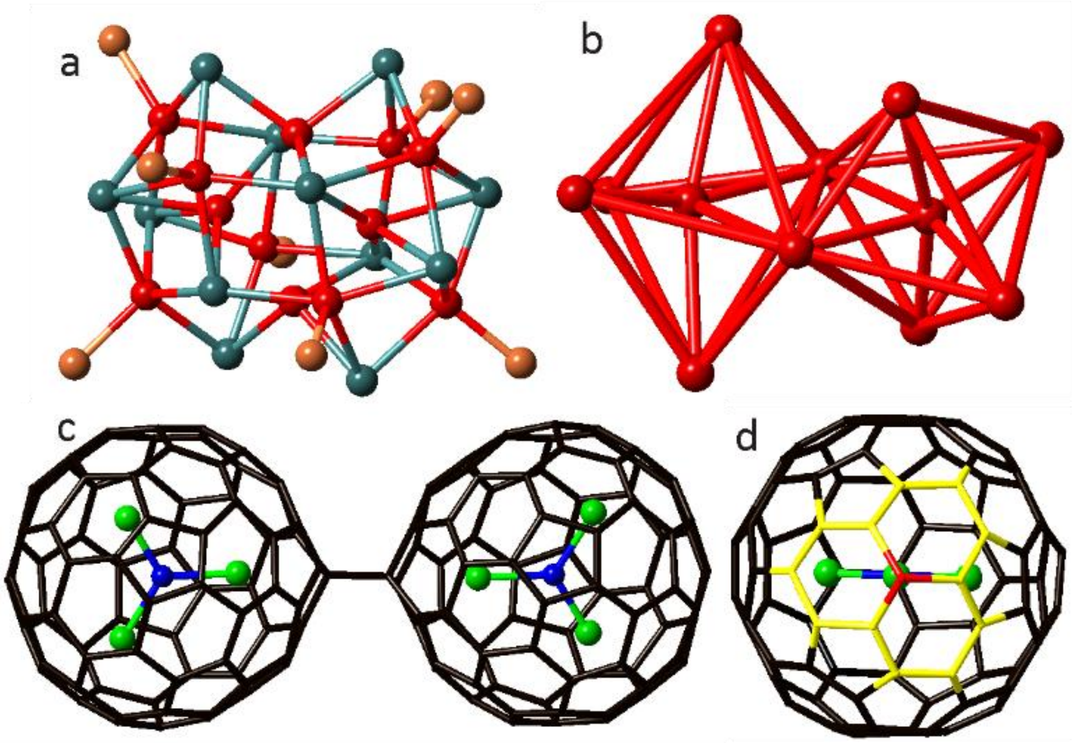

Figure 2.1. SCXRD molecular structure of (a) $Ni_{12}Te_{12}(PEt_3)_8$. (b) Structure of the Ni framework with distorted octahedra sharing a vertex. The Ni-Ni bonds are added to highlight the shape of the octahedra. (c) $[(Lu_3N@C_{80})_2]$ dimer, and (d) $Lu_3N@C_{80}$ highlighting the THJ (yellow) of the inter-cage bonded carbon (red). Color code: C, black; N, blue; Lu, green; Ni, red; Te, teal and P, orange. Ethyl groups on the phosphines are removed from (a) to clarify the view.

Figure 2.1 shows the molecular structures of $Ni_{12}Te_{12}(PEt_3)_8$ and the dianionic $[(Lu_3N@C_{80})_2]^{2-}$ dimer. The cluster $Ni_9Te_6(PEt_3)_8$ has been shown to reorganize in solution[25] and under our reaction conditions, it produces $Ni_{12}Te_{12}(PEt_3)_8$ (Figure 2.1a,b). Figure 2.1b shows the structure of $Ni_{12}Te_{12}(PEt_3)_8$ which can be viewed as two highly distorted octahedra of Ni, with each octahedron having one interstitial Ni atom in the middle and sharing one vertex across the two (Figure 2.1b). The Te atoms adopt different coordination modes, bridging 3 or 4 Ni atoms. Phosphine ligands cap the surface Ni atoms, except for the bridging Ni atoms, which have a distorted tetrahedral geometry. A nickel selenide cluster with an analogous core composition,

$Ni_{12}Se_{12}(PEt_3)_6$, was previously reported by Fenske and Ohmer[26] but the trioctahedral core of this compound is entirely different from the distorted structure of $Ni_{12}Te_{12}(PEt_3)_8$ reported here.

2.3 Structural details of the $Lu_3N@C_{80}$

The interesting result is that $Lu_3N@C_{80}$ is dimerized in the solid state, presumably because of the electron transfer from the electron-rich superatom (Figure 2.1c). Single-bonded dimers have been observed for reduced C_{60} and C_{70}, and suggested both theoretically[19] and spectroscopically[27] for endohedral fullerenes. Konarev and co-workers recently reported the first crystallographic evidence of dimerization of $[Sc_3N@C_{80}]^-$ upon reduction with sodium fluorenone ketyl.[20] The $Sc_3N@C_{80}$ dimer structure features significant disorder of the cages, the inter-cage C–C bond and the cluster but the orientation of the Sc_3N cluster with respect to the inter-cage C–C bond is clear and in agreement with theory: the triangular planar Sc_3N clusters are close to collinear with the bridging C–C single bond, and point away from each other.

The fully ordered structure for the $[(Lu_3N@C_{80})_2]^{2-}$ dimer differs significantly from that of $[(Sc_3N@C_{80})_2]^{2-}$.[20] While the inter-cage C–C bond length (1.66(6) Å) for $[(Lu_3N@C_{80})_2]^{2-}$ is comparable to that for $[(Sc_3N@C_{80})_2]^{2-}$, it selectively links the hexagon-hexagon-hexagon junctions (THJ) of neighboring C_{80} cages (Figure 2.1b). This contrasts with the $[(Sc_3N@C_{80})_2]^{2-}$ structure, in which the fullerene dimer is disordered over three positions including a mixture of THJ and PHHJ dimers. More remarkably, one N–Lu bond for each Lu_3N cluster is perfectly collinear with the inter-cage C–C bond and point directly at the other Lu_3N cluster. While the C_{80} cages are fully ordered at 100 K, the Lu_3N clusters are disordered over three rotational orientations around the axis passing through the inter-cage C–C bond. The distance between the central N atom and the Lu atom closest to the inter-cage C–C bond (2.06(2) Å) is slightly elongated, when compared to the other Lu–N bonds (2.009(19)-2.03(3) Å). The Lu–N–Lu angles are close to the ideal 120°, ranging from 117.4(9)° to 122.4(9)° and the Lu_3N cluster is almost completely flat, with the central N atom protruding from the trimetallic plane by at most 0.039(14) Å.

Figure 2.2a shows the extended packing of $[Ni_{12}Te_{12}(PEt_3)_8]_2[(Lu_3N@C_{80})_2]$, which can be visualized as the superatomic structural analogue of the binary atomic compound rubidium peroxide, Rb_2O_2. Figure 2.2b compares both structures. We present schematic views of the superatomic crystal in which a dummy atom is positioned at the center of each building block (blue represents $Lu_3N@C_{80}$ and red represents $Ni_{12}Te_{12}(PEt_3)_8$). As with the peroxide dianion $[O_2]^{2-}$, pairs of blue atoms are linked together to represent the $[(Lu_3N@C_{80})_2]^{2-}$ dimers. The packing structures of Rb_2O_2 is presented looking down all three crystallographic axes, along with views showing the same orientations for the superatomic crystal. The superstructure of $Ni_{12}Te_{12}(PEt_3)_8]_2[(Lu_3N@C_{80})_2]$ presents a small distortion of the idealized Rb_2O_2 packing resulting from a tilt of the dimer with respect to the b-axis.

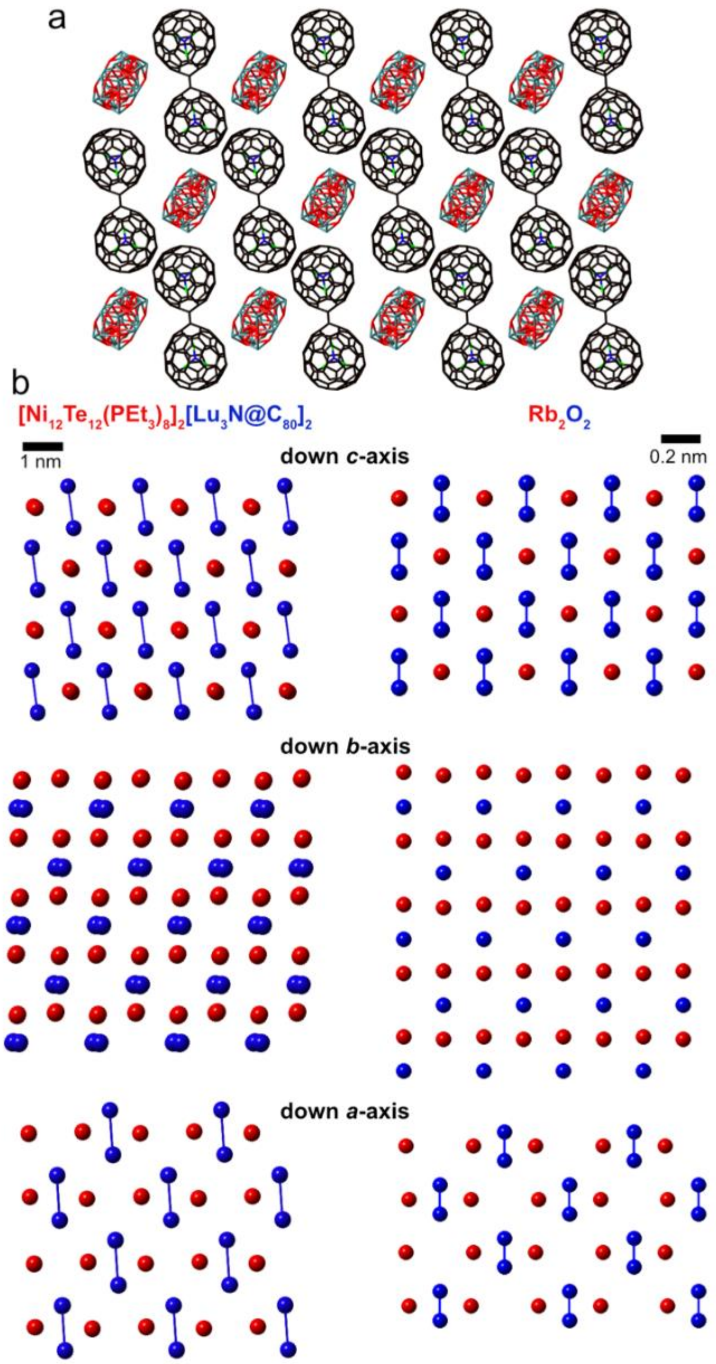

Figure 2.2. (a) Crystal packing of $[Ni_{12}Te_{12}(PEt_3)_8]_2[Lu_3N@C_{80}]_2$. Color code: C, black; N, blue; Lu, green; Ni, red; and Te, teal. The phosphines on the cluster and three quinoline molecules per formula unit are removed to clarify the view. (b) Schematic views comparing the packing of $[Ni_{12}Te_{12}(PEt_3)_8]_2[(Lu_3N@C_{80})_2]$ and Rb_2O_2. $Ni_{12}Te_{12}(PEt_3)_8$ and $Lu_3N@C_{80}$ are represented by blue and red dummy atoms positioned at the center of each building block, respectively. Pairs of blue atoms are linked together to denote the $[(Lu_3N@C_{80})_2]^{2-}$ dimer and the peroxide dianion $[O_2]^{2-}$.

2.4 Explaining the orientation of Lu_3N clusters within $[Lu_3N@C_{80}]_2$

The relative orientation of the cluster within the dimer is unexpected. In fact, the question of the relative orientation of the cluster upon exohedral functionalization has received little attention in the literature. To study this question, we performed DFT calculations for a series of $M_3N@C_{80}$: $Lu_3N@C_{80}$, $Sc_3N@C_{80}$ and $Y_3N@C_{80}$. Table 2.1 contains the computed energy of each inter-cluster orientation upon exohedral dimerization through THJ and PHHJ junctions.

Table 2.1. Relative energies for the different isomers of $[Lu_3N@C_{80}]_2^{2-}$, $[Sc_3N@C_{80}]_2^{2-}$, and $[Y_3N@C_{80}]_2^{2-}$. Energies computed at PBE/TZ2P level are in kcal·mol^{-1}. All calculations correspond to orientation 2 except for the THJ isomers, which are in the orientation 1.

Isomer	$[Lu_3N@C_{80}]_2^{2-}$	$[Sc_3N@C_{80}]_2^{2-}$	$[Y_3N@C_{80}]_2^{2-}$
THJ	0.0	16.5	0.0
PHHJ	1.1	0.0	5.3
Mixed	0.1	1.8	3.8

Figure 2.3 illustrates the two possible orientations for the M_3N cluster. At the PBE/TZ2P level, the orientation in which the Sc_3N clusters are collinear, coplanar, and pointing at each other in the THJ dimer (orientation 1, Figure 2.3a) is energetically disfavored by more than 10 kcal mol^{-1} with respect to the opposite orientation in which the clusters point away from one another (orientation 2, Figure 2,3b, 2.3c). By contrast, orientation 1 is strongly favored by 4.0 kcal mol^{-1} in the case of the Y_3N cluster. Lu_3N is the intermediate case as Lu sits between Sc and Y in terms of size and electronegativity. DFT calculations indicate that orientation 1, which is observed experimentally, is only slightly favored by 1.3 kcal mol^{-1} over orientation 2 (Figure 2.3b,23c).

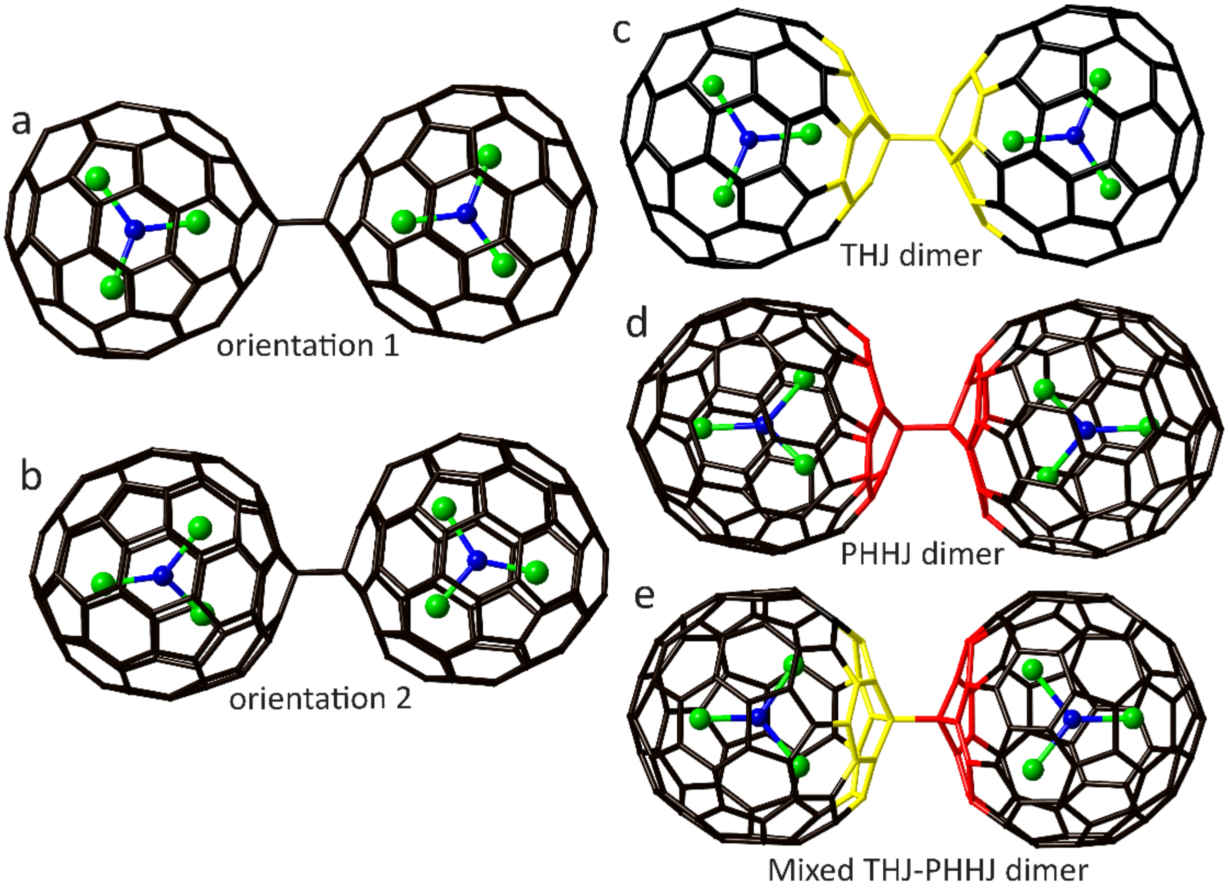

Figure 2.3. (a) and (b) Illustrations of the two possible M_3N cluster orientations in endohedral fullerene dimers, shown here linked through THJ-THJ bond. (c) THJ-THJ bonding with Lu_3N cluster in orientation 1 (d) PHHJ-PHHJ bonding with Lu_3N cluster in orientation 2, and (e) THJ-PHHJ mixed dimer with Lu_3N cluster in orientation 2.

We compare the energy differences for the various types of intercage bonding (i.e. THJ-THJ, PHHJ-PHHJ and THJ-PHHJ dimers shown in Figure 2.3) to understand why, unlike what has been reported for $[(Sc_3N@C_{80})_2]^{2-}$, the $[(Lu_3N@C_{80})_2]^{2-}$ dimer forms exclusively through the THJ junctions. As previously pointed out by Konarev and Popov, the energy differences between the THJ, PHHJ, and mixed THJ-PHHJ for the $[(Sc_3N@C_{80})_2]^{2-}$dimers computed with the PBE functional and using a continuum model solvent are small.[20] At an analogous computational level, similar results are obtained for $[(Lu_3N@C_{80})_2]^{2-}$: the three dimers are found within a range of only 1.1 kcal mol^{-1} shown in Figure 2.3 and Table 2.2.

Table 2.2. Relative energies (E_{rel}), zero-point energies (ZPE), and relative Gibbs free energies (Grel) at 240 K at PBE/TZ2P level. Relative energies using other density functionals, BP86/TZ2P and B3LYP/TZP, are included. All energies are in kcal mol^{-1}.

$[Lu_3N@C_{80}]_2^{2-}$	E_{rel}	ZPE	G_{rel}	BP86/TZ2P	B3LYP/TZP
THJ	0.0	0.0	0.0	0.4	0.0
PHHJ	1.1	0.8	2.6	0.6	2.2
Mixed	0.1	0.8	0.9	0.0	1.0

The experimentally observed THJ dimer is the lowest energy dimer for $[(Lu_3N@C_{80})_2]^{2-}$, with the mixed dimer almost at the same energy (0.1 kcal mol^{-1}), followed by the symmetric PHHJ at 1.1 kcal mol^{-1}. These very small energy differences conflict with our experimental observation that $[Ni_{12}Te_{12}(PEt_3)_8]_2[(Lu_3N@C_{80})_2]$ contains exclusively THJ-THJ dimers, hinting to additional contributions to the total free energy of the system such as the inclusion of the zero-point energies and/or the thermal and entropic contributions.

When these contributions are considered in the calculations, the relative free energies of THJ-PHHJ and PHHJ-PHHJ dimers increase compared to the THJ-THJ which becomes somewhat more stabilized (see Table 2.3). We have examined the effect of reaction temperature on each type of dimer by accounting for the zero-point energies (ZPE) and the thermal and entropic contributions in the calculations within the rigid rotor and harmonic oscillator (RRHO) approximation. The general trend is that the THJ dimer is the most abundant isomer over the whole temperature range analyzed here (see Table 2.3 and Figure 2.4), regardless of the density functional used.

Table 2.3. Relative energies for $[Lu_3N@C_{80}]_2^{2-}$ isomers. Energies in kcal mol^{-1}

$[Lu_3N@C_{80}]_2^{2-}$	E_{rel}
THJ ori1	0.0
THJ ori2	1.3
PHHJ ori1	21.5
PHHJ ori2	1.1
Mixed ori1	8.7
Mixed ori2	0.1
Mixed ori3	2.3

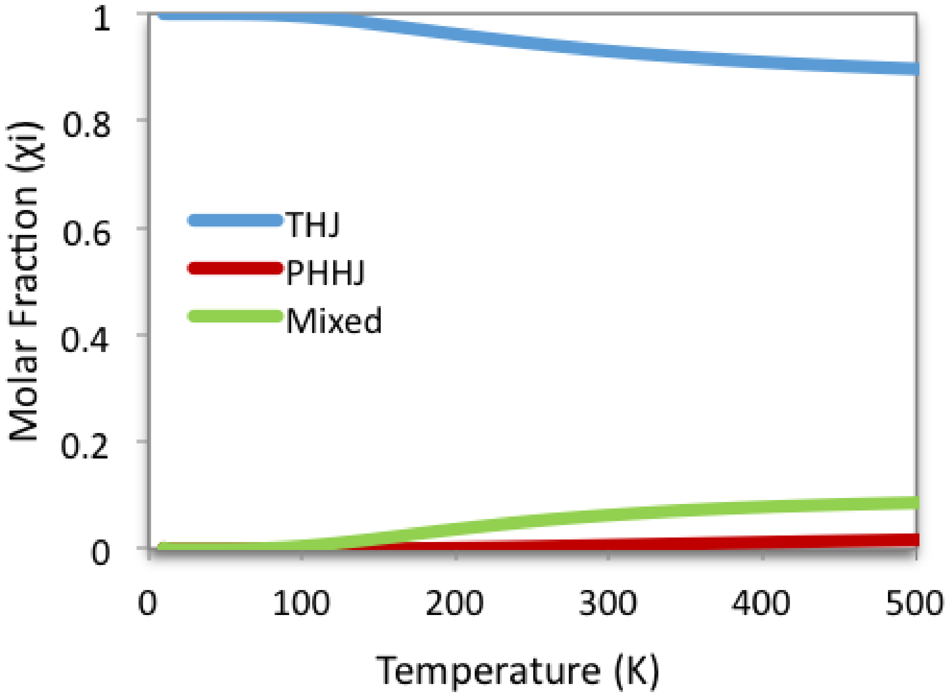

Figure 2.4. Predicted molar fractions as a function of temperature for the three THJ, PHHJ and mixed dimers computed at the PBE/TZ2P level.

To evaluate the relevance of the stabilizing effect of the environment around the dianion we have represented the molecular electrostatic potential (MEP) distribution of the THJ dimer with and without solvent. Notice that in a continuum solvent model, both solvent and countercation effects are included in the calculations. In both cases, the region around the inter-cage bond has the highest electron density (shown in red in Figure 2.5). Figure 2.5 shows that the electron density at the inter-cage junction increases significantly when the solvent environment is included in the calculation. These results suggest that the electrostatic environment surrounding the fullerenes can increase the stability of the dimer system by promoting the accumulation of electron density in the bonding hemispheres. A similar process could be at play in $[Ni_{12}Te_{12}(PEt_3)_8]_2[(Lu_3N@C_{80})_2]$ crystal as the cluster cations are located near the nucleophilic regions.

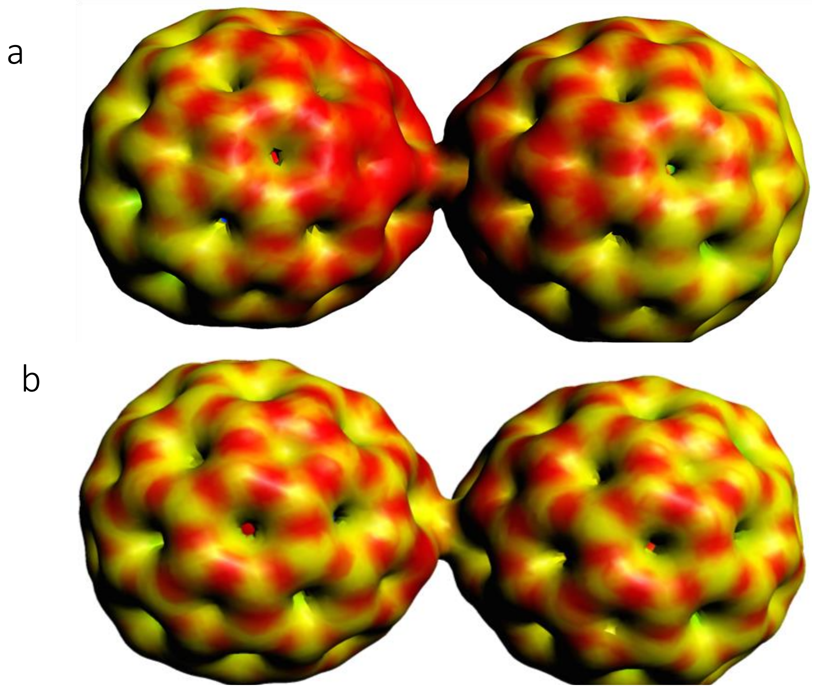

Figure 2.5. Molecular electrostatic potential distribution for the THJ dimer $[(Lu_3N@C_{80})_2]^{2-}$ (a) with and (b) without including the environment effects. More nucleophilic regions are displayed in red.

We computed spin density distribution for the monomeric radical anion $[Lu_3N@C_{80}]^-$ (calculated for both THJ and PHHJ in orientation 1). In the THJ case, the C atom at the junction point holds the largest spin density while that in the PHHJ has a smaller spin density (Figure 2.6) which is more distributed on the fullerene cage. In agreement with the spin density distribution, the HOMO and the LUMO of the THJ $[Lu_3N@C_{80}]$ dimer are essentially localized on the cage, with the HOMO describing the bond formed between the two moieties (Figure 2.7).

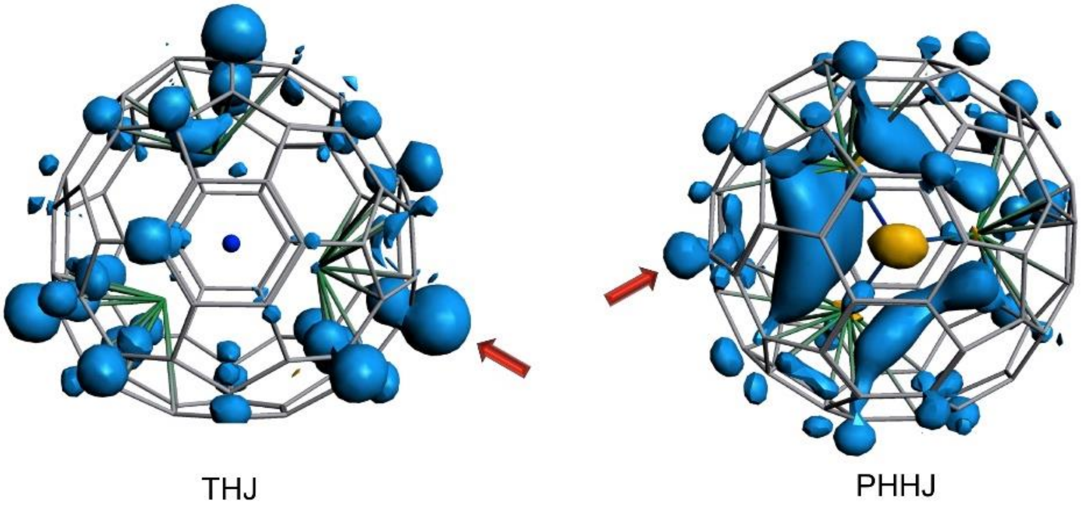

Figure 2.6. Spin density distribution of radical anion monomer $[Lu_3N@C_{80}]^-$ in the THJ dimer (left) and PHHJ dimer (right) with the cluster in orientation 1. Red arrows indicate the bonding carbon in formation of the dimer.

Our results demonstrate that the nature of the encapsulated metal cluster controls the relative stability and orientation of the dimerization product. Konarev and Popov investigated the $(Sc_3N@C_{80})_2^{2-}$ dimer though DFT calculations and found that the energy difference between the THJ and PHHJ dimers is small (less than 2 kcal mol^{-1}), in good agreement with their experimental observation that two types of dimers are present in the crystal structure. Our calculations agree well with these results and predict that the THJ dimer becomes energetically favored for

$(Lu_3N@C_{80})_2^{2-}$ and even more so for $(Y_3N@C_{80})_2^{2-}$. The crystal structure of $[Ni_{12}Te_{12}(PEt_3)_8]_2[(Lu_3N@C_{80})_2]$ reported here is consistent with this first prediction.

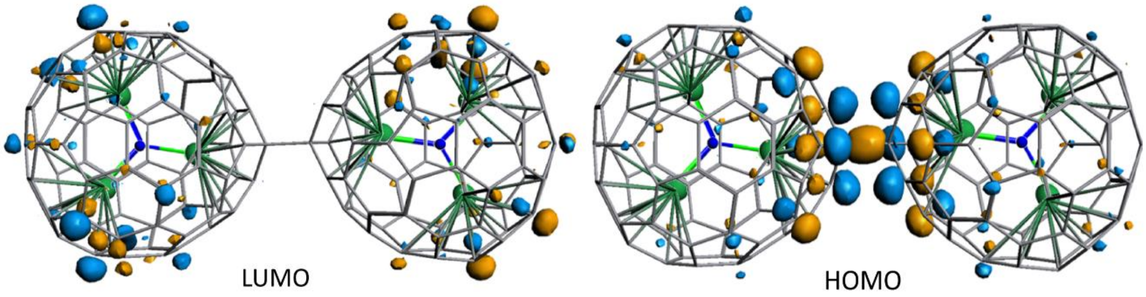

Figure 2.7. Representation of the LUMO and HOMO of the THJ $[Lu_3N@C_{80}]_2^{2-}$ dimer with Lu_3N in orientation 1.

2.5 Conclusion

Our results demonstrate that the nature of the encapsulated metal cluster controls the relative stability and orientation of the dimerization product. Konarev and Popov investigated the $(Sc_3N@C_{80})_2^{2-}$ dimer though DFT calculations and found that the energy difference between the THJ and PHHJ dimers is small (less than 2 kcal mol^{-1}), in good agreement with their experimental observation that two types of dimers are present in the crystal structure. Our calculations agree well with these results and predict that the THJ dimer becomes energetically favored for $(Lu_3N@C_{80})_2^{2-}$ and even more so for $(Y_3N@C_{80})_2^{2-}$. The crystal structure of $[Ni_{12}Te_{12}(PEt_3)_8]_2[(Lu_3N@C_{80})_2]$ reported here is consistent with this first prediction.

2.6 Synthetic Details

Materials

Ni(COD)$_2$, tellurium powder, and Et$_3$P were purchased from Sigma Aldrich. Dry and deoxygenated solvents were prepared by elution through a dual-column solvent system (MBraun SPS). All reactions were carried out under inert atmosphere in a nitrogen-filled glovebox. Ni$_9$Te$_6$(PEt$_3$)$_8$[25] and Lu$_3$N@C$_{80}$[28] were prepared according to published protocols.

Synthesis of [Ni$_{12}$Te$_{12}$(PEt$_3$)$_8$]$_2$[(Lu$_3$N@C$_{80}$)$_2$]

The endohedral fullerene of Lu$_3$N@C$_{80}$ (6 mg, 4 μmol) was dissolved in 6 mL of quinoline in a 20 mL glass vial. A solution of Ni$_9$Te$_8$(PEt$_3$)$_6$ (16 mg, 7 μmol) dissolved in a mixture of toluene (1 mL) and quinoline (3mL) was layered on top of the Lu$_3$N@C$_{80}$ solution. The vial was placed in a freezer at -35 °C. A black precipitate formed overnight but the solution is still dark brown. After 7 days at -35 °C, a few black crystals had formed at the interface between the Lu$_3$N@C$_{80}$ and Ni$_9$Te$_8$(PEt$_3$)$_6$ solutions. The solution was decanted, and the crystals were immediately collected and transferred to STP oil treatment (in the glovebox) for crystallography. The crystals are very sensitive to oxidation or desolvation and thus need to be mounted rapidly on the diffractometer otherwise they start changing color from black to brown in a few minutes and lose their crystallinity. We were not able to characterize the black powder at the bottom of the vial as it degrades too rapidly when we remove it from the mother liquor (presumably because of desolvation).

2.7 Computational Details

All the geometries were computed using the density functional theory (DFT) methodology with the ADF 2016 program.[35,36] The functional of Becke, Burke and Ernzerhoff (PBE) and the Slater TZ2P basis sets were used.[37] Relativistic corrections were included by means of the zero order regular approximation. The inclusion of solvent effects by means of the continuous conductor-like screening model (COSMO) was considered.[38,39] To define the cavity that surrounds the molecules, we use the solvent-excluding surface (SES) method and a fine tesserae. The radii of the atoms, which define the dimensions of the cavity surrounding the molecule, were chosen to be 2.27 Å for Lu, 1.55 Å for N, 1.70 Å for C, 2.00 Å for Sc and 2.19 Å for Y. The dielectric constant was set to 9.8 to model o-dichlorobenzene as solvent. In addition, the Grimme dispersion D3 BJDAMP is also included.[40] Selected orientations of THJ, PHHJ and mixed were also calculated with ADF using the BP86, B3LYP, and PBE0 functionals. In case of hybrid $[Lu_3N@C_{80}]_2{}^{2-}$ Erel THJ ori1 0.0 THJ ori2 1.3 PHHJ ori1 21.5 PHHJ ori2 1.1 Mixed ori1 8.7 Mixed ori2 0.1 Mixed ori3 2.3 $[Lu_3N@C_{80}]_2{}^{2-}$ Erel THJ ori1 0.0 PHHJ ori2 1.6 Mixed ori2 0.5 S8 functional, the TZP was used as basis sets and all electrons were described by means of single Slater functions. Structures and some electronic data for relevant species are available in ref 15.[41]

2.8 Single crystal x-ray diffraction of $[Ni_{12}Te_{12}(PEt_3)_8]_2[(Lu_3N@C_{80})_2]$

Data for $[Ni_{12}Te_{12}(PEt_3)_8]_2[(Lu_3N@C_{80})_2]$ was collected on an Agilent SuperNova diffractometer using mirror-monochromated Cu Kα radiation. Data collection, integration, scaling (ABSPACK) and absorption correction (Numeric analytical methods[29]) were performed in CrysAlisPro.[30] Structure solution was performed using ShelXT.[31] Subsequent refinement was performed by full-matrix least-squares on F2 in ShelXL.[32] Olex2[32] was used for viewing and to prepare CIF files. PLATON[33] was used for twinning analysis in TwinRotMat. Disordered solvent molecules were modeled as rigid fragments from the Idealized Molecular Geometry Library.[34]

An irregular fragment (0.09 x 0.08 x 0.03 mm) was separated carefully, mounted with STP oil treatment, and cooled to 100 K on the diffractometer. Complete data were collected to 0.815 Å. The crystal was a weakly diffracting non-merohedral twin with unequal volume fractions (87:13 in the final refinement). Twin integration was performed in CrysAlisPro and gave 67870 reflections (41110 overlapped, 26760 isolated) with R(int) 14.5% and R(sigma) 35.4%. The weaker isolated reflections of the minor twin component were omitted from the refinement data.

The structure was solved readily in P-1 using ShelXT. The endohedral fullerene was fully located in the initial solution, although subsequent refinement showed that the Lu_3N cluster is disordered over three positions related by rotation around the N-Lu axis facing the C_{80}-C_{80} intercage junction. The $Ni_{12}Te_{12}P_8$ cluster was also located immediately with many phosphine carbon atoms; the remaining phosphine C atoms were easily revealed in subsequent difference maps.

Several solvent molecules were located in difference maps. One quinoline molecule was located readily and subsequently used as a rigid-body template to locate two additional quinolines. These were refined with SAME, FLAT and SIMU restraints to stabilize their geometry and ADPs. A toluene molecule was located with the aid of a template from the IMGL and subsequently refined as a rigid body.

As expected from the weak and twinned data, the stability of the refinement was poor. All carbon and nitrogen atoms were refined with isotropic ADPs. All [$NiPEt_3$] residues were made equivalent with SAME instructions. One PEt_3 group was disordered over two positions, and disorder of other phosphine groups is possible as well, but there were many spurious Fourier features around the Ni and Te atoms of magnitude approximately +/–2 e^{-} $Å^{-3}$ that made it impossible to locate additional disordered positions of PEt_3 groups in difference maps. However, the C_{80} fullerene was fully ordered and could be refined with unrestrained coordinates.

C-H hydrogens were placed in calculated positions and refined with riding coordinates and ADPs. The final refinement (30365 data, 798 restraints, 1040 parameters) converged with R1 ($Fo > 4\sigma(Fo)$) = 11.0%, wR2 = 28.4%, S = 1.01. The largest Fourier features were 2.34 and -1.80 e^{-} $Å^{-3}$.

Table 2.4. Selected crystallographic data for $[Ni_{12}Te_{12}(PEt_3)_8]_2[(Lu_3N@C_{80})_2]$

Compound	**$[Ni_{12}Te_{12}(PEt_3)_8]_2[(Lu_3N@C_{80})_2][quinoline]_6$**
Formula	$C_{162}N_4P_8Ni_{12}Te_{12}Lu_3H_{149}$
MW	5160.23
Space group	P-1
***a* (Å)**	18.0808(9)
***b* (Å)**	21.7532(10)
***c* (Å)**	22.4086(10)
***α* (°)**	88.415(4)
***β* (°)**	66.996(5)
***γ* (°)**	66.089(5)
V ($Å^3$)	7326.5(7)
Z	2
ρ_{calc} (g cm^{-3})	2.339
T (K)	100
λ (Å)	1.54184
$2\theta_{min}$, $2\theta_{max}$	9, 142
Nref	69463
R(int), R(σ)	0.145, 0.354
μ(mm^{-1})	25.019
Size (mm)	.09 x .08 x .03
T_{max}, T_{min}	.517, .227
Data	30365
Restraints	798
Parameters	1040
R_1(obs)	0.1100
wR_2(all)	0.2842
S	1.013
Peak, hole (e^- $Å^{-3}$)	2.34, 1.80
CCDC Number	1558236

2.9 References

1. Voevodin, A.; Abella, L.; Castro, E.; Paley, D. W.; Campos, L. M.; Rodr, A.; Poblet, J. M.; Echegoyen, L.; Roy, X. Dimerization of Endohedral Fullerene in a Superatomic Crystal. *Chem. - A Eur. J.* **2017**, *23*, 13305–13308.

2. Allemand, P.M.; Khemani, K.; Koch, A.; Wudl, F. *et al.* Organic Molecular Soft Ferromagnetism in a Fullerene C60. *Science (80-.).* **2006**, *253* (5017), 301–302..

3. A. F., H.; M. J., R.; R. C., H.; D. W., M.; S. H., G.; T. T. M., P.; A.P., R.; A. R., K. Superconductivity at 18 K in Potassium-Doped C60. *Nature* **1991**, *350* (April), 600–601.

4. Roy, X.; Lee, C.-H.; Crowther, a. C.; Schenck, C. L.; Besara, T.; Lalancette, R. a.; Siegrist, T.; Stephens, P. W.; Brus, L. E.; Kim, P.; et al. Nanoscale Atoms in Solid-State Chemistry Supplementary Data. *Science (80-.).* **2013**, *341* (6142), 157–160.

5. Choi, B.; Yu, J.; Paley, D. W.; Trinh, M. T.; Paley, M. V.; Karch, J. M.; Crowther, A. C.; Lee, C. H.; Lalancette, R. A.; Zhu, X.; et al. Van Der Waals Solids from Self-Assembled Nanoscale Building Blocks. *Nano Lett.* **2016**, *16* (2), 1445–1449.

6. Reber, A. C.; Khanna, S. N.; Castleman, A. W.; Qian, M.; Reber, A. C.; Ugrinov, A.; Chaki, N. K.; Mandal, S.; Saavedra, H. M. H. M. H. M.; Khanna, S. N.; et al. Cluster-Assembled Materials: Toward Nanomaterials with Precise Control over Properties. *ACS Nano* **2010**, *4*

7. Claridge, S. A.; Castleman, A. W.; Khanna, S. N.; Murray, C. B.; Sen, A.; Weiss, P. S. Cluster-Assembled Materials. *ACS Nano* **2009**, *3* (2), 244–255.

8. Khanna, S. N.; Jena, P. Atomic Clusters: Building Blocks for a Class of Solids. *Phys. Rev. B* **1995**, *51* (19), 13705–13716.

9. Lee, C. H.; Liu, L.; Bejger, C.; Turkiewicz, A.; Goko, T.; Arguello, C. J.; Frandsen, B. A.; Cheung, S. C.; Medina, T.; Munsie, T. J. S.; et al. Ferromagnetic Ordering in Superatomic Solids. *J. Am. Chem. Soc.* **2014**, *136* (48), 16926–16931..

10. Ong, W. L.; O'Brien, E. S.; Dougherty, P. S. M.; Paley, D. W.; Fred Higgs, C.; McGaughey, A. J. H.; Malen, J. A.; Roy, X. Orientational Order Controls Crystalline and Amorphous Thermal Transport in Superatomic Crystals. *Nat. Mater.* **2017**, *16* (1), 83–88.

11. Popov, A. A.; Yang, S.; Dunsch, L. Endohedral Fullerenes. *Chem. Rev.* **2013**, *113*, 5989–6113.

12. Chaur, M. N.; Melin, F.; Ortiz, A. L.; Echegoyen, L. Chemical, Electrochemical, and Structural Properties of Endohedral Metallofullerenes. *Angew. Chemie - Int. Ed.* **2009**, *48* (41), 7514–7538.

13. Lu, X.; Feng, L.; Akasaka, T.; Nagase, S. Current Status and Future Developments of Endohedral Metallofullerenes. *Chem. Soc. Rev.* **2012**, *41* (23), 7723–7760.

14. Náfrádi, B.; Antal, Á.; Pásztor, Á.; Forró, L.; Kiss, L. F.; Fehér, T.; Kováts, É.; Pekker, S.; Jánossy, A. Molecular and Spin Dynamics in the Paramagnetic Endohedral Fullerene Gd3N@C80. *J. Phys. Chem. Lett.* **2012**, *3* (22), 3291–3296.

15. Sato, S.; Seki, S.; Luo, G.; Suzuki, M.; Lu, J.; Nagase, S.; Akasaka, T. Tunable Charge-

Transport Properties of I h-C 80 Endohedral Metallofullerenes: Investigation of La2@C80, Sc3N@C80, and Sc3C2@C80. *J. Am. Chem. Soc.* **2012**, *134* (28), 11681–

16. Li, F. F.; Rodríguez-Fortea, A.; Poblet, J. M.; Echegoyen, L. Reactivity of Metallic Nitride Endohedral Metallofullerene Anions: Electrochemical Synthesis of a Lu3N@ i h-C80 Derivative. *J. Am. Chem. Soc.* **2011**, *133* (8), 2760–2765.

17. Cardona, C. M.; Kitaygorodskiy, A.; Echegoyen, L. Trimetallic Nitride Endohedral Metallofullerenes: Reactivity Dictated by the Encapsulated Metal Cluster. *J. Am. Chem.*

18. Echegoyen, L.; Echegoyen, L. E. Electrochemistry of Fullerenes and Their Derivatives. *Acc. Chem. Res.* **1998**, *31*, 593–601.

19. Popov, A. A.; Avdoshenko, S. M.; Cuniberti, G.; Dunsch, L. Dimerization of Radical-Anions: Nitride Clusterfullerenes versus Empty Fullerenes. *J. Phys. Chem. Lett.* **2011**, *2* (13), 1592–1600.

20. Konarev, D. V.; Zorina, L. V.; Khasanov, S. S.; Popov, A. A.; Otsuka, A.; Yamochi, H.; Saito, G.; Lyubovskaya, R. N. A Crystalline Anionic Complex of Scandium Nitride Endometallofullerene: Experimental Observation of Single-Bonded (Sc3N@: I h-C80-)2 Dimers. *Chem. Commun.* **2016**, *52* (71), 10763–10766.

21. Popov, A. A.; Dunsch, L. Electrochemistry in Cavea: Endohedral Redox Reactions of Encaged Species in Fullerenes. *J. Phys. Chem. Lett.* **2011**, *2* (7), 786–794.

22. Ueno, H.; Aoyagi, S.; Yamazaki, Y.; Ohkubo, K.; Ikuma, N.; Okada, H.; Kato, T.; Matsuo, Y.; Fukuzumi, S.; Kokubo, K. Electrochemical Reduction of Cationic Li $^{+}$ @C $_{60}$ to Neutral Li $^{+}$ @C $_{60}$ $^{\cdot\,-}$: Isolation and Characterisation of Endohedral [60]Fulleride. *Chem. Sci.* **2016**, *7* (9), 5770–5774.

23. Chauhan, V.; Sahoo, S.; Khanna, S. N. Ni9Te6 (PEt 3) 8 C 60 Is a Superatomic Superalkali Superparamagnetic Cluster Assembled Material (S 3 -CAM). *J. Am. Chem. Soc.* **2016**, *138* (6), 1916–1921.

24. Segura, J. L.; Martín, N. [60]Fullerene Dimers. **2000**, 13–25.

25. Brennan, J. G.; Siegrist, T.; Stuczynski, S. M.; Steigerwald, M. L. The Transition from Molecules to Solids: Molecular Syntheses of Ni9Te6(PEt3)8, Ni20Te18(PEt3)12, and NiTe. *J. Am. Chem. Soc.* **1989**, *111* (26), 9240–9241.

26. Fenske, D.; Ohmer, J. Neue Ni-Cluster Mit Se Und Pr3 (R = Ph, Et) Als Liganden. *Angew. Chemie* **1987**, *99* (2), 155–158.

27. Huang, T.; Zhao, J.; Feng, M.; Petek, H.; Yang, S.; Dunsch, L. Superatom Orbitals of Sc3N@C80 and Their Intermolecular Hybridization on Cu(110)-(2 X 1)-O Surface. *Phys. Rev. B* **2010**, *81* (8), 085434.

28. Pinzón, J. R.; Zuo, T.; Echegoyen, L. Synthesis and Electrochemical Studies of Bingel-Hirsch Derivatives of M3N@Ih-C80 (M=Sc,Lu). *Chem. - A Eur. J.* **2010**, *16*, 4864–4869.

29. Clark, R. C.; Reid, J. S. The Analytical Calculation of Absorption in Multifaceted Crystals. *Acta Crystallogr. Sect. A* **1995**, *A51*, 887–897.

30. Agilent Technologies UK Ltd. CrysAlisPRO, Version 1.171.37.35. Oxford Diffraction/Agilent Technologies UK Ltd Yarnton, England, 2014.

31. Sheldrick, G. M. Crystal Structure Refinement with SHELXL. *Acta Crystallogr. Sect. C* **2015**, *C71*, 3–8.

32. Dolomanov, O. V; Bourhis, L. J.; Gildea, R. J.; Howard, J. A. K.; Puschmann, H. OLEX2: A Complete Structure Solution, Refinement and Analysis Program. *J. Appl. Crystallogr.* **2009**, No. 42, 339–341.

33. Spek, A. L. Research Papers Structure Validation in Chemical Crystallography Research Papers. *Acta Crystallogr. Sect. D* **2009**, *D65*, 148–155.

34. Guzei, I. A. An Idealized Molecular Geometry Library for Refinement of Poorly Behaved Molecular Fragments with Constraints. *J. Appl. Crystallogr.* **2014**, *47*, 806–809.

35. Baerends, E. J.; Ellis, D. E.; Ros, P. ADF 2013.01. Department of Theoretical Chemistry, Vrije Universiteit: Amsterdam 2016.

36. Velde, G. T. E.; Bickelhaupt, F. M.; Baerends, E. J.; Guerra, C. F.; Gisbergen, S. J. A. V. A. N. Chemistry with ADF. *J. Comput. Chem.* **2001**, *22* (9), 931–967.

37. Perdew, J. P.; Burke, K.; Ernzerhof, M. Generalized Gradient Approximation Made Simple. *Phys. Rev. Lett.* **1996**, *77* (18), 3865–3868.

38. Andzelm, J.; Kölmel, C.; Klamt, A.; Klamt, A. Incorporation of Solvent Effects into Density Functional Calculations of Molecular Energies and Geometries. *J. Chem. Phys.* **1995**, *103* (21), 9312–9320.

39. Klamt, A.; Schuurmann, G. COSMO : A New Approach to Dielectric Screening in Solvents with Explicit Expressions for the Screening Energy and Its Gradient. *J. Chem. Soc. Perkin Trans* **1993**, *2*, 799–805.

40. Grimme, S.; Antony, J.; Ehrlich, S.; Krieg, H. Parametrization of Density Functional Dispersion Correction (DFT-D) for the 94 Elements H-Pu Dispersion Correction „ DFT-D … for the 94 Elements H-Pu. *J. Chem. Phys.* **2010**, *132* (154104).

41. M., A.-M.; Graaf, C. de; Lo, N.; Maseras, F.; Poblet, J. M.; Bo, C. Managing the Computational Chemistry Big Data Problem : The IoChem-BD Platform. *J. Chem. Inf. Model.* **2015**, *55*, 95–103.

Chapter 3

Towards long range ordering of superatomic solids

3.0 Preface

This chapter presents some of the initial motivations and strategies I undertook to achieve long range ordering of superatomic solids. Although these initial explorations were largely unsuccessful at fabricating extended superatomic assemblies, nevertheless they helped develop the foundation on which the superatom-containing polymers were built from (see Chapters 4,5). I will highlight some of the interesting results that were produced by these investigations. Dan Paley performed single crystal refinement.

3.1 Introduction

Successful crystallization of monocomponent or multicomponent superatomic materials can be difficult to predict and an even greater challenge is to precisely control the crystalline order of the nanoscale building blocks. Developing a method to construct and organize superatoms at multiple length scales opens new opportunities to understand the assembly's fundamental materials properties that will also establish new structure-property relationships. To extend the assemblies of superatoms at greater length scales requires a different design strategy. My challenge was to design a bottom-up synthetic approach that would enable the controlled fabrication of superatomic assemblies beyond the nanoscale regime.

This aim is likened to the rapidly developing interest in creating bottom-up strategies that use nanoparticles as building blocks to create mesoscale assemblies.[1–3] Mesoscale materials are considered to be materials at intermediary length scales that range from tens of nanometers to tens of microns. At these length scales, it is possible to gain a new understanding of how architecture determines performance.[4–6] Achieving targeted assemblies at multiple length scales with varied architectures would generate new insight on the structure-property relationships of the superatomic assemblies and potentially reveal new applications of the functional materials. Figure 3.1 depicts some representative examples of nanoscale building blocks such as inorganic nanoparticles,[7,8] tethered particles,[9–11] macromolecules,[12,13] polymer nanoparticles,[14,15] and liquid crystals[16] that have been increasingly explored for self-assembly into mesoscale structures with potential functional applications and developing technologies. An exotic library of hybrid nano-objects have been synthesized by judicious design of some of these inorganic nanoscale building blocks that interact with organic components to coordinate, organize, and assemble the inorganic materials into higher-order structures.[17]

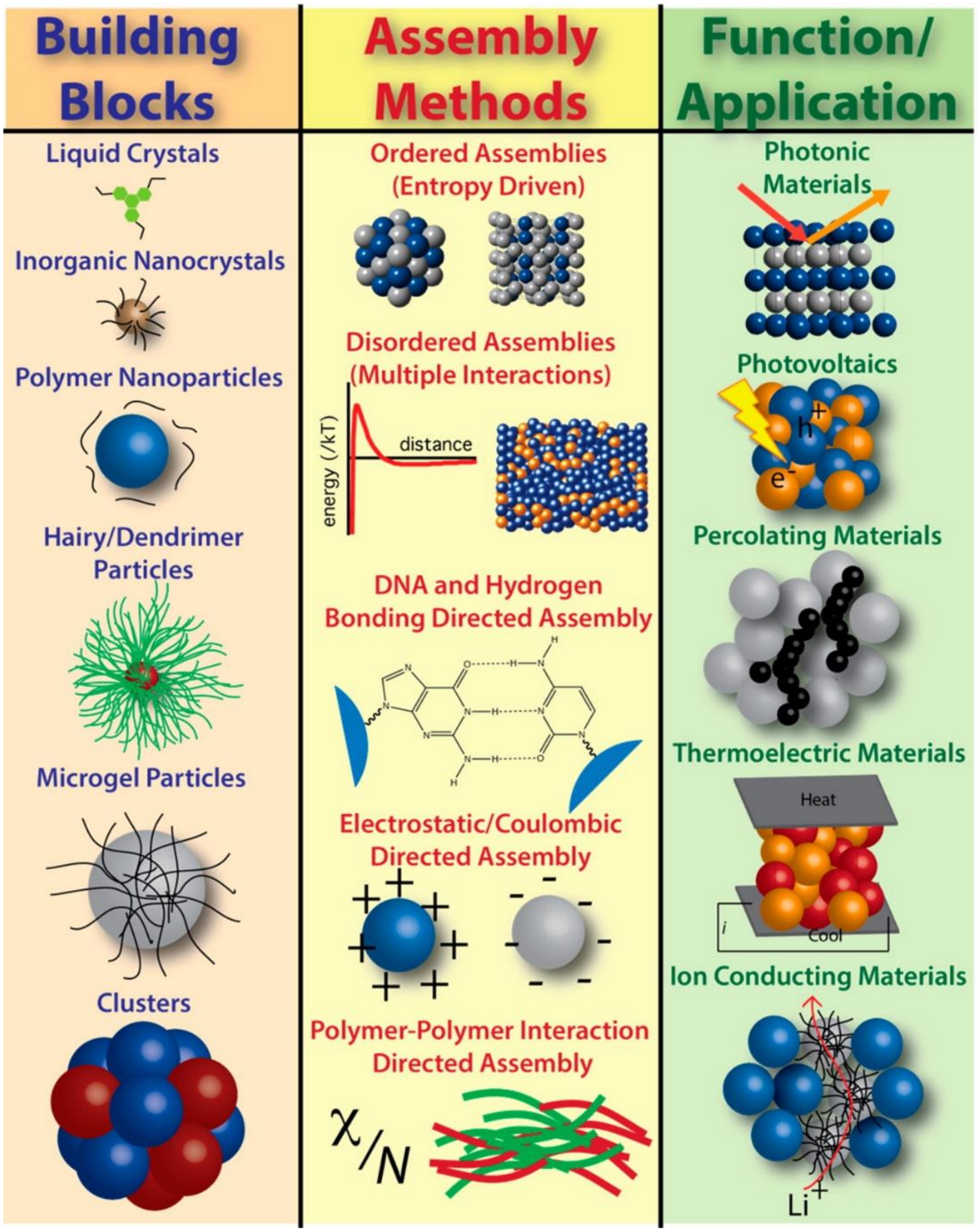

Figure 3.1. Building blocks, assembly methods, and potential applications in mesoscale polymer and macromolecular science. Reproduced from L. Renna, *et al.*, "Polymer nanoparticle assemblies: a versatile route to functional mesostructures" *Macromolecules*, 2015, 48, 6353-6368.[4]

Our first approach to control the assembly of superatoms at microscales was to harness the well-studied charge-transfer capabilities of superatoms to template higher order structures. Instead of in-situ co-crystallization of redox-complimentary nanoscale building blocks, we sought to introduce a redox-complimentary polymer template. This approach was inspired by the burgeoning work using polymer scaffolds to template nanoparticles.[18–20] Embedding building blocks such as nanoparticles, quantum dots, small molecules and proteins before[21,22] of after[19] the self-assembly of a polymer system creates polymeric nanocomposites. A chemist is provided with multiple ways to synthetically tune the self-assembly of such polymer composites such as by modifying the chemical composition, chain length, and assembly conditions (*i.e. solvent, temperature, substrate*). These tools control the achieved long-range order of the nanoparticles and select morphologies have proven superior in performance as functional materials for medical, electronic, and optical devices.[19,23–25]

Charge-transfer interactions between electron rich superatoms and fullerenes have directed the assembly of a library of ionic binary superatomic solids. We considered perylene diimide (PDI) molecules as promising alternative n-type materials that could replace the fullerene building blocks. Like fullerenes, PDI molecules have been investigated as organic small molecule acceptors for applications in engineering solar[26–29] and battery devices[30]. PDIs, like fullerenes, are redox-complimentary to superatoms that are strong electron donors such as cobalt telluride clusters.[31,32] Although PDIs lack the spherical shape similarity to metal chalcogenide clusters, they can be more easily chemically modified than fullerenes and thus provide a greater synthetic handle for fabricate tunable functional materials.

PDIs have a strong electronic absorption in the visible region and substitution of PDI molecules in their core positions tunes their lowest unoccupied molecular orbital (LUMO) levels.[33] In addition to their promising electronic properties, PDIs are robust molecules that are heat and air stable. The solubilizing imide tails of PDIs are easy to chemically modify and utilize as anchoring segments onto polymerizable units. Block copolymers that contain side chain units of PDIs have been assembled into hierarchical microscale structures.[26,34,35] Processing of PDIs either in the solid-state or embedded in a polymeric matrix has been extensively explored for photovoltaic and battery device architectures.

It is for the synthetic and electronic properties discussed above that we pursued the synthesis of a polymer template with pendant PDI units to direct the self-assembly of superatoms into higher ordered structures. Ultimately, we were not able to create ordered assemblies of superatoms using this technique. Nevertheless, several interesting results emerged in its pursuit. For example, our initial interactions of PDI molecules with metal chalcogenide clusters resulted in a new binary superatomic solid [C_5-PDI-CN_2] [$Co_6Te_8(PEt_3)_6$].

Perhaps of even greater importance was that this initial approach to use a polymer template later inspired the covalent functionalization of the site-differentiated cobalt selenide superatom[36] onto a polymerizable monomer. While the cluster-containing polymers will be discussed in later chapters, herein I will discuss some of the insights we gained from the synthesis of a PDI-containing diblock copolymer template.

3.2 In-situ reduction of PDI with $Co_6Te_8(PEt_3)_6$

The synthesis of superatomic materials that exhibit novel materials properties (*i.e. electron transport, magnetic ordering*) has been inspired by previous assembly of reactive molecules in the solid state. Organic-inorganic hybrid materials containing redox active metal chalcogenide centers with organic electroactive molecules exhibit unique electronic behavior. For example, the electrocrystallized material of ethylenedithio-tetrathiafulvane molecules with hexasubstituted metal chalcogenides forms a complex Kagome with a composition of (EDT-TTF-$CONH_2)_6[Re_6Se_8(CN)_6]$ that has semiconducting behavior below 130 K.[37] In this lattice material structural transitions caused by electron instability drive the material to insulating states at low temperatures. A series of other atomically precise clusters with M_6E_8 motifs have been reported to have charge transfer interactions with organic molecules such as TTF, TCNQ or other inorganic clusters yielding interesting conductivity behavior in assembled solids.[38–44]

Motivated by the results of inorganic-organic hybrid materials built from molecular clusters and organic molecules, we sought to use perylene diimide (PDI) as our organic acceptor building block. As described in the introduction of this chapter, PDI's have been widely explored as n-type molecules. PDIs are also well-known for their absorption from ~300-600 nm giving the molecule its signature red pigmentation –that any chemist who has worked with the molecule is well familiar with.[33] PDIs are highly reactive and their imide groups and bay-area positions can be easily chemically modified. Substitution at the bay-area positions with electron withdrawing groups such as bromines, cyanides, or fluorines has a dramatic effect on the electronics of the molecule.[28,45–48] Impressive functionalization of these positions is an exciting area of investigation that has resulted in the synthesis of cyclized macromolecules with remarkable electronic and photophysical properties for organic n-type electronic materials.[28,49–51]

Assembly of binary charge transfer materials can be achieved by solution-phase electron transfer between redox-complimentary building blocks which has resulted in the synthesis of a library of ionic binary superatomic solids.[32] The selection of building blocks is critical to ensure that electrons to flow from donor to acceptor units. We chose the electron-rich $Co_6Te_8(PEt_3)_6$ to be the electron donating nanoscale building block in co-assembly with PDI.[31]

Reduction of PDI can be monitored by electron absorption spectroscopy through the ingrowth of absorption bands between 600-900 nm indicating the presence PDI radical anion species after electron transfer to the molecule.[47] In Figure 3.2 we see the growth of these absorption bands, indicating successful reduction of PDI by $Co_6Te_8(PEt_3)_6$ which forms a radical anion PDI molecule. The absorption of the radical anion is increased by more polar solvent environments and by higher equivalents of the cluster species.

To observe the reduction of PDI by cobalt telluride, we stirred PDI, functionalized with didecylamine solubilizing chains,[26] $Co_6Te_8(PEt_3)_6$ in equal stoichiometries in tetrahydrofuran (THF), toluene, and dichloromethane (DCM) and then took the electronic absorption spectra of these reactions. In Figure 3.2a, we see the growth of reduced PDI between 600-800 nm only in solution with DCM -an observation that is consistent with studies showing the stabilization of charges in polar solvents.[52–54] While dissolved in toluene, equal equivalents of PDI and cobalt telluride do not give rise to apparent charge transfer absorptions (see Figure 3.1b). However, by increasing the concentration of cobalt telluride superatoms in solution more PDI molecules are reduced and an ingrowth of absorption peaks corresponding to the charge transfer bands is observed. Substitution of PDI in its core positions with electron withdrawing groups such as fluorine or cyano groups lowers its LUMO energy level, making it easier to reduce the molecule.[33] Figure 3.1c shows the dramatic increase in the charge transfer absorptions upon stirring equal equivalents of $Co_6Te_8(PEt_3)_6$ with dicyano-PDI[55] (C_5-PDI-CN_2) in DCM.

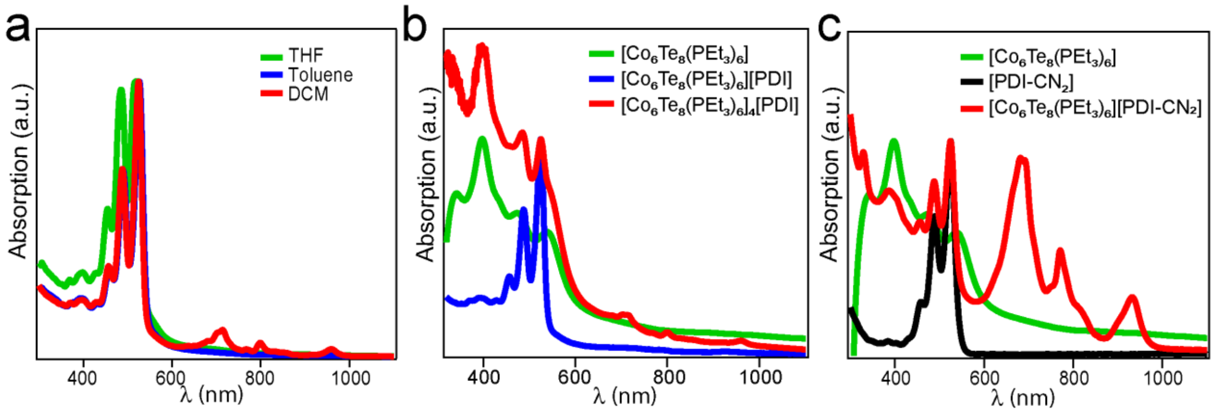

Figure 3.2. (a) $Co_6Te_8(PEt_3)_6$ with equal equivalents of PDI dissolved in tetrahydrofuran (green), toluene (blue), and dichloromethane (red). (b) $Co_6Te_8(PEt_3)_6$ (green), $Co_6Te_8(PEt_3)_6$ and PDI with 1:1 equivalents (blue), and $Co_6Te_8(PEt_3)_6$ and PDI with 4:1 (red) equivalents, respectively. All compounds dissolved in toluene. (c) $Co_6Te_8(PEt_3)_6$ (green), C_5-PDI-CN_2 (black), and $Co_6Te_8(PEt_3)_6$ and C_5-PDI-CN_2 with 1:1 molar ratio. All compounds dissolved in DCM. Electronic absorption spectra normalized to the absorption peak at 520 nm of $Co_6Te_8(PEt_3)_6$

3.3 Synthesis of the superatomic crystal [$Co_6Te_8(PEt_3)_6$][C_5-PDI-CN_2]

We reacted $Co_6Te_8(PEt_3)_6$ as shown with dicyano perylene diimide functionalized with 3-aminopentane (C_5-PDI-CN_2)[55] to co-crystallize [$Co_6Te_8(PEt_3)_6$][C_5-PDI-CN_2]. Its molecular structure as determined by single x-ray diffraction (SCXRD) is shown in Figure 3.3(a,b). By bond distance analysis, the average length of Co-P bonds is 2.17(6) Å (with a range of 2.16(8)-2.17(8) Å) and this length indicates a 2+ oxidation state of the superatom.[56] This observation confirms the electron charge transfer observed in the electronic absorption spectra from these complimentary building blocks. The sample of PDI used for co-crystallization had a mixture of the 1,6 and 1,7 cyano-functionalized isomers. The molecular structure of the solid state material, indicates that both isomers crystallized in the solid state, with the crystal structure showing disorder of the two substitution positions in a ratio of 72:28. The majority of the disorder corresponds to the trans (1,7)-dicyano isomer that is shown in Figure 3.3.

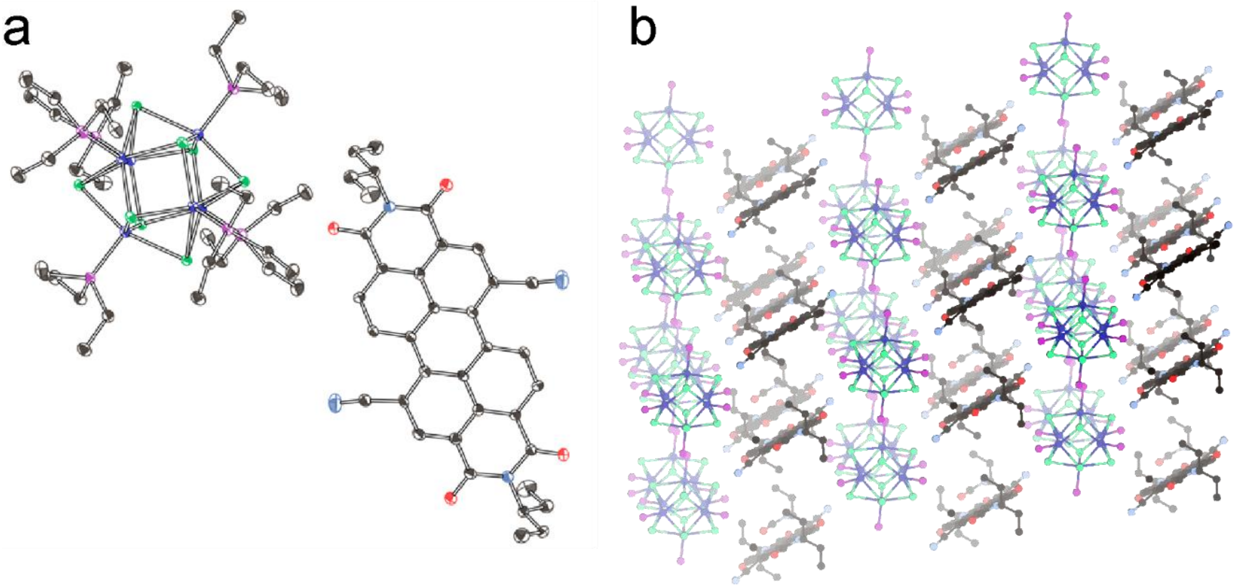

Figure 3.3. (a) SCXRD molecular structure of [C_5-PDI-CN_2][$Co_6Te_8(PEt_3)_6$] and (b) a side-view of the packed structure. Color code: C (black), Co (dark blue), N (light blue), O (red), P (pink), and Te (green). Triethyl phosphine groups have been omitted for clarity in 3.3b.

3.4 Design of a polymer template to direct the self-assembly of superatoms

The controlled fabrication of nanoscale structures of functional materials is essential for nanotechnology. The first two chapters of this thesis discuss the self-assembly of superatoms into solids with precise ordering of their nanoscale building blocks. Assembly of monocomponent and multicomponent superatomic solids has been realized by the design and selection of nanoscale building blocks to construct functional materials through strong inter-component interactions (*i.e. charge transfer, van der Waals forces, covalent coupling*).

As top-down lithographic techniques[57] approach their limit for nanoscale resolution, bottom-up approaches that assemble functional nanoscale building blocks become increasingly important. Block copolymers (BCPs) are synthesized through the covalent union of chemically distinct homopolymers. Typically, distinct homopolymers are selected to be immiscible and have complimentary physical properties that result in directed chemical self-assembly. The dissimilar blocks tend to phase-segregate and assemble into various structures with ordered domains as shown in Figure X. The targeted morphology can be selected by tuning the volume fraction of the blocks (*f*A, *f*B), and self-assembly conditions (i.e. solvent, temperature, external stimulus.[58–60]

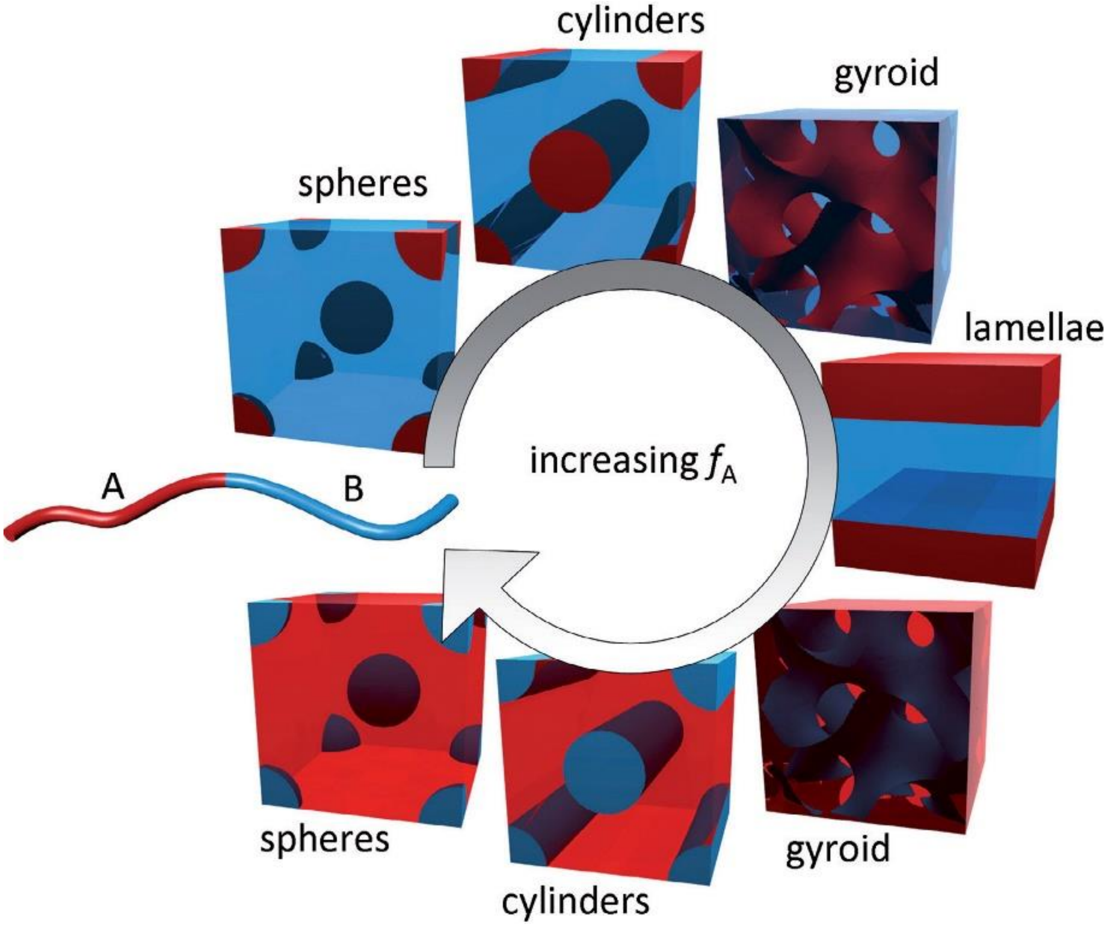

Figure 3.4. Different phases formed by self-assembly of coil-coil diblock copolymers in the bulk (when the intermolecular interaction is sufficiently large) as a function of the volume fraction of one of the blocks (*f*A). Other phases have also been reported for diblocks, and the phase diagrams of BCPs containing more than two blocks are considerably more complex. Switching out one or both coil blocks with a conjugated block that adopts a semi-flexible or rigid rod structure will also qualitatively change this phase diagram. Reproduced from I. Botiz and S.B. Darling, "Optoelectronics using block copolymer," Materials Today, vol. 13, no. 5, pp. 42-51, 2010.[60]

Block copolymers with perylene diimide side-chains have been studied for applications in self-assembly of donor-acceptor polymers[26] and for device fabrication of organic electronics.[34]

Since Asymmetrical PDI molecules can be easily synthetized by select chemical modification of one of the imide tails. This asymmetrical synthetic strategy is commonly employed to functionalize PDI as side-chain units onto polymer backbones.

In our initial efforts of developing superatomic assemblies with long-range ordering at the mesoscale, we sought to employ a BCP containing PDI chains (BCP-PDI) that could self-assemble in solution and create a template for superatoms. We hypothesized that the same charge-transfer interactions that occurred in the solid-state, resulting in the binary superatomic solid described above, would direct the self-assembly of the cobalt telluride superatoms within the polymeric matrix.

3.5 Synthesis and assembly of perylene diimide block copolymer

Figure 3.5 shows the two norbornene monomers with pendant perylene diimide (PDI) and polyethylene glycol (PEG) sidechains that were polymerized into a diblock copolymer by ring opening metathesis polymerization (ROMP). The PEG and PDI blocks form homopolymer chains linked together in the diblock copolymer that are immiscible. Physical interactions between the

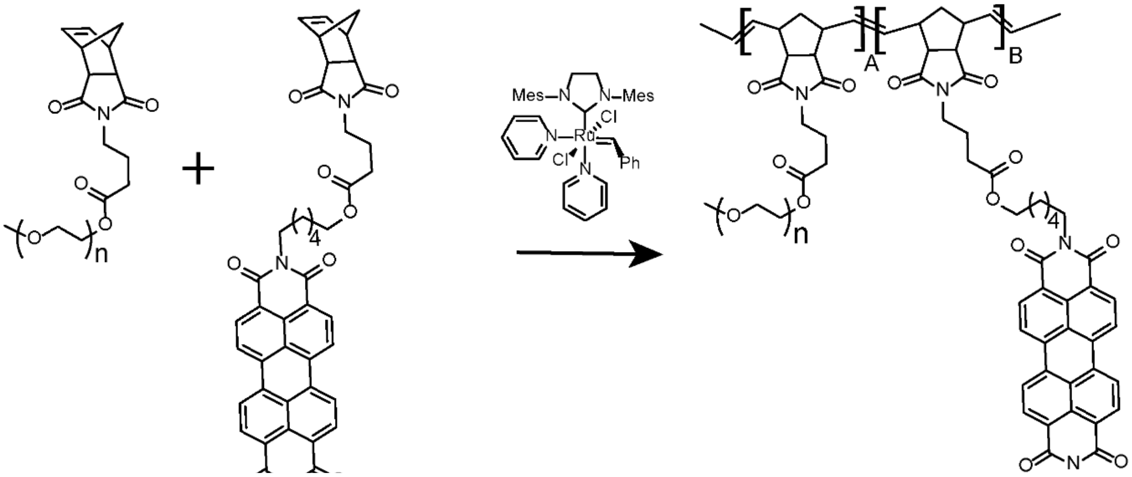

Figure 3.5. ROMP polymerization using a Grubbs III generation catalyst of norbornene monomers functionalized with PEG and PDI side chains to form BCP with A and B volume fractions of PEG and PDI respectively.

hydrophilic PEG and hydrophobic PDI blocks results in phase separation and by controlling the relative volume fractions of the blocks, a wide range of periodic morphologies should be accessible.[61]

We synthesized a variety of monodisperse BCPs having varying PEG lengths (n = 4, 750, 2000) and alternated between 50:50 and 80:20 ratios of the PEG and PDI blocks, respectively. Unfortunately, self-assembly of the BCPs resulted in irregular morphologies and produced inconsistent results. A few representative examples of the morphologies that were characterized are presented in Figure 3.6. The transmission electron micrograph (TEMs) in Figure 3.6(a,b) is of a BCP with 80 units PEG (n = 4) and 20 units of PDI. The sample was assembled by dissolving equal amounts by weight of BCP and $Co_6Te_8(PEt_3)_6$ in THF and then adding an equal volume of water to induce self-assembly. Figure 3.6c presents the assembly in DCM/MeOH of a BCP with 50 units of PEG (n=4) and 50 units of PDI, and Figure 3.6d presents the assembly in DCM/MeOH of BCP with 50:50 units of PEG:PDI but the PEG block was extended (n=750). These BCPs were assembled in-situ with equal amounts by weight of $Co_6Te_8(Pet_3)_6$. Although the assemblies resulted in very different features using the different solvent conditions, the features were generally irregular. Furthermore, later studies using the same polymer and assembly conditions failed to reproduce similar results. Due to these inconsistencies we decided to pursue a different synthetic approach for self-assembly.

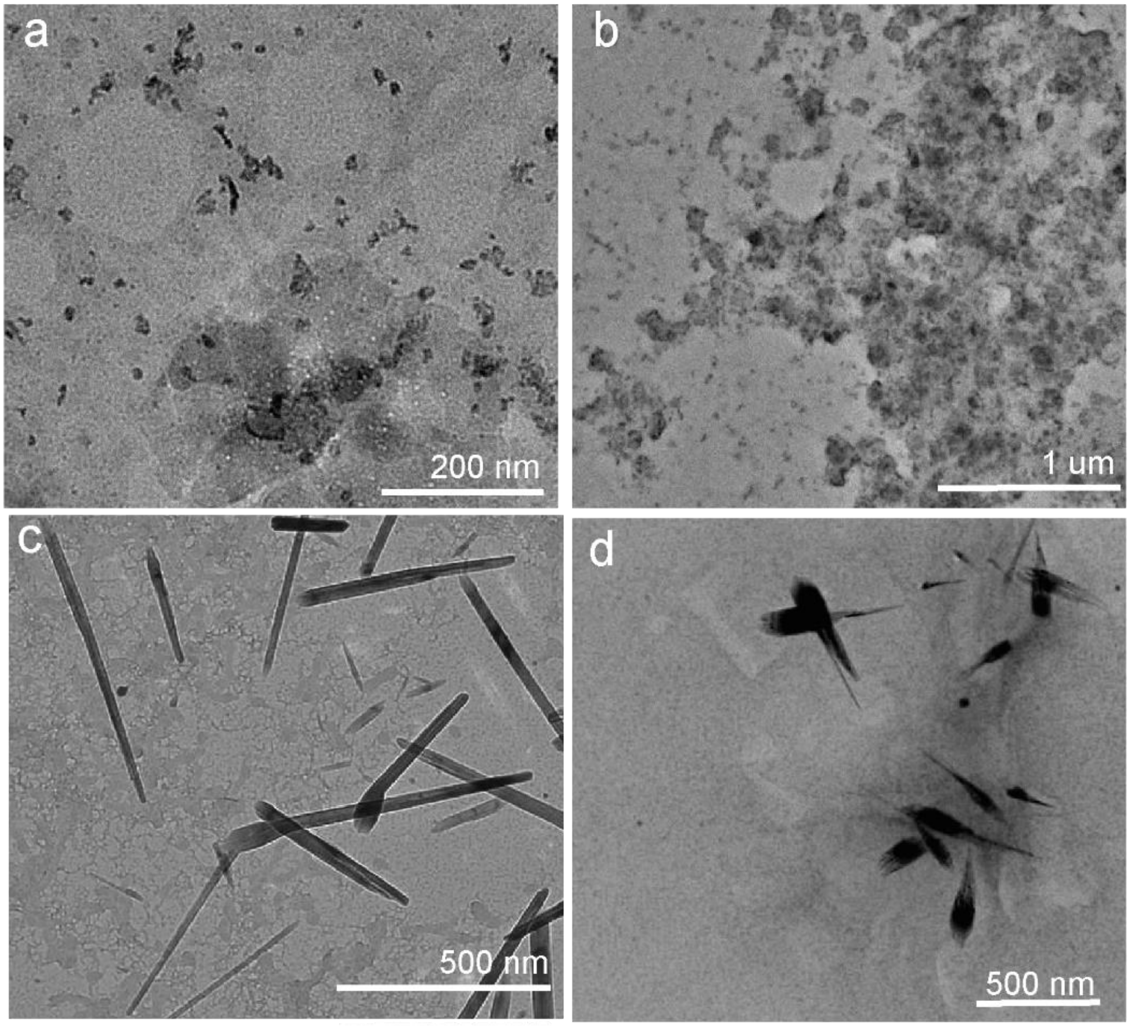

Figure 3.6. TEM micrographs of BCPs assembled with different ratios of PEG:PDI and in different solvent conditions. (a) BCP having 80:20 repeat units of PEG (n=4):PDI assembled in THF/H_2O. (b) BCP having 80:20 repeat units of PEG (n=4): PDI assembled in THF/H_2O. (c) BCP having 50:50 repeat units of PEG (n = 4): PDI assembled in DCM/MeOH and (d) BCP having 50:50 repeat units of PEG (n = 750): PDI assembled in THF/H_2O. All assemblies were carried out with the addition of $Co_6Te_8(PEt_3)_6$ dissolved with the BCP prior to self-assembly. The images show some of the irregular morphologies that were achieved by using this polymer system to template the superatoms.

3.6 Conclusion

The $[Co_6Te_8(PEt_3)_6][C_5\text{-PDI-CN}_2]$ co-crystal is a new addition to the library of ionic binary superatomic solid state materials and illustrates the effective use of charge transfer to drive self-assembly of superatomic solids. While goal in using a BCP template to access microscale assemblies of superatoms was not realized the approach of using a BCP system to form superatomic assemblies was born from these first attempts. Additionally, the time spent in experimenting with polymerization and self-assembly conditions of the BCP and learning characterization techniques of BCPs provided a foundation of knowledge off which future investigations into the synthesis, self-assembly, and characterization of the superatom-containing polymer was built.

3.7 Methods

NMR Spectroscopy

^{1}H NMR and ^{31}P NMR spectra were recorded on a Bruker DRX400 spectrometer.

Electronic Absorption Spectroscopy

Electronic absorption spectra were recorded using a 1.0 cm quartz cell on an Agilent Technologies Cary 60 UV-vis spectrophotometer.

Single Crystal X-Ray Diffraction.

Crystallographic data was collected on an Agilent SuperNova diffractometer using mirror-monochromated Cu Kα radiation.

Transmission Electron Microscopy Details

This work was performed at the Simons Electron Microscopy Center and National Resource for Automated Molecular Microscopy located at the New York Structural Biology Center, supported by grants from the Simons Foundation (SF349247), NYSTAR, and NIH National Institute of General Medical Sciences (GM103310). The FEI Tecnai F20 was used for imaging.

3.8 Synthetic Details

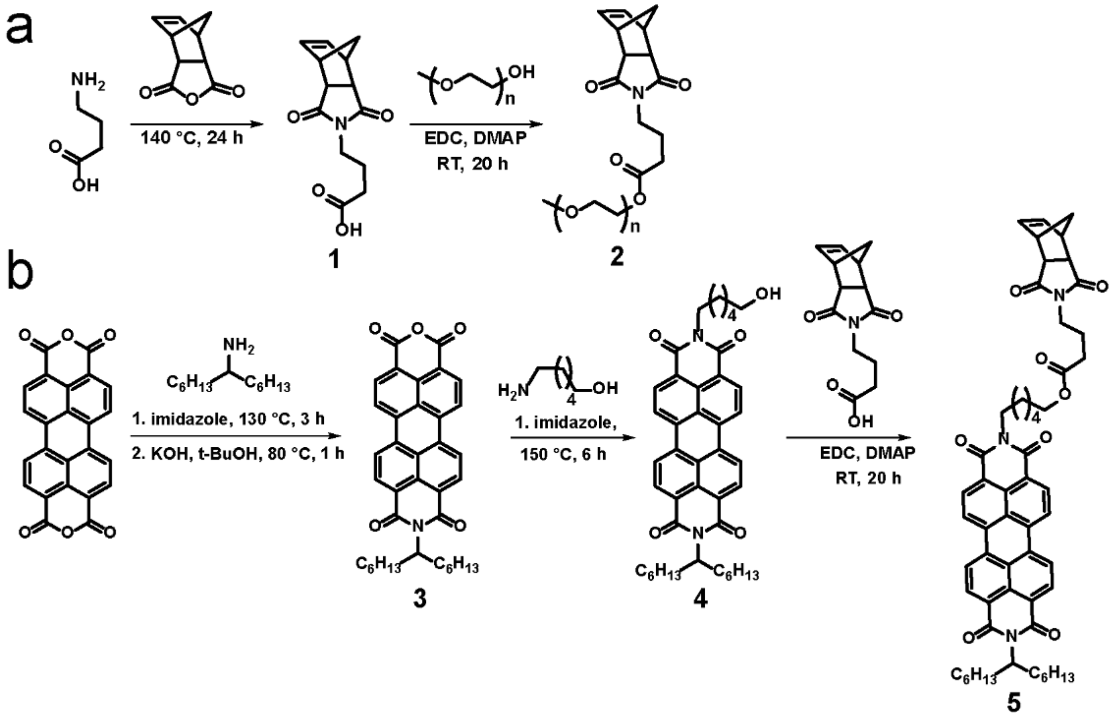

Figure 3.7. (a) Scheme of synthesis of norbornene monomer with pendant PEG chains and (b) synthesis of norbornene monomer with pendant PDI units. These monomers were used for the synthesis of the diblock copolymer.

Synthesis of 1 and 2

A previously reported literature procedure was followed.[62]

Synthesis of Perylene-3,4,9,10-tetracarboxylic di(13-decyl)imide (3).

Adapted from previously reported literature procedure.[26] Perylene dianhydride (6.24 mmol), 13-decylamine (15.86 mmol), and imidazole (218 mmol), were heated under argon at 120°C for 3 hrs. Toluene (10 mL), was added, and the mixture was cooled to room temperature. The product was precipitated in ethanol (100 mL), filtered, washed with methanol, and dried under vacuum. Purification was carried out by column chromatography with 50/50 DCM/Hexanes mixtures to isolate the di(13-decyl)imide with an 80% yield in the first step.

The diimide (2.64 mmol), potassium hydroxide pellet (85%) (5.57 mmol), and tert-butyl alcohol (40 mL) were combined in a flask and refluxed at 80 ^{o}C for 40 min. Precipitation into 1 mL acetic acid/1mL HCl(aq) gave the crude product which was extracted with DCM, washed with water, dried with NaSO4, filtered and dried under vacuum. Purification by column chromatography with 10% MeOH in DCM isolated the desired product as a red solid (95% yield).

^{1}H NMR (spectrum in Figure 3.8) (400 MHz, $CDCl_3$, δ ppm: 8.7 (m, 8H), 5.20 (m, 1H), 2.26 (m, 2H), 1.90 (m, 2H), 1.32 (m, 16H), 0.86 (m, 6H).

Synthesis of (4)

Adapted from previously reported literature procedure.[63] Perylene mono-imide (3) (3.87 mmol), 6-aminohexanol (4.65 mmol), and imidazole (38.7 mmol), were added and heated to 150 ^{o}C for 6 hours under argon. After cooling to room temperature, 50 mL of 2N HCl was added to the mixture. The mixture was extracted with 3x15 mL of DCM. The DCM solution was dried with MgSO4 and the solvent was evaporated off. The crude product was purified with silica gel chromatography using 5% methanol in chloroform to isolate the red solid (2.99 mmol, 77% yield).

^{1}H NMR (spectrum in Figure 3.9) (400 MHz, CDCl3, δ ppm: 8.7 (m, 8H), 5.22 (m, 1H), 4.25 (t, 2H), 3.69 (t, 2H), 2.27 (m, 2H), 1.86 (m, 4H), 1.65 (m, 2H), 1.52 (m, 6H), 1.30 (b, 14H), 0.86 (t, 6H)

Synthesis of (5)

Adapted from previously reported literature procedure.[64] DCM (575 mL) was added to a round bottom flask containing EDC-HCl (548 mg, 2.86 mmol), DMAP (63.5 mg, 0.52 mmol), (**1**) (713 mg, 2.86 mmol), and (**4)** (1.75 g, 2.60 mmol). The solution was stirred at room temperature for 20 hrs. The reaction was concentrated by rotary evaporation and purified with silica gel chromatography (33% Ethyl acetate/ 66% DCM). A red solid was isolated (1.80 g, 77% yield).

^{1}H NMR (spectrum in Figure 3.10) (400 MHz, CDCl3, δ ppm: 8.64 (m, 8H), 5.22 (m, 1H), 4.25 (t, 2H), 3.69 (t, 2H), 2.27 (m, 2H), 1.86 (m, 4H), 1.65 (m, 2H), 1.52 (m, 6H), 1.30 (b, 14H), 0.86 (t, 6H)

Synthesis of C_5-PDI-CN_2.

A previously reported literature procedure was followed.[55]

Synthesis of $Co_6Te_8(PEt_3)_6$.

A previously reported literature procedure was followed.[65]

Synthesis of [C_5-PDI-CN_2][$Co_6Te_8(PEt_3)_6$]

This synthesis was carried out in a nitrogen filled glovebox at room temperature. C_5-PDI-CN_2 (10 mgs, 17.2 μmol) was dissolved in 8 mLs of toluene, stirring at room temperature over an hour in a 20 mL scintillation vial. $Co_6Te_8(PEt_3)_6$ (15.7 mgs, 8.5 mmol) was dissolved in 2 mL of toluene. The solution of PDI was layered on top of the $Co_6Te_8(PEt_3)_6$ solution. Small black crystals formed at the bottom of the vial overnight.

Self-Assembly of PEG:PDI BCP

A 1mg/mL solution of a BCP with varying ratios of PEG:PDI and different lengths of PEG moieties was dissolved in either THF or DCM with equal weights of $Co_6Te_8(PEt_3)_6$. H_2O or MeOH was added to the solution to make assemblies in THF/H_2O or DCM/MeOH. The assemblies were carried out in scintillation vials and stirred at room temperature overnight with open caps to allow the lower-boiling solvent (THF or DCM) to evaporate overnight.

3.9 Select NMR Spectra

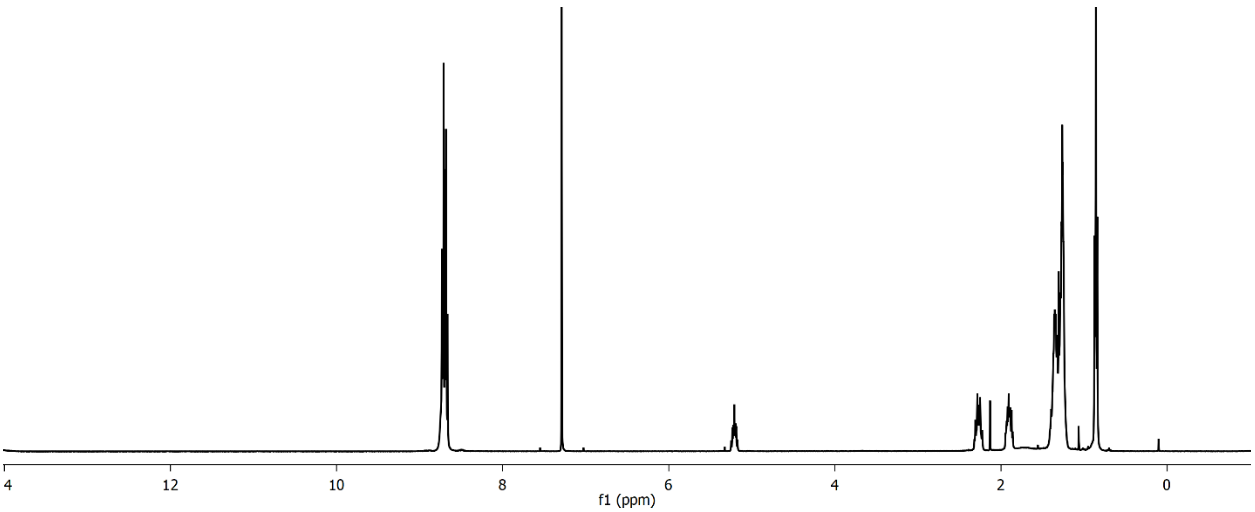

Figure 3.8. ^{1}HNMR of compound (3) taken in $CDCl_3$

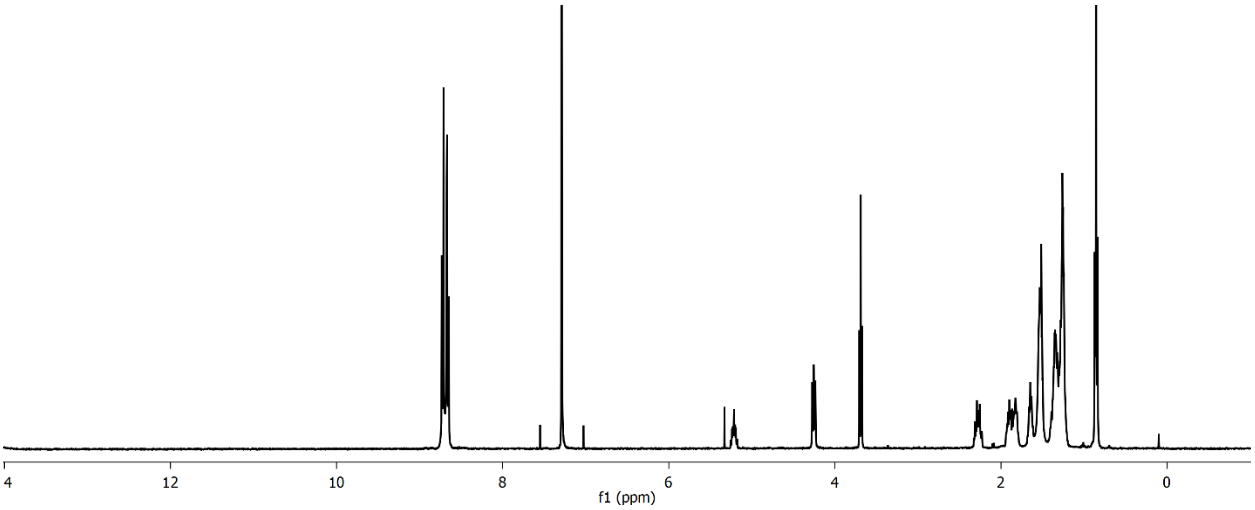

Figure 3.9. ^{1}HNMR of compound (4) taken in $CDCl_3$

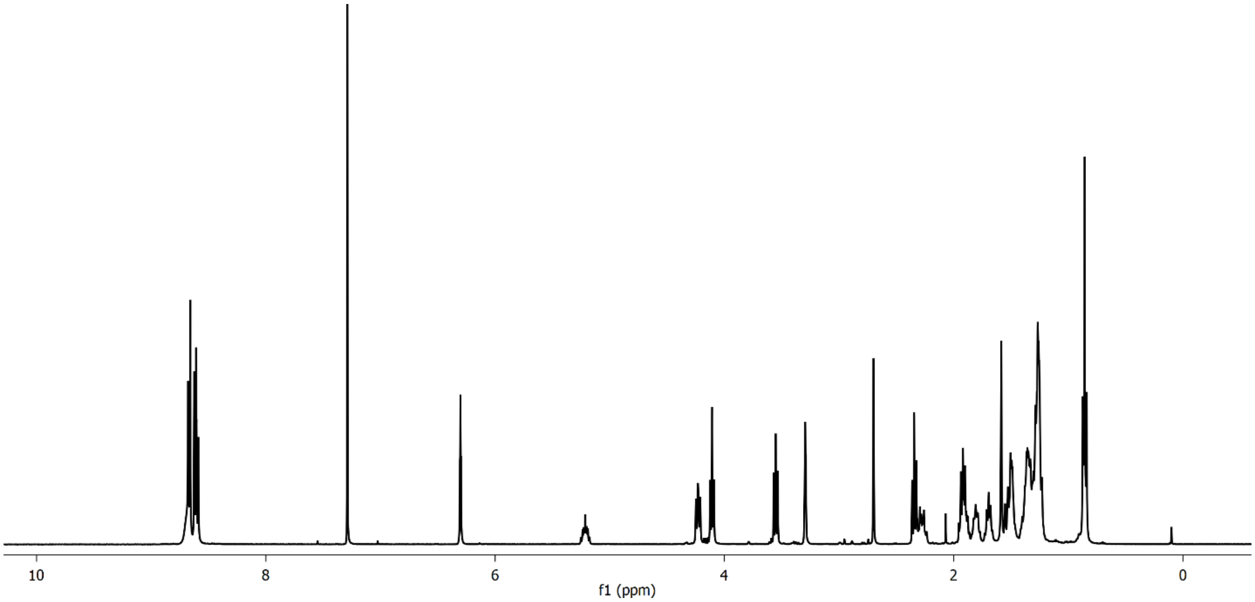

Figure 3.10. ^{1}H NMR of compound (5) taken in $CDCl_3$

3.10 Single crystal X-ray diffraction

Data for all compounds was collected on an Agilent SuperNova diffractometer using mirror-monochromated Cu Kα radiation. Data collection, integration, scaling (ABSPACK) and absorption correction (face-indexed Gaussian integration[66] or numeric analytical methods[67]) were performed in CrysAlisPro.[68] Structure solution was performed using ShelXT.[69] Subsequent refinement was performed by full-matrix least-squares on F^2 in ShelXL.[70] Olex2[71] was used for viewing and to prepare CIF files. Disordered toluene was modeled as rigid fragments with coordinates taken from the Idealized Molecular Geometry Library.[72]

Crystals were grown at room temperature by diffusion of toluene solution with PDI into concentrated solution of $Co_6Te_8(PEt_3)_6$ in toluene. The PDI molecule was disordered over two positions in a 72:28 ratio by a twofold rotation around the long axis of the molecule. The disorder was modeled with standard SAME and FLAT restraints on the coordinates of the disordered nitrile and the adjacent two C atoms in the aromatic system. The ADPs of the minor component were stabilized with a RIGU restraint. Two molecules of toluene were located on inversion centers, one of which was additionally disordered over two independent positions. Both toluenes were modeled as rigid fragments with idealized geometry; the "ordered" toluene was refined with anisotropic ADPs restrained by RIGU while the disordered toluene was refined with isotropic ADPs. Overlapping ADPs of disordered atoms were stabilized with a short-range SIMU instruction.

Table 3.1 Selected crystallographic data of $[C_5\text{-PDI-CN}_2][Co_6Te_8(PEt_3)_6]$

Compound	**$[C_5\text{-PDI-CN}_2][Co_6Te_8(PEt_3)_6]$**
Formula	$C_{86}H_{134}Co_6N_4O_4P_6Te_8$
MW	2848.16
Space group	P-1
a **(Å)**	12.1017(3)
b **(Å)**	13.0846(3)
c **(Å)**	16.6487(4)
α **(°)**	110.164(2)
β **(°)**	93.783(2)
γ **(°)**	99.810(2)
V ($Å^3$)	2416.23(11)
Z	1
ρ_{calc} (g cm^{-3})	1.957
T (K)	100
λ (Å)	1.54184
$2\theta_{min}$, $2\theta_{max}$	10, 143
Nref	29036
R(int), R(σ)	.0572, .0526
μ(mm^{-1})	27.87
Size (mm)	.27 x .10 x .04
T_{max} / T_{min}	12.6
Data	9371
Restraints	124
Parameters	577
R_1(obs)	0.0419
wR_2(all)	0.1111
S	1.031
Peak, hole (e^- $Å^{-3}$)	1.54, -1.51

3.11 References

1. Shenhar R, Rotello VM. Nanoparticles: Scaffolds and building blocks. *Acc Chem Res*. **2003**;36(7):549-561.

2. Shevchenko E V., Talapin D V., Kotov NA, O'Brien S, Murray CB. Structural diversity in binary nanoparticle superlattices. *Nature*. **2006**;439(7072):55-59.

3. Kao J, Thorkelsson K, Bai P, Rancatore BJ, Xu T. Toward functional nanocomposites: Taking the best of nanoparticles, polymers, and small molecules. *Chem Soc Rev*. **2013**;42(7):2654-2678.

4. Renna LA, Boyle CJ, Gehan TS, Venkataraman D, Weiss PS. Mesoscale Science: Lessons from and Opportunities for Nanoscience. *ACS Nano*. **2014**;8(11):11025-11026.

5. Liu AJ, Grest GS, Marchetti MC, et al. Opportunities in theoretical and computational polymeric materials and soft matter. *Soft Matter*. **2015**;11(12):2326-2332.

6. Weiss PS. Mesoscale Science: Lessons from and Opportunities for Nanoscience. *ACS Nano*. **2014**;8(11):11025-11026.

7. Talapin D V. Lego materials. *ACS Nano*. **2008**;2(6):1097-1100.

8. Nie Z, Petukhova A, Kumacheva E. Properties and emerging applications of self-assembled structures made from inorganic nanoparticles. *Nat Nanotechnol*. **2010**;5(1):15-25.

9. Nie Z, Fava D, Kumacheva E, Zou S, Walker GC, Rubinstein M. Self-assembly of metal-polymer analogues of amphiphilic triblock copolymers. *Nat Mater*. **2007**;6(8):609-614.

10. Akcora P, Liu H, Kumar SK, et al. Anisotropic self-assembly of spherical polymer-grafted nanoparticles. *Nat Mater*. **2009**;8(4):354-359.

11. Zhang Z, Horsch MA, Lamm MH, Glotzer SC. Tethered Nano Building Blocks: Toward a Conceptual Framework for Nanoparticle Self-Assembly. *Nano Lett*. **2003**;3(10):1341-1346.

12. Huang M, Hsu C-H, Wang J, et al. Selective assemblies of giant tetrahedra via precisely controlled positional interactions. *Science (80-)*. 2015;348(6233):424-428.

13. Zeng X, Ungar G, Liu Y, Percec V. Supramolecular dendritic liquid quasicrystals. **2011**;110405:1-4.

14. Gröschel AH, Schacher FH, Schmalz H, et al. Precise hierarchical self-assembly of multicompartment micelles. *Nat Commun*. **2012**;3.

15. Kietzke T, Neher D, Landfester K, Montenegro R, Guntner R, Scherf U. Novel approaches to polymer blends based on polymer nanoparticles. *Nat Mater*. **2003**;2(6):408-412.

16. Tschierske C. Liquid crystal engineering - New complex mesophase structures and their relations to polymer morphologies, nanoscale patterning and crystal engineering. *Chem Soc Rev*. **2007**;36(12):1930-1970.

17. Mann S. Self-assembly and transformation of hybrid nano-objects and nanostructures under equilibrium and non-equilibrium conditions. *Nat Mater*. **2009**;8(10):781-792.

18. Lee JY, Shou Z, Balazs AC. Modeling the self-assembly of copolymer-nanoparticle mixtures confined between solid surfaces. *Phys Rev Lett*. **2003**;91(13):1-4.

19. Jaeger HM, Lopes WA. Hierarchical self-assembly of metal nanostructures on diblock copolymer scaffolds. *Nature*. **2001**;414(6865):735-738.

20. Kao J, Xu T. Nanoparticle assemblies in supramolecular nanocomposite thin films: Concentration dependence. *J Am Chem Soc*. **2015**;137(19):6356-6365.

21. Sun Y Sen, Jeng US, Liang KS, Yeh SW, Wei KH. Transitions of domain ordering and domain size in a spherical-forming polystyrene-block-poly(ethylene oxide) copolymer and its composites with colloidal cadmium sulfide quantum dots. *Polymer (Guildf)*. **2006**;47(4):1101-1107.

22. Lin Y, Boker A, He J, et al. Self-directed self-assembly of nanoparticle / copolymer mixtures. *Nature*. **2005**;434:55-59.

23. Bockstaller MR, Mickiewicz RA, Thomas EL. Block copolymer nanocomposites: Perspectives for tailored functional materials. *Adv Mater*. **2005**;17(11):1331-1349.

24. Urbas A, Sharp R, Fink Y, Thomas EL, Xenidou M, Fetters LJ. Tunable block copolymer/homopolymer photonic crystals. *Adv Mater*. **2000**;12(11):812-814.

25. Cho KY, Cho A, Kim HJ, et al. Control of hard block segments of methacrylate-based triblock copolymers for enhanced electromechanical performance. *Polym Chem*. **2016**;7(48):7391-7399.

26. Zhang Q, Cirpan A, Russell TP, Emrick T. Donor-acceptor poly(thiophene-block-perylene diimide) copolymers: Synthesis and solar cell fabrication. *Macromolecules*. **2009**;42(4):1079-1082.

27. Wu Q, Zhao D, Schneider AM, Chen W, Yu L. Covalently Bound Clusters of Alpha-Substituted PDI-Rival Electron Acceptors to Fullerene for Organic Solar Cells. *J Am Chem Soc*. **2016**;138(23):7248-7251.

28. Zhong Y, Kumar B, Oh S, et al. Helical ribbons for molecular electronics. *J Am Chem Soc*. **2014**;136(22):8122-8130.

29. Sharenko A, Proctor CM, Van Der Poll TS, Henson ZB, Nguyen TQ, Bazan GC. A high-performing solution-processed small molecule: Perylene diimide bulk heterojunction solar cell. *Adv Mater*. **2013**;25(32):4403-4406.

30. Milton M, Cheng Q, Yang Y, Nuckolls C, Hernández Sánchez R, Sisto TJ. Molecular Materials for Nonaqueous Flow Batteries with a High Coulombic Efficiency and Stable Cycling. *Nano Lett*. **2017**;17(12):7859-7863.

31. Turkiewicz A, Paley DW, Besara T, et al. Assembling hierarchical cluster solids with atomic precision. *J Am Chem Soc*. **2014**;136(45):15873-15876.

32. Roy X, Lee C-H, Crowther a. C, et al. Nanoscale Atoms in Solid-State Chemistry Supplementary Data. *Science (80-)*. **2013**;341(6142):157-160.

33. Jones BA, Facchetti A, Wasielewski MR, Marks TJ. Tuning orbital energetics in arylene diimide semiconductors. Materials design for ambient stability of n-type charge transport. *J Am Chem Soc*. **2007**;129(49):15259-15278.

34. Tran H, Gopinadhan M, Majewski PW, et al. Monoliths of semiconducting block copolymers by magnetic alignment. *ACS Nano*. **2013**;7(6):5514-5521.

35. Xia J, Busby E, Sanders SN, et al. Influence of Nanostructure on the Exciton Dynamics of Multichromophore Donor-Acceptor Block Copolymers. *ACS Nano*. **2017**;11(5):4593-4598.

36. Champsaur AM, Velian A, Paley DW, et al. Building Diatomic and Triatomic Superatom Molecules. *Nano Lett*. **2016**;16(8):5273-5277.

37. Baudron SA, Batail P, Coulon C, et al. (EDT-TTF-CONH2)6[Re6Se8(CN) 6], a metallic Kagome-type organic-inorganic hybrid compound: Electronic instability, molecular motion, and charge localization. *J Am Chem Soc*. **2005**;127(33):11785-11797.

38. Cecconi F, Ghilardi CA, Midollini S, Orlandini A. Dimerization of the stellated octahedral unit Co6S8P6: synthesis and x-ray crystal structure of [Co12(μ3-S)14(μ4-S)2(PEt3)10][TCNQ]2, where TCNQ=tetracyanoquinodimethane. *Inorganica Chim Acta*. **1993**;214(1-2):13-15.

39. Renault A, Pouget J-P, Parkin SSP, Torrance JB, Ouahab L, Batail P. Evidence for a Spin-Peierls-Like transition in the 1-D Organic Cation Radical Salt:B-(TMTSF) 2 Re 6 Se 5 Cl 9 . *Mol Cryst Liq Cryst Inc Nonlinear Opt*. **2007**;161(1):329-334.

40. Pénicaud A, Batail P, Coulon C, Canadell E, Perrin C. Novel Redox Properties of the Paramagnetic Hexanuclear Niobium Cluster Halide Nb6Cl183− and the Preparation, Structures, and Conducting and Magnetic Properties of Its One-Dimensional Mixed-Valence Tetramethyltetra(selena and thia)fulvalenium Salts: [TMTSF. *Chem Mater*. **1990**;2(2):123-132.

41. Allen DP, Bottomley F, Day RW, et al. Organometallic Oxides: Oxidation of the Cubane [(η-C 5 R 5)Cr(μ 3 -O)] 4 and the Structures and Magnetic Properties of the Salts {[(η-C 5 R 5)Cr(μ 3 -O)] 4 }{tcnq} and {[(η-C 5 R 5)Cr(μ 3 -O)] 4 }{BF 4 } . *Organometallics*. **2007**;20(9):1840-1848.

42. Feliz M, Llusar R, Uriel S, Vicent C, Coronado E, Gómez-García CJ. Cubane-type Mo3CoS4 molecular clusters with three different metal electron populations: Structure, reactivity and their use in the synthesis of hybrid charge-transfer salts. *Chem - A Eur J*. **2004**;10(17):4308-4314.

43. Baird P, Bandy JA, Green MLH, et al. Charge-transfer salts formed from redox-active cubane cluster cations [M 4 (η-C 5 H 4 R) 4 (μ 3 -E) 4] n+ (M = Cr, Fe or Mo; E = S or Se) and various anions . *J Chem Soc, Dalt Trans*. **2004**;12(9):2377-2393.

44. Karadas F, Avendano C, Hilfiger MG, Prosvirin A V., Dunbar KR. Magnetic quantum tunneling: Insights from simple molecule-based magnets. *Dalt Trans*. **2010**;39(20):4698-4977.

45. Zhong Y, Trinh MT, Chen R, et al. Efficient organic solar cells with helical perylene diimide electron acceptors. *J Am Chem Soc*. **2014**;136(43):15215-15221.

46. Briseno AL, Mannsfeld SCB, Reese C, et al. Perylenediimide nanowires and their use in fabricating field-effect transistors and complementary inverters. *Nano Lett*. **2007**;7(9):2847-2853.

47. Wilson TM, Tauber MJ, Wasielewski MR. Toward an n-type molecular wire: Electron hopping within linearly linked perylenediimide oligomers. *J Am Chem Soc*. **2009**;131(25):8952-8957.

48. Zhan X, Facchetti A, Barlow S, et al. Rylene and related diimides for organic electronics. *Adv*

Mater. **2011**;23(2):268-284.

49. Ball M, Zhong Y, Fowler B, et al. Macrocyclization in the Design of Organic n-Type Electronic Materials. *J Am Chem Soc*. **2016**;138(39):12861-12867.

50. Ball M, Zhong Y, Wu Y, et al. Contorted polycyclic aromatics. *Acc Chem Res*. **2015**;48(2):267-276.

51. Zhong Y, Trinh MT, Chen R, et al. Molecular helices as electron acceptors in high-performance bulk heterojunction solar cells. *Nat Commun*. **2015**;6:1-8.

52. Margulies EA, Miller CE, Wu Y, et al. Enabling singlet fission by controlling intramolecular charge transfer in π-stacked covalent terrylenediimide dimers. *Nat Chem*. **2016**;8(12):1120-1125.

53. Maroncelli M, Macinnis J, Fleming GR. Electron-Transfer Reactions. *Science (80-)*. 1988;243(**1978**):1674-1681.

54. Hwang JK, Warshel A. Microscopic Examination of Free-Energy Relationships for Electron Transfer in Polar Solvents. *J Am Chem Soc*. **1987**;109(3):715-720.

55. Jones BA, Ahrens MJ, Yoon M, Facchetti A, Marks TJ, Wasielewski MR. High-Mobility Air-Stable n-Type Semiconductors with Processing Versatility: Dicyanoperylene- 3,4:9,10-bis(dicarboximides)**. *Angew Chemie - Int Ed*. **2004**;43:6363-6366.

56. Champsaur AM, Hochuli TJ, Paley DW, Nuckolls C, Steigerwald ML. Superatom Fusion and the Nature of Quantum Confinement. *Nano Lett*. **2018**;18:4564-4569.

57. Bang BJ, Jeong U, Ryu DY, Russell TP, Hawker CJ. Block Copolymer Nanolithography : Translation of Molecular Level Control to Nanoscale Patterns. *Adv Mater*. **2009**;21:4769-4792.

58. Tritschler U, Pearce S, Gwyther J, Whittell GR, Manners I. 50th Anniversary Perspective : Functional Nanoparticles from the Solution Self-Assembly of Block Copolymers. *Macromolecules*. **2017**;50:3439-3463.

59. Mai Y, Eisenberg A. Self-assembly of block copolymers. *Chem Soc Rev*. **2012**;41(2011):5969-5985.

60. Botiz I, Darling SB. Optoelectronics using block copolymers Block copolymers , either as semiconductors themselves or as. *Mater Today*. **2010**;13(5):42-51.

61. Ruzette A-V, Leibler L. Block copolymers in tomorrow's plastics. *Nat Mater*. **2005**;4(1):19-31.

62. Poly N, Liu J, Burts AO, et al. " Brush-First " Method for the Parallel Synthesis of Photocleavable, Nitroxide-Labeled Poly(ethylene glycol) Star Polymers. *J Am Chem Soc*. **2012**;134:16337-16344.

63. Zhang X, Chen Z, Würthner F. Morphology control of fluorescent nanoaggregates by co-self-assembly of wedge- and dumbbell-shaped amphophilic perylene bisimides. *J Am Chem Soc*. **2007**;129(16):4886-4887.

64. Liu J, Burts AO, Li Y, et al. " Brush-First " Method for the Parallel Synthesis of Photocleavable, Nitroxide-Labeled Poly(ethylene glycol) Star Polymers. *J Am Chem Soc*.

2012;134:16337-16344.

65. Steigerwald ML, Siegrist T, Stuczynski SM. (Et3P)6Co6Te8 and a connection between Chevrel clusters and the NiAs structures. *Inorg Chem*. **1991**;30:2256-2257.

66. Blanc E, Schwarzenbach D, Flack HD. Evaluation of transmission factors and their first derivatives with respect to crystal shape parameters. *J Appl Crystallogr*. **1991**;24(pt 6):1035-1041.

67. Clark RC, Reid JS. The analytical calculation of absorption in multifaceted crystals. *Acta Crystallogr Sect A*. **1995**;A51:887-897.

68. Agilent Technologies UK Ltd. CrysAlisPRO, Version 1.171.37.35. **2014**.

69. Sheldrick GM. No Title. *Acta Crystallogr Sect A2*. **2015**;A71:3-8.

70. Sheldrick GM. Crystal structure refinement with SHELXL. *Acta Crystallogr Sect C*. **2015**;C71:3-8.

71. Dolomanov O V, Bourhis LJ, Gildea RJ, Howard JAK, Puschmann H. OLEX2: a complete structure solution, refinement and analysis program. *J Appl Crystallogr*. **2009**;(42):339-341.

72. Guzei IA. An idealized molecular geometry library for refinement of poorly behaved molecular fragments with constraints. *J Appl Crystallogr*. **2014**;47:806-809.

Chapter 4

Designing a superatom-containing polymer

4.0 Preface

This chapter presents some of the initial motivations and strategies in designing a cluster-containing polymer. I will discuss the synthesis of a superatom-containing homopolymer and preliminary results in using this homopolymer to fabricate thin films. Anouck Champsaur provided guidance on the synthesis of the carbonylated cobalt selenide cluster[1] and its reactivity for substitution. Dan Paley performed single crystal refinement.

4.1 Introduction

The initial attempts at using the chemical synthetic tunability of BCPs to template long range ordering of superatoms into targeted morphologies at the mesoscale inspired the design of a BCP system with covalent tethering of a superatom onto the polymer backbone. Rather than relying on charge transfer interactions to drive the assembly of superatoms, covalent functionalization provides greater synthetic control to fabricate materials having extended ordering. The ability to covalently functionalize a superatom onto a polymer scaffold was enabled by the synthesis of the reactive, photolabile, site-differentiated $Co_6SE_8CO(PEt_3)_5$ superatom.[1] The photolabile CO group is a useful synthetic handle that can be easily exchanged with other reactive ligands including phosphines. As discussed in Chapter 1, covalent union of the superatom into dimers, trimers, and small oligomers is an exciting route to create extended assemblies of superatoms with enhanced inter-superatom coupling.[1,2] The synthetic utility of the mono-carbonylated cobalt selenide superatom played an essential role in designing a cluster-containing polymer system.

Another motivation to synthesize superatom-containing polymers is the limited library of metal-containing polymers reported to date. Organometallic polymers have shown potential in advancing technologies for sensing, catalysis, and media storage.[3,4] Yet synthetic challenges such as polymer solubility that also make it difficult to properly characterize the materials using NMR and gel permeation chromatography has widely limited the compositional scope of metal-containing polymers.[3] The first report of transition metal-containing polymer contained a ferrocene moiety, and the library of metal-containing polymers has continued to be dominated by metallocene-containing polymers specifically.[5] The ability to tether a multinuclear metal cluster to an organic polymer scaffold presents an exciting opportunity to contribute to the growth in this research area.

4.2 Synthetic routes for cluster-containing homopolymer

We developed two initial strategies to synthesize a homopolymer with Co_6SE_8 pendant superatoms shown in Figure 4.1.

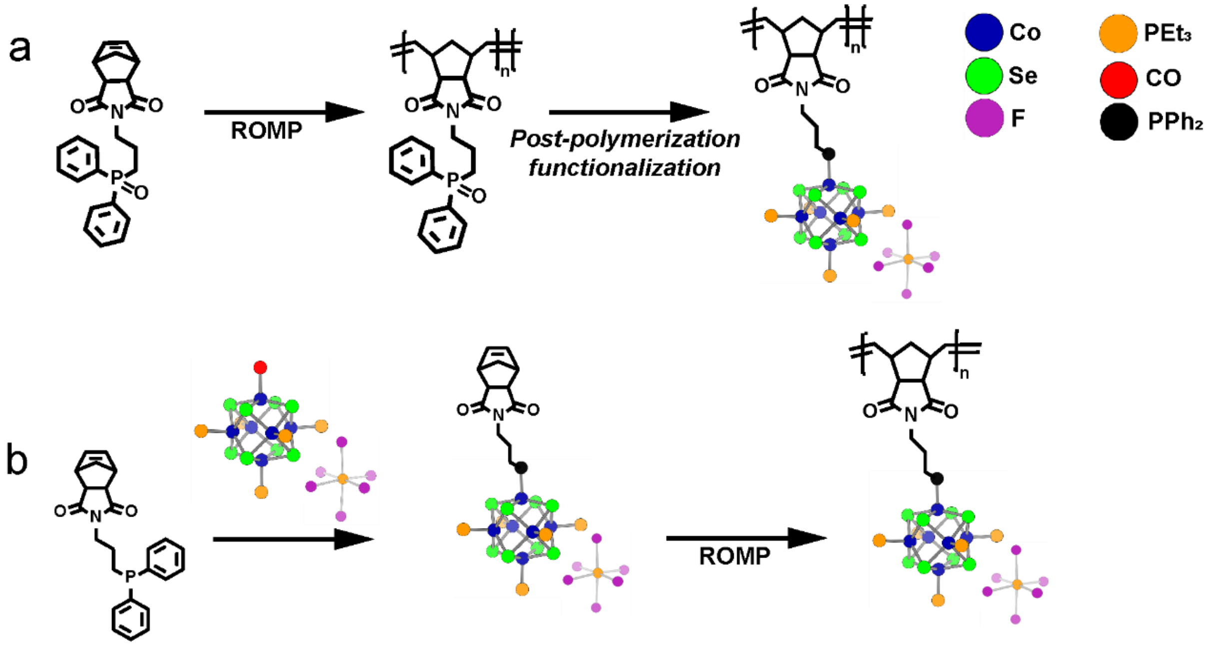

Figure 4.1. Two approaches for the synthesis of a superatom-containing polymer. In (a) a phosphine oxide monomer is the ROMP polymerizable precursor and in (b) a superatom-containing monomer (SCM) is first synthesized prior to ROMP polymerization.

In the first approach shown in Figure 4.1a, we first synthesize a ROMP polymerizable monomer with a pendant diphenyl phosphine oxide group. After polymerization, the diphenyl phosphine oxide must be reduced to the free phosphine, which is a suitable L-type ligand for the photolabile $Co_6Se_8CO(PEt_3)_5$ cluster. Disassociation of the CO group occurs upon exposure of the cluster to UV light at room temperature, and the site-differentiated superatom can then bind to the pendant free phosphines. The post-polymerization functionalization approach is attractive because it is possible to fully characterize the polymer's molecular weight and dispersity by gel permeation chromatography (GPC) and NMR, prior to the covalent attachment of the cluster. Once the superatom-containing polymer is formed, characterization of the polymer properties by traditional polymer characterization techniques can be quite challenging due to solubility challenges and the cluster-polymer’s composition as compared to the GPC’s polystyrene standards that are used for calibration of the instrument.

In the second approach shown in Figure 4.1b, a similar phosphine monomer is first synthesized, but the pendant phosphine is not oxidized. The $Co_6Se_8(PEt_3)_5$ cluster is attached to the monomer after which it is polymerized under ROMP conditions. In both synthetic approaches, the superatom is oxidized to 1+ with a PF_6 counterion. The oxidized cluster is air stable which enables easy handling and purification of the monomers and polymers on the benchtop. A remarkable advantage of this is the ability to use traditional silica-gel chromatography to purify the superatom-containing monomer (SCM) prior to polymerization. Purification of the cationic monomer removes any unfunctionalized monomers and cluster and ensures that every unit in the polymer is bound to a pendant cobalt selenide cluster.

The post-polymerization approach first synthesizes a new phosphorus containing polymer. There has been considerable interest in the synthesis of dendrimers and polymers having donor ligands like phosphorus in their scaffold in order to tether transition metals onto support materials.[6–9] Incorporation of phosphorus units into extended matrices has potential to design efficient functional materials for metal catalysis. The challenge encountered in the post-polymerization approach was achieving complete reduction of the phosphine oxide after polymerization -a necessary step for association of the pendant diphenyl phosphine with the cobalt selenide superatom.

4.3 Synthesis of ROMP polymerizable superatom-containing monomer

Figure 4.2 illustrates our synthetic strategy to prepare a polymerizable superatom-containing monomer (SCM). The monomer was synthesized by treating a norbornene dicarboxylic acid anhydride derivative with 3-(diphenylphosphino)-1-propylamine. This formed a ROMP polymerizable norbornene monomer with a pendant diphenyl phosphine which was then coupled to the molecular cluster $Co_6Se_8(PEt_3)_5$ through coordination of the free phosphine to the inorganic core. The coupling occurred under UV photolytic conditions with the cationic $[Co_6Se_8(CO)(PEt_3)_5][PF_6]$ during which the photolabile CO ligand on the cluster was substituted with diphenyl phosphine. The substitution reaction is monitored by infrared (IR) spectroscopy by monitoring the disappearance of the CO stretching mode at 1968 cm^{-1}. IR traces of both the crude

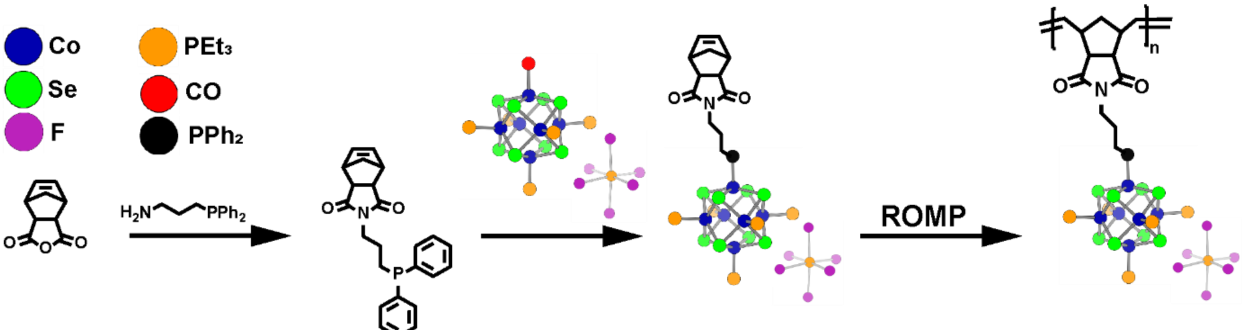

Figure 4.2. Synthesis of SCM and its polymerization to form superatom-containing homopolymer (SHP).

The cationic cluster is air-stable enabling purification of the monomer by traditional silica gel chromatography. With long enough reaction time (24-48 hr) the substitution of the CO cluster is quantitative. To expediate the reaction time, excess diphenyl phosphine monomer was added, and silica gel chromatography removed excess unfunctionalized diphenyl phosphine norbornene monomer and cluster. The substituted monomer was crystallized by diffusing hexanes into a dichloromethane (DCM) solution of the compound.

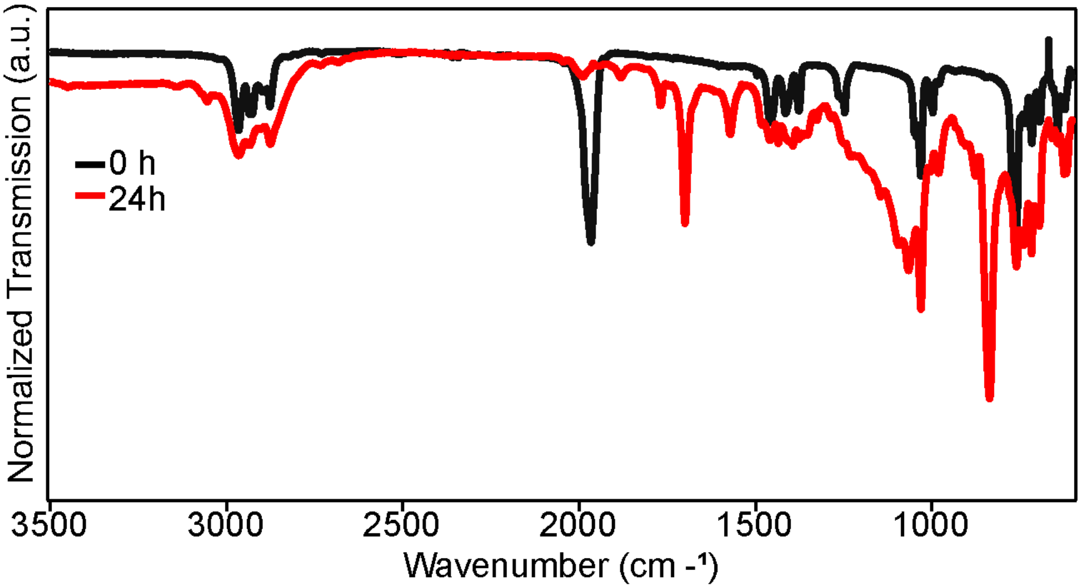

Figure 4.3. IR spectra of crude mixture of $[Co_6Se_8CO(PEt_3)_5][PF_6]$ and diphenyl phosphine monomer before UV-irradiation (0h, black) monitoring the CO stretch at 1968 cm^{-1} which disappears after 24h of irradiation (red).

Figure 4.4 presents the crystal structure of SCM as determined by single crystal x-ray diffraction (SCXRD). The core of the cluster is an octahedron of Co atoms, concentric with a cube of Se atoms. Five Co atoms are capped with PEt_3 and the sixth Co is bonded to the diphenyl phosphine connecting the norbornene unit. SCM crystallizes with a single PF_6^- anion.

The molecular structure underscores the size difference between the norbornene and the pendent cluster units, highlighting the limited space available to bind to the ROMP catalyst during polymerization. By comparison, typical metal-containing monomers (*e.g., monomers with a* *pendent metallocene group*) are much less sterically hindered.[5,10] Full crystallographic details are included in the synthetic methods at the end of Chapter 4.

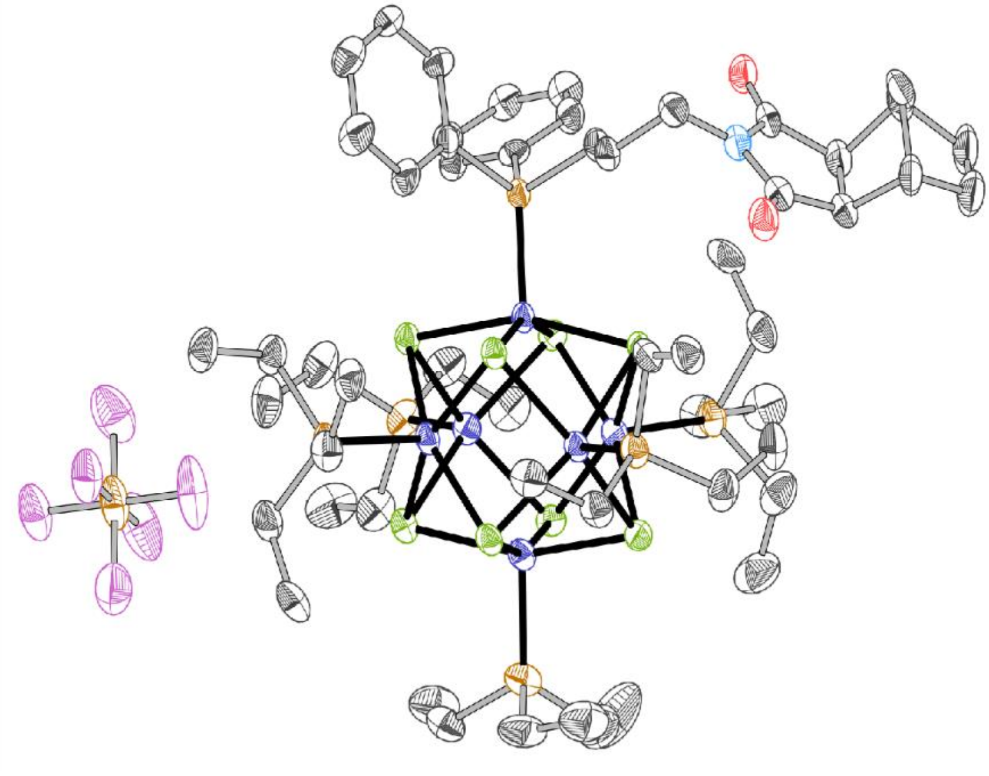

Figure 4.4. Molecular structure of SCM, as determined by SCXRD. Color code: C, black; N, light blue; O, red; Se, green; Co, blue; P, yellow; F, purple.

A cluster-containing homopolymer (SHP) was synthesized by ROMP in dichloromethane, using Grubbs catalyst 3rd generation. Stoichiometric ratios of the monomer: catalyst was varied. With high feed ratios of the monomer (>50:1 monomer:GIII), the resulting cationic polymer was highly insoluble in almost all solvents (*i.e. dimmethylformamide, dichloromethane, chloroform, methanol*). Relatively short SHPs with n=25 chain lengths were synthesized and were soluble enough for characterization. Figure 4.5 shows the ^{1}H NMR spectra of SCM and SHP, respectively. The broad peaks below 0 ppm come from the PEt_3 on the cationic paramagnetic cluster. The key feature that identifies the ring opening metathesis polymerization is the disappearance of the vinylic protons on the norbornene rings which appear at 6.3 ppm in the monomer. The disappearance of the vinylic peak at 6.3 ppm and the appearance of two resonances at 5.5 and 5.7 ppm indicates the formation of the ring opened norbornene backbone polymer.

Gel permeation chromatography (GPC) characterization of metal-containing polymers is challenging due to solubility and interactions between metals and the column during analysis. Furthermore, molecular weight as determined by GPC is not an appropriate characterization method for such exotic polymers, as the polymer's molecular structure is strikingly different from that of the polystyrene standards used for GPC calibration. These challenges make it difficult to accurately determine the molecular weight of our cluster-containing polymer. In Chapter 5, I will

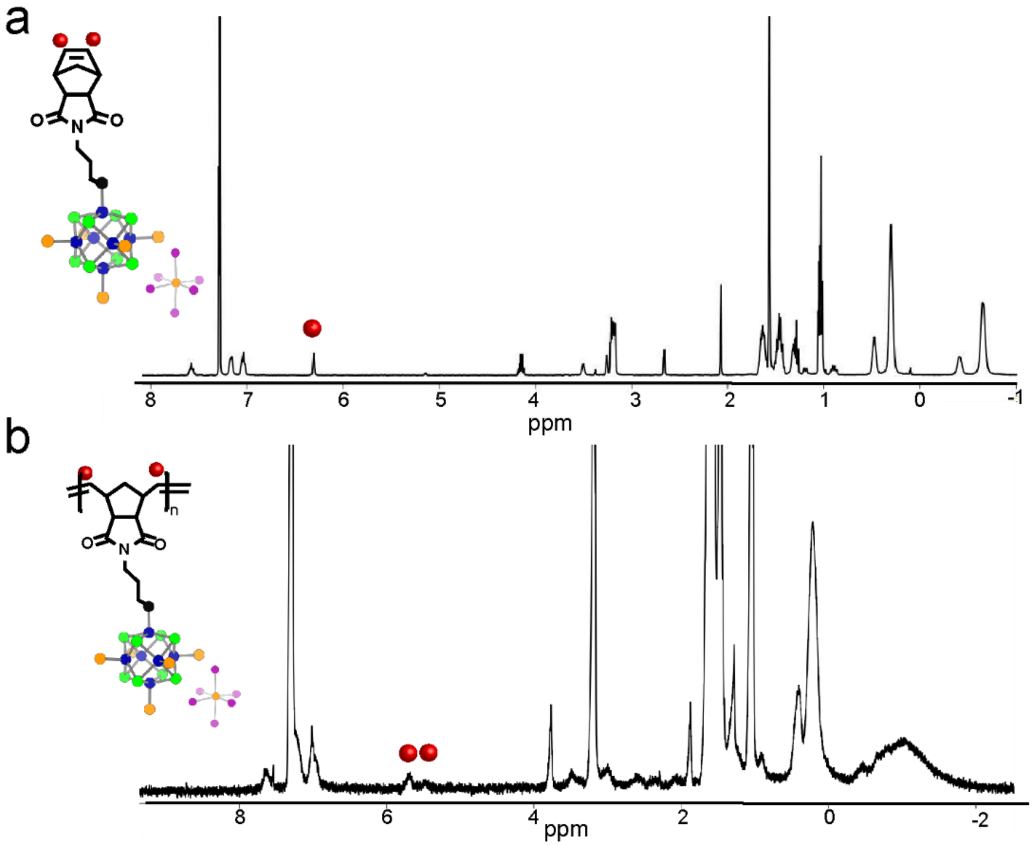

Figure 4.5. (a) ^{1}H NMR spectrum of SCM, taken in CDCl$_3$. Norbornene vinyl peaks are highlighted with red circles. (b) 1H NMR spectrum of SHP, taken in CDCl$_3$. Backbone polymer peaks are identified in red circles.

discuss an approach that we used to determine the molecular weight of the cluster-containing diblock polymer that incorporates both ^{1}H NMR and GPC analysis.

4.4 Fabrication of thin films using layer-by-layer (LBL) deposition

Thus far, the discussion has widely focused on using the cluster-containing block copolymer to achieve long-range ordering of the superatoms at the nano and microscale. Chapter 5 will continue discussion on the self-assembly behavior of the cluster-containing diblock polymer synthesis introduced here. Despite some of the solubility challenges in working with SHP, there are several potential applications of the SHP as a functional nanomaterial.

Over the past few decades, there has been increasing interest in controlling the characteristics of functional materials at the nanoscale such as size, shape, morphology, and composition to tune the emergent optical, electrical, mechanical, and other physiochemical properties. Self-assembled monolayers (SAMs) have emerged as an increasingly researched area to fabricate ordered monolayers. Achieving high-coverage SAMs remains a technological challenge that often requires pre-treatment of the substrate with strongly binding molecules (i.e. thiols) prior to deposition. New techniques such as chemical vapor deposition (CVD), polymer grafting, and pulsed-laser ablation have been developed, but these technologies are limited by substrate selection and deposited material. Several of the afore mentioned techniques also require expensive and tedious protocols.

By contrast, Layer-by-layer (LBL) assembly of thin films is a remarkably simple bottom-up technology that can employed on variety of substrates to fabricate thin films with various compositions.[11,12] . LBL assembly is a cyclical process that builds alternating layers of oppositely charged materials. The cyclical methodology adsorbs the first material onto the substrate during immersion or spin-coating, excess of the material is washed, and then adsorption of the oppositely charged material occurs. The amount of adsorbed material onto the substrate can be tuned by altering the adsorption time, dissolving solvent, and oppositely charged materials. Thin films fabricated using LBL have been used in various applications including catalysis, optics, energy, membranes, and biomedicine.[11] The simplicity and versatility of this thin film technique is attractive for fabrication of thin films with controlled thickness and morphology onto various substrates with direct applications in various fields.

Having synthesized the cationic SHP, we used the LBL technique to fabricate thin films. Using the immersion technique, we alternated dipping a glass substrate into solutions of positively charged cluster-containing polymer and of negatively charged poly(styrenesulfonate) (PSS). Figure 4.6 presents an image of three different glass substrates that have been immersed in alternating solutions of PSS and either the oxidized cobalt selenide cluster, SCM, or SHP. The substrates have all been immersed 10 times in PSS and 10 times in the solutions of the cobalt selenide, SCM, or SHP (20 minutes per immersion) and washed and dried in between soaks. It is visibly apparent that there is significant more buildup of layers on the substrate dipped in SHP than the glass slides with layers of the cationic cluster or SCM.

We monitored the absorption of the polymer onto the glass using solid-state UV-Vis absorption. Figure 4.6c and 4.6d show the electronic absorption of alternating layers of PSS and SHP. The first layer corresponds to 1 PSS and 0 layers of SHP or cluster. It is apparent that the SHP had significant more adsorption onto the glass substrate in comparison to that of the cluster. By taking the maximum absorption peak at 364 nm, we plot the adsorption of the glass slide after buildup of PSS:SHP and PSS:[$Co_6Se_8(PEt_3)$][PF_6]. The first layer corresponds to an initial layer of PSS on the substrate (1 PSS: 0 SHP) and subsequent even number of layers correspond to equal

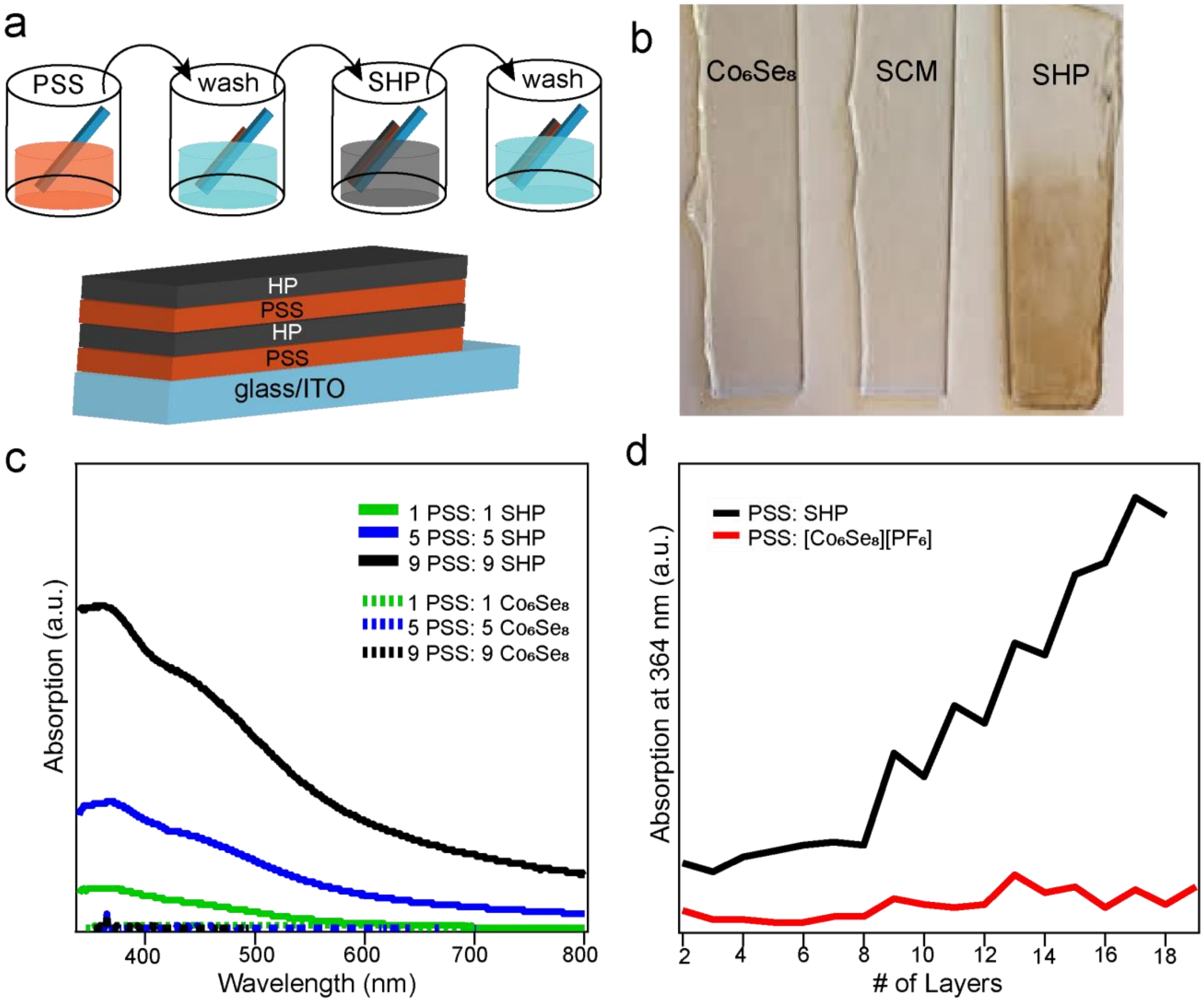

Figure 4.6. (a) Layer by layer assembly of PSS and SHP onto a glass substrate by alternating immersions of the glass substrate into solutions of PSS and SHP. The glass was washed in between soaks with polymers. (b) Photograph of glass substrates after 10 immersions of PSS and oxidized cobalt selenide cluster (left), SCM (middle) and SHP (right). (c) Solid-state electronic absorption spectra of 1,5, and 9 layers of PSS and oxidized cobalt selenide cluster and 1,5, and 9 layers of PSS and SHP. (d) Plot of electronic absorption at 364 nm of LBL assembly of PSS:SHP and PSS:Co_6Se_8 after each immersion in PSS and SHP or cluster. Layer 1 was immersion into PSS, and the layers with even numbers (*i.e. 2,4,6*) correspond to equal layers of PSS:SHP or PSS:Co_6Se_8.

layers of PSS and SHP or cluster (i.e. 2 layers = 1 PSS: 1 SHP). As shown in Figure 4.6b, a significant increase in absorption was observed after building up 4 layers of SHP:PSS each (8 layers total). Furthermore, absorption dropped after each deposition of PSS layer on top of the

SHP layer. Immersion of the glass slide in solution with oxidized cluster showed very limited layer buildup of the material as seen visibly by eye on the glass substrates and by tracking the electronic absorption of the substrate.

We performed the same LBL process of PSS:SHP onto a silicon wafer that we imaged using atomic force microscopy (AFM). Figure 4.7 presents AFM images of a silicon wafer substrate built up with 5 layers of PSS and 5 layers of SHP. The films are relatively smooth having a height differential of less than 2 nm and roughness average (R_a) of 0.150 nm across the image of Figure 4.7(b).

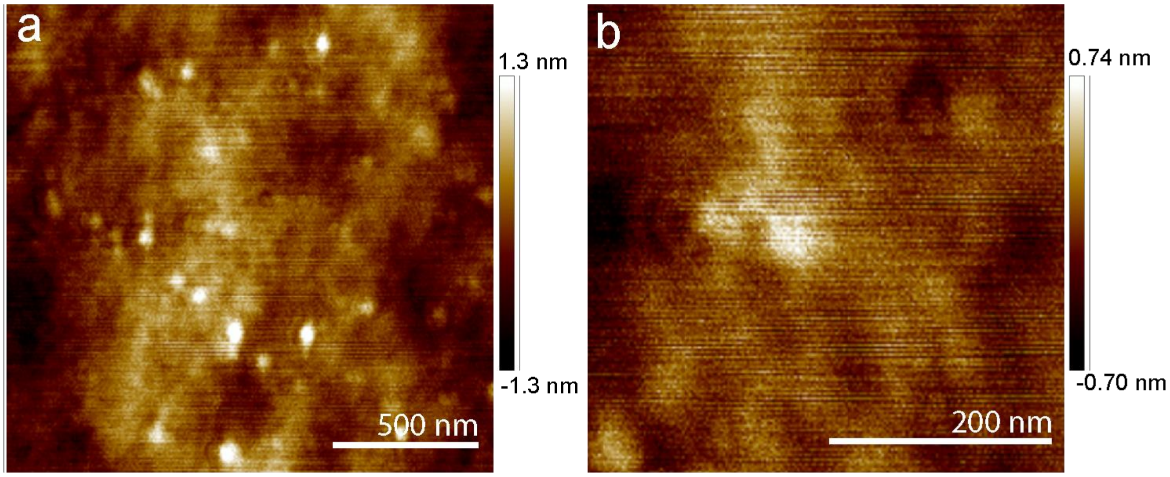

Figure 4.7. AFM images of LBL assembly on silicon wafer with 5 layers of PSS and 5 layers of SHP deposited.

The functionalization of the cluster onto a polymer backbone enabled its adsorption onto glass and is one example of the additional processing power that the polymer system provides. As another example, we used the same LBL procedure to deposit layers of PSS and **SHP** onto carbon foam. Carbon foam has attracted much research interest as a substrate for electrodes because of its high surface area, stability, flexibility, and high electronic and thermal conductivity.[13,14] We followed a similar LBL strategy to build up layers of the superatomic material onto nitrogen-doped

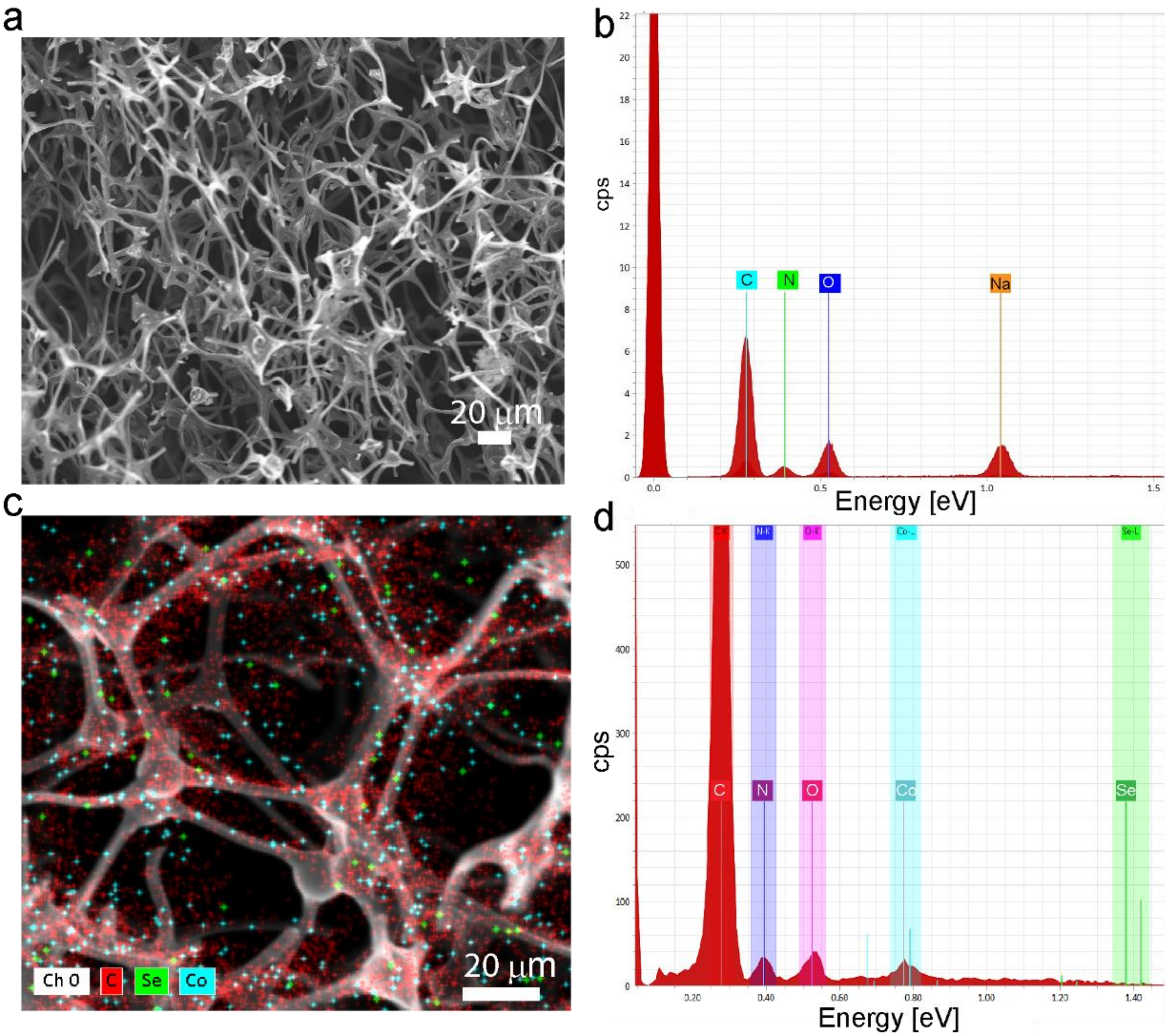

Figure 4.8. SEM images of LBL assembly of PSS:SHP onto carbon substrate. (a) shows the carbonized melamine foam and (b) has EDS mapping showing strong signals for carbon, oxygen, and sodium. (c) is SEM image with EDS mapping of carbon foam substrate with 6 layers of PSS and SHP. EDS mapping traces carbon (red), selenium (green), and cobalt (blue) along the porous substrate. (d) shows the corresponding EDS spectrum which picks up addition signals of cobalt and selenium after LBL assembly.

carbon foam.[13] The carbon foam shown in the scanning electron microscope (SEM) image in Figure 4.8a was prepared by carbonizing commercially available melamine foam (a Mr. Clean Magic Eraser® was purchased at the local grocery store) under a constant stream of nitrogen. SEM and EDS mapping in Figure 4.8(c,d) after depositing 6 PSS and 6 SHP layers confirms that the SHP adsorbed onto the carbon foam.

This promising result of LBL assembly of a cluster-containing homopolymer opens new opportunities to functionalize thin films of superatomic solids onto various substrate surfaces. The ability to control the deposition of layers of superatoms onto materials with high surface areas could open new opportunities for further chemical transformations, functionalization, and applications in surface mediated catalysis.

4.5 Conclusion

We have developed the first polymerizable superatom-containing monomer and homopolymer. The tethering of this molecular cluster onto a norbornene moiety charts new opportunities for the development of functional materials with high processability that can be easily modified. In the following chapter we will extend this synthesis of the homopolymer to the block copolymer system and demonstrate some of the remarkable assembly and electrochemical properties of this polymer system. Here we have described some preliminary results in using the superatom-containing homopolymer for the fabrication of thin films on various substrates.

4.6 Methods

Column Chromatography.

Chromatography was performed using a Teledyne Isco Combiflash Rf200 and Redisep Rf Silica columns.

NMR Spectroscopy.

^{1}H NMR and ^{31}P NMR spectra were recorded on a Bruker DRX400 spectrometer.

Electronic Absorption Spectroscopy.

Electronic absorption spectra were recorded using a 1.0 cm quartz cell on an Agilent Technologies Cary 60 UV-vis spectrophotometer.

Infrared (IR) Spectroscopy.

IR spectra were recorded on a Perkin Elmer Spectrum Two LITA FT-IR.

Photochemical Substitution.

The photochemical reactor lamp was purchased from Hanovia Specialty lighting LLC. The lamp is a medium-pressure mercury lamp emitting 200-400 nm broadband radiation. The lamp was placed inside a quartz jacket, with cooling water circulating throughout to maintain the reactions at ambient temperature.

Atomic Force Microscopy (AFM).

AFM images were acquired in PeakForce QNM tapping mode using a Bruker Dimension FastScan AFM.

Single Crystal X-Ray Diffraction.

Crystallographic data was collected on an Agilent SuperNova diffractometer using mirror-monochromated Cu Kα radiation.

4.7 Synthetic Details

Synthesis of exo-N-3-diphenylphosphine-norbornene-5,6-dicarboximide.

This compound was prepared using a modified protocol.[15] The compound (3-aminopropyl)diphenyl phosphine (3.00 g, 12.33 mmol) and cis-5-norbornene-exo-2,3-dicarboxylic anhydride (1.56 g, 9.50 mmol) were loaded in a 100 mL Schlenk flask. Toluene (130 mL) was added to the flask which was then transferred to a Schlenk line under N_2. The flask was fitted with a flame-dried Dean-Stark trap under nitrogen and connected to flame-dried reflux condenser. The reaction was heated to reflux for 24 h under N_2. The solution was then concentrated in vacuo, by passing through a short silica plug using ethyl acetate/hexanes. The solvent was evaporated from the collected fractions, yielding a pale yellow solid (3.17 g, 86% yield).

^{1}H NMR (Figure 4.9) (400 MHz, $CDCl_3$, δ ppm): 7.30-7.47 (m, 10H), 6.30 (s, 2H), 3.60 (t, 2H), 3.27 (s, 2H), 2.68 (s, 2H), 2.05 (m, 2H), 1.73 (m, 2H), 1.50 (d, 1H), 1.20 (d, 1H).

^{31}P NMR (Figure 4.10) (161.9 MHz, CDCl3, δ ppm): -16 ppm

Synthesis of phosphine oxide monomer.

This compound was prepared by oxidation of the phosphine monomer (3.17 g) using excess 30% H_2O_2 (20 mLs) over 3 hrs. The compound was extracted dichloromethane, washed with water, and dried with magnesium sulfate. The solution was concentrated in vacuo. The purified product was isolated with silica gel chromatography (50% Ethyl Acetate/ 50% hexanes and dried in vacuo to achieve a white solid (3.13 g, 95% yield).

^{1}H NMR (Figure 4.11) (400 MHz, $CDCl_3$, δ ppm): 7.74 (m, 4H), 7.52 (m, 6H), 6.30 (s, 2H), 3.60 (t, 2H), 3.27 (t, 2H), 2.68 (t, 2H), 2.30 (m, 2H), 1.91 (m, 2H), 1.64 (d, 1H), 1.19 (d, 1H).

^{31}P NMR (Figure 4.12) (161.9 MHz, $CDCl_3$, δ ppm): 31 ppm

Synthesis of phosphine oxide homopolymer.

GIII (24.4 μmol, 24 mL) was dissolved in THF. Phosphine oxide monomer (990 mgs, 2.4 mmol) was dissolved in 24.4 mL of THF. GIII was added to monomer solution and the reaction flask was stirred for 6 h. The homopolymer was quenched with excess ethyl vinyl ether. The solvent was evaporated in vacuo, redissolved in DCM, and precipitated with cold hexanes followed by precipitation into THF. A pale-yellow solid was collected (800 mgs).

^{1}H NMR (Figure 4.13) (400 MHz, $CDCl_3$, δ ppm): Broadened peaks are all attributed to the phosphine oxide monomer. The appearance of two new peaks appear at 5.45 and 5.70 ppm (corresponding to the ring-opened norbornene) and the complete disappearance of the peak at 6.3 ppm indicates complete polymerization.

^{31}P NMR (Figure 4.14) (161.9 MHz, $CDCl_3$, δ ppm): 32 ppm

Layer-by-layer deposition details.

A solution of 5 mg/ml of SHP, $[Co_6Se_8(PEt_3)_6][PF_6]$, and SCM was stirred at room temperature overnight. An ITO glass substrate was cleaned by sonicating for 30 minutes in acetone and isopropanol before drying under nitrogen stream. A polyethylene imine monolayer was first prepared by immersing the glass substrate in 1% solution of poly(ethylene imine) PEI (25 000) for 30 minutes to form an initial polyelectrolyte monolayer and was then washed with water, acetone, and dried under vacuum. After this initial layer, we count the first layer to be the first time the substrates were immersed in poly(sodium 4-styrenesulfonate) solution (MW = 70,000, 30 wt% in H2O) for 30 minutes, washed with water, acetone, and dried under vacuum. The second layer was built from immersion in solutions of 5 mg/mL of SHP, $[Co_6Se_8(PEt_3)_6][PF_6]$, or SCM dissolved in DMF. The glass substrates were washed with DMF, water, acetone and dried under vacuum in between layers.

4.8 NMR Spectra

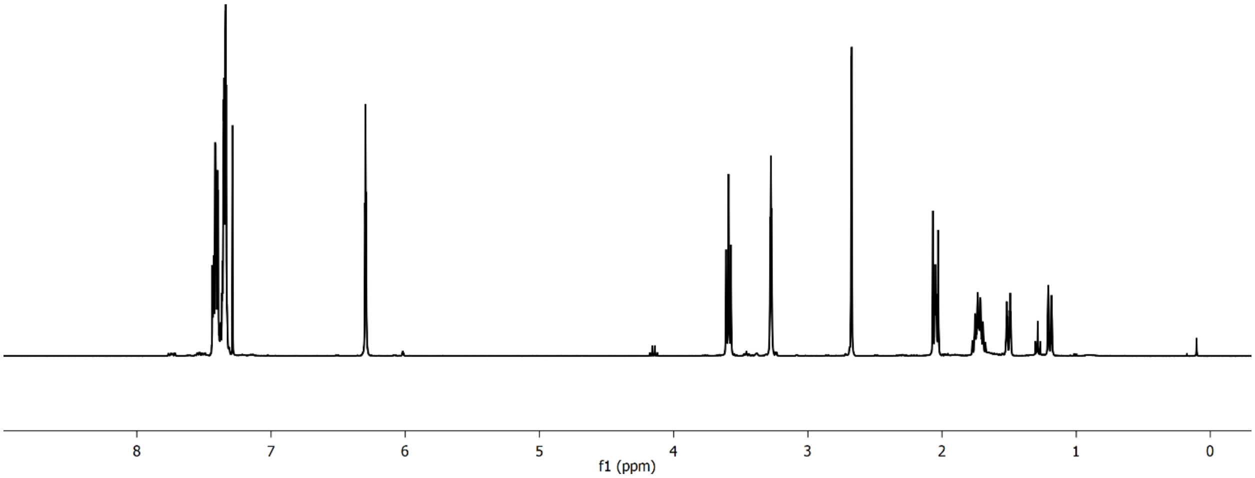

Figure 4.9. ^{1}H NMR of phosphine monomer taken in $CDCl_3$.

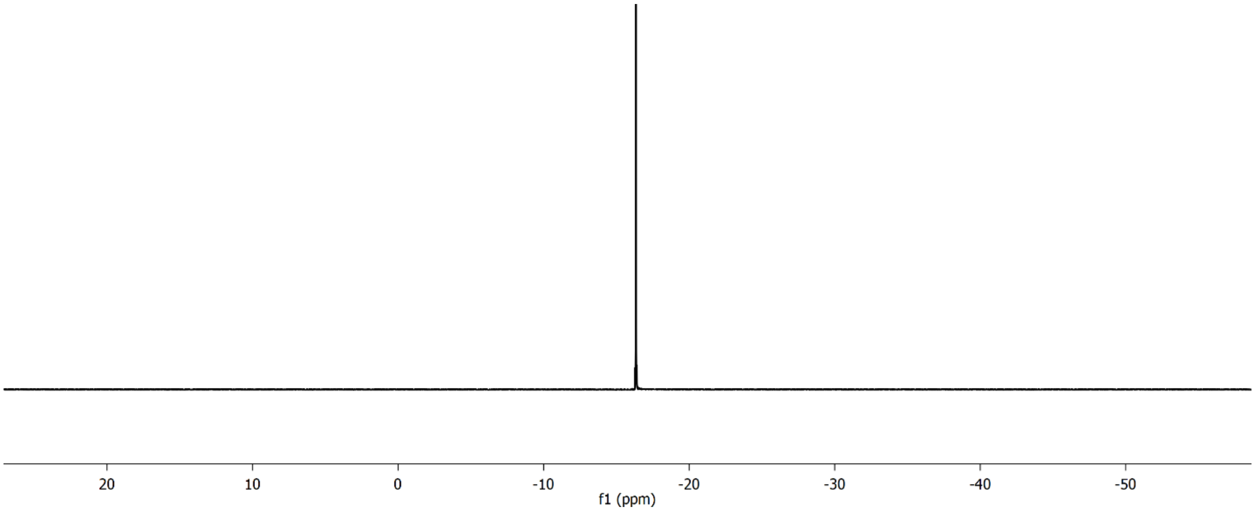

Figure 4.10. ^{31}P NMR spectrum of phosphine monomer.

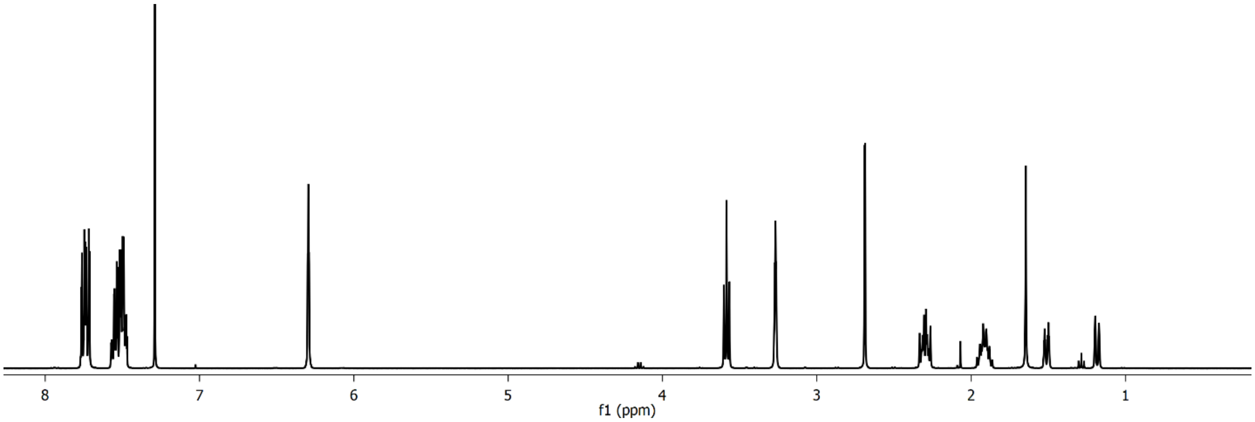

Figure 4.11. ^{1}H NMR spectrum of phosphine oxide monomer taken in $CDCl_3$.

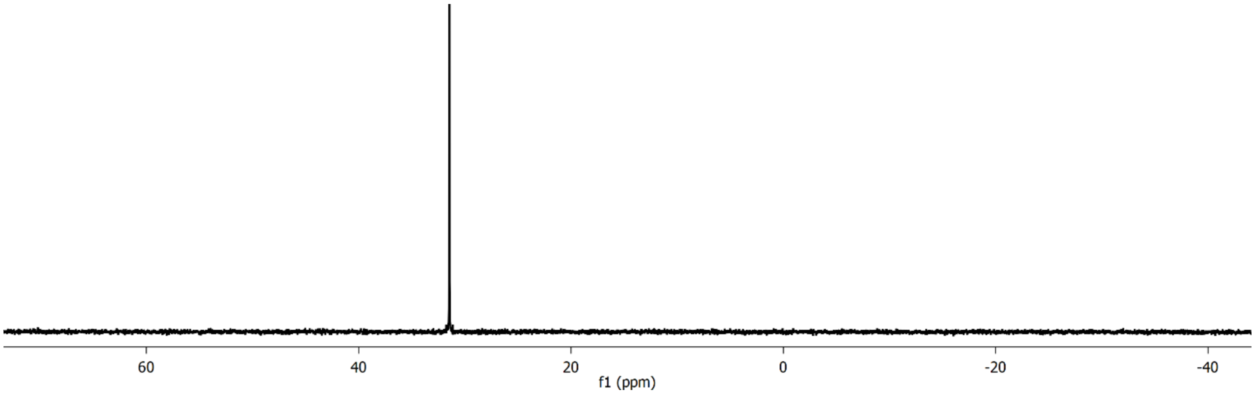

Figure 4.12. ^{31}P NMR spectrum of phosphine oxide monomer.

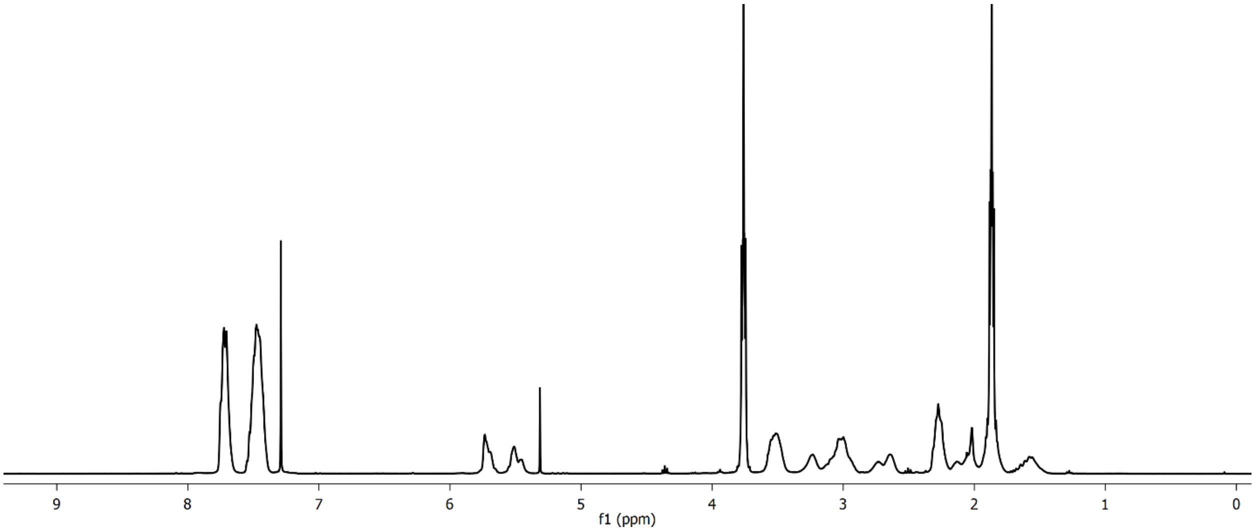

Figure 4.13. ^{1}H NMR of phosphine oxide polymer taken in $CDCl_3$.

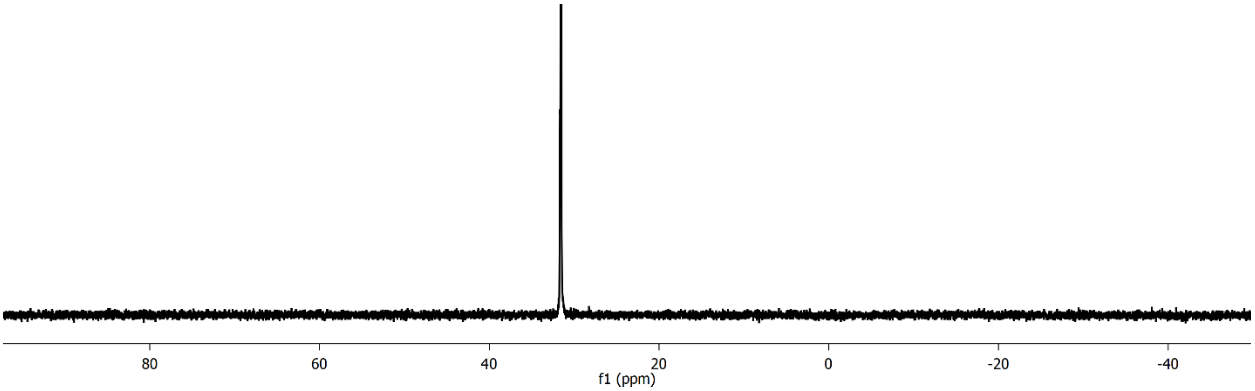

Figure 4.14. ^{31}P NMR of phosphine oxide polymer.

4.9 Crystallographic Details

Data was collected on an Agilent SuperNova diffractometer using mirror-monochromated Cu Kα radiation. Data collection, integration, scaling (ABSPACK) and absorption correction (face-indexed Gaussian integration[16] or numeric analytical methods[17]) were performed in CrysAlisPro.[18] Structure solution was performed using ShelXT.[19] Subsequent refinement was performed by full-matrix least-squares on F^2 in ShelXL.[19] Olex2[20] was used for viewing and to prepare CIF files. ORTEP graphics were prepared in CrystalMaker.[21] Thermal ellipsoids are rendered at the 50% probability level.

Crystals were grown at room temperature by slow diffusion of hexanes into a concentrated solution of SCM in dichloromethane. Black crystals were obtained after 24 hours. The solution was decanted, and the crystals were used directly for crystallography.

An irregular fragment (0.28 x 0.14 x 0.05 mm) was separated carefully, mounted with Paratone oil, and cooled to 100 K on the diffractometer. The crystal appeared to be monoclinic, and complete data for the Laue group were collected to 0.8 Å resolution. 44055 reflections were collected (15331 unique, 11404 observed) with R(int) 8.1% and R(sigma) 10.0% after Gaussian absorption and beam profile correction (Tmin .130).

The space group was assigned as $P2_1/c$ based on the systematic absences. The structure solved readily in ShelXT with 1 molecule in the asymmetric unit. The heavy atoms (Co, Se, P) and most C atoms were located in the initial solution. Two triethyl phosphine groups were each disordered over two positions, which were modeled with SAME restraints on their atomic positions and RIGU restraints on their displacement parameters. The hexafluorophosphate anion was disordered over two positions, which were restrained to approximate octahedral symmetry with the use of floating DFIX restraints on the P-F and F-F distances. (The average P-F distance refined to approximately 1.59 Å.) Finally, two molecules of dichloromethane were identified in the asymmetric unit, disordered over two and four positions respectively. All dichloromethanes were restrained to similar geometry using SAME restraints. The molecule that was disordered over four positions was modeled with isotropic ADPs; all other atoms were modeled with anisotropic ADPs. Overlapping ADPs of disordered atoms were made similar with a short-range SIMU instruction. Hydrogen atoms were placed in calculated positions and refined with riding coordinates and ADPs.

Table 4.1. Select crystallographic data of SCM.

Compound	**SCM**
Formula	$C_{56}H_{103}NO_2F_6P_7Co_6Se_8Cl_4$
MW	2280.24
Space group	$P2_1/c$
a **(Å)**	13.6351(3)
b **(Å)**	23.0852(7)
c **(Å)**	25.6213(5)
α **(°)**	90
β **(°)**	90.584(2)
γ **(°)**	90
V (Å^3)	8064.4(3)
Z	4
ρ_{calc} **(g cm^{-3})**	1.878
T (K)	100
λ **(Å)**	1.54184
$2\theta_{min}$, $2\theta_{max}$	7, 146
Nref	44055
R(int), R(σ)	.0817, .1000
μ(mm^{-1})	16.536
Size (mm)	.28 x .14 x .05
T_{max}, T_{min}	1, .13
Data	15331
Restraints	541
Parameters	1043
R_1**(obs)**	0.0566
wR_2**(all)**	0.1525
S	1.023
Peak, hole (e$^-$ Å^{-3})	1.09, -0.86

4.10 References

1. Champsaur, A. M.; Velian, A.; Paley, D. W.; Choi, B.; Roy, X.; Steigerwald, M. L.; Nuckolls, C. Building Diatomic and Triatomic Superatom Molecules. *Nano Lett.* **2016**, *16* (8), 5273–5277.

2. Champsaur, A. M.; Hochuli, T. J.; Paley, D. W.; Nuckolls, C.; Steigerwald, M. L. Superatom Fusion and the Nature of Quantum Con Fi Nement. *Nano Lett.* **2018**, *18*, 4564–4569.

3. Abd-El-Aziz, A.; Manners, I. *Frontiers in Transition-Metal-Containing Polymers*; John Wiley & Sons: Hoboken, NJ, 2007.

4. Wang, X.; McHale, R. Metal-Containing Polymers: Building Blocks for Functional (Nano)Materials Www.Mrc-Journal.De. *Macromol. Rapid Commun.* **2010**, *31* (4), 331.

5. Hardy, C. G.; Zhang, J.; Yan, Y.; Ren, L.; Tang, C. Metallopolymers with Transition Metals in the Side-Chain by Living and Controlled Polymerization Techniques. *Prog. Polym. Sci.* **2014**, *39* (10), 1742–1796.

6. Kim, S.; Kim, S.; Tracy, J. B.; Jasanoff, A.; Bawendi, M. G. Phosphine Oxide Polymer for Water-Soluble Nanoparticles. *J. Am. Chem. Soc.* **2005**, *127*, 4556–4557.

7. Tsang, C.; Yam, M.; Gates, D. P. The Addition Polymerization of a P d C Bond : A Route to New Phosphine Polymers. *J. Am. Chem. Soc.* **2003**, *125*, 1480–1481.

8. Dasgupta, M.; Peori, M. B.; Kakkar, A. K. Designing Dendritic Polymers Containing Phosphorus Donor Ligands and Their Corresponding Transition Metal Complexes. *Coord. Chem. Rev.* **2002**, *234*, 223–235.

9. Wang, D.; Astruc, D. Dendritic Catalysis — Basic Concepts and Recent Trends. *Coord. Chem. Rev.* **2013**, *257* (15–16), 2317–2334.

10. Kraft, S. J.; Sánchez, R. H.; Hock, A. S. A Remarkably Active Iron Catecholate Catalyst Immobilized in a Porous Organic Polymer. *ACS Catal.* **2013**, *3* (5), 826–830.

11. Richardson, J.; Bjornmalm, M.; Caruso, F. Technology-Driven Layer-by-Layer Assembly of Nanofilms. *Science (80-.).* **2015**, *348* (6233).

12. Xiao, F.-X.; Pagliaro, M.; Xu, Y.-J.; Liu, B. Layer-by-Layer Assembly of Versatile Nanoarchitectures with Diverse Dimensionality: A New Perspective for Rational Construction of Multilayer Assemblies. *Chem. Soc. Rev.* **2016**, *45*, 3088–3121.

13. Shen, L.; Wang, J.; Xu, G.; Li, H.; Dou, H.; Zhang, X. NiCo 2 S 4 Nanosheets Grown on Nitrogen-Doped Carbon Foams as an Advanced Electrode for Supercapacitors. *Adv. Energy Mater.* **2015**, *5* (1400977), 2–8.

14. Chen, J.; Xu, J.; Zhou, S.; Zhao, N.; Wong, C. P. Nitrogen-Doped Hierarchically Porous Carbon Foam: A Free-Standing Electrode and Mechanical Support for High-Performance Supercapacitors. *Nano Energy* **2016**, *25*, 193–202.

15. Poly, N.; Liu, J.; Burts, A. O.; Li, Y.; Zhukhovitskiy, A. V; Ottaviani, M. F.; Turro, N. J.; Johnson, J. A. “ Brush-First ” Method for the Parallel Synthesis of Photocleavable, Nitroxide-Labeled Poly(Ethylene Glycol) Star Polymers. *J. Am. Chem. Soc.* **2012**, *134*, 16337–16344.

16. Blanc, E.; Schwarzenbach, D.; Flack, H. D. Evaluation of Transmission Factors and Their First

Derivatives with Respect to Crystal Shape Parameters. *J. Appl. Crystallogr.* **1991**, *24* (pt 6), 1035–1041.

17. Clark, R. C.; Reid, J. S. The Analytical Calculation of Absorption in Multifaceted Crystals. *Acta Crystallogr. Sect. A* **1995**, *A51*, 887–897.

18. Oxford Diffraction/Agilent Technologies UK Ltd. Version 1.171.37.35. Yarnton, England 2014.

19. Sheldrick, G. M. No Title. *Acta Crystallogr. Sect. A2* **2015**, *A71*, 3–8.

20. Dolomanov, O. V; Bourhis, L. J.; Gildea, R. J.; Howard, J. A. K.; Puschmann, H. OLEX2: A Complete Structure Solution, Refinement and Analysis Program. *J. Appl. Crystallogr.* **2009**, No. 42, 339–341.

21. CrystalMaker Software Ltd. Oxford, England.

Chapter 5

Multifunctional vesicles from a self-assembled superatom-containing diblock copolymer

5.0 Preface

Significant portions of this chapter are adapted from the publication on this research entitled *Multifunctional Vesicles from a Self-Assembled Cluster-containing Diblock Copolymer* by Anastasia Voevodin, Luis Campos, and Xavier Roy published in *Journal of American Chemical Society*, **2018**, 140 (16), pp 5607-5611.[1] Anouck Champsaur provided guidance on the synthesis of the carbonylated cobalt selenide superatom and its reactivity for substitution.[2] Dan Paley performed single crystal refinement. Grisha Etkin and Dan Paley assisted with the gel permeation chromatography. I synthesized all materials and performed SEM, AFM, and TEM imaging.

5.1 Introduction

Materials that combine the attractive mechanical properties and processability of polymers, with the optical, electronic and magnetic properties of inorganic compounds are of great scientific interest for the design of functional devices.[3–7] In this context, metal-containing polymers have received widespread attention for applications in light-harvesting and light-emitting devices, nanoelectronics, nanopatterning and sensing.[8,9] Metal-containing block copolymers capable of self-assembly have also been used as templates to create unique inorganic nano- and mesostructures.[10,11] While the vast majority of metal-containing polymers comprise a single metal atom per repeating unit,[12,13] the integration of complex multinuclear metal components (*e.g., molecular clusters*) into well-defined macromolecular systems remains a major synthetic challenge.[3,12] Nonetheless, in the past decades, a select number of research groups have reported homopolymers[13,14] and a few block copolymers[14–17] containing simple transition metal carbonyl clusters[18,19] which have been used to fabricate striking metal nanostructures.[20–22]

Metal chalcogenide molecular clusters are particularly attractive functional units[23–25] to incorporate into macromolecular systems. They offer unique and exciting opportunities for tunable multi-electron redox processes, luminescence, magnetism and catalysis.[2,24–27] The design of such cluster-containing polymers, however, is complicated by the multiple non-differentiated sites for ligand attachment on the cluster surface, leading to the formation of cross-linked networks.[28–30] Though Zheng and co-workers have exploited the multiple coordination sites on the Re_6Se_8 cluster core to synthesize a dendrimer with six arms,[31] creating well defined linear polymer chains with metal chalcogenide clusters on every repeating unit has remained a challenge.

Here we report the synthesis and self-assembly of the first diblock copolymer containing the redox-active cluster Co_6Se_8 in one of the blocks. The multifunctional diblock copolymer (SC-BCP) is prepared by sequential polymerization of a photoactive monomer (M1) and a cluster-containing monomer (SCM), the latter prepared by substituting a polymerizable group for CO on the photolabile differentially-functionalized cluster $Co_6Se_8(PEt_3)_5(CO)$.

This synthetic approach creates high molecular weight diblock copolymers with low dispersity index. Remarkably, we show that the multiple redox states of the cluster are reversibly accessible in this system. Moreover, by self-assembling the diblock copolymer, we can shut down the electron transfer process to the redox-active cluster. In the charged state, the polymer self-assembles into vesicles and we demonstrate that methylene blue can be encapsulated inside these vesicles whose walls can be crosslinked to retain the molecular cargo.

5.2 Synthesis of a cluster-containing diblock copolymer

Figure 5.1a presents our synthetic strategy to prepare the multifunctional SC-BCP via sequential ring-opening metathesis polymerization (ROMP) of M1 and SCM. For both monomers, we use polymerizable norbornene moieties to form the backbone. M1 is prepared by first reacting cis-5-norbornene-exo-2,3-dicarboxylic anhydride with 6-amino-1-hexanol to form the norbornene dicarboximide with a pendent hydroxyl, which is then coupled with cinnamic acid via esterification to append the photoactive cinnamoyl group.

SCM is obtained by first treating the same norbornene dicarboxylic anhydride derivative with 3-(diphenylphosphino)-1-propylamine to append a diphenyl phosphine, and then coupling the

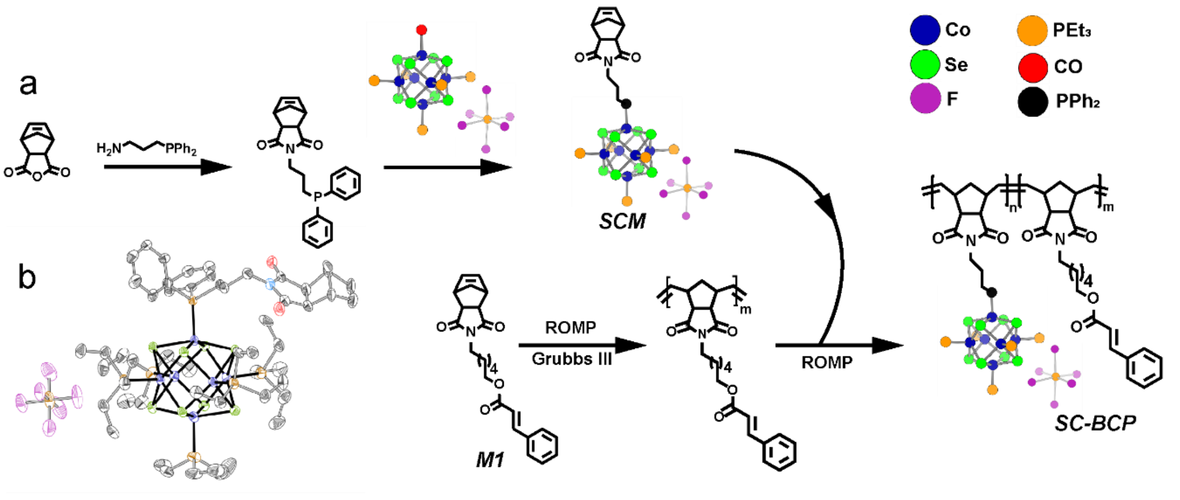

Figure 5.1. (a) Synthesis of SCM and SC-BCP. (b) Molecular structure of SCM, as determined by SCXRD. Color code: C, black; N, light blue; O, red; Se, green; Co, blue; P, yellow; F, purple.

resulting norbornene dicarboximide to the molecular cluster $Co_6Se_8(PEt_3)_5$ by coordinating the pendent phosphine to the inorganic core. The coupling reaction is performed under UV photolytic conditions using the cationic cluster $[Co_6Se_8(CO)(PEt_3)_5][PF_6]$ and an excess of the norbornene-bearing phosphine pro-ligand. The synthesis of $[Co_6Se_8(CO)(PEt_3)_5][PF_6]$ was recently reported by Champsaur *et al.*[2] Briefly, it is prepared by reacting $Co_2(CO)_8$ with an excess of Se and PEt_3 to form $Co_6Se_8(CO)_x(PEt_3)_{6-x}$. $[Co_6Se_8(CO)(PEt_3)_5][PF_6]$ is then isolated from a silica column after treatment with $TBAPF_6$. Under UV irradiation, the photolabile CO ligand is substituted with the phosphine. The substitution reaction is monitored by IR spectroscopy by following the disappearance of the CO stretching mode at 1968 cm^{-1}.[2]

While the neutral cluster $Co_6Se_8(CO)(PEt_3)_5$ can also be used for the coupling reaction, the cationic compound is stable under ambient conditions, facilitating purification and handling. After complete disappearance of the CO stretch, SCM is purified by column chromatography to remove excess pro-ligand and then crystallized by diffusing hexanes into a dichloromethane (DCM)

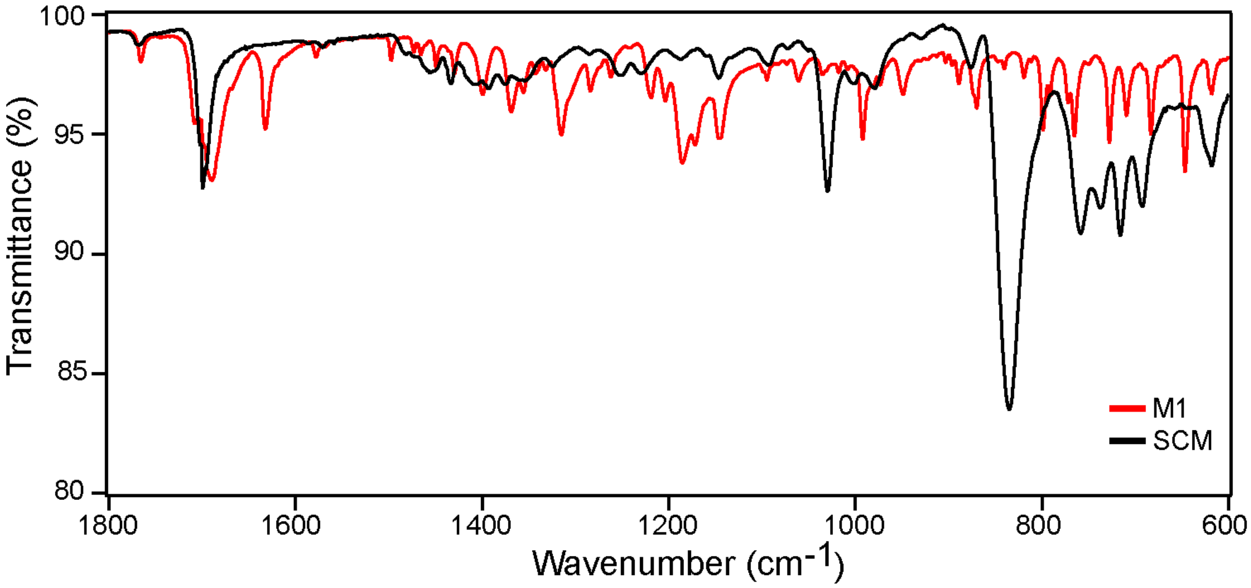

Figure 5.2. FTIR spectra of M1 (red) and SCM (black).

solution of the compound. A Fourier-transformed infrared spectroscopy (FTIR) spectra of both M1 and SCM is shown in Figure 5.2.

Figure 5.1b)presents the crystal structure of SCM, as determined by single crystal x-ray diffraction (SCXRD). This molecular structure was first introduced in Chapter 4 where its structural details are further explained. In brief here, we find it remarkable that despite the size difference between the norbornene moiety and superatom, polymerization under ROMP conditions with a Grubbs III catalyst of this monomer is successful. Full crystallographic details are included in Chapter 4.

SC-BCP is synthesized by sequential ROMP of M1 and SCM in dichloromethane (DCM), using Grubbs catalyst 3rd generation. The stoichiometric ratio of the components in the reaction is 150 M1:50 SCM:1 catalyst. The polymerization is stopped with the addition of ethyl vinyl ether, and SC-BCP is precipitated with hexanes and washed with toluene to remove any remaining monomer. Figure 4.3 a,b shows the ^{1}H NMR spectra of SCM and SC-BCP, respectively. The full spectrum of SC-BCP, (see Figure 4.22) is broad and complex but all the peaks derive from M1 or SCM. The broad peaks below 0 ppm come from the PEt_3 on the cationic paramagnetic cluster. In addition to the broadness of the spectrum, there are a few key features that verify the ring opening metathesis polymerization. The peak at 6.3 ppm, corresponding to the vinylic protons on the norbornene rings, is present in the ^{1}H NMR spectra of M1 and SCM but is absent in that of SC-SC-BCP. Instead, two resonances at 5.5 and 5.7 ppm are present in the SC-BCP spectrum, indicating the formation of the norbornene ring-opened polymer backbone. The M1:SCM stoichiometric ratio in the polymer can be estimated from the integration of the peaks at ~6.4 and ~7.2 ppm (shown in Figure 5.3 as blue and green circles, respectively). These peaks correspond to the M1 cinnamoyl vinylic protons and one set of phenyl protons on SCM, respectively. The M1:SCM ratio calculated from the ^1H NMR spectrum of SC-BCP is 3.3:1, in good agreement with the 3:1 stoichiometric ratio introduced in the reaction.

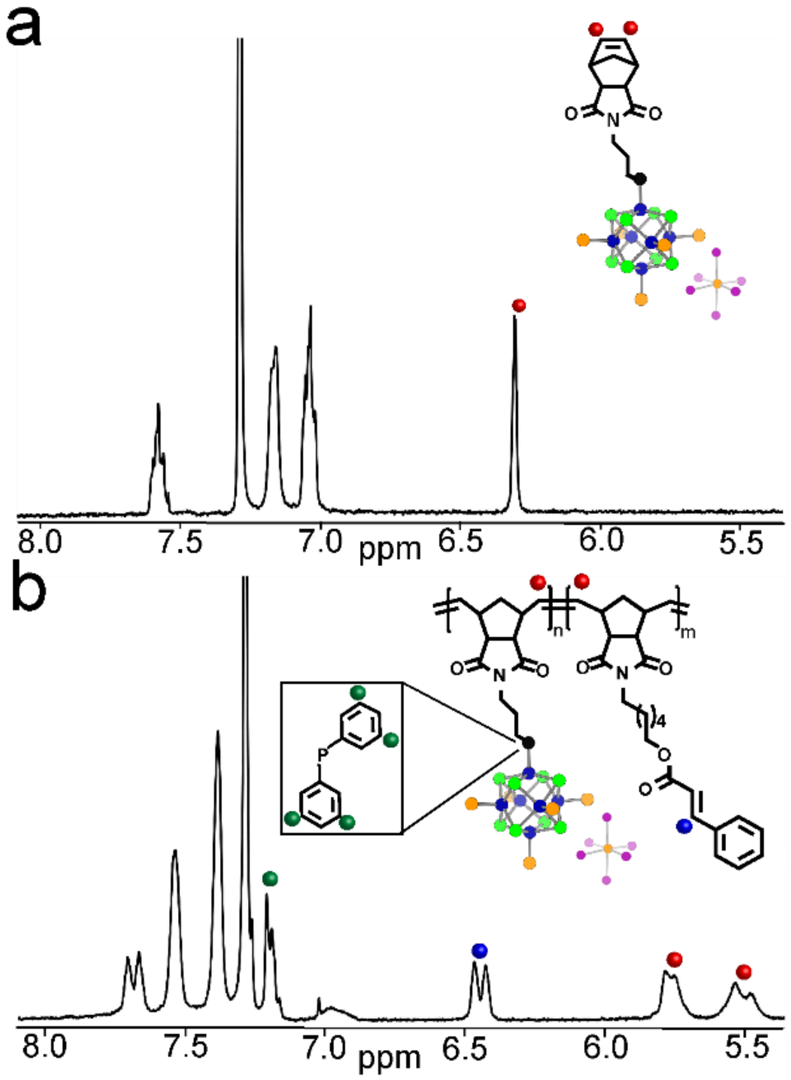

Figure 5.3. (a) ^1H NMR spectrum of SCM in the range 5.3-8.0 ppm, taken in $CDCl_3$. Norbornene vinyl peaks are highlighted with red circles (b) ^1H NMR spectrum of SC-BCP in the range 5.3-8.0 ppm, taken in $CDCl_3$. One set of SCM diphenyl phosphine protons are identified by green circles, set of cinnamoyl's vinylic protons identified with blue circle, and backbone polymer peaks identified in red circles

5.3 Determination of molecular weight and dispersity of SC-BCP

Determining the molecular weight of SC-BCP is challenging because of its limited solubility in many solvents, its strong tendency to self-assemble (discussed later in section 5.4), and the presence of charged clusters tethered to one of the blocks. To get an estimate of the molecular weight, we take a small aliquot from the M1 polymerization (i.e., just before the addition of SCM), and measure its molecular weight using gel permeation chromatography (GPC) with polystyrene standard. We then use the ratio obtained from the ^{1}H NMR spectrum to infer the SC-BCP molecular weight, Mw ~ 155 000 g/mol (details in the). GPC is also used to assess the dispersity of the polymer: Figure 5.14 shows the unimodal gel permeation chromatogram of SC-BCP in N,N-dimethylformamide (DMF) with 0.1% LiBr. The shape of the peak in the chromatogram indicates a narrow dispersity index, Đ ~ 1.2.

5.4 Self-assembly of SC-BCP

Composed of two blocks with vastly different solubility properties, SC-BCP is an amphiphile that should readily self-assemble in solution. Using a mixed-solvent system of tetrahydrofuran (THF) and water (as the minor solvent), we observe the formation of synthetic vesicles, sometimes called polymersomes (Figure 5.4a). Figure 5.4(b,c) displays scanning electron microscopy (SEM) and transmission electron microscopy (TEM) images of the vesicles obtained in a 90:10 v/v THF:water mixture.

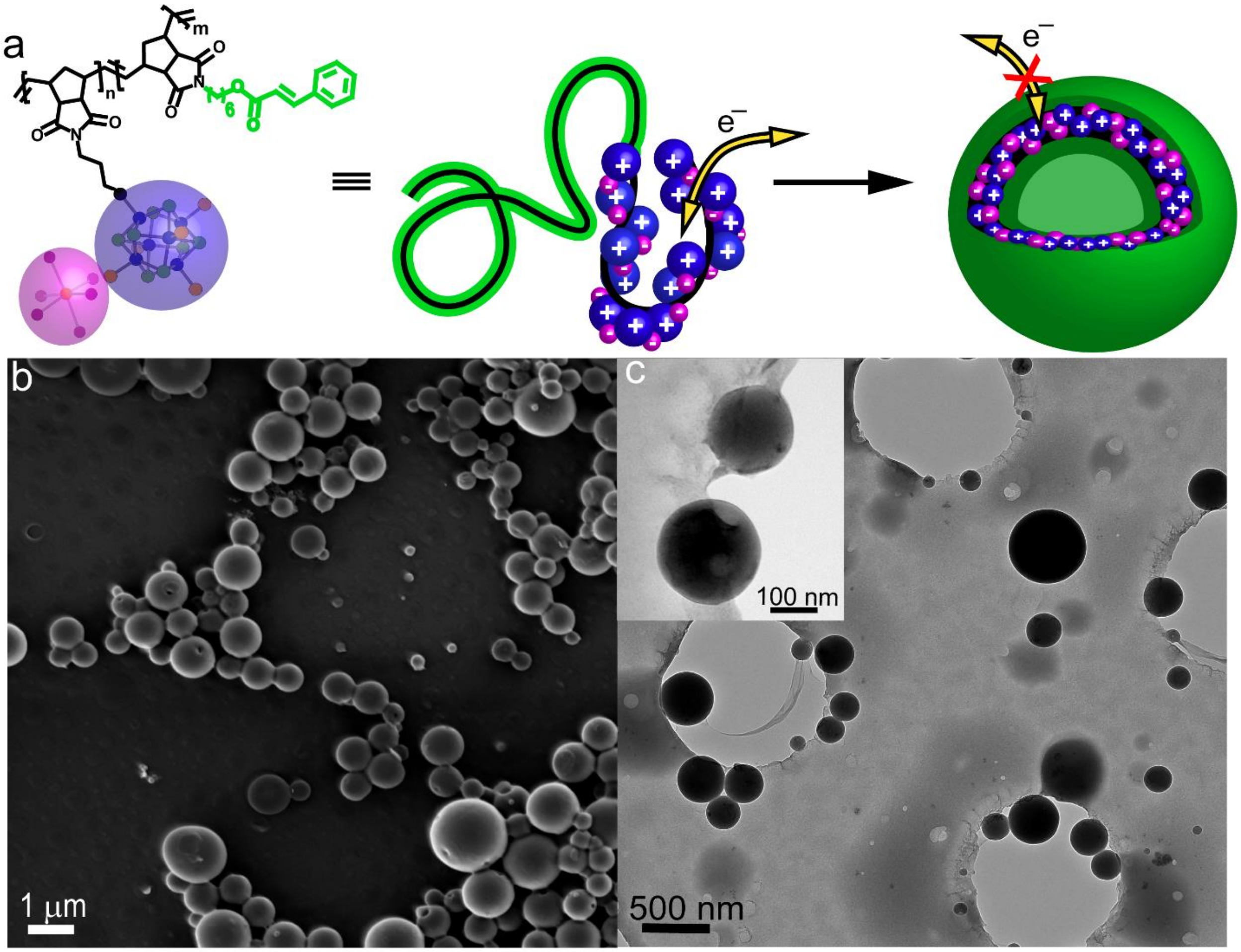

Figure 5.4. (a) Schematic of SC-BCP self-assembly into vesicles. The cinnamoyl block is shown in green and the cluster is shown in blue, with its counter ion in pink. Dissolved SC-BCP can reversibly access three redox states, but self-assembled SC-BCP is no longer redox active. (b) SEM image of SC-BCP vesicles assembled in a 90:10 THF:H_2O solvent mixture. (c) TEM image of SC-BCP vesicles assembled in the same conditions. Inset: TEM image showing the hollowness of the vesicles.

Additional micrographs as well as atomic force microscopy (AFM) images are presented in Figures 5.5-5.7. The spherical structures typically range from 500 nm to 2 μm in diameter. We note that chemical staining is not required for TEM imaging due to the presence of the metal chalcogenide cluster in one of the blocks. The hollowness of the structures is evident in the inset of Figure 5.4c. Moreover, small indentations (or dimples) are visible on the particles, presumably a result of the partial collapse of the vesicular walls as solvent evaporates from the hollow cores. Based on the high solubility of the cinnamoyl block, and the insolubility of the cluster-containing block in THF, we hypothesize that the vesicular wall is an inverse bilayer in which the cationic cluster block is sandwiched between hydrophobic cinnamoyl segments (Figure 5.4a). Presumably, the water preferentially migrates to the ionic inner-wall to swell the shell and decrease the curvature. Indeed, much smaller particles with more irregular morphologies are obtained when dry THF is used for the assembly (Figure 5.5e-f).

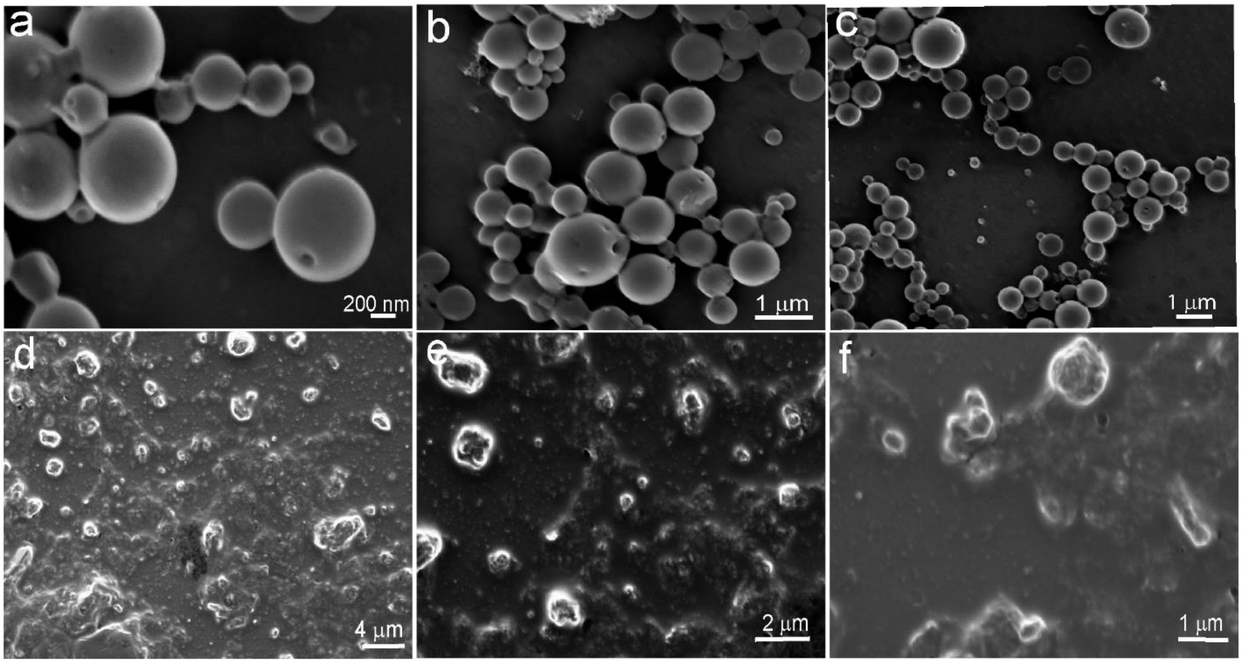

Figure 5.5. (a-c) SEM images of SC-BCP vesicles assembled in a 90:10 v/v THF: H_2O solvent mixture. (d-f) SEM images of SC-BCP assembled in THF showing irregular morphology.

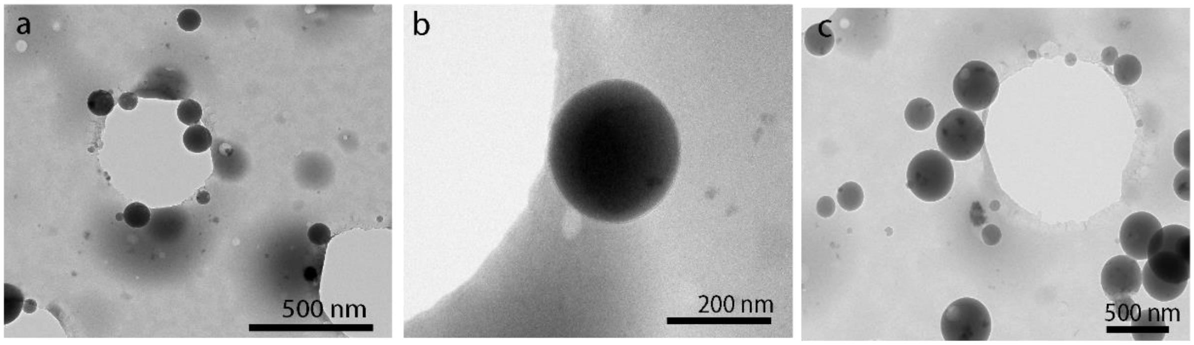

Figure 5.6. TEM micrographs of SC-BCP vesicles assembled in 90:10 v/v THF:H_2O solvent mixture.

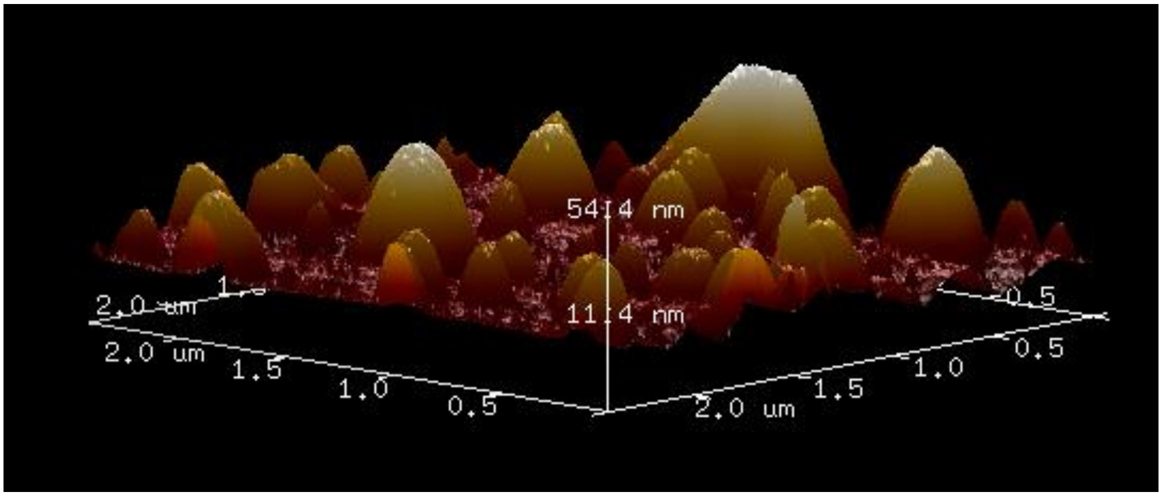

Figure 5.7. 3D AFM image of the SC-BCP vesicles on a Si wafer

5.5 Electrochemistry of BCP

The cluster Co_6Se_8 is capable of reversible multiple electron redox processes, opening the door to the creation of polymeric systems in which each repeating unit can access three or more charge states. While multiple redox states can be accessed in metallocenes using unusually harsh conditions,[32–34] to the best of our knowledge such behavior has never been observed in a polymeric system.

To examine the electrochemical behavior of the tethered Co_6Se_8 core, we performed cyclic voltammetry on SCM and SC-BCP in DMF with 0.1 M tetrabutylammonium hexafluorophosphate ($TBAPF_6$) supporting electrolyte. The cyclic voltammograms in Figure 4.8(a,b) are qualitatively similar, showing two reversible redox processes at $E_{1/2}$ ~ –0.8 and –0.2 V versus ferrocene/ferrocenium (Fc/Fc^+). These two redox couples correspond to the 0/1+ and 1+/2+ transformations, respectively. We note that the current measured at the SC-BCP 1+/2+ redox couple is smaller than that at the 0/1+ redox couple. This is presumably due to the lower solubility of the polymer in the higher charge state, as well as the increased driving force for self-assembly, which will decrease both diffusion to the electrode surface and electron transfer. These results demonstrate that SC-BCP can access three charge states: neutral, 1+ and 2+. Based on previous electrochemical studies of the Co_6Se_8 cluster,[2] we expect that even more charge states can be accessed; however, the poor solubility of the diblock copolymer in the 3+ state prevents us from measuring reversible waves.

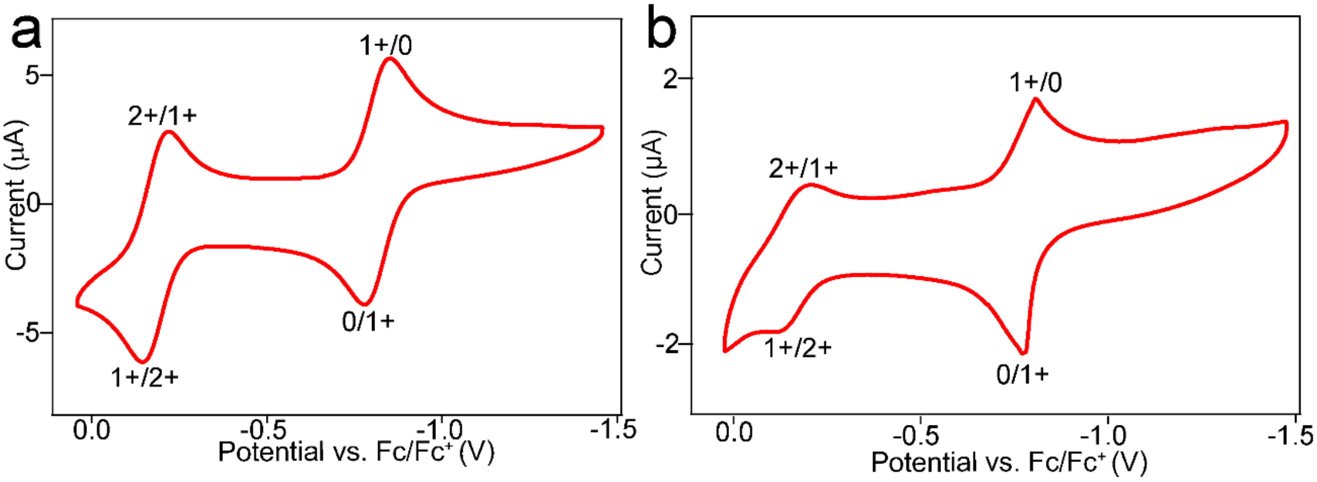

Figure 5.8. Cyclic voltammograms (CV) of (a) SCM and (b) SC-BCP showing three reversible redox states assigned to neutral, 1+, and 2+. CVs are taken in DMF with 0.1 M $TBAPF_6$ and referenced Fc/Fc^+ redox couple.

Increasing the scan rate from 10 mV/s to 100 mV/s broadens the observed two redox couples shown in Figure 4.9(a). Remarkably, no redox peaks are observed in the cyclic voltammogram of the SC-BCP after self-assembly into vesicles in THF/H_2O (Figure 5.9b); presumably the assembly segregates the redox-active clusters inside the walls of the vesicles, which are covered with an insulating shell that inhibits electron transfer.

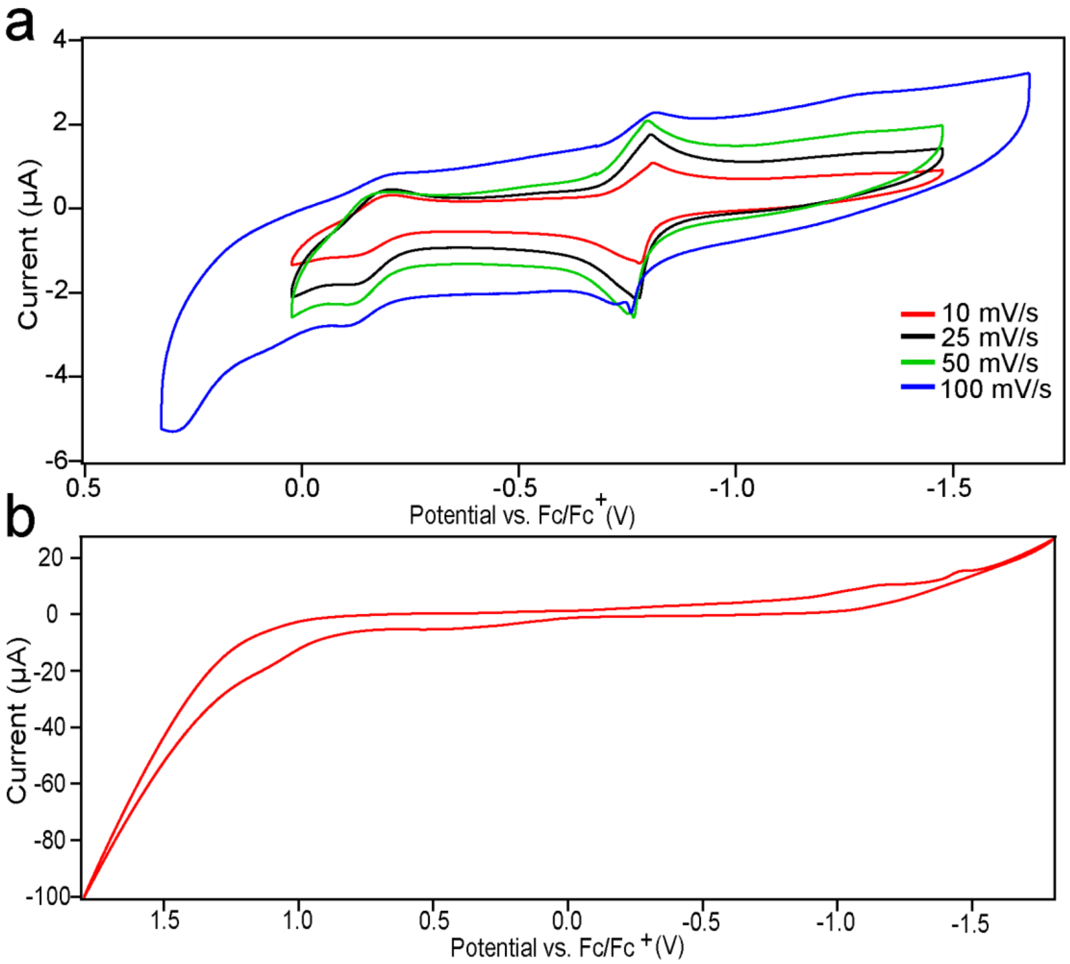

Figure 5.9. Cyclic voltammograms of (a) SC-BCP in DMF at 10 (red), 25 (black), 50 (green), and 100 (blue) mV/s scan rates and (b) of SC-BCP assembled in THF. CVs are taken with 0.1 M $TBAPF_6$ and referenced Fc/Fc^+ redox couple.

5.6 Crosslinking of vesicle walls

The SC-BCP vesicular walls can be crosslinked by irradiating the assemblies with >300 nm light, which drives the 2+2 cycloaddition of the cinnamoyl group (Figure 5.10a).[30–32] Cross-linking is monitored by IR spectroscopy (Figure 5.10(b,c)). Prior to crosslinking, the IR spectrum of the vesicles features distinct peaks for M1 at 1632 and 978 cm^{-1}, corresponding to the stretching frequency of the cinnamoyl vinylic C=C group.[33] An additional peak of M1 at 1690 cm^{-1}, corresponding to the phenyl on the cinnamoyl group, overlaps with the aromatic stretches of SCM (at 1700 cm^{-1}) arising from the diphenyl phosphine moiety. After irradiating the self-assembled SC-BCP (XBCP), the peaks at ~1700, 1632, and 978 cm^{-1} broaden and decrease in intensity, consistent with conversion of the cinnamoyls to cyclobutane dimers.[30–32] We note that the expected shift of the cinnamoyl 1690 cm^{-1} peak upon dimerization is obscured by the overlap with SCM.

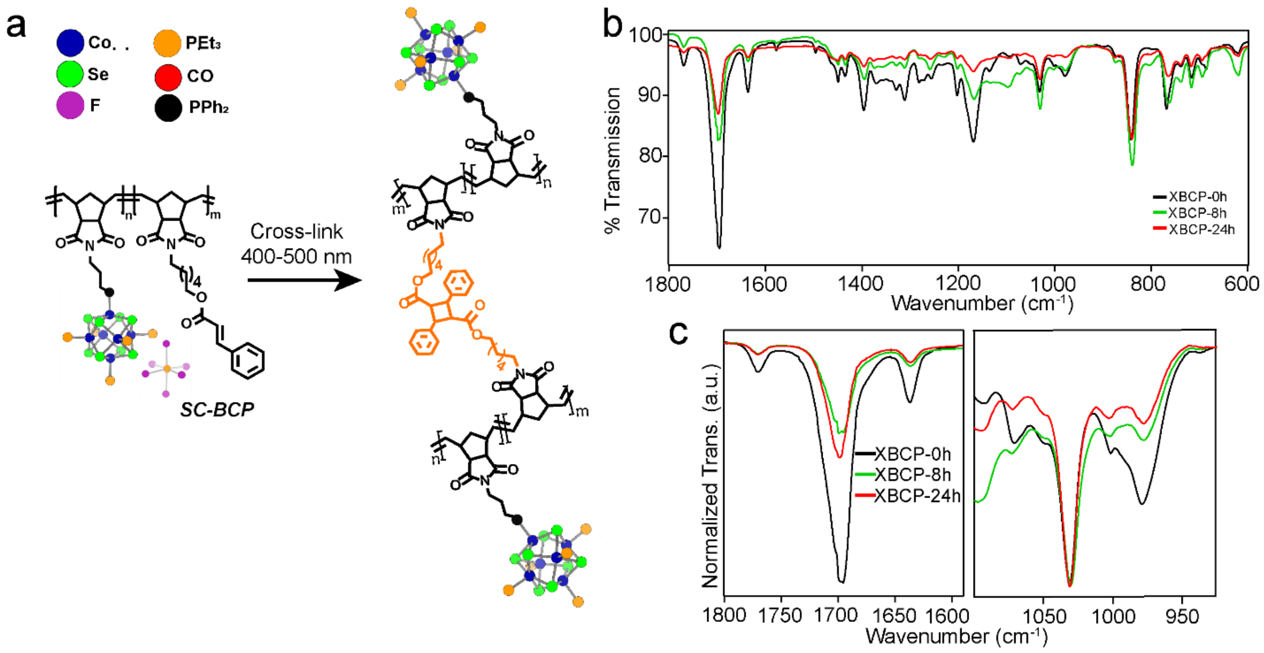

Figure 5.10. (a) Crosslinking of SC-BCP to XBCP upon exposure to 400-500 nm light forming a 2+2 cycloaddition across SC-BCP chains (b) FTIR monitoring of crosslinking after 0 (black), 8 (green), and 24 hours (red) and (c) normalized transmission to monitor the vibrational changes at 1700 and 1020 cm^{-1}.

While the cluster absorbs some of the 400-500 nm light, both UV–Vis and IR indicate that it remains intact (see Figures 5.10, 5.11).

5.7 Encapsulation of small molecules within vesicles

We also demonstrate the use of these vesicles as containers by encapsulating the molecular dye methylene blue (MB) illustrated in Figure 5.11. To load the vesicles, an aqueous solution of MB is added to a THF solution of SC-BCP to give a 90:10 v/v THF:water solvent mixture. Under these conditions, MB is soluble and SC-BCP self-assembles into vesicles over a period of ~12 h, trapping MB molecules inside the solvent-filled core. Next, we irradiate the solution with 400-500 nm light for 24 h to crosslink the vesicles, then add DCM to the solution and finally repeatedly wash the organic phase with water, until no blue color is present in the aqueous phase.

This process of dispersing the vesicles into DCM and then extracting the aqueous phase collapses the containers. Figure 5.11(c,d) shows the morphology of the collapsed vesicles assembled without and with encapsulated MB, respectively. For comparison, the insets show the spherical morphology of the same vesicles drop cast from the THF/water solvent mixture.

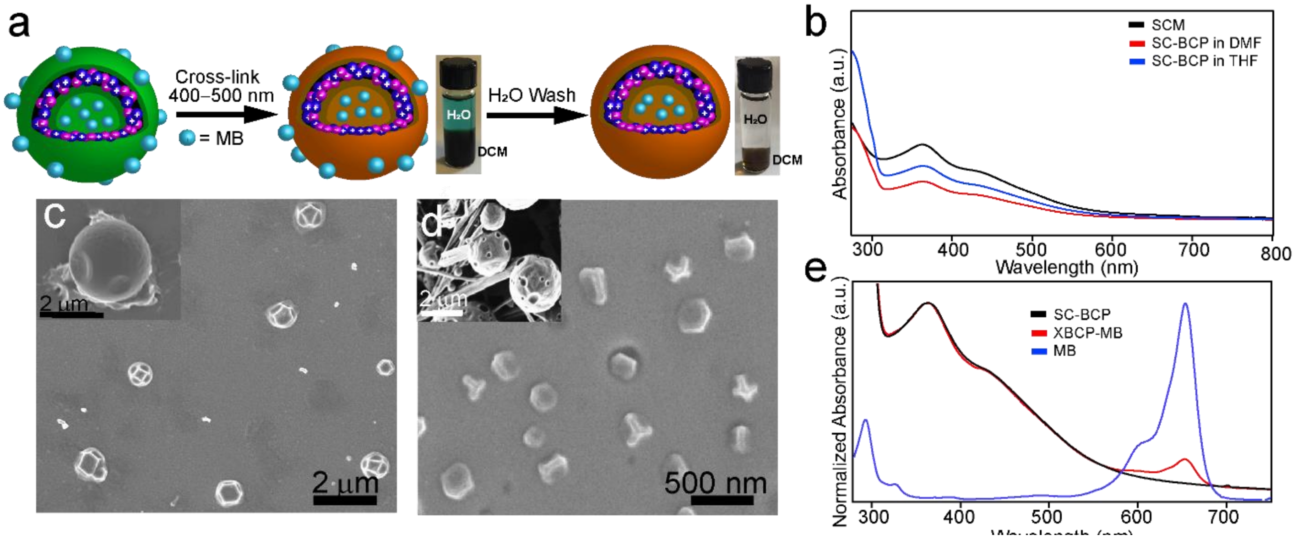

Figure 5.11. (a) Schematic of the encapsulation of MB in SC-BCP vesicles. Cross-linking of the outer cinnamoyl shell upon irradiation with 300-400 nm light is followed by extraction of excess MB with successive water washes. The optical images show the DCM solution of BCP-MB with water layer on top. (b) Electronic absorption spectra of SCM, and SC-BCP dissolved in DMF and assembled in THF. (c) SEM image of collapsed SC-BCP vesicles, obtained when DCM is added to the THF/H_2O solution and the water is removed. The inset shows an intact vesicle before transfer to DCM and removal of H_2O. (d) SEM image of collapsed BCP-MB vesicles after extraction of excess MB with H_2O. The inset shows an intact vesicle before transfer to DCM and extraction of MB with H_2O. The crystals in the inset are from excess MB not encapsulated in the containers. (e) Normalized electronic absorption spectra of MB, SC-BCP, and XBCP-MB in DCM

The solution-phase electronic absorption spectra of the vesicles with and without encapsulated MB show broad absorption features between 300 and 500 nm, corresponding to the Co_6Se_8 core. The BCP-MB spectrum contains two additional optical transitions in the range 580-700 nm, which can be attributed to MB. When compared to MB in solution, the MB peaks in the BCP-MB spectrum are broadened. This is consistent with previous reports of MB encapsulation into polymer containers.[34] Irradiating the vesicles crosslinks the walls and diminishes the amount of MB released from the container during the washing. Figure 5.12 illustrates this point: the MB concentration in the aqueous wash is visibly lower when the vesicles are crosslinked.

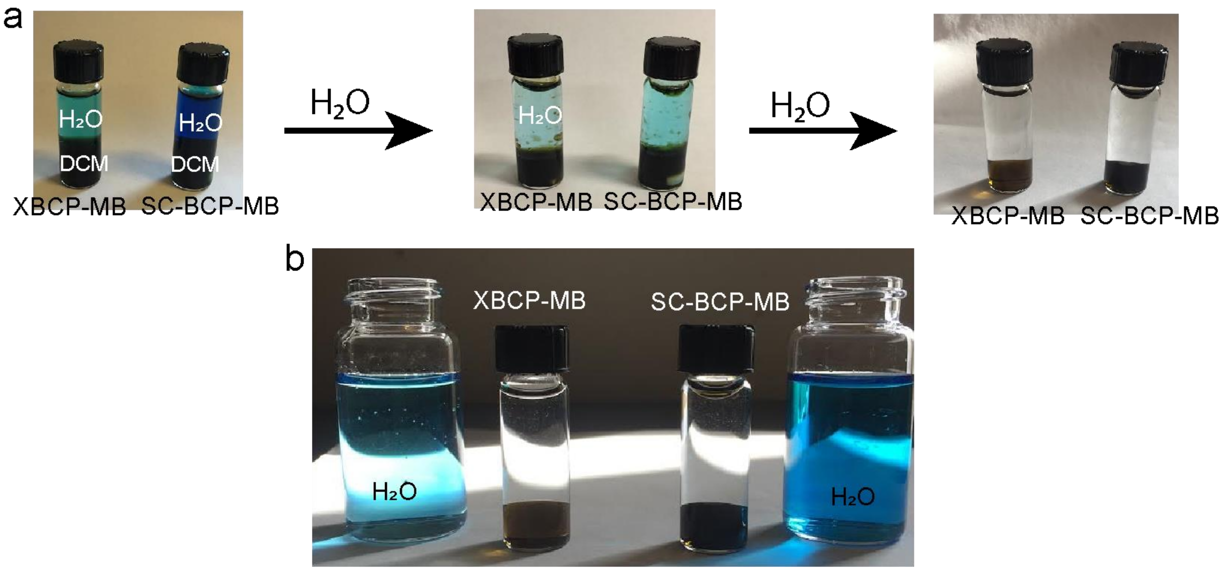

Figure 5.12. (a) Extraction of non-encapsulated MB with distilled water in crosslinked (XBCP-MB) and not crosslinked (SC-BCP-MB) samples. (b) Comparison of the aqueous phase containing the extracted non-encapsulated MB. The solution for the non-crosslinked vesicles (SC-BCP-MB) visibly contains more MB than that of the crosslinked vesicles (XBCP-MB).

5.8 Conclusion

By tethering a molecular cluster to a norbornene moiety, we have designed a new redox-active monomer that can be combined with a photo-crosslinkable segment to create a multifunctional diblock copolymer. The molecular cluster provides unique access to three reversible charged states in DMF. In THF, the diblock copolymer self-assembles into vesicles when the cluster is in the 1+ charge state. The formation of these self-assembled structures segregates the redox-active clusters inside the walls and inhibits electron transfer. Moreover, the vesicles can be used as containers to encapsulate molecular cargo such as methylene blue. By exploiting the photoreactivity of the cinnamoyl group incorporated in the hydrophobic block, we can crosslink the walls of the vesicles. The integration of molecular clusters into well-defined block copolymers offers exciting possibilities to develop multifunctional assemblies for applications in catalysis, electrochemistry and biomedicine. In addition, this cluster-containing polymer could be used to direct the hierarchical assembly of novel metal chalcogenide mesostructures.

5.9 Materials and Methods

Unless otherwise noted, all reactions were performed in a nitrogen atmosphere using standard Schlenk techniques or in a nitrogen-filled glovebox. Triethyl phosphine (99%) was purchased from Sigma-Aldrich. Selenium and dicobalt octacarbonyl (stabilized with 1-5% hexane) were obtained from STREM Chemicals. All other reagents were purchased from Sigma-Aldrich. Chemicals were used without further purification. Dry and deoxygenated solvents were prepared by elution through a dual-column solvent system (MBraun SPS). Deuterated solvents used for NMR spectroscopy were purchased from Cambridge Isotope Laboratories, Inc.

Column Chromatography.

Chromatography was performed using a Teledyne Isco Combiflash Rf200 and Redisep Rf Silica columns.

NMR Spectroscopy

^{1}H NMR and ^{31}P NMR spectra were recorded on a Bruker DRX400 spectrometer.

Electronic Absorption Spectroscopy

Electronic absorption spectra were recorded using a 1.0 cm quartz cell on an Agilent Technologies Cary 60 UV-vis spectrophotometer.

Infrared (IR) Spectroscopy

IR spectra were recorded on a Perkin Elmer Spectrum Two LITA FT-IR.

Cyclic Voltammetry

Cyclic voltammetry was performed using a CH166 electrochemical potentiostat using a glassy carbon electrode as the working electrode, and Pt electrodes as both reference and counter electrodes. SC-BCP voltammograms were collected in both N,N-dimethylformamide and tetrahydrofuran.

Photochemical Substitution

The photochemical reactor lamp was purchased from Hanovia Specialty lighting LLC. The lamp is a medium-pressure mercury lamp emitting 200-400 nm broadband radiation. The lamp was placed inside a quartz jacket, with cooling water circulating throughout to maintain the reactions at ambient temperature.

Crosslinking

Crosslinking was carried out using a Kessil H150 LED Blue Grow Light emitting 400-500 nm light.

Gel Permeation Chromatography (GPC)

GPC run in THF was collected on a Waters 1515 Isocratic HPLC Pump with a Waters 2414 Refractive Index Detector, Waters 2998 Photoiode Array Detector, and a Waters 2707 Autosampler. GPC run in DMF was collected on an Agilent Technologies 1260 Infinity instrument.

Transmission Electron Microscopy (TEM)

TEM images were obtained on a FEI TALOS F200X instrument using holey carbon grids.

Scanning Electron Microscopy (SEM). SEM images were obtained on a Zeiss SIGMA VP instrument equipped with a Schottky Thermal Emission Type electron gun.

Atomic Force Microscopy (AFM).

AFM images were acquired in PeakForce QNM tapping mode using a Bruker Dimension FastScan AFM.

Single Crystal X-Ray Diffraction.

Crystallographic data was collected on an Agilent SuperNova diffractometer using mirror-monochromated Cu Kα radiation.

5.10 Synthetic Details

Synthesis of M1 precursor (M1-P):

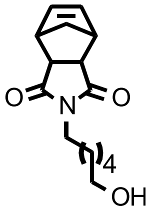

M1-P was synthesized following a reported literature procedure.[35]

Synthesis of M1:

M1 was synthesized using a modified literature procedure.[36] A 100 mL Schlenk flask was loaded with M1-P (2.00 g, 9.04 mmol) and placed under N_2. Dichloromethane (20 mL) was added followed by N-(3-dimethylaminopropyl)-N'-ethylcarbodiimide hydrochloride (2.17 g, 11.32 mmol) and dimethylaminopyridine (0.09 g, 0.76 mmol). *Trans*-cinnamic acid (1.36 g, 9.18 mmol) was dissolved in ~5 mL dichloromethane and quickly added to the reaction flask using a syringe needle. The reaction was stirred at room temperature for 8 h. The reaction mixture was transferred to a separatory funnel, washed with water (2 x 40 mL) and dried over $MgSO_4$. The pale-yellow oil was purified by silica gel chromatography (1:3 Ethyl Acetate/Hexanes) and concentrated in vacuo to yield a white solid (2.40 g, 6.83 mmol, 76% yield).

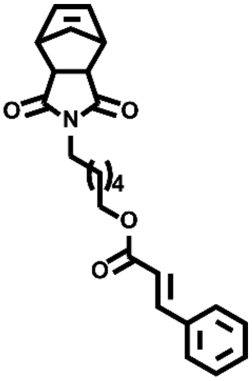

^{1}H NMR (spectrum in Figure 5.15) (400 MHz, $CDCl_3$, δ ppm): 7.70 (d, 1H), 7.56 (s, 2H), 1.41 (s, 2H), 6.45 (d, 1H), 6.30 (s, 2H), 4.21 (t, 2H), 3.50 (t, 2H), 3.30 (t, 2H), 1.8-1.2 (m, 8H), 1.25 (d, 1H)

Synthesis of [$Co_6Se_8(CO)(PEt_3)_5$][PF_6]:

The mono-carbonylated cluster [$Co_6Se_8(CO)(PEt_3)_5$][PF_6] was prepared according to a literature procedure.[2]

Synthesis of exo-N-3-diphenylphosphine-norbornene-5,6-dicarboximide (PM):

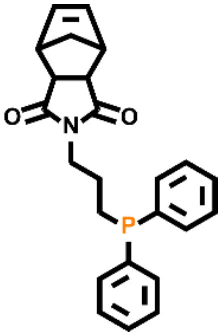

This compound was prepared using a modified protocol.[37] Synthetic details, ^{1}H NMR and ^{31}P NMR are presented in Chapter 4.

Synthesis of SCM:

Exo-N-3-diphenylphosphine-norbornene-5,6,-dicarboxmide (PM) (125 mg, 0.32 mmol) and [$Co_6Se_8(CO)(PEt_3)_5$][PF_6] (491 mg, 0.28 mmol) were loaded into a 20 mL scintillation vial. Tetrahydrofuran (10 mL) was added and the solution was stirred for 10 min. The solution was capped with a septum and transferred out of the glovebox and irradiated with a mercury lamp for 24 h. The reaction was monitored by IR for the disappearance of the broad CO peak at 1960-1970 cm^{-1}. After complete conversion, the reaction mixture was concentrated in vacuo. The product was purified by column chromatography with 1:1 ethyl acetate: hexanes. A brown solid was recovered after evaporating the solvent from the dark brown band fraction (402 mg, 68% yield).

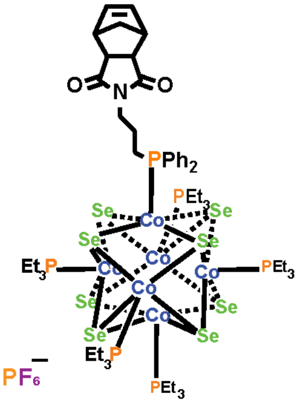

^{1}H NMR (spectrum in Figure 5.16) (400 MHz, $CDCl_3$, δ ppm):[3] 7.60 (m, 2H), 7.17 (m, 4H), 7.02 (m, 4H), 6.30 (s, 2H), 3.50 (s, 2H), 3.27 (s, 2H), 2.66 (s, 2H), 2.07 (m, 2H), 1.2-1.7 (4H) 0.50 (9H, b), 0.30 (36H, b), -0.41 (b, 6H), -0.65 (b, 24H).

^{31}P NMR: (spectrum in Figure 5.17) (161.9 MHz, $CDCl_3$, δ ppm): -144.36 ($^1J_{P,F}$ = 712 Hz)

Additional peaks found in the ^{1}HNMR and ^{31}PNMR spectra are attributed to excess tetra butyl ammonium hexafluorophosphate and residual solvent.

Preparation of Grubbs III catalyst:

Grubbs catalyst generation III (GIII) was prepared from commercially available Grubbs catalyst generation II following a literature procedure.[38]

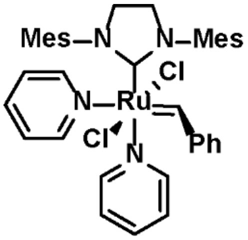

^{1}H NMR: (spectrum in Figure. 5.18) (400 MHz, $CDCl_3$, δ ppm)[5]: 8.67 (s, 2H), 7.87 (s, 2H), 7.67 (d, 3H), 7.50 (m, 2H), 7.29 (s, 3H), 7.10 (m, 4H), 6.98 (s, 2H), 6.78 (s, 2H), 4.14 (d, 4H), 2.68 (s, 6H), 2.30 (m, 12H)

Synthesis of SC-BCP:

A stock solution of GIII in THF (5 mg/mL) was prepared. M1 (37.5 mg, 106.8 μmol) was dissolved in 5 ml THF. 104 μl (0.7 μmol) of GIII stock solution was added to the M1 solution.

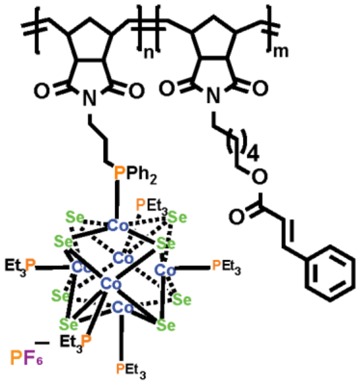

After 10 min, 0.3 ml was syringed from the polymerization reaction for GPC analysis of the M1 homopolymer (HP). A solution of SCM (75 mg, 35.6 μmol) in 2 mL of THF was added to the reaction vial and the polymerization reaction was stirred for 16 h at room temperature. The diblock copolymer was quenched with excess ethyl vinyl ether. The solvent was evaporated in vacuo; the solid was redissolved in dichloromethane and precipitated with cold hexanes. The solid was then washed with toluene and dried in vacuo. A brown solid was obtained (24 mg).

^{1}H NMR of HP (spectrum in Figure 5.19) (400 MHz, $CDCl_3$): Broadened peaks are all attributed to M1. The ratio of either vinylic protons at 5.3 and 5.75 ppm (corresponding to the ring opened norbornene) to the cinnamoyl vinylic proton at 6.45 ppm is 1. This indicates that all the M1 present in the sample is polymerized. This is further supported by the complete disappearance of the peak at 6.3 ppm, which corresponds to the closed norbornene backbone.

^{1}H NMR of SC-BCP: (spectrum in Figure 5.20) (400 MHz, $CDCl_3$): All peaks can be attributed to M1 or SCM. The M1 cinnamoyl peak at 6.45 ppm is set at an integration value of 150 based on the feed ratio. Using this integration base value, the peak at 7.17 ppm (corresponding to two protons on each phenyl rings of SCM) integrates to 182. The M1:SCM ratio in SC-BCP is therefore 150:(182/4) = 3.3:1, in good agreement with the feed ratio.

5.11 Gel Permeation Chromatography Spectra and Details

Analysis of HP:

GPC was performed with a THF solution of HP. The GPC was calibrated with polystyrene standards. The trace shown is from the UV signal at 254 nm.

Analysis of SC-BCP:

GPC was performed with DMF solution of SC-BCP, with 0.1% LiBr. The GPC was calibrated with PEG-PEO standards. The trace shown is from the UV signal at 300 nm.

Table 5.1. Dispersity of **HP** and **SC-BCP** determined by GPC taken in THF and DMF, respectively.

Compound	**Dispersity (Đ)**
HP	1.2
SC-BCP	1.2

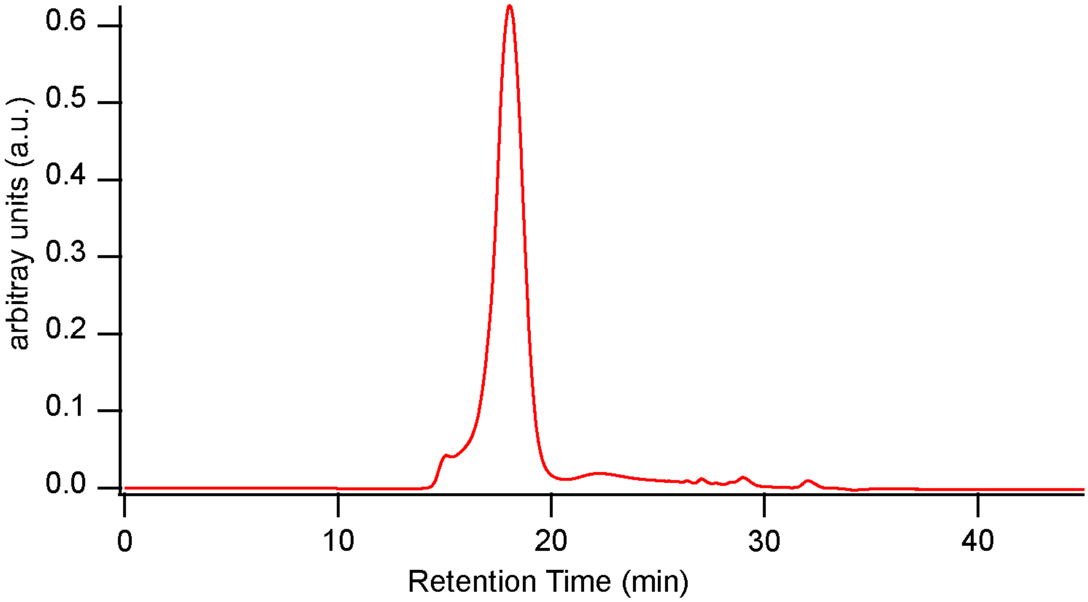

Figure 5.13. GPC chromatogram of HP in THF.

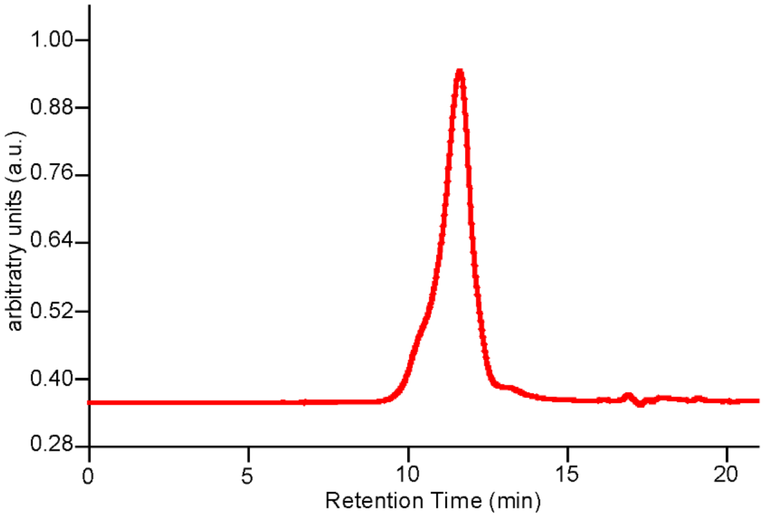

Figure 5.14. GPC chromatogram of SC-BCP in DMF with 0.1% LiBr.

Determination of SC-BCP Molecular Weight (M_w):

GPC analysis of HP gives a M_w of ~55, 216 g/mol, which is in good agreement with the ideal M_w of ~52,710 g/mol based on a 150:1 M1:GIII feed ratio. GPC analysis cannot be used to directly measure M_w for SC-BCP because it has a very different structure, composition, charge, solvation properties and interactions with the column than those of the PEG-PEO standard.

The M_w of SC-BCP is estimated from the ratio M1:SCM determined by ^{1}H NMR. The M_w of HP 55,216 g/mol determined by GPC indicates an average of ~157 M1 repeat units per chain. Using the M1:SCM ratio (3.3:1), we find that polymer chains on average contain 48 SCM repeat units, giving a M_w 101,307 g/mol for the segment. The combined molecular weight for SC-BCP is 156,523 g/mol, only slightly smaller than the expected M_w of 158,238 g/mol.

The GPC of SC-BCP is used to estimate a dispersity index Đ ~1.2, unchanged from that of HP.

5.12 Self-Assembly Details

Self-Assembly of SC-BCP:

A 90:10 solvent mixture of anhydrous THF: distilled H_2O was added to SC-BCP (3 mg) in a 3 ml scintillation vial. The solution was stirred at room temperature for ~16 hours.

Self-Assembly of BCP-MB: A stock solution of methylene blue (MB) in distilled water (5 mg/ml) was prepared. The stock MB solution (0.2 ml) was added to a solution of SC-BCP (6 mg) in dry THF (1.8 ml). The resulting blue solution was stirred at room temperature for 16 h. Half of this solution was transferred to a 1cm quartz cuvette and irradiated with blue light for crosslinking to give XBCP-MB.

Preparation of XBCP and XBCP-MB:

Solutions of self-assembled vesicles in THF were transferred to a 1 cm quartz cuvette. The cuvette was irradiated with a Kessil H150 LED blue lamp. Aliquots were syringed at regular intervals for IR and UV-Vis and electronic absorption characterization.

Extraction of non-encapsulated MB: Dichloromethane (1ml) was added to the vials containing the solutions of XBCP-MB and SC-BCP-MB in THF. Distilled water (2 ml) was added to the vials and the mixture were stirred at room temperature for 15 minutes. Water containing excess MB was removed. The extraction was repeated until no blue color was observed in the aqueous layer.

5.13 NMR Spectra

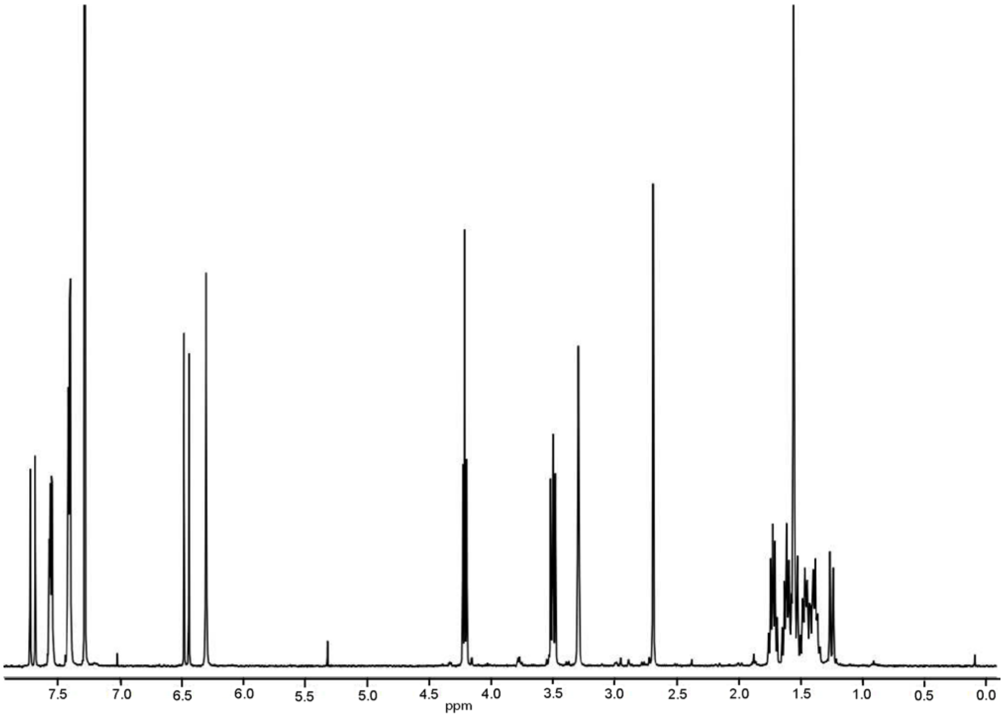

Figure 5.15. ^{1}H NMR spectrum of M1 in $CDCl_3$.

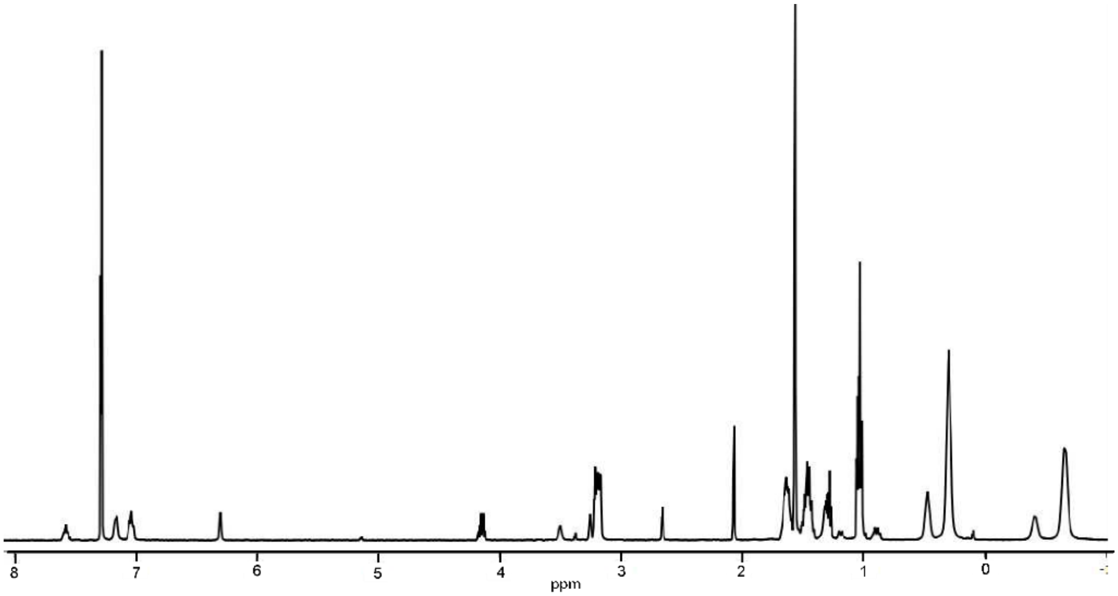

Figure 5.16. ^{1}H NMR spectrum of SCM in $CDCl_3$.

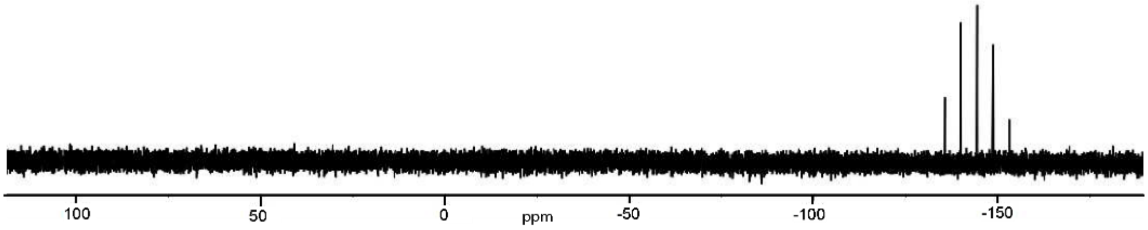

Figure 5.17. ^{31}P NMR spectrum of SCM in $CDCl_3$. The broad peak for the phosphine on the neutral cluster is typically found at ~60 ppm. It disappears when the cluster is oxidized and becomes paramagnetic, as in SCM.

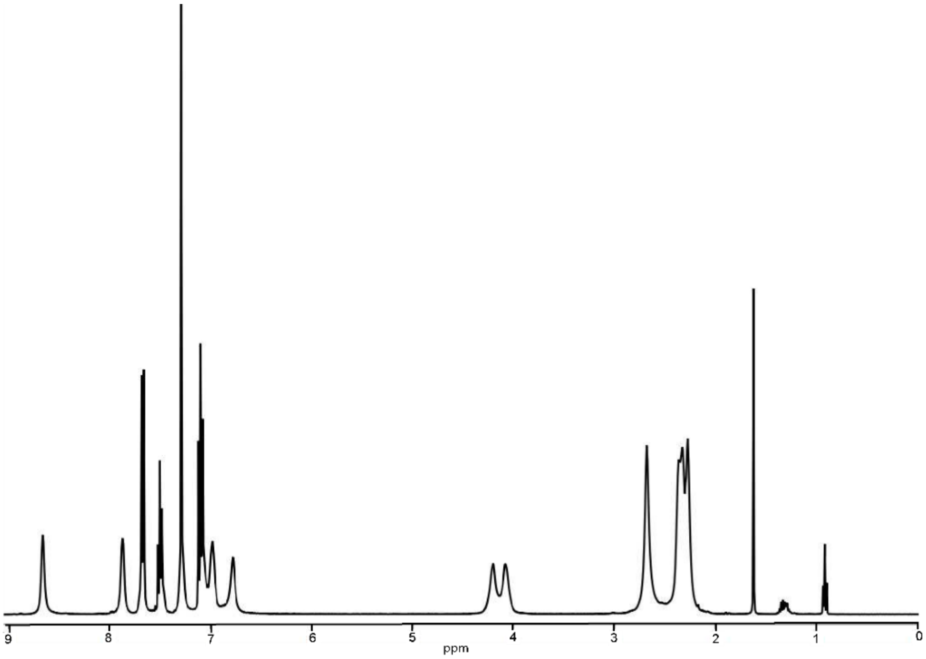

Figure 5.18. ^{1}H NMR spectrum of GIII in $CDCl_3$.

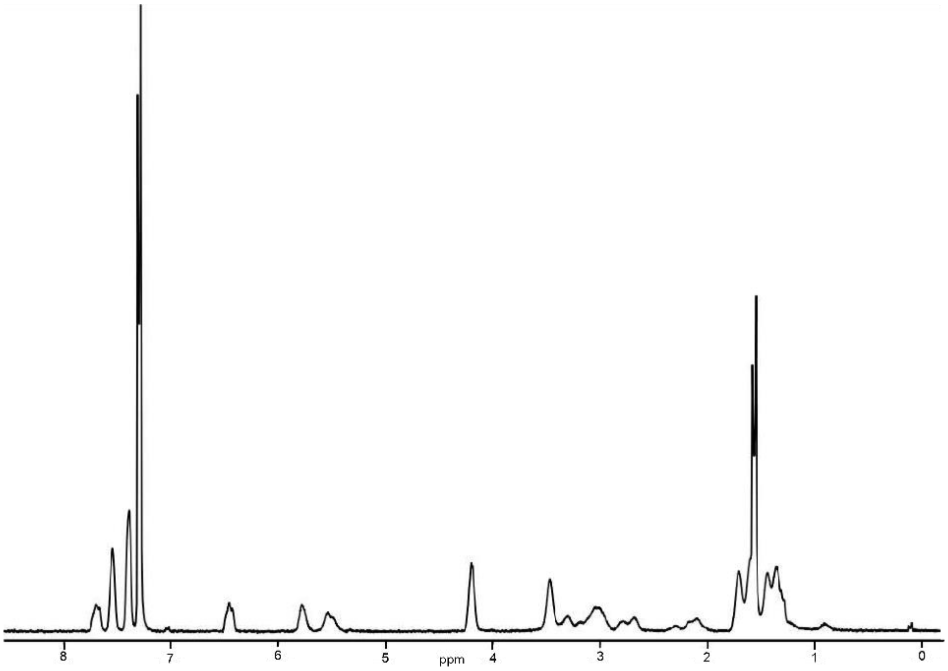

Figure 5.19. ^{1}H NMR spectrum of HP taken in CDCl$_3$.

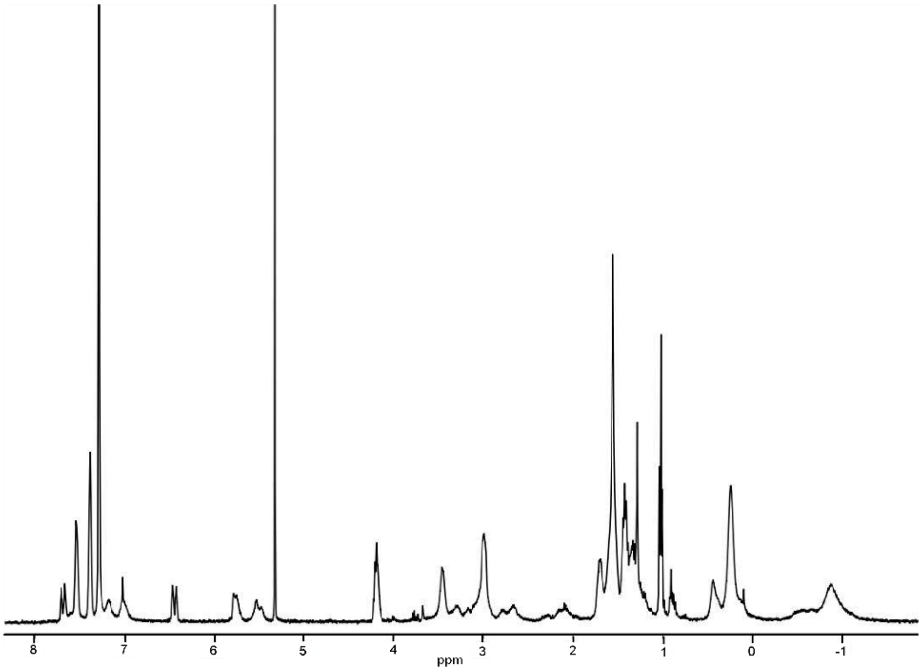

Figure 5.20. ^{1}H NMR spectrum of SC-BCP in CDCl$_3$.

5.14 References

1. Voevodin, A.; Campos, L. M.; Roy, X. Multifunctional Vesicles from a Self-Assembled Cluster-Containing Diblock Copolymer. *J. Am. Chem. Soc.* **2018**, *140* (16), 5607–5611.

2. Champsaur, A. M.; Velian, A.; Paley, D. W.; Choi, B.; Roy, X.; Steigerwald, M. L.; Nuckolls, C. Building Diatomic and Triatomic Superatom Molecules. *Nano Lett.* **2016**, *16* (8), 5273–5277.

3. Whittell, G. R.; Hager, M. D.; Schubert, U. S.; Manners, I. Functional Soft Materials from Metallopolymers and Metallosupramolecular Polymers. *Nat. Mater.* **2011**, *10* (3), 176–188.

4. Holliday, B. J.; Stanford, T. B.; Swager, T. M. Chemoresistive Gas-Phase Nitric Oxide Sensing with Cobalt-Containing Conducting Metallopolymers. *Chem. Mater.* **2006**, *18* (24), 5649–5651.

5. Tanaka, K. A Discrete Self-Assembled Metal Array in Artificial DNA. *Science (80-.).* **2003**, *299* (5610), 1212–1213.

6. Wu, F. I.; Yang, X. H.; Neher, D.; Dodda, R.; Tseng, Y. H.; Shu, C. F. Efficient White-Electrophosphorescent Devices Based on a Single Polyfluorene Copolymer. *Adv. Funct. Mater.* **2007**, *17* (7), 1085–1092.

7. Arsenault, A. C.; Puzzo, D. P.; Manners, I.; Ozin, G. A. Photonic-Crystal Full-Colour Displays. *Nat. Photonics* **2007**, *1* (8), 468–472.

8. Suzuki, D.; Sakai, T.; Yoshida, R. Self-Flocculating/Self-Dispersing Oscillation of Microgels. *Angew. Chemie - Int. Ed.* **2008**, *47* (5), 917–920.

9. Winter, A.; Friebe, C.; Chiper, M.; Hager, M. D.; Schubert, U. S. Self-Assembly of Pi-Conjugated Bis(Terpyridine) Ligands with Zinc(II) Ions: New Metallosupramolecular Materials for Optoelectronic Applications. *J. Polym. Sci. Part A Polym. Chem.* **2009**, *47*, 4083–4098.

10. Kulbaba, K.; Manners, I. Polyferrocenylsilanes: Metal-Containing Polymers for Materials Science, Self-Assembly and Nanostructure Applications. *Macromol. Rapid Commun.* **2001**, *22* (10), 711–724.

11. Malenfant, P. R. L.; Wan, J.; Taylor, S. T.; Manoharan, M. Self-Assembly of an Organic-Inorganic Block Copolymer for Nano-Ordered Ceramics. *Nat. Nanotechnol.* **2007**, *2* (1), 43–46.

12. Hardy, C. G.; Zhang, J.; Yan, Y.; Ren, L.; Tang, C. Metallopolymers with Transition Metals in the Side-Chain by Living and Controlled Polymerization Techniques. *Prog. Polym. Sci.* **2014**, *39* (10), 1742–1796.

13. Zhang, J.; Ren, L.; Hardy, C. G.; Tang, C. Cobaltocenium-Containing Methacrylate Homopolymers, Block Copolymers, and Heterobimetallic Polymers via RAFT Polymerization. *Macromolecules* **2012**, *45* (17), 6857–6863.

14. Ren, L.; Zhang, J.; Bai, X.; Hardy, C. G.; Shimizu, K. D.; Tang, C. Preparation of Cationic Cobaltocenium Polymers and Block Copolymers by “Living” Ring-Opening Metathesis Polymerization. *Chem. Sci.* **2012**, *3* (2), 580–583.

15. Mîinea, L. A.; Sessions, L. B.; Ericson, K. D.; Glueck, D. S.; Grubbs, R. B. Phenylethynylstyrene-Cobalt Carbonyl Block Copolymer Composites. *Macromolecules* **2004**, *37* (24), 8967–8972.

16. Massey, J. A.; Temple, K.; Cao, L.; Rharbi, Y.; Raez, J.; Winnik, M. A.; Manners, I. Self-Assembly of Organometallic Block Copolymers: The Role of Crystallinity of the Core-Forming Polyferrocene Block in the Micellar Morphologies Formed by Poly(Ferrocenylsilane-b-Dimethylsiloxane) in n-Alkane Solvents. *J. Am. Chem. Soc.* **2000**, *122* (47), 11577–11584.

17. Jiang, B.; Hom, W. L.; Chen, X.; Yu, P.; Pavelka, L. C.; Kisslinger, K.; Parise, J. B.; Bhatia, S. R.; Grubbs, R. B. Magnetic Hydrogels from Alkyne/Cobalt Carbonyl-Functionalized ABA Triblock Copolymers. *J. Am. Chem. Soc.* **2016**, *138* (13), 4616–4625.

18. Chabanne, L.; Matas, I.; Patra, S. K.; Manners, I. Organic-Metalloblock Copolymers via Photocontrolled Living Anionic Ring-Opening Polymerization. *Polym. Chem.* **2011**, *2* (11), 2651–2660.

19. Al-Badri, Z. M.; Maddikeri, R. R.; Zha, Y.; Thaker, H. D.; Dobriyal, P.; Shunmugam, R.; Russell, T. P.; Tew, G. N. Room Temperature Magnetic Materials from Nanostructured Diblock Copolymers. *Nat. Commun.* **2011**, *2* (1), 482–485.

20. Bravaya, N. M.; Pomogailo, A. D.; Maksakov, V. A.; Kirin, V. P.; Grachev, V. P.; Kuzaev, A. I. Preparation and Reactivity of Metal Containing Monomers: 43. Synthesis and Properties of Copolymers of Styrene or Acrylonitrile with Triosmium Carbonyl Cluster Monomers. *Russ. Chem. Bull.* **1995**, *44* (6), 1062–1067.

21. Wing, Y. C.; Clendenning, S. B.; Berenbaum, A.; Lough, A. J.; Aouba, S.; Ruda, H. E.; Manners, I. Highly Metallized Polymers: Synthesis, Characterization, and Lithographic Patterning of Polyferrocenylsilanes with Pendant Cobalt, Molybdenum, and Nickel Cluster Substituents. *J. Am. Chem. Soc.* **2005**, *127* (6), 1765–1772.

22. Pomogailo, S. I.; Shilov, G. V.; Ershova, V. A.; Virovets, A. V.; Pogrebnyak, V. M.; Podberezskaya, N. V.; Golovin, A. V.; Dzhardimalieva, G. I.; Pomogailo, A. D. Preparation, X-Ray Structure, Copolymerization with Styrene of [(μ-H)Os3(μ-OCNMe2)(CO)9{P(CH 2CHCH2)Ph2}] and Catalytic Properties of the Cluster/Styrene Copolymer. *J. Organomet. Chem.* **2005**, *690* (19), 4258–4264.

23. Roy, X.; Lee, C.-H.; Crowther, a. C.; Schenck, C. L.; Besara, T.; Lalancette, R. a.; Siegrist, T.; Stephens, P. W.; Brus, L. E.; Kim, P.; et al. Nanoscale Atoms in Solid-State Chemistry Supplementary Data. *Science (80-.).* **2013**, *341* (6142), 157–160.

24. Choi, B.; Yu, J.; Paley, D. W.; Trinh, M. T.; Paley, M. V.; Karch, J. M.; Crowther, A. C.; Lee, C. H.; Lalancette, R. A.; Zhu, X.; et al. Van Der Waals Solids from Self-Assembled Nanoscale Building Blocks. *Nano Lett.* **2016**, *16* (2), 1445–1449.

25. Castleman Jr., A. W.; Khanna, S. N. Superatoms: Building Blocks of New Materials. *J. Phys. Chem. C.* **2009**, *113* (7), 2664–2675.

26. Kraft, S. J.; Sánchez, R. H.; Hock, A. S. A Remarkably Active Iron Catecholate Catalyst Immobilized in a Porous Organic Polymer. *ACS Catal.* **2013**, *3* (5), 826–830.

27. Hernández Sánchez, R.; Betley, T. A. Meta-Atom Behavior in Clusters Revealing Large Spin Ground States. *J. Am. Chem. Soc.* **2015**, *137* (43), 13949–13956..

28. Efremova, O. A.; Brylev, K. A.; Kozlova, O.; White, M. S.; Shestopalov, M. A.; Kitamura, N.; Mironov, Y. V.; Bauer, S.; Sutherland, A. J. Polymerisable Octahedral Rhenium Cluster Complexes as Precursors for Photo/Electroluminescent Polymers. *J. Mater. Chem. C* **2014**, *2* (40),

8630–8638.

29. Golubeva, N. D.; Adamenko, O. A.; Boiko, G. N.; Petrova, L. A.; Ol'khov, Y. A.; Pomogailo, A. D. Synthesis, Structure, and Properties of New Hybrid Nanocomposites Containing the [Mo6(M3-Cl)8]4+ Cluster. *Inorg. Mater.* **2004**, *40* (3), 306–313.

30. Gu, H.; Ciganda, R.; Hernández, R.; Castel, P.; Vax, A.; Zhao, P.; Ruiz, J.; Astruc, D. Diblock Metallocopolymers Containing Various Iron Sandwich Complexes: Living ROMP Synthesis and Selective Reversible Oxidation. *Polym. Chem.* **2016**, *7* (13), 2358–2371.

31. Wang, R.; Zheng, Z. Dendrimers Supported by the [Re6Se8]2+ Metal Cluster Core [11]. *J. Am. Chem. Soc.* **1999**, *121* (14), 3549–3550.

32. Bard, A. J.; Garcia, E.; Kukharenko, S.; Strelets, V. V. Electrochemistry of Metallocenes at Very Negative and Very Positive Potentials. Electrogeneration of 17-Electron Cp2Co2+, Cp2Co2−, and Cp2Ni2−Species. *Inorg. Chem.* **1993**, *32* (16), 3528–3531.

33. Geiger, W. E. Electroreduction of Cobaltocene. Evidence for a Metallocene Anion. *J. Am. Chem. Soc.* **1974**, *96* (8), 2632–2634.

34. Malischewski, M.; Adelhardt, M.; Sutter, J.; Meyer, K.; Seppelt, K. Isolation and Structural and Electronic Characterization of Salts of the Decamethylferrocene Dication. *Science (80-.).* **2016**, *353* (6300), 678–682.

35. Johnson, J. A.; Lu, Y. Y.; Burts, A. O.; Lim, Y.; Finn, M. G.; Koberstein, J. T.; Turro, N. J.; Tirrell, D. A.; Grubbs, R. H. Polymers by ROMP : Grafting-Through and Clicking-To. **2011**, No. 23, 559–566.

36. Matson, J. B.; Grubbs, R. H. Synthesis of Fluorine-18 Functionalized Nanoparticles for Use as in Vivo Molecular Imaging Agents. *J. Am. Chem. Soc.* **2008**, No. 130, 6731–6733.

37. Poly, N.; Liu, J.; Burts, A. O.; Li, Y.; Zhukhovitskiy, A. V; Ottaviani, M. F.; Turro, N. J.; Johnson, J. A. " Brush-First " Method for the Parallel Synthesis of Photocleavable, Nitroxide-Labeled Poly(Ethylene Glycol) Star Polymers. *J. Am. Chem. Soc.* **2012**, *134*, 16337–16344.

38. Sanford, M. S.; Love, J. A.; Grubbs, R. H. Mechanism and Activity of Ruthenium Olefin Metathesis Catalysts. **2001**, No. 15, 6543–6554.

39. Blanc, E.; Schwarzenbach, D.; Flack, H. D. Evaluation of Transmission Factors and Their First Derivatives with Respect to Crystal Shape Parameters. *J. Appl. Crystallogr.* **1991**, *24* (pt 6), 1035–1041.

40. Clark, R. C.; Reid, J. S. The Analytical Calculation of Absorption in Multifaceted Crystals. *Acta Crystallogr. Sect. A* **1995**, *A51*, 887–897.

41. Oxford Diffraction/Agilent Technologies UK Ltd. Version 1.171.37.35. Yarnton, England 2014.

42. Sheldrick, G. M. No Title. *Acta Crystallogr. Sect. A2* **2015**, *A71*, 3–8.

43. Dolomanov, O. V; Bourhis, L. J.; Gildea, R. J.; Howard, J. A. K.; Puschmann, H. OLEX2: A Complete Structure Solution, Refinement and Analysis Program. *J. Appl. Crystallogr.* **2009**, No. 42, 339–341.

44. CrystalMaker Software Ltd. Oxford, England.

Chapter 6

Surface binding of bisaminocyclopropenylidenes (BACs) on Au(111)

6.0 Preface

This chapter is adapted from a manuscript in preparation for publication of this research by Anastasia Voevodin, Evan Doud, Rachel Starr, Yaping Zang, Giacomo Lovat, Gregor Kladnik, Enrique Montes, Percy Zahl, Hector Vazquez, Latha Venkataraman, and Xavier Roy. Hector Vazquez and Enrique Montes at Institute of Physics, Academy of Sciences of the Czech Republic performed the computational work. Percy Zahl from the Center for Functional Nanomaterials at Brookhaven National Laboratory performed the single molecule imaging using STM-AFM with assistance from Yaping Zang (a post-doc in Prof. Latha Venkataraman's group at Columbia University). Prof. Latha Venkataraman, Giacomo Lovat, and Gregor Kladnik performed the NEXAFS measurements at the Elettra Synchotron Trieste in Italy. Dan Paley performed single crystal refinement. Evan Doud prepared the $NiBr_2(PPh_2)_2$ complex. I synthesized the BAC molecules and assisted with sample preparation for STM-AFM imaging.

6.1 Introduction

Cyclopropene chemistry has attracted interest from theoretical and experimental chemists because of its unique reactivity as the smallest unsaturated cyclic molecule.[1] The cyclopropenium ion is the smallest of the Huckel aromatic systems and has been widely explored for its synthetic utility in aromatic cation based catalysis.[2–4] Cyclopropenylidene[5,6] is the smallest aromatic carbene wherein one of the atoms in the three-membered ring is a divalent carbon and it is amongst the most studied compounds in the carbocyclic family. This class of carbenes has been widely explored in theoretical[7] and experimental studies as potential ligands for transition metals in preparation of synthetic catalysts. For example, several monomeric and dimeric palladium(II) complexes have been studied for their catalytic abilities in Suzuki[8], Heck[9], and C-N[10,9] coupling reactions. Bis(amino)cyclopropenylidenes (BACs) are a sub-class of cyclopropenylidenes where two of the ring's carbons are bonded to amino groups rather than alkanes. BACs were first isolated on the benchtop by Bertrand and co-workers in 2006.[11–13] Despite their instability in air, these molecules which behave as strong σ-donors, stabilized by nitrogens' π-donation, are kinetically and thermally stable[14,15] making them attractive targets as catalysts in organic synthetic reactions. The small steric properties of the molecule enable metal centers to accommodate multiple BAC ligands such as in substitution of triphenylphosphine, TMEDA, and COD ligands for BACs.[16]

BACs reactivity and use in catalysis is often compared to that of the more widely studied N-heterocyclic carbenes (NHCs) that are capable of binding to practically all transition metals. Like BACs, NHCs are a class of stable singlet carbenes, however these molecules have the divalent carbon atom bonded directly to the nitrogen substituents whereas in BACs the nitrogen substituents are one carbon atom further removed from the central carbene.[17] The difference in proximity of the stabilizing nitrogen atoms in NHCs vs BACs has pronounced effects on the carbene's reactivity and bonding capabilities to metals. Although both classes of carbenes bind strongly to metals by sigma-donation and have unique electronic structures,[5,18] NHCs have thus far attracted significantly more interest as exciting prospects for surface functionalization to target applications in selective heterogeneous catalysis,[19] nanotechnology,[19–21] and sensing.[20,22,23] Developing these technologies relies on the ability of electron-transport across the carbene-electrode interface which is dependent on the extent of coupling between metal surface and carbene molecule.

Although carbenes have been predominately explored for their use in catalysis of chemical reactions, NHCs have been recently introduced as exceptional molecules for the functionalization of gold surfaces. NHCs were reported to form ultra-stable bonds with gold atoms on Au(111) surfaces to form self-assembled monolayers (SAMs).[22,24] The binding orientation and related conductivity through the NHCs at the carbene-electrode junction was modified by varying the composition of the alkyl groups that are bound to the nitrogen atoms.[25,26] These recent initial explorations into the use of NHCs to form molecule-electrode interfaces offers new opportunities for the design of nanoscale electronic devices. The related class of carbenes, BACs to the best of our knowledge yet to be explored for their comparative potential as molecules for surface functionalization and design of molecule-electrode contacts.

Herein we use introduce BACs as a new molecule for surface gold functionalization. Beginning with the cyclopropenium cation, we report an efficient synthetic method to deposit pure BACs onto an Au(111) surface. We use synchrotron radiation to perform high-resolution X-ray photoelectron spectroscopy (HR-XPS) and near-edge X-ray photoelectron spectroscopy (NEXAFS), high-resolution scanning tunneling and atomic force microscopy (HR-STM/AFM), and combine these results with density functional theory (DFT) calculations to establish a detailed picture of the geometry and bonding of BACs onto Au(111) in ultra-high vacuum (UHV). HR-XPS combined with NEXAFS data provides chemically sensitive information on the core-level electron binding energies from the BAC-Au interactions to determine both the composition and orientation of the surface-bound molecules. HR-STM/AFM imaging and DFT calculations confirm the observations from HR-XPS and NEXAFS measurements to provide a fuller understanding of the first report of BACs bound to Au(111) surfaces. We also report a new transition metal complex of bis-adduct of BACs onto a nickel complex using the same carbonylated BAC precursor that is used for surface deposition onto gold. This study extends the library of molecules capable of surface functionalization onto gold and compares the binding motif, orientation and strength to that of previously reported surface metal NHC-Au bonds. It further shows how thermal annealing of surface-bound BACs results in the reorganization of the BACs on the gold surface.

6.2 Synthesis of BAC-CO_2

A bis(diisopropylamino)cyclopropenylidene sodium tetrafluoroborate carbene salt (BAC-BF_4) was prepared following previously reported procedures.[12] The free carbene was generated by deprotonation of bis(diisopropylamino)cyclopropenium salt with KHMDS (KHMDS = potassium bis(trimethylsilyl)amide) at low temperature in diethyl ether to form the free carbene (see Figure 6.1). The BAC-CO_2 adduct was made by removal of the diethyl ether solvent, re-dissolving the free carbene in hexanes, and bubbling carbon dioxide while stirring at room temperature.[27] An insoluble white BAC-CO_2 precipitate was visibly formed and isolated by removal of the solvent and purified with subsequent washes in hexanes. The BAC-CO_2 adduct has been previously reported,[27] but it has yet to be used as the precursor in forming transition metal complexes. Unlike the free BAC, the CO_2 adduct is relatively air stable allowing it to be a stable precursor for facile synthetic strategies.

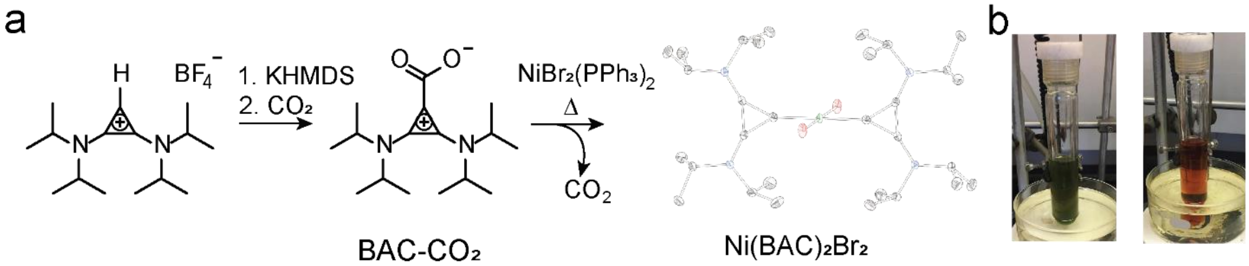

Figure 6.1. (a) Synthesis of Ni(BAC)$_2$Br$_2$ and its molecular structure as determine by single crystal x-ray diffraction. Color code: C, black; N, blue; Br, red; N, blue; Ni, green. Thermal ellipsoids are set at 50%. (b) Images showing the change in color from green to orange of after substitution of the triphenylphosphine ligands for BACs on the nickel complex.

As an exploratory reaction, the CO$_2$-adduct (BAC-CO$_2$) was reacted with dibromobis(triphenylphosphine)nickel(II) in dry toluene and heated to 110 °C overnight. As seen in Figure 6.1b, the starting green solution turned to a bright orange color after reaching 100^{o}C and was left overnight after which it was observed that the orange color had deepened, and the insoluble white precipitate disappeared. Orange crystals were grown and isolated of the complex and its molecular structure was determined using single X-ray diffraction (SCXRD) presented in Figure 6.1a. The structure shows the substitution of the triphenylphosphine ligands by the free BAC carbene that is formed after decarbonylation of the BAC-CO$_2$ precursor which occurs around 100°C. The bis-adduct of the BACs forms a square planar complex with Br-Ni-BAC angles measuring at 88.06° and 91.94°. The bond lengths in the BAC ring are slightly different, with the C2-C3 bond being about 0.02 Å (1.374 Å) shorter than the C1-C2 (1.392 Å) and C1-C3 (1.389 Å). Accordingly, the bond angles in the three-membered ring vary slightly as listed in Table 6.1. The bond lengths and angles in our nickel complex match well with previously reported bond lengths of BACs on transition metal complexes.[16]

Table 6.1. Bond lengths and angles of the BAC ring in [$NiBr_2(BAC)_2$]

Bond	Bond Length	Angle	°
C1-C2	1.392 Å	C1-C2-C3	60.3°
C1-C3	1.389 Å	C1-C3-C2	60.5°
C2-C3	1.374 Å	C2-C1-C3	59.2°
C1-Ni	1.896 Å		

Transition metal complexes featuring similar dimeric bonding of BAC onto the metal have been previously reported and their synthesis directly used the free carbene.[16,28] While the free carbene is highly reactive, it is also fairly unstable and care must be taken to ensure the molecule does not oxidize, decompose, or form other side products during synthesis. Using the BAC-CO_2 complex as the precursor eliminates the need to further purify the product and is an efficient reaction to generate transition metal complexes from air-stable precursors.

6.3 Surface functionalization of BACs on Au(111) surfaces

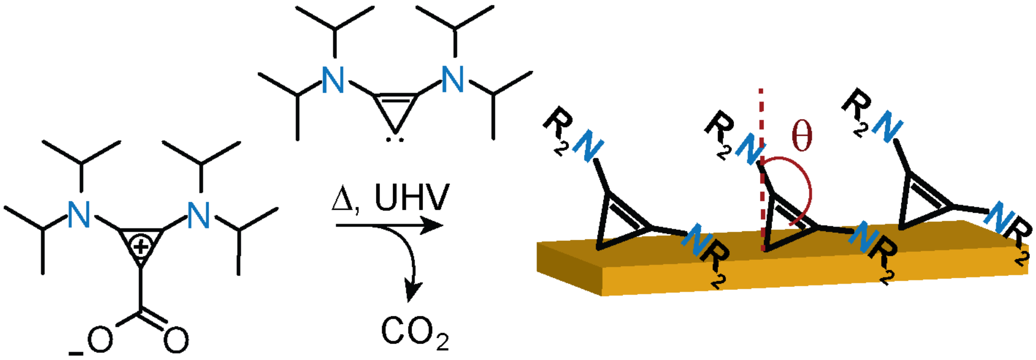

Figure 6.2. Deposition of BACs onto gold surfaces that occurs upon heating BAC-CO_2 under ultra-high vacuum in the presence of the gold substrate.

To prepare thin films of the cyclopropenylidene carbene onto Au(111) surfaces, a vacuum deposition method was used similar to that employed for the deposition of NHCs onto Au(111) surfaces.[25] Shown in Figure 6.3a, a sub-monolayer of BACs was prepared in UHV via thermal decomposition. In brief, a substrate with Au(111) deposited on mica was placed into a quartz tube on one end while at the opposite end of the tube, a small sample of BAC-CO_2 was placed. The tube was connected to the UHV and placed into a tube furnace. The furnace was heated to 110 °C overnight after which the BAC-CO_2 had disappeared. AFM images of the monolayer on the Au(111) surfaces in Figure 6.3b shows a drastic change in the surface roughness of the gold plateaus on the substrate after deposition.

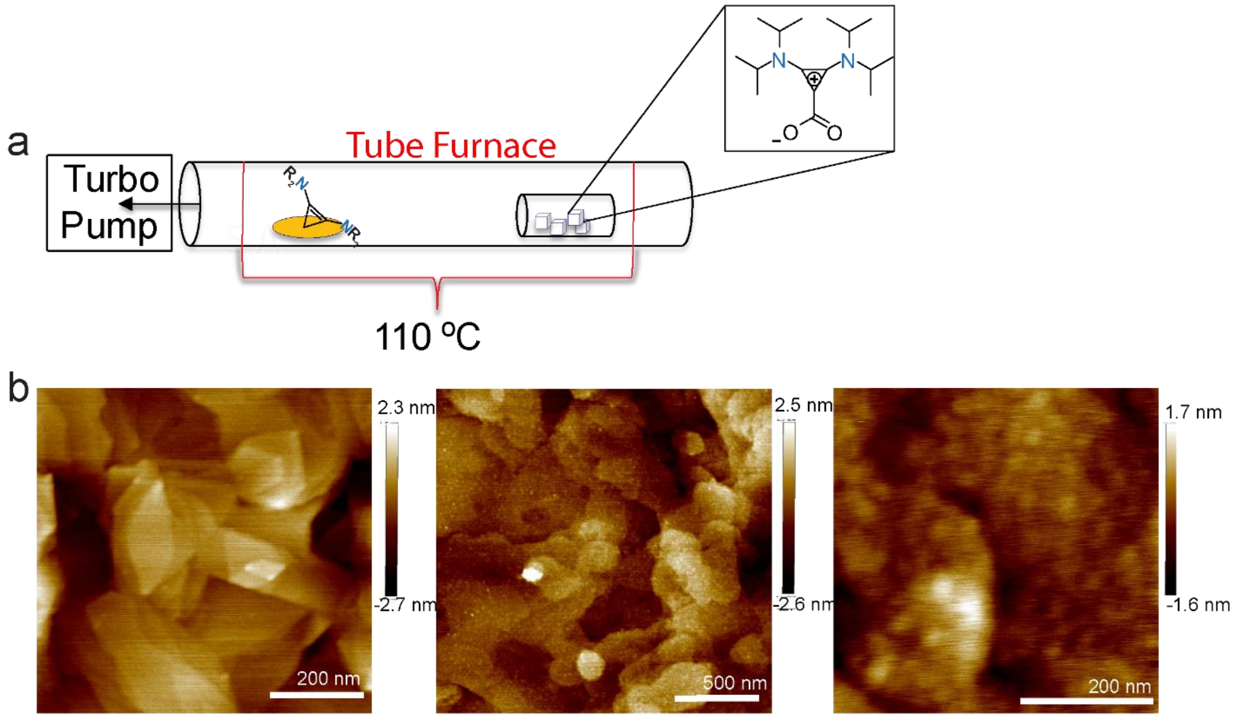

Figure 6.3. (a) Schematic showing the set-up for depositing BACs onto a gold surface under vacuum. The BAC-CO_2 was placed opposite of an annealed Au(111) substrate in a quartz tube which was connected to a turbo pump. The tube was heated to 110° overnight. (b) AFM images of clean annealed Au(111) on mica seen on the left before BAC deposition, and after deposition (middle and right) having greater surface roughness as compared to the clean gold substrate.

6.4 Determining the orientation of surface bound BAC

A similar procedure was performed in UHV via thermal decomposition/sublimation of BAC-CO_2 precursors onto a gold surface for NEXAFS and XPS measurements in a similar methodology as previously performed with NHC-CO_2 precursors.[25] Briefly, the precursors are placed in a Pyrex cell and connected to the pre-chamber through a leak valve. The cell is evacuated, heated to 110 °C and the carbene is introduced as a vapor into a pre-chamber containing a clean Au(111) crystal that was also heated to 110 °C. After deposition, X-ray photoelectron (XPS) results confirm the precursors have lost their CO_2 moieties by measuring the O 1s spectrum (see Figure 6.4). While the signals indicate the presence of carbon and nitrogen, there is no oxygen 1 s signal detected confirming successful thermal decomposition of the BAC-CO_2 molecule.

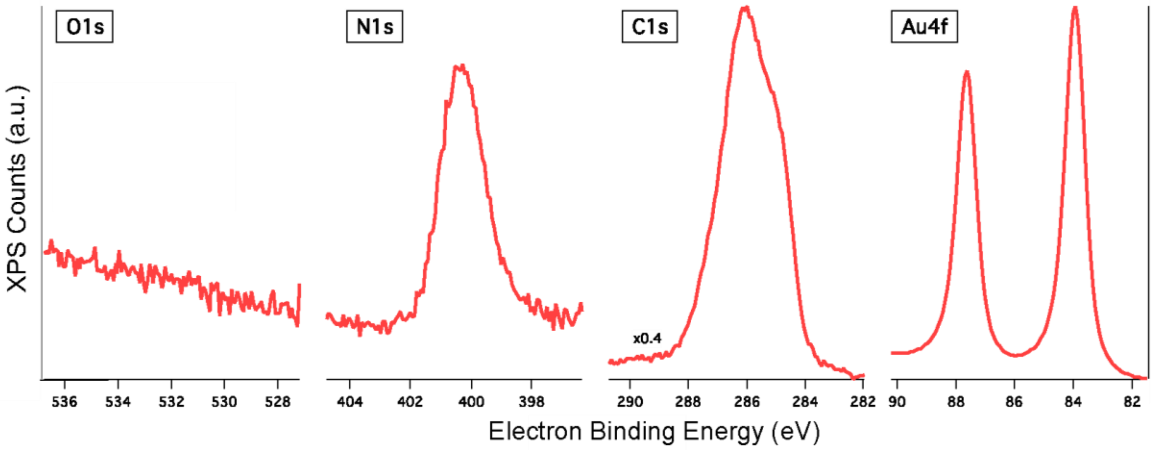

Figure 6.4. XPS O 1s, N 1s, C 1s, and Au 4f of BAC on Au(111). The XPS spectra shows no detection of oxygen on the sample, indicating complete decarboxylation of BAC-CO_2 after deposition.

Previous studies on the binding modes of NHCs onto gold surfaces have used NEXAFS and STM to determine the binding orientation of the free carbenes.[25] We have similarly explored the binding orientation of the cyclopropenylidene carbene on a gold surface. Our studies with BAC indicate a different binding orientation and strength in comparison to that of the NHCs. NEXAFS results indicate the orientation of the BAC relative to the Au(111) surface normal (defined as the tilt angle theta in Fig. 6.1). Figure 6.5a shows the NEXAFS spectra collected at the N K-edge with the electric field of the incident photons perpendicular (*p*-polarization) and parallel (*s*-polarization) to the surface for BAC. In Figure 6.5a we see that upon first deposition, two N 1s features are observed at 399 and 403 eV in both the *s*- and *p*-polarized orientations with little dichroism. The appearance of these features in both orientations indicate that the molecule is initially lying at an intermediate angle relative to the surface. After flash annealing of the sample at 155 °C, the dichroism is remarkably enhanced. The *p*-polarized X-rays show a merged peak of the two N 1s features into a single strong peak while the *s*-polarized shows no absorption of the irradiation. The enhanced dichroism following annealing of the sample is indicative of the molecule adopting relatively flat orientation onto the gold surface at an angle of ~26 degrees relative to the plane of the surface. In the case of the NHC carbenes, the intensity of the dichroism varied with variation of the alkyl substituents. In the case of NHCs with diisopropyl alkyl groups, the steric bulk of the groups forced the binding of the NHC carbene into a vertical orientation. For BACs the one-atom removal of the diisopropyl group from the cyclopropene ring, allows the relaxation of the molecule to lie flat onto the gold surface.

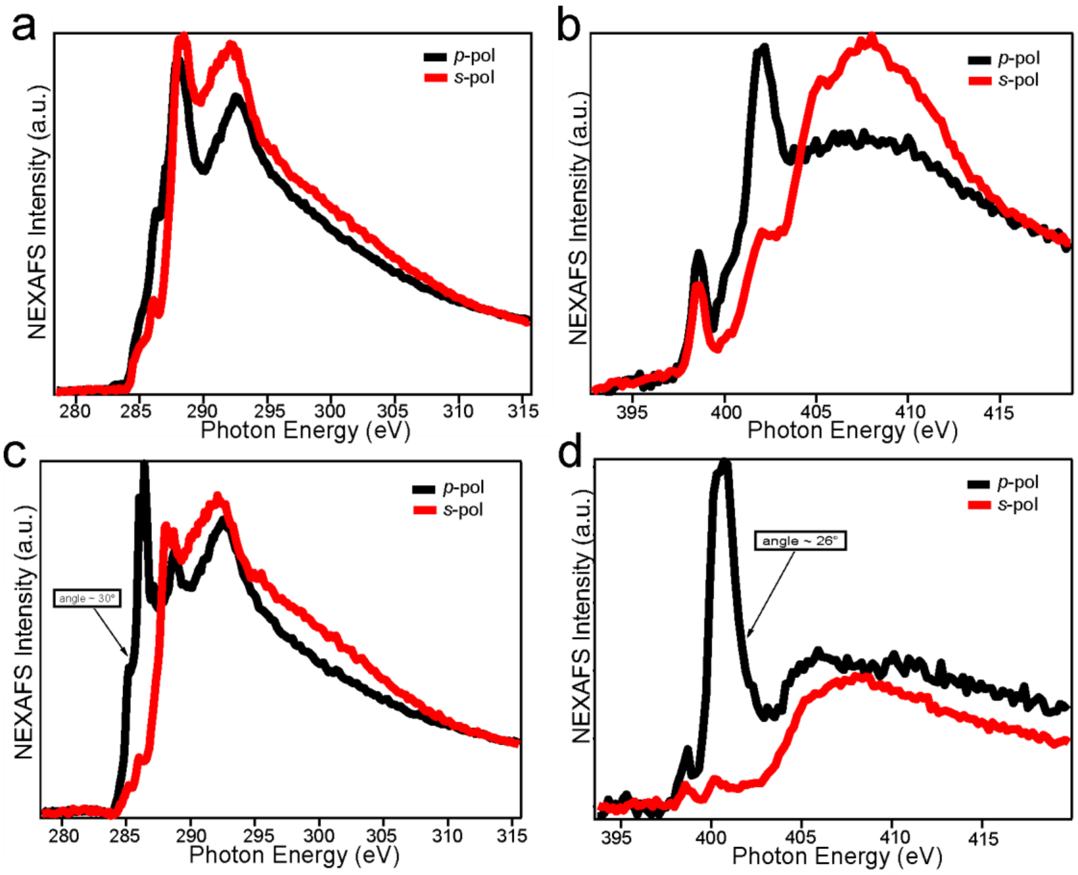

Figure 6.5. NEXAFS spectra collected of the carbon (a,c) and nitrogen (b,d) 1s with *s* and *p* polarizations shown in red and black traces, respectively. Top spectra (a,b) are measurements of the sample as deposited and bottom spectra (c,d) are after flash annealing of the sample to 150 °C. Magic angle computed from dichroism in spectra is shown in (c,d)

Another remarkable difference in the binding of the BAC (compared to that of the NHC adduct) is the absence of gold adatom formation with BACs. The XPS signal of the Au 4f core levels (Figure 6.6b) shows no satellite peaks indicative of adatom formation even after flash annealing the samples. The lack of adatom formation seen in the XPS spectra corroborates the observation that the BAC molecule lies relatively flat on the gold surface as shown in the NEXAFS spectra in Figure 6.6. NHCs show adatom formation upon binding to the gold surface after deposition and suggests that BAC-Au interface interactions are relatively weaker than those of NHC-Au.

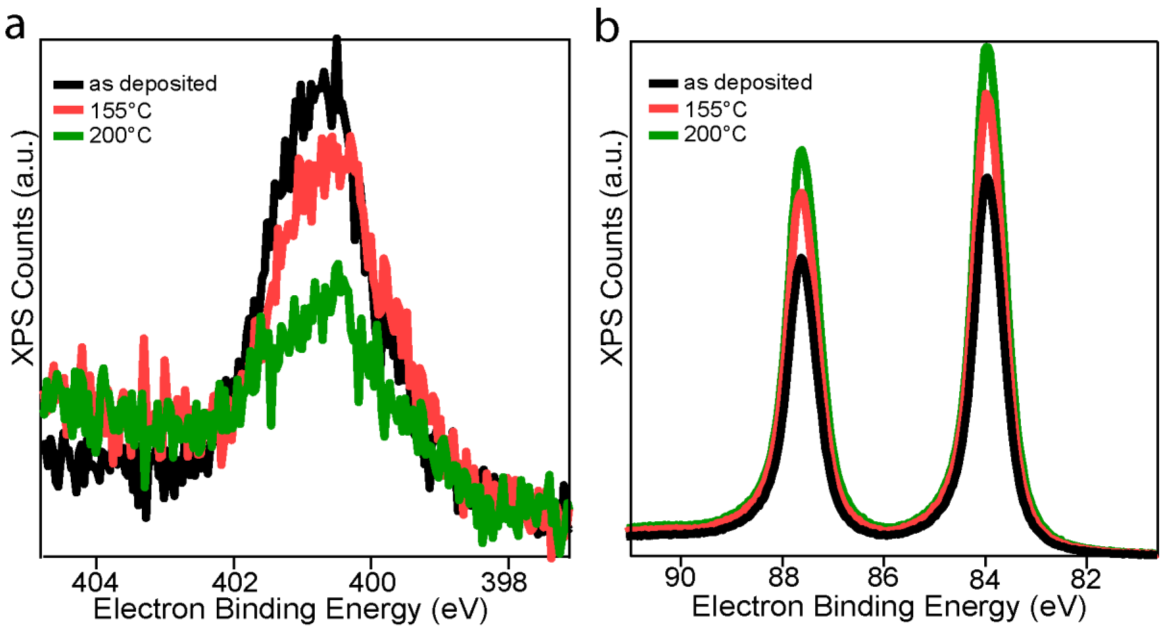

Figure 6.6. (a) XPS spectra of the N 1s (a) and Au 4f (b) signals after deposition (black), after flash annealing to 155 °C (red) and 200 °C (green).

A lack of screening related shifts of BE bands in the XPS after annealing suggest that thick layers on top of the gold surface were not formed. Additionally, after annealing, both the C 1s and N 1s signals show desorption related changes: the C 1s signal has a lower binding energy (BE) peak at 285.2 eV which remains constant after annealing, while the higher BE component at 286.0 eV is reduced. Upon flash annealing to 155 and 200 °C the intensity of the N 1s drops while the Au 4f satellites increase as more molecules are desorbed on the surface.

6.5 Single Molecule Imaging of BAC on Au(111)

Scanning tunneling microscopy (STM) and atomic force microscopy (AFM) are key tools for characterization in nanoscience. High resolution STM (HR-STM) imaging at low temperature can provide submolecular imaging of atomic and electronic structures of single molecules on surfaces. Single molecule imaging using HR-STM has widely been limited to that of planar molecules such as aromatic pentacene systems.[29] The relatively flat three-membered ring of the BAC gave us the opportunity to use HR-STM/AFM to image the binding of our BAC onto a gold surface.

Preparation of the sample was carried out as before: a small sample of BAC-CO_2 was deposited under UHV onto an annealed Au(111) surface that was attached to a thermocouple which was raised to 400 meV. A significant drop in pressure was quickly observed during deposition,

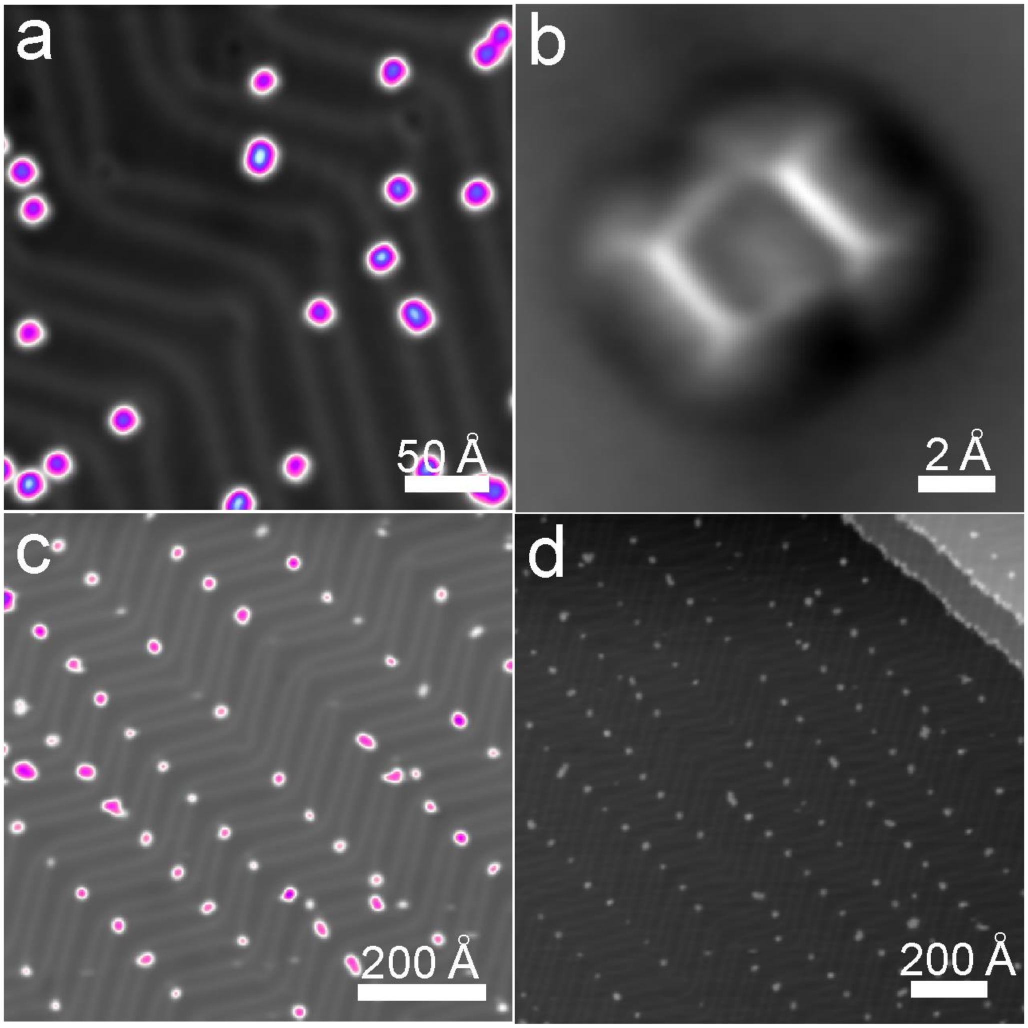

Figure 6.7. (a) STM image of BAC deposited onto gold substrate and a high-resolution AFM image in (b) of a single BAC molecule. (c) and (d) are STM images taken after flash annealing of the sample.

presumably indicating the thermal decomposition of the CO_2 moiety on the precursor. After stabilization of the vacuum, low-temperature STM and AFM imaging was carried out on the sample.

STM imaging of the deposited sample indicates a sub-monolayer deposition of the molecule suitable for targeting single molecule images. In Figure 6.7a we see several molecules having asymmetrical features. The triangular molecules generally have two higher-energy lobes and one lower energy feature as is more apparent in Figure 6.7b. Presumably the higher-energy lobes can be matched the bulky diisopropyl groups of the BAC molecule giving the molecule its asymmetric appearance.

Low-temperature AFM imaging was carried out on some of the single molecules. Figure 6.6c shows the AFM image of a single molecule BAC on the gold surface. The AFM image matches the flat orientation observed in the NEXAFS measurement. The skeleton of the bulky diisopropyl groups forms a U-type image with the corners of the U matching each of the four central carbons on the diisopropyl groups. Taking a line cut across the back of the single molecule

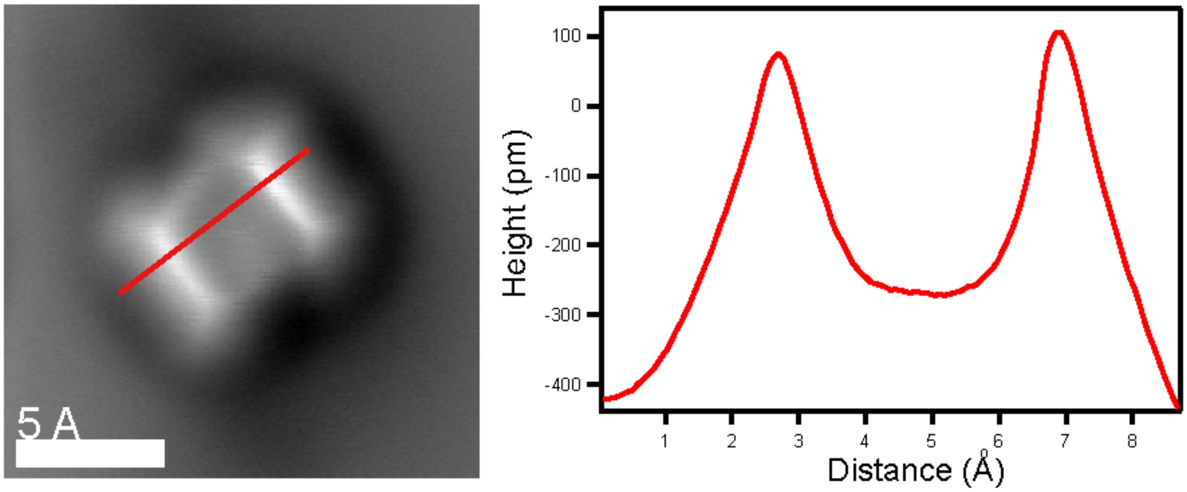

Figure 6.8. A line cut across the single molecule image of the BAC showing the feature heights of the two sides of the molecule. Measuring across this line cut gives a distance of roughly 4 Å, which corresponds to the N-N distance as measured from the BAC adduct on the nickel complex.

image as shown in Figure 6.8, the molecule measures roughly 4 Å across the two high-profile features. This measured distance matches with the N-N distance of 3.72 Å determined from the molecular structure of the $NiBr_2(BAC)_2$ complex described above. The three-membered ring is ostensibly hidden underneath the bulky alkyl groups, as is expected upon a somewhat planar orientation of the molecule to the gold surface.

A flash annealing of the molecule in the STM-AFM setup was carried out by raising the temperature to 110 ^oC for a few seconds. After re-stabilization of the low-temperature STM/AFM setup, AFM and STM imaging was attempted again. Remarkably, the flash annealing had a drastic effect on the arrangement of the molecules on the gold surface. After annealing, the molecules became mobile and primarily moved to the herringbone edges between the hcp and fcc domains and along the step edges of the Au(111) surface (Figure 6.8 c,d). This mobility upon annealing has been previously observed in AFM imaging of molecules along the surface.[30] The elbows of the gold herringbone structure stabilize the trapped molecules and provide a lowest-energy position for the mobile BACs. The weak binding of the molecules on the gold surface initially that was indicated by the lack of adatom formation and increased desorption after flash annealing in XPS measurements, ostensibly supports the ability of the molecules to become mobile and rearrange to lowest-energy positions on the gold surface after thermal treatment. Unfortunately, after annealing the high-resolution imaging of the molecules became impossible as the molecules continuously stuck to the STM tip during scanning.

6.6 Computational Studies

We perform DFT-based atomistic calculations to quantify the impact of the BAC structure and determine the strength of the BAC-Au interaction. We have considered two adsorption models for the molecules, a single BAC molecule adsorbed either on a pristine Au(111) surface or an Au adatom in a hollow site of the Au(111) surface. Geometry optimization calculations are performed using the SIESTA code,[31] considering an exchange correlation functional to account for Van der Waals interactions. The surface is modeled using a 3-layer Au(111) slab comprising 5×5 surface unit cells. The binding energy (BE) is defined as the difference between the energy of the combined system and the sum of the energies for each component separately. The tilt angle (Ɵ) between the

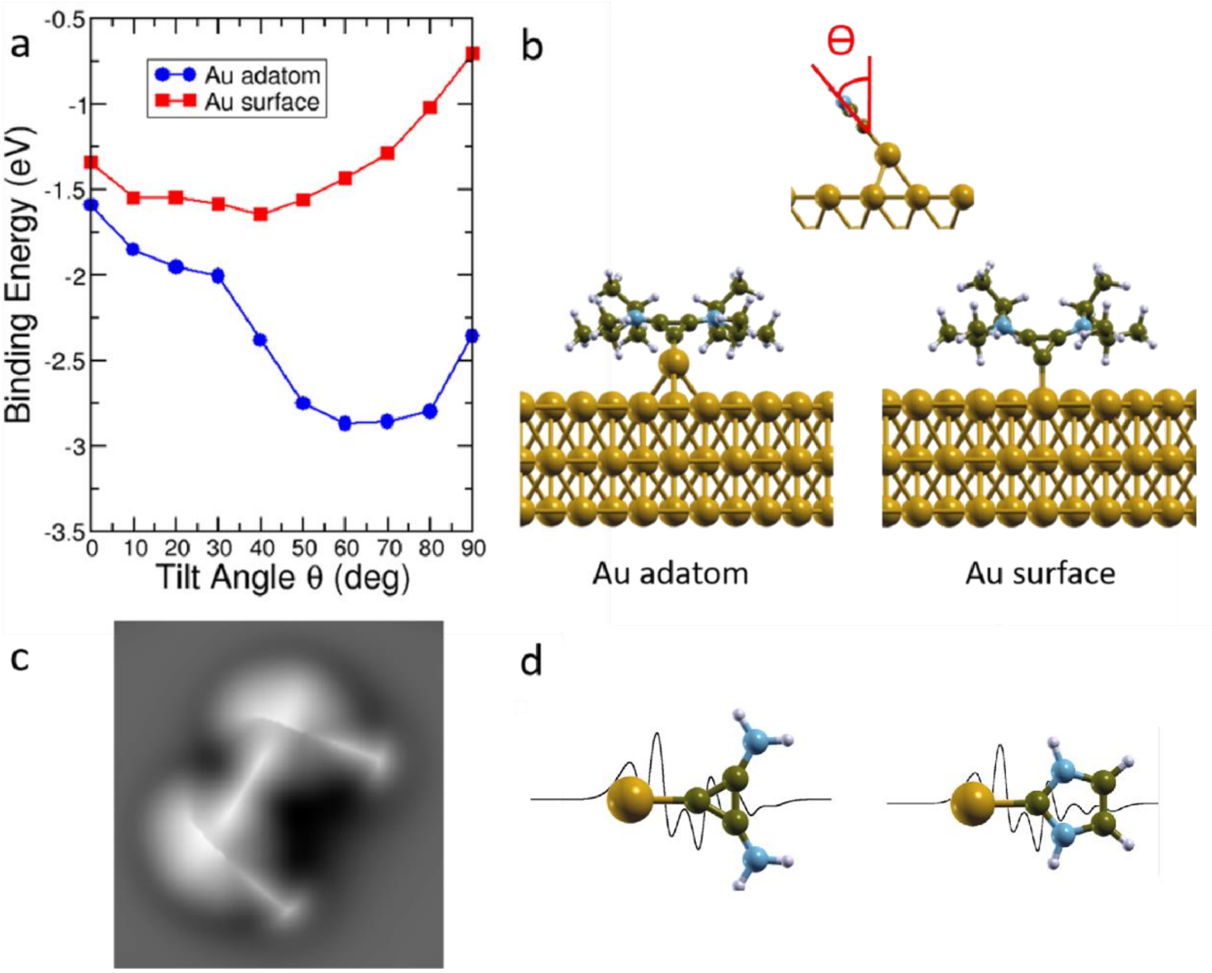

Figure 6.9. (a) Variation of the binding energy of BAC molecule adsorbed on either Au adatom and Au(111) surface. (b) Illustrative representation of tilt angle Ɵ and structures on their most stable conformation, BAC molecule adsorbed on Au adatom and Au(111) surface, Ɵ ~ 60deg and Ɵ ~ 40deg, respectively. (c) Simulated AFM image of BAC molecule adsorbed on Au adatom on its more stable conformation. (d) Plane-averaged charge density difference of BAC (left) and NHC (right) with passivated side groups bound to a single Au atom.

plane of the molecule and the vector normal to it is constrained by fixing the relative position of the atoms in the central ring of the BAC molecule (one C and two N) without restricting their displacement as a rigid unit.

The variation of the BE as a function of the tilt angle is presented in Figure 6.9a, and in Figure 6.9b we present a representative plot that illustrates the way in which the tilt angle is determined, and the way BAC is adsorbed on an Au adatom and on the Au(111) surface for their most stable conformations, with tilt angles of ϴ ~ 60 deg and ϴ ~ 40 deg, respectively. The binding energy for the molecule adsorbed on an Au adatom is -2.87 eV, more than 1 eV larger than when the molecule is absorbed on the flat Au(111) surface (-1.65 eV). The stronger binding of the molecule on an Au adatom results in a stronger donor-acceptor bond resulting in a shorter BAC-Au bond length when the molecule of 2.07 Å, as compared to adsorption on the Au(111) surface resulting in a BAC-Au bond length of 2.20 Å. Using the probe particle model[29] we have simulated the AFM image of the BAC molecule adsorbed on the Au adatom in the most stable conformation (ϴ ~ 60 deg) and we present it in Fig. 6.9c. The simulated image compares directly with the experimental HR-AFM image in Figure 6.7b and 6.8 with both images having a U-type shape of the BAC molecule on the gold surface.

In order to study the chemical strength of BAC molecule, we compare the binding energy of the BAC molecule adsorbed on an Au adatom with the adsorption energy of NHC carbene which was previously shown to be more energetically favorable.[25] At its most stable conformation (ϴ ~ 70 deg) the binding energy of the NHC molecule is -2.23 eV, about 0.6 eV smaller than for BAC molecule as seen in Figure 6.10. For small tilt angles (ϴ < 30 deg) the binding energies of both molecules are rather similar, while they have large differences for higher tilt angles. In general, this can be attributed to the bulkier side groups of BAC molecule and its Van der Waals interaction with the Au surface.

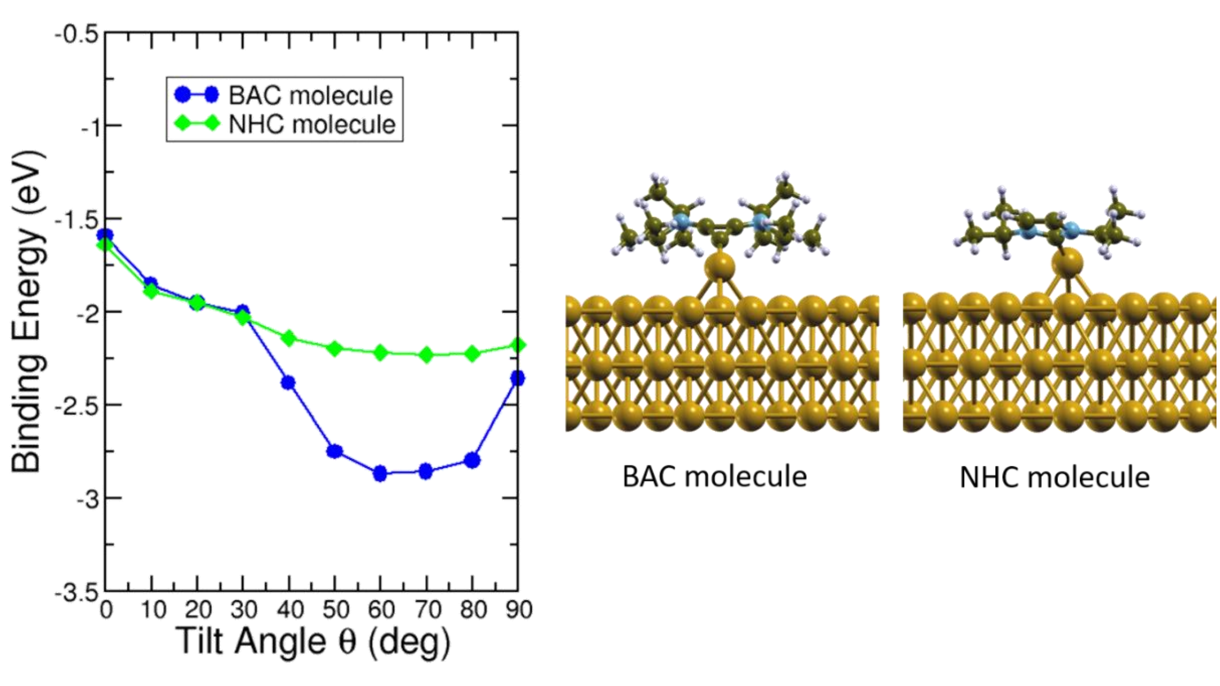

Figure 6.10. Comparison of binding energy for BAC and NHC molecules adsorbed on Au adatom as a function of tilt angle Θ.

However, the nature of the carbene central groups must play a key role for the higher binding energies. Therefore, we studied the charge transfer upon adsorption for BAC and NHC's carbene central groups, where the bulky alkyl side groups are passivated with H atoms bonded to a single Au atom. The charge density difference is defined in terms of the plane-averaged difference between the electron density of the combined system and that of its components separately. For charge density difference of BAC and NHCs is plotted in Figure 6.9. Inside the molecule, negative charge difference corresponds to electron depletion, while positive charge difference corresponds to electron accumulation; which is the more evident behavior at the Au atom. Therefore, molecules behave as charge donors. The net charge is calculated by integrating the plane-averaged charge density difference between negative infinite position to the Au-C midpoint, in agreement with previous works.[32] BAC molecule transfers 0.18 electrons to the Au atom, while NHC molecule transfers 0.17 electrons to the Au atom.

Additionally, states of BAC molecules show a stronger hybridization than NHC molecule to an Au adatom. In Figure 6.11 we plot the density of states projected on the atoms involved in bonding for BAC and NHC molecules adsorbed on Au adatom, i.e. the lower carbon atom of carbene ring (C1) and the Au adatom. This shows the stronger hybridization of C1 with an Au atom for the BAC molecule as compared to that of NHC.

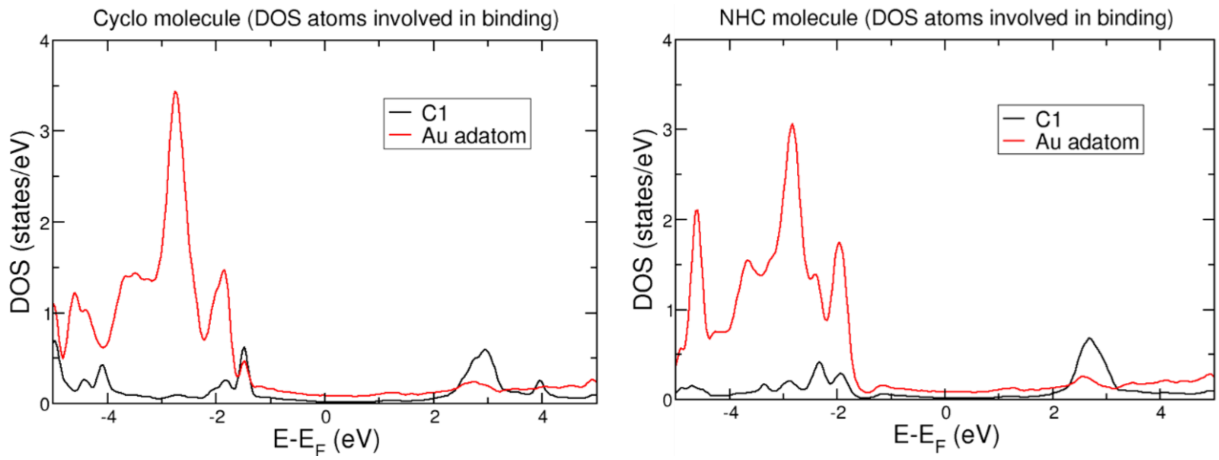

Figure 6.11. Density of states projected on atoms involved on binding for BAC and NHC molecules adsorbed on Au adatom.

6.7 Conclusion

The isolation of cyclopropenylidenes has been relatively recent, and this class of carbenes has yet to be explored for its application in materials chemistry. Inspired by recent work that showed NHCs as possible alternative candidates to form stable molecule-gold bonds, we carried out an initial exploration into the ability of BACs to bind to gold surfaces. By combining high resolution X-ray photoelectron spectroscopy, high resolution atomic force and scanning tunneling microscopy, and computational modeling, this work is the first demonstration of binding BACs to metal surfaces. Through our studies we can determine the adsorption energy, molecular orientation, and metal surface structure in a sub-monolayer of deposited BAC molecules. We show that BACs with diisopropyl moieties adopt a relatively flat geometry on gold surfaces and form weaker bonds with gold atoms on the surface. We expect that future investigations with modified alkyl substituents on the BAC molecules could indicate new binding motifs and interactions with Au surfaces.

6.8 Methods

NMR Spectroscopy.

^{1}H NMR and ^{31}P NMR spectra were recorded on a Bruker DRX400 spectrometer.

Atomic Force Microscopy (AFM).

AFM images were acquired in PeakForce QNM tapping mode using a Bruker Dimension FastScan AFM.

Single Crystal X-Ray Diffraction.

Crystallographic data was collected on an Agilent SuperNova diffractometer using mirror-monochromated Cu Kα radiation.

Scanning Tunneling Microscopy and Atomic Force Microscopy.

HR-STM/AFM images were acquired at Brookhaven National Laboratories at the Center for Functional Nanomaterials using a customized Createc low-temperature UHV scanning tunneling and atomic force microscope (NC-AFM/STM). Sample NC-AFM data (frequency shift) of custom designed precursors molecules which were surface synthesized into GNR assemblies. Data acquired using GXSM-3.0 + SR-MK3-A810/PLL operating a modified CREATEC based LT-STM/AFM in force detection mode, constant height operation at approx. 70pm oscillation amplitude using a Q-Plus (TM Franz J. Giessibl) Sensor @29.84kHz and a "magic" functionalized tip not to be disclosed here. Sample preparation chamber equipped with liquid helium cooled manipulator and low-energy electron diffraction. Fast exchange deposition source port, various gas and molecule dosing options "in-situ" at low temperature.

6.9 Synthetic Details

Synthesis of BAC-BF_4:

A previously reported literature was followed.[12]

Synthesis of BAC-CO_2:

A previously reported literature procedure was followed.[27]

Synthesis of [$NiBr_2(BAC)_2$]:

In a nitrogen-filled glovebox, BAC-CO_2 (40 mgs, 0.142 mmol) was added to a solution of $NiBr_2(PPh_3)_2$ (53 mgs, 0.071 mmol) in 20 mL of toluene in a pressure vessel. The reaction was heated to 110 ^oC overnight. Upon heating to 100^oC, a change in color from green to orange was observed and the insoluble BAC-CO_2 compound began to dissolve into solution. The reaction was cooled to room temperature and the solvent was removed under vacuum. The product was re-dissolved (~3 mL) and layered with hexanes. After several days, several long needle-type crystals had formed. The solution was decanted, and the crystals were collected and transferred to STP oil treatment for crystallography.

6.10 Computational Details

We use SIESTA to simulate the adsorption of BAC and NHC on Au(111) surface. We use an exchange correlation functional that accounts for the Van der Waals iteration. All structures were fully relaxed until the Hellmann-Feynman forces are smaller than 0.02 eV/Å and the energies calculated on a 2×2×1 Monkhorst pack grid. Adsorption relaxation were performed using a 3-layer Au(111) slab with 5×5 surface unit cells. The pristine surface and surface with an Au adatom were first optimized prior to optimizing the adsorption of molecules. The tilt angle is defined with the plane of central carbine ring and its normal vector. The tilt angle is constrained by fixing the relative position of the atoms in the central carbine ring of the without restricting their displacement as a rigid unit. Initially the molecules are relaxed without its side groups, in order to allow a faster movement on central carbene ring, following the side groups are added and the system is relaxed, always keeping the last two Au(111) constrained in position. The binding energy is calculated as the difference between the energy of the combined system and the sum of the energies for each component separately were the use of ghost atoms is employed.

We show the comparison of binding energy between BAC molecule and NHC, both adsorbed on an Au adatom.

6.11 Single crystal X-ray diffraction

Data for all compounds was collected on an Agilent SuperNova diffractometer using mirror-monochromated Cu Kα radiation. Data collection, integration, scaling (ABSPACK) and absorption correction (face-indexed Gaussian integration[33] or numeric analytical methods[34]) were performed in CrysAlisPro.[35] Structure solution was performed using ShelXT.[36] Subsequent refinement was performed by full-matrix least-squares on F^2 in ShelXL.[37] Olex2[38] was used for viewing and to prepare CIF files. Disordered toluene was modeled as rigid fragments with coordinates taken from the Idealized Molecular Geometry Library.[39]

The refinement was routine and all non-H atoms were refined with anistropic ADPs and no restraints. C-H hydrogens were placed in calculated positions and refined with riding coordinates and ADPs.

6.10. Selected Crystallographic Data

Table 6.2. Selected crystallographic data for [$NiBr_2(BAC)_2$]

Compound	**$NiBr_2(BAC)_2$**
Formula	$C_{30}H_{56}Br_2N_4Ni$
MW	691.31
Space group	$P2_1/n$
a (Å)	9.52430(10)
b (Å)	11.77890(10)
c (Å)	15.2851(2)
α (°)	90
β (°)	104.9470(10)
γ (°)	90
V (Å^3)	1656.75(3)
Z	2
ρ_{calc} (g cm^{-3})	1.386
T (K)	100
λ (Å)	1.54184
$2\theta_{min}$, $2\theta_{max}$	10, 146
Nref	17679
R(int), R(σ)	.0203, .0150
μ(mm^{-1})	3.837
Size (mm)	.25 x .09 x .07
T_{max} / T_{min}	2.5
Data	3309
Restraints	0
Parameters	177
R_1(obs)	0.0201
wR_2(all)	0.0519
S	1.072
Peak, hole (e^- Å^{-3})	0.37, -0.20

6.12. References

1. Zhu, Z. Bin; Wei, Y.; Shi, M. Recent Developments of Cyclopropene Chemistry. *Chem. Soc. Rev.* **2011**, *40* (11), 5534–5563.

2. Krebs, A. W. Cyclopropenylium Compounds and Cyclopropenones. *Angew. Chemie Int. Ed. English* **2003**, *4* (1), 10–22.

3. Vanos, C. M.; Lambert, T. H. Cyclopropenium-Activated Beckmann Rearrangement. Catalysis versus Self-Propagation in Reported Organocatalytic Beckmann Rearrangements. *Chem. Sci.* **2010**, *1* (6), 705–708.

4. D'yakonov, I. A.; Kostikov, R. R. The Cyclopropenyl Cation. *Russ. Chem. Rev.* **1967**, *36* (8), 557–563.

5. Öfele, K.; Tosh, E.; Taubmann, C.; Herrmann, W. A. Carbocyclic Carbene Metal Complexes. *Chem. Rev.* **2009**, *109* (8), 3408–3444.

6. Melaimi, M.; Jazzar, R.; Soleilhavoup, M.; Bertrand, G. Cyclic (Alkyl)(Amino)Carbenes (CAACs): Recent Developments. *Angew. Chemie - Int. Ed.* **2017**, *56* (34), 10046–10068.

7. Hemberger, P.; Noller, B.; Steinbauer, M.; Fischer, I.; Alcaraz, C.; Cunha De Miranda, B. K.; Garcia, G. A.; Soldi-Lose, H. Threshold Photoelectron Spectroscopy of Cyclopropenylidene, Chlorocyclopropenylidene, and Their Deuterated Isotopomeres. *J. Phys. Chem. A* **2010**, *114* (42), 11269–11276.

8. Herrmann, W. A.; Öfele, K.; Taubmann, C.; Herdtweck, E.; Hoffmann, S. D. Catalysis of CC-Coupling Reactions by Cyclopropenylidene Palladium Complexes. *J. Organomet. Chem.* **2007**, *692* (18), 3846–3854.

9. Wass, D. F.; Hey, T. W.; Rodriguez-Castro, J.; Russell, C. A.; Shishkov, I. V.; Wingad, R. L.; Green, M. Cyclopropenylidene Carbene Ligands in Palladium C-N Coupling Catalysis. *Organometallics* **2007**, *26* (19), 4702–4703.

10. Taubmann, C.; Tosh, E.; Öfele, K.; Herdtweck, E.; Herrmann, W. A. Carbocyclic Carbene Ligands in Palladium-Catalyzed C-N Coupling Reactions. *J. Organomet. Chem.* **2008**, *693* (13), 2231–2236.

11. Lavallo, V.; Canac, Y.; Donnadieu, B.; Schoeller, W. W.; Bertrand, G. Cyclopropenylidenes : From Interstellar in the Laboratory. *Science (80-.).* **2006**, *312* (May), 722–725.

12. Lavallo, V.; Ishida, Y.; Donnadieu, B.; Bertrand, G. Isolation of Cyclopropenylidene-Lithium Adducts: The Weiss-Yoshida Reagent. *Angew. Chemie - Int. Ed.* **2006**, *45* (40), 6652–6655.

13. Kinjo, R.; Ishida, Y.; Donnadieu, B.; Bertrand, G. Isolation of Bicyclopropenylidenes: Derivatives of the Smallest Member of the Fulvalene Family. *Angew. Chemie - Int. Ed.* **2009**, *48* (3), 517–520.

14. Pintér, B.; Veszprémi, T. Synthesizability of the Heavy Analogues of Disubstituted Cyclopropenylidene: A Theoretical Study. *Organometallics* **2008**, *27* (21), 5571–5576.

15. Johnson, L. E.; Dupré, D. B. Mechanism of the Electronic Stabilization of the 3MR and Divalent Carbon of Bis(Diisopropylamino)Cyclopropenylidene. *J. Phys. Chem. A* **2007**, *111* (43), 11066–11073.

16. Kuchenbeiser, G.; Donnadieu, B.; Bertrand, G. Stable Bis(Diisopropylamino)Cyclopropenylidene (BAC) as Ligand for Transition Metal Complexes. *J. Organomet. Chem.* **2008**, *693* (5), 899–904.

17. Arduengo, A. J. Looking for Stable Carbenes: The Difficulty in Starting Anew. *Acc. Chem. Res.* **1999**, *32* (11), 913–921.

18. Hopkinson, M. N.; Richter, C.; Schedler, M.; Glorius, F. An Overview of N-Heterocyclic Carbenes. *Nature* **2014**, *510* (7506), 485–496.

19. Herrmann, W. A.; Elison, M.; Fischer, J.; Köcher, C.; Artus, G. R. J. Metal Complexes of N-Heterocyclic Carbenes—A New Structural Principle for Catalysts in Homogeneous Catalysis. *Angew. Chemie Int. Ed. English* **1995**, *34* (21), 2371–2374.

20. Zhukhovitskiy, A. V.; Mavros, M. G.; Van Voorhis, T.; Johnson, J. A. Addressable Carbene Anchors for Gold Surfaces. *J. Am. Chem. Soc.* **2013**, *135* (20), 7418–7421.

21. Zhukhovitskiy, A. V.; MacLeod, M. J.; Johnson, J. A. Carbene Ligands in Surface Chemistry: From Stabilization of Discrete Elemental Allotropes to Modification of Nanoscale and Bulk Substrates. *Chem. Rev.* **2015**, *115* (20), 11503–11532.

22. Crudden, C. M.; Horton, J. H.; Narouz, M. R.; Li, Z.; Smith, C. A.; Munro, K.; Baddeley, C. J.; Larrea, C. R.; Drevniok, B.; Thanabalasingam, B.; et al. Simple Direct Formation of Self-Assembled N-Heterocyclic Carbene Monolayers on Gold and Their Application in Biosensing. *Nat. Commun.* **2016**, *7*, 1–7.

23. Weidner, T.; Baio, J. E.; Mundstock, A.; Große, C.; Kartha¨user, S.; Bruhn, C.; Ulrich Siemeling. NHC-Based Self-Assembled Monolayers on Solid Gold Substrates. *Aust. J. Chem.* **2011**, *64*, 1177–1179.

24. Crudden, C. M.; Horton, J. H.; Ebralidze, I. I.; Zenkina, O. V.; McLean, A. B.; Drevniok, B.; She, Z.; Kraatz, H. B.; Mosey, N. J.; Seki, T.; et al. Ultra Stable Self-Assembled Monolayers of N-Heterocyclic Carbenes on Gold. *Nat. Chem.* **2014**, *6* (5), 409–414.

25. Lovat, G.; Doud, E.; Lu, D.; Kladnik, G.; Inkpen, Mi.; Steigerwald, M. L.; Cvetko, D.; Hybertsen, M.; Morgante, A.; Roy, X.; et al. Determination of the Structure and Geometry of N-Heterocyclic Carbenes on Au(111) Using High-Resolution Spectroscopy. *Chem. Sci.* **2019**, 930–935.

26. Doud, E. A.; Inkpen, M. S.; Lovat, G.; Montes, E.; Paley, D. W.; Steigerwald, M. L.; Vázquez, H.; Venkataraman, L.; Roy, X. In Situ Formation of N-Heterocyclic Carbene-Bound Single-Molecule Junctions. *J. Am. Chem. Soc.* **2018**, *140* (28), 8944–8949.

27. Kuchenbeiser, G.; Soleilhavoup, M.; Donnadieu, B.; Bertrand, G. Reactivity of Cyclic (Alkyl)(Amino)Carbenes (CAACs) and Bis(Amino)Cyclopropenylidenes (BACs) with Heteroallenes: Comparisons with Their N-Heterocyclic Carbene (NHCs) Counterparts. *Chem. - An Asian J.* **2009**, *4* (11), 1745–1750.

28. Lavallo, V.; El-Batta, A.; Bertrand, G.; Grubbs, R. H. Insights into the Carbene-Initiated Aggregation of [Fe(Cot)2]. *Angew. Chemie - Int. Ed.* **2011**, *50* (1), 268–271.

29. Hapala, P.; Kichin, G.; Wagner, C.; Tautz, F. S.; Temirov, R.; Jelínek, P. Mechanism of High-Resolution STM/AFM Imaging with Functionalized Tips. *Phys. Rev. B - Condens. Matter Mater. Phys.* **2014**, *90* (8), 1–9.

30. Böhringer, M.; Morgenstern, K.; Schneider, W. D.; Berndt, R. Reversed Surface Corrugation in STM Images on Au(111) by Field-Induced Lateral Motion of Adsorbed Molecules. *Surf. Sci.* **2000**, *457* (1), 37–50.

31. Soler, J. M.; Artacho, E.; Gale, J. D.; Garcia, A.; Junquera, J.; Ordej, P.; Sanchez-Portal, D. The SIESTA Method for Ab Initio Order- N Materials. *IOP Sci.* **2002**, *14*, 2745–2779.

32. Foti, G.; Vázquez, H. Tip-Induced Gating of Molecular Levels in Carbene-Based Junctions. *Nanotechnology* **2016**, *27* (12).

33. Blanc, E.; Schwarzenbach, D.; Flack, H. D. Evaluation of Transmission Factors and Their First Derivatives with Respect to Crystal Shape Parameters. *J. Appl. Crystallogr.* **1991**, *24* (pt 6), 1035–1041.

34. Clark, R. C.; Reid, J. S. The Analytical Calculation of Absorption in Multifaceted Crystals. *Acta Crystallogr. Sect. A* **1995**, *A51*, 887–897.

35. Diffraction/Agilent Technologies UK Ltd Yarnton, England, 2014.

36. Sheldrick, G. M. No Title. *Acta Crystallogr. Sect. A2* **2015**, *A71*, 3–8.

37. Sheldrick, G. M. Crystal Structure Refinement with SHELXL. *Acta Crystallogr. Sect. C* **2015**, *C71*, 3–8.

38. Dolomanov, O. V; Bourhis, L. J.; Gildea, R. J.; Howard, J. A. K.; Puschmann, H. OLEX2: A Complete Structure Solution, Refinement and Analysis Program. *J. Appl. Crystallogr.* **2009**, No. 42, 339–341.

39. Guzei, I. A. An Idealized Molecular Geometry Library for Refinement of Poorly Behaved Molecular Fragments with Constraints. *J. Appl. Crystallogr.* **2014**, *47*, 806–809.